frontiers | Research Topics

Current trends in targeted and non-targeted metabolomics in analytical toxicology

Edited by
Geraldine M. Dowling and Markus R. Meyer

Published in
Frontiers in Molecular Biosciences

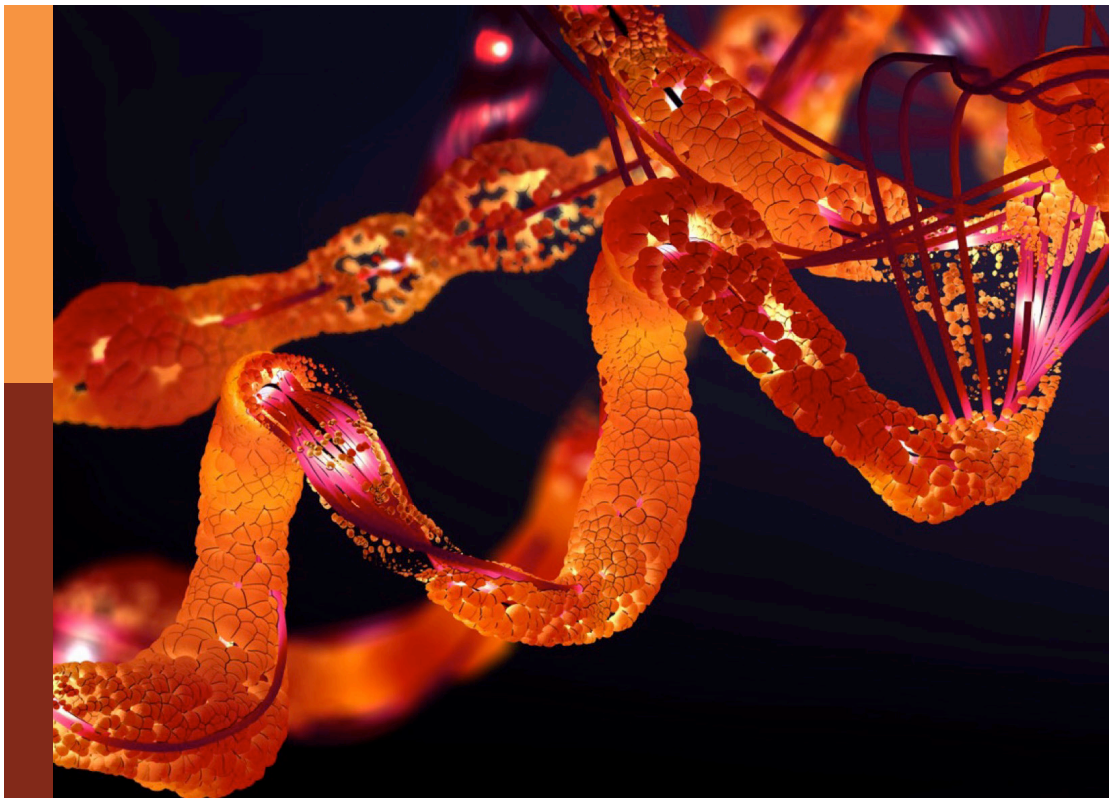

ISSN 1664-8714
ISBN 978-2-8325-6471-4
DOI 10.3389/978-2-8325-6471-4

About Frontiers

Frontiers is more than just an open access publisher of scholarly articles: it is a pioneering approach to the world of academia, radically improving the way scholarly research is managed. The grand vision of Frontiers is a world where all people have an equal opportunity to seek, share and generate knowledge. Frontiers provides immediate and permanent online open access to all its publications, but this alone is not enough to realize our grand goals.

Frontiers journal series

The Frontiers journal series is a multi-tier and interdisciplinary set of open-access, online journals, promising a paradigm shift from the current review, selection and dissemination processes in academic publishing. All Frontiers journals are driven by researchers for researchers; therefore, they constitute a service to the scholarly community. At the same time, the *Frontiers journal series* operates on a revolutionary invention, the tiered publishing system, initially addressing specific communities of scholars, and gradually climbing up to broader public understanding, thus serving the interests of the lay society, too.

Dedication to quality

Each Frontiers article is a landmark of the highest quality, thanks to genuinely collaborative interactions between authors and review editors, who include some of the world's best academicians. Research must be certified by peers before entering a stream of knowledge that may eventually reach the public - and shape society; therefore, Frontiers only applies the most rigorous and unbiased reviews. Frontiers revolutionizes research publishing by freely delivering the most outstanding research, evaluated with no bias from both the academic and social point of view. By applying the most advanced information technologies, Frontiers is catapulting scholarly publishing into a new generation.

What are Frontiers Research Topics?

Frontiers Research Topics are very popular trademarks of the *Frontiers journals series*: they are collections of at least ten articles, all centered on a particular subject. With their unique mix of varied contributions from Original Research to Review Articles, Frontiers Research Topics unify the most influential researchers, the latest key findings and historical advances in a hot research area.

Find out more on how to host your own Frontiers Research Topic or contribute to one as an author by contacting the Frontiers editorial office: frontiersin.org/about/contact

Current trends in targeted and non-targeted metabolomics in analytical toxicology

Topic editors

Geraldine M. Dowling — Atlantic Technological University, Ireland

Markus R. Meyer — Saarland University, Germany

Citation

Dowling, G. M., Meyer, M. R., eds. (2025). *Current trends in targeted and non-targeted metabolomics in analytical toxicology*. Lausanne: Frontiers Media SA. doi: 10.3389/978-2-8325-6471-4

Table of contents

frontiers | Frontiers in Molecular Biosciences

TYPE Editorial
PUBLISHED 04 June 2025
DOI 10.3389/fmolb.2025.1614399

OPEN ACCESS

EDITED AND REVIEWED BY
Michal Ciborowski,
Medical University of Bialystok, Poland

*CORRESPONDENCE
Geraldine M. Dowling,
geraldine.dowling@atu.ie

RECEIVED 18 April 2025
ACCEPTED 19 May 2025
PUBLISHED 04 June 2025

CITATION
Dowling GM and Meyer MR (2025) Editorial: Current trends in targeted and non-targeted metabolomics in analytical toxicology.
Front. Mol. Biosci. 12:1614399.
doi: 10.3389/fmolb.2025.1614399

Editorial: Current trends in targeted and non-targeted metabolomics in analytical toxicology

Geraldine M. Dowling[1,2,3]* and Markus R. Meyer[4]

[1]Department of Life Sciences, School of Science, Atlantic Technological University, Sligo, Ireland, [2]Cameron Forensic Medical Sciences, William Harvey Research Institutes, Barts and The London School of Medicine and Dentistry, Queen Mary University of London, London, United Kingdom, [3]Department of Analytical, Environmental and Forensic Sciences, School of Cancer and Pharmaceutical Sciences, Faculty of Life Sciences and Medicine, King's College London, London, United Kingdom, [4]Experimental and Clinical Toxicology and Pharmacology, Center for Molecular Signaling (PZMS), PharmaScienceHub (PSH), Saarland University, Homburg, Germany

KEYWORDS

analytical toxicology, personalised medicine, metabolomics, interdisciplinary approach, medicine

Editorial on the Research Topic
Current trends in targeted and non-targeted metabolomics in analytical toxicology

Analytical toxicology is at the frontline of detecting, identifying, and quantifying xenobiotics, drugs, and their metabolites in biological specimens. This essential discipline intersects with several fields, including analytical and clinical chemistry, pharmacology, and environmental health. Particularly in personalised medicine, analytical toxicology plays an essential role as metabolomics, analyzing small molecules in biological systems, plays a pivotal role in this evolution. By enabling both targeted and untargeted analyses, metabolomics allows for rapid screening of metabolites, helping to identify changes in physiological states triggered by toxic exposure or drug interactions. This approach not only enhances the precision of toxicological testing but also broadens the scope of detection, allowing for a deeper understanding of how substances affect human health on a molecular level (Zhu et al.; Barla et al.). This allows the integration of metabolomics into personalised medicine, opening up new frontiers in both research (Mojsak et al.) and clinical applications. What makes metabolomics particularly pioneering in the context of personalized medicine is its ability to capture the individual biochemical responses to drugs or toxins. Every person's metabolic profile differs, influencing how they process and react to substances. By incorporating metabolomics into analytical toxicology, we can better understand these unique individual responses, paving the way for tailored therapeutic strategies. This strategy allows clinicians to move away from one-size-fits-all treatments, instead offering interventions that are finely tuned to each patient's specific metabolic makeup. In turn, this can improve patient outcomes by optimizing drug efficacy and reducing adverse effects. Furthermore, metabolomics allows for more precise monitoring of ongoing drug use or exposure, offering the option of real-time adjustments to treatment plans. In the case of substance misuse, metabolomics could help track metabolites over

time, enabling more effective management strategies, personalized detoxification protocols and faster recovery timelines. This flexibility is essential for addressing the evolving nature of drug misuse and ensuring that healthcare approaches are not only reactive but proactive.

As the landscape of drug misuse also continues to evolve, the importance of advanced analytical methods in toxicology testing has never been greater. Fundamentally, analytical toxicology serves a critical function in ensuring the safety and wellbeing of individuals by providing accurate testing for drug misuse, environmental toxins, and other harmful substances. However, the escalating complexity of substances involved in drug abuse and toxic exposure demands persistent innovation in analytical techniques. The struggle lies in keeping up with new drugs, metabolites, and their potentially changeable effects on the human body. For this reason, joint communication and collaboration between clinicians, legal experts, law enforcement, and toxicologists are essential to effectively address these issues.

The combination of analytical toxicology, metabolomics, and personalized medicine is poised to revolutionize the way we approach drug misuse, exposure, and treatment. This interdisciplinary approach promises better detection, more precise diagnoses, and customized therapeutic strategies that improve both health outcomes and public safety. As research in these fields continues to evolve, so too will our ability to provide smarter, more effective solutions for patients and society as a whole.

This editorial Research Topic highlights how the integration of metabolomics into analytical toxicology offers fresh perspectives. As personalized medicine continues to gain momentum, metabolomics stands at the forefront of tailoring healthcare to the individual. By offering deeper insights into how specific drugs and toxins affect each person, we move closer to precision medicine—where treatments are based on a comprehensive understanding of an individual's metabolic and biochemical makeup.

Zhu et al. employed mass spectrometry-based metabolomics to investigate the effects and underlying mechanisms of isochlorogenic acid A in MC3T3-E1 cells. Their findings offer valuable insights into the therapeutic potential of 3,5-DiCQA for osteoporosis and demonstrate the effectiveness of metabolomics in advancing the understanding of traditional Chinese medicine (TCM).

In their study, Mojsak et al. applied gas chromatography–mass spectrometry (GC-MS)-based metabolomics to investigate how metabolite profiles change post-mortem in porcine blood, comparing samples collected with and without EDTA anticoagulant. Using linear mixed models, they examined how metabolite levels were influenced by time since death and the presence of EDTA, while also accounting for variability between individual animals. Their results revealed that 16 metabolites—primarily amino acids—were significantly affected by both post-mortem interval (PMI) and anticoagulant use. The authors emphasized that for a biomarker to be reliable in estimating PMI, its concentration should be driven solely by the time elapsed after death, without being impacted by external factors such as EDTA.

Barla et al. investigated the biochemical disruptions in the kidneys and liver of mice treated with a clinically relevant dose of colistin. Their analysis identified six metabolites (including PAA, DA4S, and 2,8-DHA) that responded in a dose-dependent manner, along with notable disturbances in renal dopamine regulation and significant alterations in purine metabolism within the kidneys. Additionally, the researchers observed changes in hepatic suberylglycine levels—a metabolite associated with fatty liver disease. Elevated concentrations of xanthine and uric acid were also detected in kidney tissue, both known to enhance acetylcholinesterase (AChE) activity, which in turn accelerates the breakdown of acetylcholine. These findings support a simplified hypothesis suggesting a possible link between colistin methanesulfonate (CMS)-induced kidney toxicity and its potential to cause neurotoxic effects—an association that warrants deeper investigation.

Isaiah et al. conducted a study examining the urinary metabolic profile of children in South Africa with advanced tuberculous meningitis (TBM). Their analysis revealed a distinct set of 29 urinary metabolites associated with advanced stages of the disease. These metabolites were linked to six major disruptions in metabolic function: (1) enhanced breakdown of tryptophan, indicating interference with vitamin B pathways; (2) abnormalities in amino acid metabolism; (3) a surge in energy production consistent with a metabolic burst; (4) imbalances in gut microbiota-related metabolism; (5) signs of ketoacidosis; and (6) elevated nitrogen elimination. This work offers novel biological insights into a urinary metabolic signature that may help distinguish paediatric TBM cases within this regional population.

Moses et al. outlined the potential of ion mobility spectrometry in the context of untargeted metabolomics. In this review, the authors compare ion mobility-based separation with liquid chromatography, trace the evolution of ion mobility techniques within metabolomics, present the current advancements and methodologies, and offer perspectives on future developments in the field.

Wang et al. investigated the therapeutic effects and underlying mechanisms of YiYiFuZi powder (YYFZ) in the context of chronic heart disease (CHD), employing both metabolomics and network pharmacology approaches. YYFZ is a traditional Chinese medicinal formula frequently used in clinical practice to manage CHD, though its precise pharmacological actions remain insufficiently understood. Using UPLC-Q-TOF/MS, the researchers conducted metabolomic profiling of rat plasma to identify biomarkers and explore affected metabolic pathways. Additionally, network pharmacology was applied to uncover key molecular targets and signaling pathways involved in YYFZ's effects. The metabolomic analysis revealed 19 metabolites associated with pathways including amino acid and fatty acid metabolism. The network analysis indicated that YYFZ may exert its effects via the PI3K/Akt, MAPK, and Ras signaling pathways. In conclusion, YYFZ appears to influence systemic metabolism and activate multiple phosphorylation-related signaling cascades in CHD; however, more research is needed to clarify which specific changes are critical to its therapeutic action.

Su et al. conducted a comprehensive investigation involving untargeted serum metabolomics and whole-body fat assessment using dual-energy X-ray absorptiometry (DXA) in a cohort of 517 Chinese women. The study examined four DXA-derived body fat (BF) traits simultaneously to uncover shared metabolite associations and highlight key metabolic contributors. Using a pathway topology approach, the researchers identified biological processes closely linked to body fat regulation. The analysis was

further extended by evaluating how these candidate BF-associated metabolites relate to fat traits across different sexes and ethnic groups using two independent validation cohorts. Among the findings, acetylglycine emerged as a standout metabolite, showing strong anti-obesity properties confirmed *in vivo* using multiple models of diet-induced obesity (DIO) in mice. In total, 18 metabolites and 14 metabolic pathways were significantly associated with BF traits, with six metabolites validated across populations of different gender and ethnicity. The consistent, cross-species efficacy of acetylglycine underscores its potential as a therapeutic agent for obesity prevention. Overall, this study highlights the metabolic underpinnings of fat distribution and the biological mechanisms that may influence obesity risk and its management, pointing to acetylglycine as a promising target for future interventions.

Wandy et al. conducted a study comparing data acquisition strategies in untargeted metabolomics by evaluating how well simulated results reflect real-world performance. They enhanced the Virtual Metabolomics Mass Spectrometer (ViMMS) platform by integrating a module for Data-Independent Acquisition (DIA), enabling a detailed *in silico* comparison between DIA and Data-Dependent Acquisition (DDA) approaches. Their findings revealed that method performance is highly dependent on the number of ions eluting simultaneously. When few compounds overlap, DIA delivers superior results; however, as ion overlap increases, DDA proves more effective since DIA struggles to resolve the complexity of densely overlapping chromatographic signals. These simulation outcomes were corroborated using a physical mass spectrometer, confirming that ViMMS simulations can reliably predict real experimental behavior. A major strength of this study lies in ViMMS's ability to flexibly model and test various parameters across both acquisition modes. This approach not only enhances understanding of DIA and DDA performance but also significantly reduces the need for extensive laboratory testing, offering a powerful tool for advancing LC-MS/MS method development in metabolomics research.

Ji et al. explored how Tongdu Huoxue Decoction (THD) influences the biological network involved in lumbar spinal stenosis (LSS) through a clinical metabolomics approach. Patients were assessed both before and after treatment using the Visual Analogue Scale (VAS) and Japanese Orthopaedic Association (JOA) scores to evaluate pain and lumbar function. Serum levels of Interleukin-1β (IL-1β), Tumor Necrosis Factor-alpha (TNF-α), and Prostaglandin E2 (PGE2) were measured pre- and post-treatment using ELISA assays. Additionally, targeted metabolomic profiling was performed on serum samples from patients (both before and after treatment) as well as from healthy individuals, using Ultra Performance Liquid Chromatography (UPLC). Multivariate statistical analysis was then applied to identify significant changes in metabolites and disrupted metabolic pathways. The clinical findings showed that THD effectively alleviates pain, enhances lumbar function, and reduces inflammatory markers in LSS patients. Mechanistically, these therapeutic effects appear to involve the modulation of purine metabolism, steroid hormone synthesis, and amino acid metabolism-related biomarkers.

Author contributions

GD: Conceptualization, Writing – review and editing, Writing – original draft, Validation. MM: Writing – review and editing.

Funding

The author(s) declare that no financial support was received for the research and/or publication of this article.

Conflict of interest

The authors declare that the research was conducted in the absence of any commercial or financial relationships that could be construed as a potential conflict of interest.

Generative AI statement

The author(s) declare that no Generative AI was used in the creation of this manuscript.

Publisher's note

frontiers | Frontiers in Molecular Biosciences

TYPE Original Research
PUBLISHED 07 March 2023
DOI 10.3389/fmolb.2023.1130781

OPEN ACCESS

EDITED BY
Louis Felix Nothias,
University of Geneva, Switzerland

REVIEWED BY
Hosein Mohimani,
Carnegie Mellon University, United States
Tao Huan,
University of British Columbia, Canada
Florian Meier,
University Hospital Jena, Germany

*CORRESPONDENCE
Vinny Davies,
Vinny.davies@glasgow.ac.uk

SPECIALTY SECTION
This article was submitted to Metabolomics, a section of the journal Frontiers in Molecular Biosciences

RECEIVED 23 December 2022
ACCEPTED 24 February 2023
PUBLISHED 07 March 2023

CITATION
Wandy J, McBride R, Rogers S, Terzis N, Weidt S, van der Hooft JJJ, Bryson K, Daly R and Davies V (2023), Simulated-to-real benchmarking of acquisition methods in untargeted metabolomics. *Front. Mol. Biosci.* 10:1130781. doi: 10.3389/fmolb.2023.1130781

Simulated-to-real benchmarking of acquisition methods in untargeted metabolomics

Joe Wandy[1], Ross McBride[2], Simon Rogers[2], Nikolaos Terzis[3], Stefan Weidt[1], Justin J. J. van der Hooft[4], Kevin Bryson[2], Rónán Daly[1] and Vinny Davies[3]*

[1]Glasgow Polyomics, University of Glasgow, Glasgow, United Kingdom, [2]School of Computing Science, University of Glasgow, Glasgow, United Kingdom, [3]School of Mathematics and Statistics, University of Glasgow, Glasgow, United Kingdom, [4]Bioinformatics Group, Wageningen University and Research, Wageningen, Netherlands

Data-Dependent and Data-Independent Acquisition modes (DDA and DIA, respectively) are both widely used to acquire MS2 spectra in untargeted liquid chromatography tandem mass spectrometry (LC-MS/MS) metabolomics analyses. Despite their wide use, little work has been attempted to systematically compare their MS/MS spectral annotation performance in untargeted settings due to the lack of ground truth and the costs involved in running a large number of acquisitions. Here, we present a systematic *in silico* comparison of these two acquisition methods in untargeted metabolomics by extending our Virtual Metabolomics Mass Spectrometer (ViMMS) framework with a DIA module. Our results show that the performance of these methods varies with the average number of co-eluting ions as the most important factor. At low numbers, DIA outperforms DDA, but at higher numbers, DDA has an advantage as DIA can no longer deal with the large amount of overlapping ion chromatograms. Results from simulation were further validated on an actual mass spectrometer, demonstrating that using ViMMS we can draw conclusions from simulation that translate well into the real world. The versatility of the Virtual Metabolomics Mass Spectrometer (ViMMS) framework in simulating different parameters of both Data-Dependent and Data-Independent Acquisition (DDA and DIA) modes is a key advantage of this work. Researchers can easily explore and compare the performance of different acquisition methods within the ViMMS framework, without the need for expensive and time-consuming experiments with real experimental data. By identifying the strengths and limitations of each acquisition method, researchers can optimize their choice and obtain more accurate and robust results. Furthermore, the ability to simulate and validate results using the ViMMS framework can save significant time and resources, as it eliminates the need for numerous experiments. This work not only provides valuable insights into the performance of DDA and DIA, but it also opens the door for further advancements in LC-MS/MS data acquisition methods.

KEYWORDS

liquid chromatography tandem mass spectrometry, metabolomics, data-dependent acquisition, data independent acquisition, digital twin

1 Introduction

Liquid chromatography tandem mass spectrometry (LC-MS/MS) is one of the dominant analytical platforms for untargeted metabolomics. LC-MS/MS acquisition strategies can be categorised as either Data-Dependent Acquisition (DDA) or Data-Independent Acquisition (DIA). In the former, MS2 scans are scheduled to target particular ions observed in full scan (MS1) survey scans. After each MS1 survey scan, a small number of ions will be prioritised (normally based upon their intensity) and fragmented in a series of MS/MS (MS2) scans. This will be followed by another MS1 survey scan from which the next batch of fragmentation events will be decided. In DIA, fragmentation is not based upon ions observed in survey scans but instead fixed m/z windows are isolated and fragmented, regardless of the ions present. The m/z windows can range from the whole m/z range (All-Ion Fragmentation, or AIF) or can be broken into a series of smaller windows that are iterated over in consecutive scans (e.g., Sequential Window Acquisition of all Theoretical Mass Spectra, or SWATH) (Gillet et al., 2012). DIA therefore removes the need to choose which ions to target at acquisition time at the cost of introducing an additional deconvolution step into the data analysis pipeline. Note that in this paper, we use the term "DIA" to refer to all data-independent acquisition methods, including both SWATH and AIF.

Various different DDA and DIA strategies have been introduced (Kaufmann and Walker, 2016; Guan et al., 2020; Davies et al., 2021; Guo et al., 2021) and although each new method is compared with other approaches, no clear consensus has emerged as to which overall strategy is best in which situation (Fernández-Costa et al., 2020; Guo and Huan, 2020a; Guo and Huan, 2020b). An advantage of DDA is that MS2 spectra are generated nearly ready to use, as each MS2 spectrum targets a particular ion, and we can be reasonably confident that the fragment ions observed do indeed come from the targeted ion. Sometimes multiple ions can end up in the same isolation window (Lawson et al., 2017), but this, in general, is not considered to be a major problem, as most of the times there is one dominant ion species giving rise to the mass fragments. Critics of DDA point to the lack of reproducibility (i.e., due to its stochastic nature, different peaks will be fragmented if the same sample is injected twice) and the low coverage–only a subset of the ions present in the sample are fragmented (Zhang et al., 2020). On the other hand, DIA offers chromatographic traces for all detected fragment ions, which can be useful in the identification of complex samples, particularly those containing isomers, where chromatographic information can help distinguish between them. The increased fragmentation capabilities of DIA can also be beneficial in the case of nearby-eluting isomers, where DDA might trigger only one MS2 spectrum due to dynamic exclusion. As DIA does not prioritise based on the contents of MS1 survey scans, it is more reproducible (we know beforehand exactly the properties of any scan). It also, at least in theory, overcomes the coverage issues as it is able to assign MS2 fragments to any detected MS1 ion.

The analysis of complex samples using DIA presents a unique set of challenges. In DIA, multiple ions from different compounds are fragmented during each MS2 scan, leading to complex spectra that require deconvolution to identify individual components. This can be particularly challenging in untargeted metabolomics where the compounds present and their fragmentation patterns are unknown prior to analysis, making it difficult to set up a pre-determined table of metabolites of interest to compare their fragmentation spectra to. Deconvolution, using software such as MS-DIAL (Tsugawa et al., 2015), is a process that separates the complex spectra generated by the fragmentation of multiple compounds into individual components, enabling the identification of the compounds present in the sample. However, deconvolution is a complex process and it is widely recognised that the high coverage provided by DIA comes at the cost of lower quality spectra (Bern et al., 2010).

Although there have recently been two studies (Guo and Huan, 2020a; Guo and Huan, 2020b) that compare DDA with DIA for its use in untargeted metabolomics, in general comparisons between the two acquisition strategies are still lacking. This is mainly due to the lack of ground truth for real experimental matrices and the cost of running large numbers of injections. While validation on real injections is vital, simulation can also play an important role in answering such questions. For example, the number of ions that can be targeted in a DDA analysis is a complex function of scan times, chromatographic peak widths, and the number of peaks eluting at a particular time. Similarly, the number of spectra that can be accurately deconvoluted in a DIA analysis depends on the number of co-eluting ions in the same isolation window, and how correlated their chromatographic profiles are. In both cases, analysis on real injections is hampered by a lack of knowledge of the true make-up of that sample, or samples being overly simplistic if they consist of just a handful of known standards. Simulation can overcome these limitations by permitting complete control over the ground truth in terms of both the fragment spectra present, the number of chemical ions in the sample, and how and when they elute.

In our previous work we introduced ViMMS (Wandy et al., 2019; Wandy et al., 2022), a virtual metabolomics mass spectrometry simulator framework, and demonstrated how it could be used to develop new, and improve existing DDA strategies. One of the main advantages of using ViMMS to develop new strategies lies in its ability to develop methods without the overhead costs of using a real mass spectrometer (MS). Within the ViMMS framework, it is possible to prototype methods and optimise them *in silico* before transferring the developed method for validation to an actual instrument. New DDA methods, such as WeightedDEW and SmartROI, have been developed on top of ViMMS and shown to outperform Top-N in terms of the number of peaks that were fragmented in both simulated and real experiments (Davies et al., 2021). More recent work has used ViMMS to develop improved methods for multi-sample and -injection DDA strategies (McBride et al., 2023).

In the current work we utilised ViMMS as a method for accurately benchmarking DIA and DDA through simulations. We firstly introduce two DIA controllers (SWATH and AIF) into the ViMMS framework, before conducting extensive simulated experiments to evaluate the comparative performance of DIA and DDA (Top-N) across a range of different simulated conditions, effectively creating a "digital twin" of the real situation. The DIA methods prototyped on the simulator were transferred with ease to run on an actual MS instrument with no code changes in the implementation–evidencing the capability of

ViMMS to develop DIA methods in a simulated-to-real setting. As such, we used ViMMS to validate the *in silico* experiments using complex beer samples in real LC-MS/MS experiments. The real experimental results were first benchmarked using an online reference spectral library (GNPS/NIST14) to assess spectral matches to a database of known molecules. This approach follows that of Guo and Huan (2020a), but importantly compares SWATH as well as AIF. Improving upon Guo and Huan (2020a), we also more systematically compare the results for DDA (Top-N) and DIA (SWATH and AIF) by evaluating our results against a database created on the specific sample using a recently developed, but computationally expensive multiple injection data acquisition method (McBride et al., 2023). This multi-injection dataset was constructed specifically to evaluate the maximum spectral coverage from a realistic experimental setting, complementing the standard approach of evaluating against a database of known molecules.

Our results found that over a wide range of experimental conditions, DIA is generally more effective at fragmenting more features, both in simulations and reality. However, DDA outperforms DIA in terms of the number of chemical ions for which high-quality spectra are recovered. Based on simulated and real instrumental results, we were able to provide a clear, actionable guideline on when a particular acquisition method (whether DDA or DIA) should be used.

In summary, the contributions of this paper are as follows.

1) We have introduced two new DIA controllers (SWATH, AIF) into the ViMMS framework.
2) We have conducted extensive simulated experiments to evaluate the performance of DDA (Top-N) vs. DIA with a known *in silico* ground truth.
3) We have validated the simulated results through benchmarking on the actual instrument using two reference datasets: the GNPS/NIST14, and our own Multi-Injection libraries.

2 Materials and methods

2.1 DDA and DIA data acquisition

To validate performance on a real instrument, we performed DDA and DIA acquisition using six beer samples. Each beer sample was acquired once using the Fullscan, Top-N, AIF and SWATH controllers in ViMMS when connected to an actual mass spectrometer (more details in Section 2.4). To create the Multi-Injection reference library (described in Section 2.5), each beer sample was further injected ten times repeatedly for acquisition using the Intensity Non-overlap method in ViMMS (McBride et al., 2023).

For sample extraction, chloroform and methanol were added to beer samples (detailed names in Supplementary Section S1) in a 1:1:3 ratio and mixed with a vortex mixer. The mixture was centrifuged to remove protein and other precipitates, and the supernatant was stored at −80°C. Chromatographic separation was performed with a Thermo Scientific UltiMate 3000 RSLC liquid chromatography system and a SeQuant ZIC-pHILIC column. The gradient elution used 20 mM ammonium carbonate and acetonitrile. 10 μL of each sample was injected with an initial 80% acetonitrile concentration, maintaining a linear gradient from 80% to 20% acetonitrile over 15 min, and finally a wash of 5% acetonitrile for 2 min, before re-equilibration at 80% acetonitrile for 9 min. The flow rate was 300 μL/min and the column oven temperature was 40°C.

A Thermo Orbitrap Fusion tribrid-series mass spectrometer was used to generate mass spectra data, controlled through Thermo Instrument Application Programming Interface (IAPI) managed by ViMMS (more details in Section 2.4). Full scan spectra were acquired in positive mode at a resolution of 120,000 and a mass range of 70–1,000 m/z. Fragmentation spectra for both DDA and DIA were acquired using the Orbitrap mass analyser at resolution 7,500. In DDA mode, precursor ions were isolated using 0.7 m/z width and fragmented with fixed HCD collision energy of 25%. The AGC was set as 200,000 for MS1 scans and 30,000 for MS2 scans. *N* was set to 10 Top-N. The dynamic exclusion window (DEW) was set to 15 s to prevent repeated fragmentation of the same ion. A minimum intensity threshold of 5,000 was also used before a precursor ion can be selected for MS2 fragmentation. For DIA (AIF), an MS1 source CID energy of 25% was used. For DIA (SWATH), a window of 100 m/z was used with no overlap between the windows.

2.2 Developing DIA methods using ViMMS

In previous work (Davies et al., 2021), ViMMS was used to develop DDA methods, but the capability of the framework is not limited to that. Here we introduced two new methods, SWATH and AIF, on top of the framework, demonstrating that DIA methods can also be developed on top of ViMMS. Rather than prioritising ions for fragmentation based on their abundance as is commonly done for DDA, DIA methods operate by fragmenting all precursor ions within a large m/z window. In AIF, all precursors in the entire m/z range are fragmented, whereas in SWATH, a series of smaller and potentially overlapping windows are used to fragment ions in the window. Both AIF and SWATH were implemented as controllers in ViMMS, allowing their performance to be benchmarked in the simulator and validated on an actual instrument easily, as previously done with DDA methods (Davies et al., 2021).

Figure 1 shows a schematic of the DIA method implementations in ViMMS illustrating how the new DIA methods were introduced. The ViMMS framework can be divided into two parts: a “Simulated Environment” where simulated scans are generated by querying synthetic chemicals, and a “Real Environment” where actual scans are generated through measurements using an LC-MS instrument. In the Simulated Environment (Figure 1A), the Virtual MS is seeded with synthetic molecules that are created by either sampling chemical databases or extracted from existing experimental mzML files. Once generated, molecules can be used to produce scans during virtual mass spectrometry. Scans are generated based on which molecules elute at a particular retention time, and generated chemicals are dispatched to the appropriate controllers. In ViMMS, a *controller* class is a specific implementation of an acquisition method in Python that follows a predefined Python interface to receive scans and schedule the next MS1 and MS2 scans. The new DIA methods are implemented as the SWATH and AIF controller classes in ViMMS (solid purple box in Figure 1A),

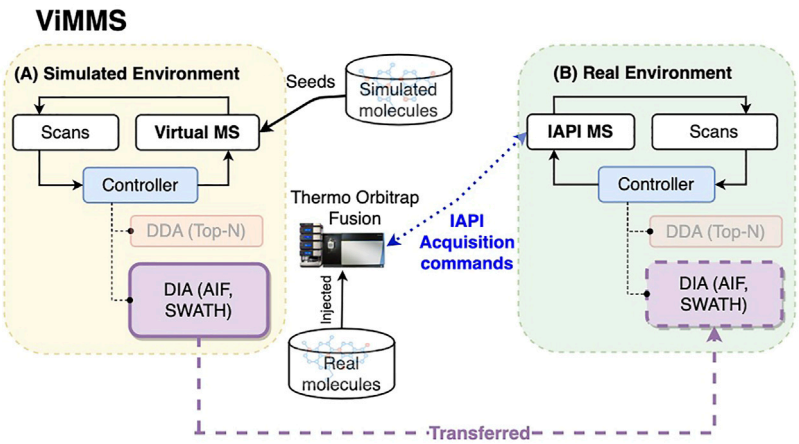

FIGURE 1
The overall schematic of the ViMMS framework. **(A)** The Simulated Environment in ViMMS allows for new acquisition methods to be developed against a Virtual MS that takes simulated molecules as input. The new DIA methods, e.g., SWATH and AIF (solid purple box), as well as existing DDA methods (faded orange box), are implemented as controllers and initially tested here in the Simulated Environment. A controller is a specific Python implementation of an acquisition method in ViMMS. **(B)** Acquisition methods can be run for method validation on the Real Environment in ViMMS, connected to a Thermo Orbitrap Fusion instrument *via* IAPI, to acquire real experimental scans. Controllers developed in the Simulated Environment can be transferred to the Real Environment easily (shown by the dashed purple line). As different environments abstract the low-level scan generation process, the underlying Python controller codes for the new DIA methods remain unchanged when transferred from the Simulated to the Real Environment (dashed purple box).

extending from the base Controller class (blue box in Figure 1A). Different experiments can be performed in the Simulated Environment, allowing for different data characteristics to be explored.

Once tested and optimised, the developed DIA controllers can be transferred to run on an actual mass spectrometer instrument with no change to their implementations. This is accomplished by swapping the Simulated Environment to a Real Environment (Figure 1B), where an IAPI MS is used in place of the Virtual MS. The IAPI MS class has the same interface as the Virtual MS to ensure code compatibility, however the IAPI MS relies upon the Instrument Application Programming Interface (IAPI) (Thermo Fisher Scientific, 2022) to communicate with an actual Thermo Orbitrap Fusion instrument. All developed controller implementations, whether DDA or DIA that were initially tested against the Simulated Environment in ViMMS, can run without any change in the Real Environment (for the new DIA methods, this is the dashed purple box in Figure 1B). In this manner, real experimental data can be seamlessly acquired using the AIF and SWATH controllers initially developed in the simulator.

2.3 Simulating DDA and DIA methods

2.3.1 Generation of simulated data

Simulations allow us to flexibly define different scenarios to validate hypotheses without costly instrument time. To compare the two types of acquisition methods, we use the Simulated Environment in ViMMS (Figure 1A) to generate simulated data with an increasing number of co-eluting chemicals present to test the limit of deconvolution empirically. While these chemicals are purely synthetic, they allow us to know the ground truth and evaluate the results of the different methods more accurately without being reliant on inconsistent database matching.

In the simulated study, each chemical is generated by first choosing a formula randomly from the HMDB database, ensuring that its observed monoisotopic mass is between 100–1,000 Da (the mass distribution of e.g., the 5,000 sampled chemicals is shown in Supplementary Section S5). Next the chemical is assigned a uniformly-sampled retention time value between 0–400 s. The choice of uniform distribution here is motivated by the narrow retention time range used. When the number of chemicals are high (e.g., 5,000), this results in dense regions of co-eluting ions throughout the entire simulated injection, which could challenge spectral deconvolution and potentially demonstrate the limit of such approaches.

Finally for each chemical, a chromatogram is generated. The maximum intensity value of the apex of the chromatogram was sampled from a uniform distribution between 1E4–1E7. A Gaussian chromatographic peak shape with a mean centered at the chemical's RT value, and a standard deviation of 5 s is assumed. This chromatographic peak shape assumption matches that of MS-DIAL, thus making the task of peak picking easier. Each chemical's observed MS2 spectra are also generated randomly by sampling fragment peaks' m/z uniformly between 70 m/z to the exact mass of the formula (assuming a positive charge of +1). The intensity of a fragment peak is also set to be between the specified minimum (0.1) and maximum (0.8) proportions of the chemical's apex intensity. The number of fragment peaks in an MS2 scan is generated by sampling from a Poisson distribution with the mean 10. This Poisson mean was chosen to produce sufficient expected numbers of fragment peaks per MS2 scan for spectral matching later.

Simulated samples containing the specified number of chemicals are generated in a case-vs-control setup, where each sample set

consists of 5 case and five control samples, and each sample contains observation from the specified number of chemicals. To reduce the influence of peak picking and alignment during data processing of DIA data, chemicals were generated such that the same chemical has identical m/z and RT values across samples, although their intensity values change across the case and control groups. While simple, this setup represents a realistic case that captures the essence of many real biological mass spectrometry-based experiments. Varying numbers of chemicals are generated during simulation, ranging from 10, 20, 50, 100, 200, 500, 1,000, 2000, and 5,000. The entire experiment is repeated 5 times, resulting in multiple experimental replicates. DDA (Top-N) and DIA (AIF, SWATH) controllers were run for every sample that was simulated, resulting in an mzML file for each acquisition run. Parameters of these controllers were set to be the same as that used for real data acquisition (detailed in Section 2.1.

2.3.2 Processing of simulated data

Once simulated data has been generated in Section 2.3.1, chemicals need to be mapped to their respective fragmentation spectra. For DDA, the association between observed fragmentation scans to chemicals is known unambiguously as their mapping can be read from the simulation state directly. For DIA, spectral deconvolution needs to be performed to assign the deconvoluted fragment peaks to chemicals. We chose MS-DIAL (Tsugawa et al., 2015) for peak picking and spectral deconvolution on the resulting mzML files produced by simulating DIA methods (see Supplementary Section S2 for the MS-DIAL parameter settings). MS-DIAL was chosen as it was widely used by the community for processing DIA data.

From MS-DIAL output, we can extract for each sample set a list of features that were detected and aligned across the DIA mzML files (5 cases and five controls). Each feature is potentially associated with a fragmentation spectra, which has been deconvoluted by MS-DIAL. To assign fragmentation spectra, we matched simulated chemicals to features using the m/z tolerance of 5 ppm and RT tolerance of 10 s, therefore linking chemicals to their deconvoluted spectra. If there are multiple possible candidates during matching, the feature closest in m/z value to the chemical's monoisotopic peak will be chosen. Finally for each simulated chemical, its true fragmentation spectra are known. This can be used to construct a library of true reference spectra for matching. Observed (and deconvoluted, in the case of DIA) spectra are matched to the true spectral library using cosine similarity. For matching, a bin width of 0.05 Da is used and a minimum of at least three matching peaks is required.

2.4 Validation on a real instrument

2.4.1 Generation of real data

The Real Environment in ViMMS was used to validate that the simulated results translate to real experiments (Figure 1B). This environment can be connected to a Thermo Orbitrap Fusion tribrid-series mass spectrometer, allowing us to perform data acquisition on a series of beer samples using the fullscan, Top-N, and the newly introduced SWATH and AIF controllers. The result from data acquisition is a series of mzML files, one for each beer sample and controller used. For more details on real data acquisition, refer to Section 2.1.

2.4.2 Processing of real data

Peak picking and alignment was performed using MS-DIAL on the real experimentally-derived fullscan mzML files. Unlike in simulations, here the exact chemical composition of the sample is unknown. As such, fullscan features from peak picking on the fullscan data are used as a proxy for chemicals. The fullscan data, which contains the most MS1 information and therefore the best chromatographic peak shapes, was chosen for feature extraction using MS-DIAL. MS-DIAL parameters were chosen by hand to give a reasonable number of peaks comparable to what we have seen from past experiments using this kind of sample on the same instrument (details in Supplementary Section S3). The result from this is a list of fullscan features detected and aligned from the fullscan beer mzML files.

Next DDA fragmentation spectra were to be assigned to fullscan features, with the following procedure employed to bypass the need to do further peak picking on the DDA mzML files (which can be problematic due to the lower number of MS1 scans in fragmentation files). *pymzML* (Bald et al., 2012) was used to load MS2 scans from each DDA mzML file. For each MS2 scan, we used its precursor m/z, isolation window and RT values to assign the scan (and therefore fragmentation spectra) to its corresponding fullscan feature. This assignment was done based on whether the isolation window and RT values of a chemical overlap with the feature's bounding box from peak picking. If a fullscan feature had multiple MS2 scans associated with it, the scan that was fragmented at the highest intensity within the feature's bounding box was chosen.

Finally, just like in simulation, MS-DIAL was used to perform peak picking and spectral deconvolution on the DIA mzML files. Peak picking was performed using the same parameters as the fullscan data, and an additional deconvolution step was done using MS-DIAL (detailed parameters in Supplementary Section S3). From MS-DIAL output we extracted a list of fragmentation features detected in the DIA mzML files and their corresponding MS-DIAL deconvoluted spectra. Fullscan features (without fragmentation information) were matched to the DIA fragmentation features (with deconvolved spectral information) using an m/z tolerance of 5 ppm and RT tolerance of 10 s. If there were several possible candidates during matching, the one closest in m/z value was chosen. The results of this procedure from both the DDA and DIA data is the assignment of a fullscan feature to fragmentation spectra. Such spectra can be used for matching fullscan features to the reference libraries during benchmarking experiments.

2.5 Matching experimental spectra to reference libraries

To assess mass spectral quality, we match the fragmentation spectra from DDA and DIA methods to two reference spectra libraries. These reference libraries can be used to match against the observed and deconvoluted spectra from DDA and DIA methods. For matching, a bin width of 0.05 Da is used and a minimum of at least three matching peaks is required.

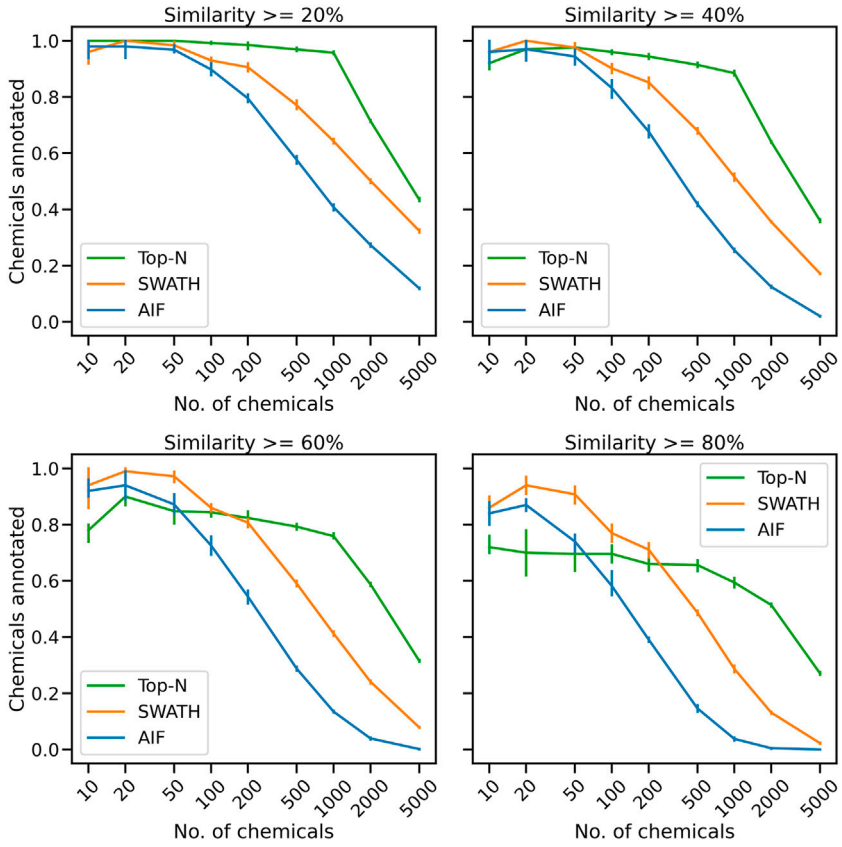

FIGURE 2
The mean proportion of unique chemical annotations at varying numbers of chemicals and similarity thresholds across five replicates. The error bar shows the 95% confidence interval.

The first reference library is the "GNPS Matches to NIST14" dataset obtained from the GNPS library (Wang et al., 2016). This dataset contains 5,763 high confidence matches to NIST14 M/MS library spectra. Filtering by polarity is performed to select spectra in positive mode only that can be used as reference to assess spectral annotation quality. For experiments, we call this the *GNPS/NIST14* library. Its purpose is to assess how many potentially unknown metabolites could be annotated in an untargeted metabolomics experiment using the different acquisition methods.

Additionally, we also introduced our own multiple-injection reference library for spectral matching, which we call the *Multi-Injection* Library. Each beer sample was injected ten times and data acquisition is performed by taking advantage of replicate information using the Intensity Non-overlap method available in ViMMS (detailed in Supplementary Section S4). Intensity Non-overlap is an iterative DDA-based method that detects regions-of-interests (ROIs) in real-time and avoids re-fragmenting the same ROI multiple times across successive injections. An ROI is scored for fragmentation based on its overlapping area weighted by intensity, with higher scoring ROIs selected more often (for more details, refer to Supplementary Section S4 and McBride et al. (2023)). In the presence of multiple injections, Intensity Non-overlap has been shown to outperform Top-N by a large margin as it is able to target more unique features across injections, while fragmenting each feature closer to its apex.

To convert the acquired Multi-Injection mzML files into spectral library, for each beer sample, we perform peak picking using MS-DIAL on its corresponding fullscan mzML file, generating a list of fullscan feature for that beer sample. Fragmentation spectra, acquired *via* exhaustive fragmentation of each sample using Intensity Non-overlap, were extracted from mzML files and matched to the detected fullscan features following the DDA procedure outlined in Section 2.4.2. The purpose of introducing this Multi-Injection reference library is to assess the coverage of the benchmarked DDA (Top-N) and DIA (AIF, SWATH) methods when only a single replicate is available (a common occurrence) and increasing the number of replicates is not possible due to cost or other constraints.

3 Results

3.1 Simulated results

Acquired fragmentation spectra could help deduce the chemical identities of measured compounds. From the proposed simulated experiment in Section 2.3, for each acquisition method the number

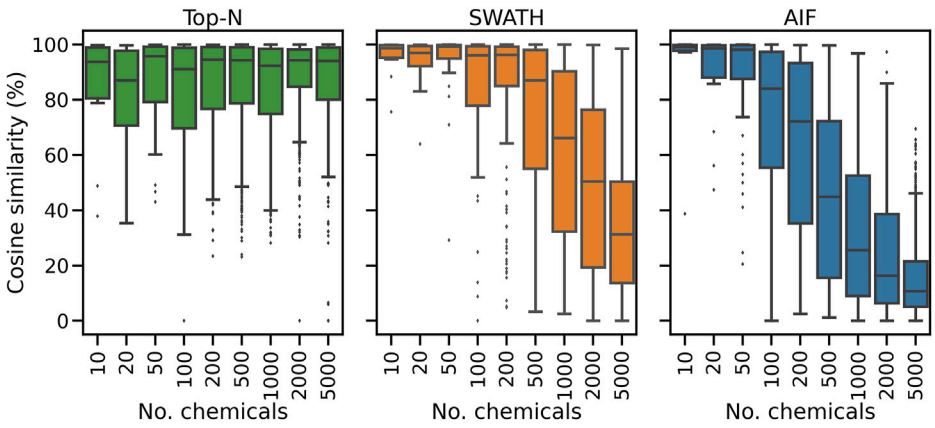

FIGURE 3
The distribution of cosine similarity scores when matching observed spectra to the true reference spectra for varying numbers of chemicals.

of chemicals that could be annotated based on spectral matching is obtained. The number of unique chemical annotations in the dataset is counted at varying thresholds for cosine similarity score of at least 20%, 40%, 60% and 80% (Figure 2). The results across five replicates show that for small numbers of chemicals, all benchmarked methods, whether DDA or DIA, have similar annotation performance. At similarity threshold 60% and with only 100 chemicals, AIF annotated a mean of 72.6% of chemicals, SWATH 86.0% and Top-N 84.4%. As the number of chemicals increases, the gap between the benchmarked methods widen leading to lower annotation rates from DIA. When the number of chemicals increased to 200, at 60% similarity threshold, AIF managed to annotate 54.4% chemicals, SWATH 80.7% and Top-N 82.4%. For 500 chemicals, AIF annotates 28.8% of chemicals, SWATH 59.0% and Top-N 79.3%.

With a greater number of chemicals, Top-N outperforms the two DIA methods across all thresholds. At the highest number of chemicals (5,000), the annotations obtained from SWATH and AIF are nearly 0% while Top-N managed a mean of 31.5% across replicates. It can be observed that increasing the cosine similarity threshold from 20% to 80% lowers the results of all methods, but the overall trend remains. The supplementary section also includes additional results obtained from varying the matching threshold. Supplementary Figure S2 displays the results of matching with a bin width of 0.005 Da, while Supplementary Figure S3 illustrates the results of matching with a bin width of 0.50 Da. The results in Supplementary Figure S2 demonstrate that the tolerance level was too narrow, leading to a decrease in performance for all acquisition methods. Despite this, Top-N still demonstrates superior performance compared to the DIA methods when a high number of chemicals are present. The results in Supplementary Figure S3, obtained using a larger bin width of 0.50 Da, are consistent with those presented in Figure 2 which utilised a bin width of 0.05 Da. This consistency in results highlights that the trend of Top-N outperforming DIA methods holds true for a large number of chemicals (> 200). Supplementary Figure S4 also shows the results from using different window sizes of 100 m/z, 50 m/z and 25 m/z in the SWATH simulation. It can be observed from Supplementary Figure S4 that making the window size smaller produces a slight annotation improvement in SWATH when the number of chemicals are large (2000 and 5,000). However this improvement is small, and the overall trend of Top-N outperforming both SWATH and AIF in this regime holds.

To further explain the annotation results in Figure 2, here we consider for one replicate the distribution of spectral similarity scores when matching DDA and DIA spectra to the known ground truth of true chemical fragmentation spectra. The results are shown in Figure 3 for the entire range of chemicals tested. From Figure 3, it can be seen that Top-N generally performs best in returning high similarity scores, followed by SWATH then AIF. For Top-N, the cosine similarities of matches generally remain high even with an increasing number of chemicals. For the two DIA methods, their cosine similarities gradually decrease with more co-eluting chemicals. This could be explained by the fact that as the elution profile gets more crowded, more precursor ions are isolated and fragmented in the same window, making deconvolution harder. SWATH performs marginally better than AIF with increasing chemicals. This makes sense as the window used for isolating multiple peaks in SWATH is smaller than AIF where all ions in the entire scan range are used, making the deconvolution problem slightly easier for SWATH.

Inspecting the hardest case of 5,000 chemicals in Figure 4, it can be observed that AIF returns most of its matches at low cosine similarity achieving a median score of 10.7%, Top-N returns most matches at high cosine similarity with a median of 94.1%. SWATH outperforms AIF (median similarity 31.3%) but not as well as Top-N. To explain the decrease in similarity scores, we inspect the pairwise cosine similarity of all observed/deconvolved spectra for each acquisition method (Figure 5). The results show that the pairwise similarity of the ground truth and Top-N spectra is nearly 0 for nearly the entire range of chemicals. However, most likely due to the increased difficulty in deconvolution, pairwise spectral similarities in the SWATH and AIF results are higher with increasing chemicals–resulting in a decrease in identification hits, and fewer matches at high cosine similarity as the experimental mass spectra become more similar to each other and less similar to the true mass spectra of the chemicals.

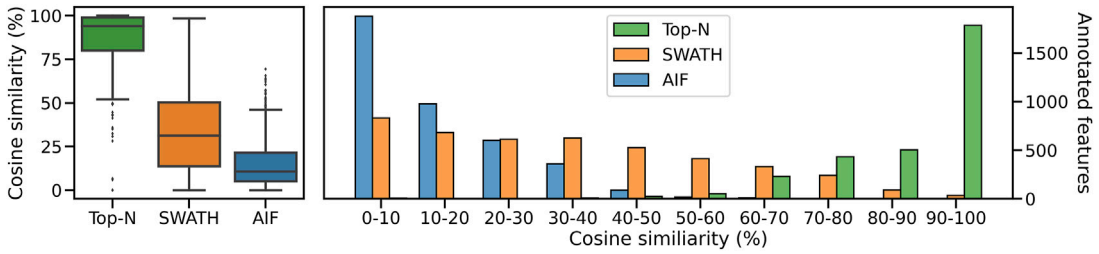

FIGURE 4
The distribution of cosine similarity scores as a boxplot (left) and a histogram (right) when matching observed spectra to the true reference spectra for 5,000 chemicals.

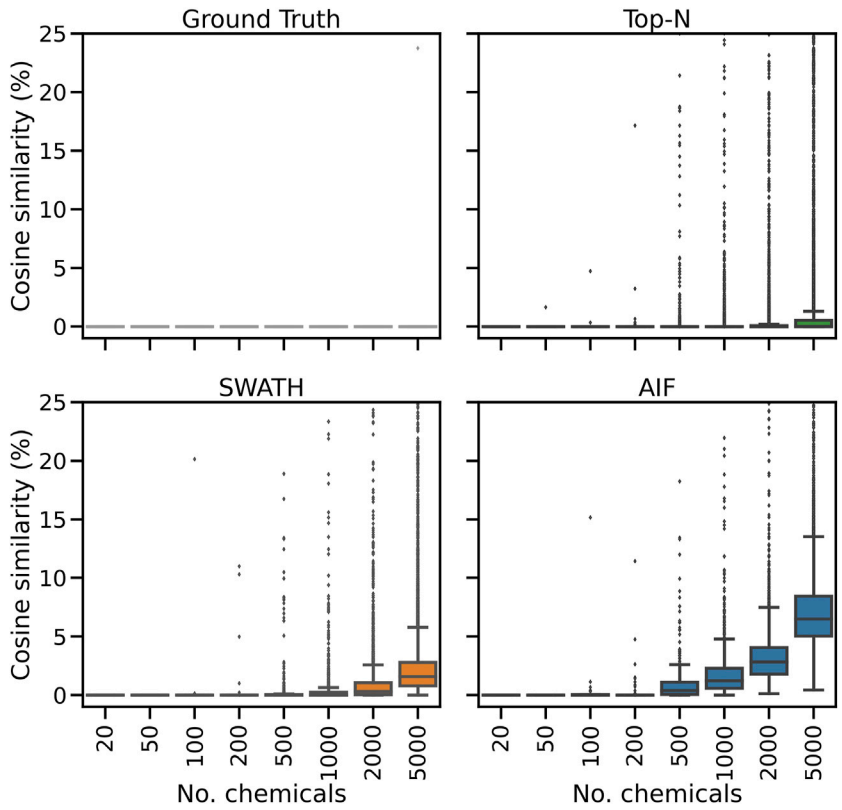

FIGURE 5
The distribution of pairwise cosine similarity scores of the ground truth (true chemical spectra), and fragmentation spectra from Top-N, SWATH and AIF. The plot y-axes are truncated at 25% similarity.

3.2 Real experimental results

3.2.1 Mapping features to fragmentation spectra

Simulated results were further validated on real instruments by running the benchmarked DDA and DIA methods on actual beer samples. Following the procedure in Section 2.4.2 to map fullscan features to fragmentation spectra, 6090 fullscan features initially were detected from the fullscan data after peak picking and alignment. After matching the fullscan features to fragmentation data, DIA methods produce the largest number of matched features, with SWATH at 3889 and AIF at 4381. In contrast, Top-N only has 2,895 matched features. Figure 6 summarises the proportion of fullscan features that can be matched to the fragmentation spectra. Our results here agree with Guo and Huan (2020a) in how DIA (AIF) is able to fragment more features than DDA (Top-N). We note some slight differences in our methodology to (Guo and Huan, 2020a). In this work, we perform peak picking to extract features on the fullscan data, which has more reliable MS1 signals. Fragmentation mzML files are used only to map fragmentation scans to the detected fullscan features. Whereas in (Guo and Huan, 2020a) the peak picking is performed directly on the fragmentation mzML files, potentially leading to poorer extracted chromatographic

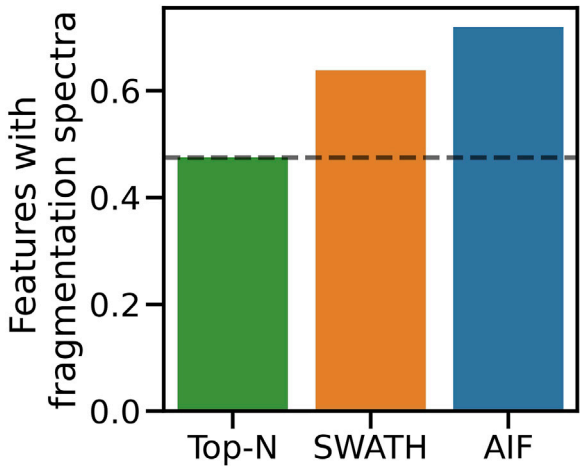

FIGURE 6
Proportion of matched features to the total number of detected features from the fullscan data.

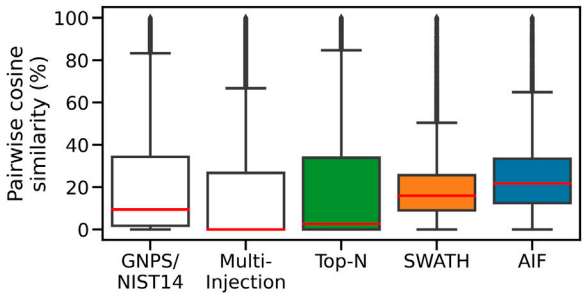

FIGURE 7
Pairwise similarities of spectra in each dataset. DIA methods (AIF, SWATH) produce deconvoluted spectra that are more similar to each other.

peak shapes due to sparser MS1 data points in the mzML files. Despite these differences in the experimental set up, the conclusions from both our study and (Guo and Huan, 2020a) agree that AIF outperforms Top-N in the number of fragmented features. Additionally SWATH was not included in (Guo and Huan, 2020a) but it was hypothesised to perform in the middle of Top-N and AIF, as the windowing approach used in SWATH lies between the two extremes of fragmenting everything (AIF) and fragmenting only a few selected precursor ions (Top-N). Our results here confirmed that SWATH achieves a higher coverage than Top-N but lower than AIF.

3.2.2 Pairwise spectral similarity

By following the methodology of Section 2.5, two reference mass spectral libraries were constructed, one based on the GNPS spectra matched to NIST-14 at high reliability (the GNPS/NIST14 library), and another based on an exhaustive multiple-injection approach we constructed ourselves (the Multi-Injection library). The purpose of the GNPS/NIST14 library is to assess how many unknown molecules can be identified from spectral matching for each acquisition method, whereas the purpose of the Multi-Injection library is to determine the extent of coverage with respect to an exhaustive and expensive multiple-injection method. After filtering by polarity, we obtain 5,274 positive-mode spectra from the GNPS/NIST14 library, whereas for the Multi-Injection library, in total 4987 features were available for matching in this library.

To assess spectral quality, we first compute the pairwise similarity of spectra in the same dataset, and also within each of the two reference libraries. For each feature, we find the matches to fragmentation spectra in the same dataset by computing the cosine similarity (ms2_tol = 0.05 Da, min match peaks = 3), with the results shown in Figure 7. The Multi-Injection reference library has a median of nearly 0% for pairwise similarities, demonstrating that the acquired reference spectra using the Intensity Non-overlap method are sufficiently different from each other. The GNPS reference library has a higher pairwise similarity of 9.5%, suggesting that some of the curated molecules share similar structures and therefore similar mass fragmentation spectra. This is a reasonable assumption as shared structures is the core underlying assumption for models to discover chemical substructures, such as MS2LDA (van Der Hooft et al., 2016) that has been applied to reference libraries like MassBank and GNPS.

The Top-N dataset also has the same low median pairwise similarity (2.7%) in its member spectra. This is expected given the nature of DDA. Assuming that deconvolution works well for DIA data and the resulting spectra are dissimilar to each other in a manner similar to the Top-N results, we expect to observe lower pairwise similarities from the DIA datasets too. However the higher median pairwise similarity scores for SWATH (16%) and AIF (22%) suggest that deconvolved spectra from SWATH and AIF tend to be more similar to each other. This could be due to the difficulty in deconvolving spectra. The results here generally agree with simulated results in Section 3.1, where DIA methods are also shown to exhibit higher pairwise similarity in simulation.

3.2.3 Spectral matching results

We compute the cosine similarity of features to the GNPS/NIST14 reference spectra. Similar to before, features were matched to reference spectra based on their cosine similarity (ms2_tol = 0.05 Da, min match peaks = 3). If there are multiple matches for each feature, the one with the best score (highest) is kept. Figure 8A shows the score distributions for the three methods. From Figure 8A (left panel), it can be observed that Top-N obtains the highest median cosine similarity (26.5%) followed by SWATH (19.5%) and finally AIF (15.2%). Consequently this results in Top-N (DDA) obtaining the most high-scoring matches at ≥ 60% similarity, followed by SWATH and AIF last (Figure 8A). The results here are consistent with the simulated results in Section 3.1 and also with Guo and Huan (2020a) but in that work, only Top-N and AIF were compared. Our results further confirmed the hypothesis in Guo and Huan (2020a) that SWATH should perform in the middle of Top-N and AIF when it comes to spectral quality. This is because deconvolution using SWATH data is easier than AIF due to the smaller window sizes.

Next we perform spectral matching to the Multi-Injection reference library. When matched against Top-N and DIA methods, Top-N performs best (90.5% median) followed by

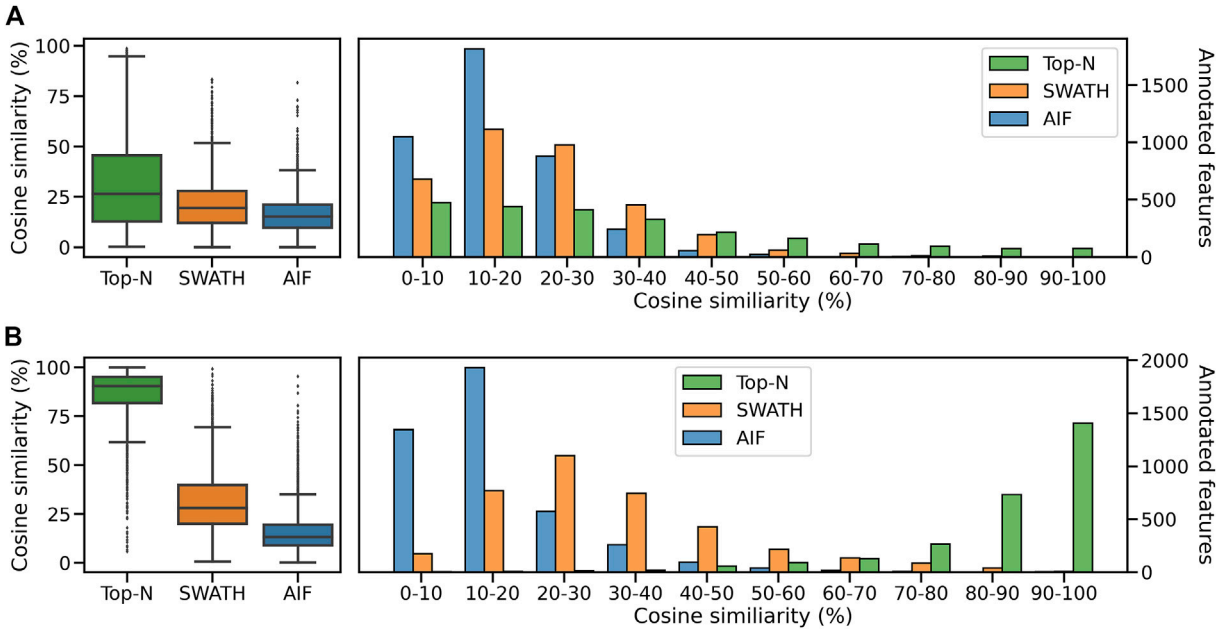

FIGURE 8
Distribution of cosine similarity of annotated features for Top-N and DIA methods for the **(A)** GNPS/NIST14 library and **(B)** Multi-Injection library.

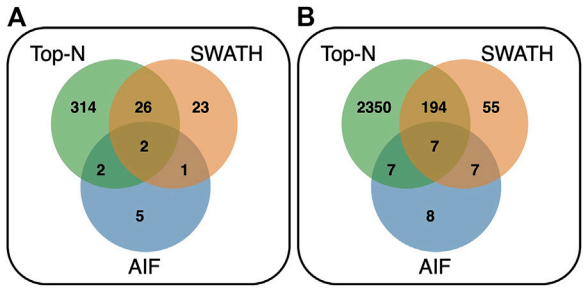

FIGURE 9
Venn diagram showing the overlap of annotated features between Top-N, SWATH and AIF at matching threshold ≥60% for the **(A)** GNPS/NIST14 library, and **(B)** Multi-Injection library.

SWATH (28.1%) and AIF (13.3%) (Figure 8B). The results here are consistent with the GNPS results above. However we see that the median similarity of Top-N is much higher compared to the two DIA methods here. That is because the reference spectra contains more query spectra since it is based on the same sample, only fragmented exhaustively, and unlike GNPS/NIST14 there are fewer missing matches.

Comparing the overlap of annotated features at matching threshold ≥60% (Figure 9) for both reference libraries, it can be observed that Top-N (DDA) obtains the most hits, being able to annotate the most unique features (295 for GNPS/NIST14, and 2,231 for Multi-Injection). In both cases, there is a large overlap between Top-N and DIA annotations, and most DIA annotations are also recovered by Top-N. Between AIF and SWATH, there is also a lot of overlap with SWATH being able to recover most of the annotations of AIF. The results here for AIF and Top-N generally agree with Guo and Huan (2020a), with SWATH a new addition in our results that perform in between those two.

4 Discussion and conclusion

In this study, we performed a comprehensive comparison of DDA vs. DIA methods, first in the simulator, followed by validation using real experimental mass spectrometry data. We simulated experiments at various complexity levels to challenge DDA acquision methods and DIA deconvolution methods. Here, we observed that the quality of deconvolution using MS-DIAL is limited by the number of co-eluting chemicals. Identification performance is limited in DIA compared to DDA with a large number (more than 1,000) of simulated chemicals or observed molecular features. We further benchmarked this scenario using a real untargeted metabolomics dataset acquired on the mass spectrometer generated from beer samples. Mass spectral matching of experimental mass fragmentation spectra from this real dataset on two sets of reference mass spectral libraries confirmed our simulated results. This validates our motivation that a simulator framework such as ViMMS can be used to benchmark the performance of both types of methods. Simulation helps to provide an environment that can be used to prototype and validate advanced deconvolution methods–without the need of costly instruments (i.e., a “digital twin”). This encourages the development of better deconvolution methods, since known ground truths were generated *in silico*, thus making benchmarking easier. The ViMMS framework could also be used to simulate various scenarios that we have not covered in this study, for instance simulating different column properties and elution profile of chemicals, and assessing how that affects deconvolution.

In the context of LC-MS/MS analysis, a complex sample would contain a large number of different metabolites, while a simple sample would contain only a few metabolites. Determining the complexity of a sample is important for choosing the appropriate acquisition strategy for LC-MS/MS analysis. ViMMS can generate simulated samples of varying complexity, which can be used to assess whether DDA or DIA methods should be used in specific scenarios. By varying average number of co-eluting ions, we found that DIA being more effective at lower numbers and DDA having an advantage at higher numbers where DIA struggles to handle the large amount of overlapping ion chromatograms. From both simulated and real results, DDA was also found to generally perform better than DIA when it comes to matching unidentified features to spectra in both reference libraries (GNPS and Multi-Injection). DIA fragments more features than DDA but their quality for spectral matching is typically lower. Our results on this are not unique as a similar work in (Guo and Huan, 2020a) confirms our findings. Crucially, our study improves upon that prior work in several key aspects. The first is that SWATH was not included in the comparison of Guo and Huan (2020a), whereas our study did include both AIF and SWATH. Secondly, while spectral matching to a library of known fragmentation spectra (e.g., GNPS, or MassBank) can be done, many compounds present in such databases have no matches thus reducing the identification rate observed from both DDA and DIA methods. Thus we introduce another dataset, constructed using an advanced multiple-injection method, to measure how well DDA and DIA methods perform with respect to exhaustive fragmentation procedures. Exhaustive fragmentation procedures have been shown to perform best with respect to coverage when a large number of replicates are available. However, real experiments are often constrained by cost or time, limiting the number of replicates that could be produced. In this setting, our analysis shows that DDA still performs best compared to DIA in recovering coverage when multiple replicates are not easily available.

Our recommendation on which acquisition method to choose is therefore.

- If the sample complexity is expected to be **low** to **medium**, OR it is preferred to **fragment as many features** as possible, even if they are not all identified, it is recommended to use DIA for data acquisition (keeping in mind the necessary deconvolution step).
- If the sample complexity is expected to be **high**, OR it is preferred to **obtain as many identified features** as possible, it is recommended to use DDA, which targets a specific ion for each MS2 scan thus generating fragmentation spectra that are almost immediately usable for analysis.

It is worth emphasizing that our results do not negate the usefulness of running DIA methods. Using DIA, we obtain the largest number of coverage of features, resulting in the most number of fragmented molecules–many of whom could be used for further investigation in the future. However acquired DIA scans need to be deconvoluted in order to translate the results to actual identification. Improvements in deconvolution methods are therefore needed to fully maximise the usefulness of DIA data. The work introduced here shows that a large margin of improvement is still possible in spectral deconvolution of DIA results–an avenue for further research that could be explored by the community. The work here also shows that through a simulation framework such as ViMMS, researchers could first test their deconvolution method *in silico*. The portable nature of ViMMS means controllers (fragmentation methods) developed in simulators can be easily ported to run on the real instrument. DIA methods such as AIF and SWATH were implemented as controllers on top of ViMMS, tested in the simulator, and easily deployed to run on the actual instrument. This makes it easy for others to reproduce our results in simulation. It also opens the path for more advanced DIA methods to be developed in the future on top of ViMMS. What makes ViMMS particularly valuable is its ability to simulate a range of different method parameters for both DDA and DIA, allowing researchers to easily evaluate the performance of different LC-MS/MS data acquisition methods. This feature not only provides valuable insights into the strengths and limitations of each acquisition method, but it also opens the door for further advancements in LC-MS/MS data acquisition methods. By using ViMMS, researchers can optimize their choice of acquisition method and obtain more accurate and robust results, while saving significant time and resources as they eliminate the need for numerous experiments. In other fields such as molecular machine learning, having a standardized benchmark dataset (Wu et al., 2018) fosters development and collaborations as now a common reference exists onto which we can compare the performance of different methods. It is our hope that the simulated experiment introduced here could also serve as a standard and reproducible benchmark to which other deconvoluted methods can be compared to.

Our study has several limitations, including the fact that our comparison of DDA and DIA acquisition methods is based solely on the analysis of processed and, in the case of DIA, deconvoluted data. While data processing, particularly the deconvolution step, is a crucial aspect of DIA data analysis, other important factors such as the increased computational demands for deconvolution in DIA are not considered in detail. Additionally, the impact of instrument configuration and sample preparation on the data is not evaluated in our study, which can also influence the performance of both acquisition methods. Further research is necessary to gain a comprehensive understanding of the strengths and limitations of both DDA and DIA in untargeted metabolomics and to determine the optimal approach for various scenarios. Our findings primarily emphasise the MS/MS spectral annotation performance and do not extensively address other factors such as quantitative performance. We only used MS-DIAL for the pre-processing of DIA data. MS-DIAL is de-facto the most popular tool used for spectra deconvolution and analysis of DIA data. However, other deconvolution tools exist, such as those of Yin et al. (2019) and Graca et al. (2022), that we do not include in our comparison. Parameters from MS-DIAL in our study were picked by hand to obtain reasonable results–similar to the limitation in Guo and Huan (2020a). Furthermore, DDA and DIA methods exist that can exploit information across multiple samples (Koelmel et al., 2017; Tada et al., 2020) but these were not included in our evaluation. Using ViMMS, we could generate samples in multiple replicates and assess the performance of DDA and DIA methods when replicates are available. This validation to some extent has been done to compare

standard DDA vs. multiple samples/injections DDA in McBride et al. (2023) but not in the context of comparing to DIA methods.

Another aspect to take into account is the choice of cosine similarity as the metric for spectral matching. While cosine similarity is a commonly used metric in MS-DIAL, there are more advanced techniques available, such as Spec2Vec (Huber et al., 2021) and Tanimoto similarity, which have been shown to better preserve chemical similarity in spectral matching. However, for the purposes of this study, cosine similarity was selected as the metric because it can be applied to both real and synthetic data. The goal of this study was to demonstrate that simulated results can be translated to experimental results, and cosine similarity was chosen as the metric for spectral matching because of its broad applicability to both types of data.

For future work, the developed *in silico* benchmarking pipeline introduced in this work can also serve as the foundation to develop and validate a hybrid method that combines the benefit of both approaches. DDA and DIA methods exist in a spectrum: DDA isolates a certain precursor m/z for fragmentation, and DIA isolates multiple ions in a range of windows. This behaviour is the same across the entire run. It would be interesting to explore the potential of a hybrid method that combines the benefits of both DDA and DIA approaches. Such a method could potentially take advantage of the strengths of both approaches, allowing for more accurate and comprehensive analysis of complex samples. Such work has already been attempted (Guo et al., 2021) but that integration happens in data processing, not during the data acquisition itself. A hybrid acquisition method could use DDA to isolate certain prioritised precursor ions for fragmentation, and use DIA to isolate the remaining ions within a range of windows. This hybrid approach would allow for a more flexible and comprehensive analysis of samples, and could potentially improve the accuracy and reliability of results. This would lead to a more effective use of untargeted metabolomics, as more molecular features will be fragmented with higher-quality mass spectra associated to them. Ultimately, that will improve the biochemical interpretation of metabolomics profiles across the life sciences and other research areas.

Data availability statement

The dataset consisting of the DDA (Top-N, Intensity Non-overlap) and DIA (AIF, SWATH) mzML files generated and analysed for this study can be found under the following DOI: 10.5525/gla.researchdata.1382.

Author contributions

JW led software development (*in silico* and on the actual instrument), data acquisition and analysis. RM and NT developed the evaluation codes for data analysis. SW performed sample preparation and instrument calibration. SR and VD conceptualised the research project. SR, RD and VD acquired funding. VD, KB and RD supervised the project. JV, KB, RD, and SR performed manuscript review and editing. All authors contributed to the manuscript draft and the submitted version.

Funding

JW, VD, SW, SR, and RD were supported by the EPSRC project EP/R018634/1 on Closed-loop data science for complex, computationally and data-intensive analytics. Additionally JW and VD were supported by a Reinvigorating Research Grant from the University of Glasgow. NT and VD were supported by an Edinburgh Mathematical Society student research bursary.

Conflict of interest

JJJVdH is member of the Scientific Advisory Board of NAICONS Srl. Milano, Italy. All other authors declare that the research was conducted in the absence of any commercial or financial relationships that could be construed as a potential conflict of interest.

Publisher's note

Supplementary material

The Supplementary Material for this article can be found online at: https://www.frontiersin.org/articles/10.3389/fmolb.2023.1130781/full#supplementary-material

References

Bald, T., Barth, J., Niehues, A., Specht, M., Hippler, M., and Fufezan, C. (2012). pymzML—Python module for high-throughput bioinformatics on mass spectrometry data. *Bioinformatics* 28, 1052–1053. doi:10.1093/bioinformatics/bts066

Bern, M., Finney, G., Hoopmann, M. R., Merrihew, G., Toth, M. J., and MacCoss, M. J. (2010). Deconvolution of mixture spectra from ion-trap data-independent-acquisition tandem mass spectrometry. *Anal. Chem.* 82, 833–841. doi:10.1021/ac901801b

Davies, V., Wandy, J., Weidt, S., Van Der Hooft, J. J., Miller, A., Daly, R., et al. (2021). Rapid development of improved data-dependent acquisition strategies. *Anal. Chem.* 93, 5676–5683. doi:10.1021/acs.analchem.0c03895

Fernández-Costa, C., Martínez-Bartolomé, S., McClatchy, D. B., Saviola, A. J., Yu, N.-K., and Yates, J. R., III (2020). Impact of the identification strategy on the reproducibility of the DDA and DIA results. *J. Proteome Res.* 19, 3153–3161. doi:10.1021/acs.jproteome.0c00153

Gillet, L. C., Navarro, P., Tate, S., Röst, H., Selevsek, N., Reiter, L., et al. (2012). Targeted data extraction of the ms/ms spectra generated by data-independent acquisition: A new concept for consistent and accurate proteome analysis. *Mol. Cell. Proteomics* 11, O111.016717. doi:10.1074/mcp.O111.016717

Graca, G., Cai, Y., Lau, C.-H. E., Vorkas, P. A., Lewis, M. R., Want, E. J., et al. (2022). Automated annotation of untargeted All-Ion Fragmentation LC–MS metabolomics

data with MetaboAnnotatoR. *Anal. Chem.* 94, 3446–3455. doi:10.1021/acs.analchem.1c03032

Guan, S., Taylor, P. P., Han, Z., Moran, M. F., and Ma, B. (2020). Data dependent-independent acquisition (DDIA) proteomics. *J. Proteome Res.* 19, 3230–3237. doi:10.1021/acs.jproteome.0c00186

Guo, J., and Huan, T. (2020a). Comparison of full-scan, data-dependent, and data-independent acquisition modes in liquid chromatography–mass spectrometry based untargeted metabolomics. *Anal. Chem.* 92, 8072–8080. doi:10.1021/acs.analchem.9b05135

Guo, J., and Huan, T. (2020b). Evaluation of significant features discovered from different data acquisition modes in mass spectrometry-based untargeted metabolomics. *Anal. Chim. Acta* 1137, 37–46. doi:10.1016/j.aca.2020.08.065

Guo, J., Shen, S., Xing, S., and Huan, T. (2021). DaDIA: Hybridizing Data-Dependent and Data-Independent acquisition modes for generating high-quality metabolomic data. *Anal. Chem.* 93, 2669–2677. doi:10.1021/acs.analchem.0c05022

Huber, F., Ridder, L., Verhoeven, S., Spaaks, J. H., Diblen, F., Rogers, S., et al. (2021). Spec2vec: Improved mass spectral similarity scoring through learning of structural relationships. *PLoS Comput. Biol.* 17, e1008724. doi:10.1371/journal.pcbi.1008724

Kaufmann, A., and Walker, S. (2016). Nested data independent MS/MS acquisition. *Anal. Bioanal. Chem.* 408, 5031–5040. doi:10.1007/s00216-016-9607-8

Koelmel, J. P., Kroeger, N. M., Gill, E. L., Ulmer, C. Z., Bowden, J. A., Patterson, R. E., et al. (2017). Expanding lipidome coverage using LC-MS/MS data-dependent acquisition with automated exclusion list generation. *J. Am. Soc. Mass Spectrom.* 28, 908–917. doi:10.1007/s13361-017-1608-0

Lawson, T. N., Weber, R. J., Jones, M. R., Chetwynd, A. J., Rodriguez-Blanco, G., Di Guida, R., et al. (2017). msPurity: automated evaluation of precursor ion purity for mass spectrometry-based fragmentation in metabolomics. *Anal. Chem.* 89, 2432–2439. doi:10.1021/acs.analchem.6b04358

McBride, R., Wandy, J., Weidt, S., Rogers, S., Davies, V., Daly, R., et al. (2023). TopNEXt: Automatic DDA exclusion framework for multi-sample mass spectrometry experiments. *bioRxiv*. doi:10.1101/2023.02.16.527961

Tada, I., Chaleckis, R., Tsugawa, H., Meister, I., Zhang, P., Lazarinis, N., et al. (2020). Correlation-based deconvolution (CorrDec) to generate high-quality MS2 spectra from Data-Independent Acquisition in multisample studies. *Anal. Chem.* 92, 11310–11317. doi:10.1021/acs.analchem.0c01980

Thermo Fisher Scientific (2022). *Thermo Fisher application programming interface*. [Dataset].

Tsugawa, H., Cajka, T., Kind, T., Ma, Y., Higgins, B., Ikeda, K., et al. (2015). MS-DIAL: Data-independent MS/MS deconvolution for comprehensive metabolome analysis. *Nat. methods* 12, 523–526. doi:10.1038/nmeth.3393

van Der Hooft, J. J. J., Wandy, J., Barrett, M. P., Burgess, K. E., and Rogers, S. (2016). Topic modeling for untargeted substructure exploration in metabolomics. *Proc. Natl. Acad. Sci.* 113, 13738–13743. doi:10.1073/pnas.1608041113

Wandy, J., Davies, V., Van Der Hooft, J. J., Weidt, S., Daly, R., and Rogers, S. (2019). *In silico* optimization of mass spectrometry fragmentation strategies in metabolomics. *Metabolites* 9, 219. doi:10.3390/metabo9100219

Wandy, J., Davies, V., McBride, R., Weidt, S., Rogers, S., and Daly, R. (2022). ViMMS 2.0: A framework to develop, test and optimise fragmentation strategies in LC-MS metabolomics. *J. Open Source Softw.* 7, 3990. doi:10.21105/joss.03990

Wang, M., Carver, J. J., Phelan, V. V., Sanchez, L. M., Garg, N., Peng, Y., et al. (2016). Sharing and community curation of mass spectrometry data with global natural products social molecular networking. *Nat. Biotechnol.* 34, 828–837. doi:10.1038/nbt.3597

Wu, Z., Ramsundar, B., Feinberg, E. N., Gomes, J., Geniesse, C., Pappu, A. S., et al. (2018). MoleculeNet: A benchmark for molecular machine learning. *Chem. Sci.* 9, 513–530. doi:10.1039/c7sc02664a

Yin, Y., Wang, R., Cai, Y., Wang, Z., and Zhu, Z.-J. (2019). DecoMetDIA: Deconvolution of multiplexed MS/MS spectra for metabolite identification in SWATH-MS-based untargeted metabolomics. *Anal. Chem.* 91, 11897–11904. doi:10.1021/acs.analchem.9b02655

Zhang, F., Ge, W., Ruan, G., Cai, X., and Guo, T. (2020). Data-independent acquisition mass spectrometry-based proteomics and software tools: A glimpse in 2020. *Proteomics* 20, 1900276. doi:10.1002/pmic.201900276

frontiers | Frontiers in Molecular Biosciences

TYPE Original Research
PUBLISHED 21 March 2023
DOI 10.3389/fmolb.2023.1074500

OPEN ACCESS

EDITED BY
Liangcai Zhao,
Wenzhou Medical University, China

REVIEWED BY
Jun Nagai,
Brigham and Women's Hospital and Harvard Medical School, United States
He-Bin Tang,
South-Central University for Nationalities, China

*CORRESPONDENCE
Xugui Li,
spine672@163.com
Ying Li,
995052246@qq.com

†These authors have contributed equally to this work and share first authorship

SPECIALTY SECTION
This article was submitted to Metabolomics, a section of the journal Frontiers in Molecular Biosciences

RECEIVED 29 October 2022
ACCEPTED 13 March 2023
PUBLISHED 21 March 2023

CITATION
Ji L, Huang P, Wang Q, Li X and Li Y (2023), Modulation of the biological network of lumbar spinal stenosis by Tongdu Huoxue Decoction based on clinical metabolomics.
Front. Mol. Biosci. 10:1074500.
doi: 10.3389/fmolb.2023.1074500

Modulation of the biological network of lumbar spinal stenosis by Tongdu Huoxue Decoction based on clinical metabolomics

Luhong Ji[1†], Ping Huang[1,2†], Qiong Wang[1], Xugui Li[3*] and Ying Li[1*]

[1]Hubei University of Chinese Medicine, Wuhan, Hubei, China, [2]Department of Rehabilitation Medicine, Central Theater General Hospital, Wuhan, Hubei, China, [3]Hubei 672 Orthopaedic Hospital of Integrated Traditional Chinese and Western Medicine, Wuhan, Hubei, China

Objective: To explore the clinical efficacy and metabolic mechanism of Tongdu Huoxue Decoction (THD) in treating lumbar spinal stenosis (LSS).

Methods: A total of 40 LSS patients and 20 healthy participants were recruited from January 2022 to June 2022. The patients' pre- and post-treatment visual analogue scale (VAS) and Japanese Orthopaedic Association (JOA) scores were recorded. ELISA kits were used to assess pre- and post-treatment levels of serum Interleukin-1beta (IL-1β), Alpha tumour necrosis factor (TNF-α) and prostaglandin E2 (PGE2). Finally, the patients' pre- and post-treatment and healthy human sera were subjected to extensively targeted metabolomics using Ultra Performance Liquid Chromatography (UPLC) to identify potential differential metabolites and metabolic pathways using multivariate statistical analysis.

Results: Compared to the pre-treatment (group A), the patients' VAS scores decreased significantly ($p < 0.05$), while JOA scores increased significantly ($p < 0.05$) post-treatment (group B), indicating that THD could effectively improve the pain and lumbar spine function of LSS patients. Moreover, THD could effectively inhibit the expression of IL-1β, TNF-α and PGE2-associated inflammatory factors in serum. Regarding metabolomics, the levels of 41 differential metabolites were significantly different in the normal group (group NC) compared to group A, and those were significantly restored after treatment with THD, including chenodeoxycholic acid 3-sulfate, taurohyodeoxycholic acid, 3,5-Dihydroxy-4-methoxybenzoic acid, pinocembrin. These biomarkers are mainly involved in purine metabolism, steroid hormone biosynthesis and amino acid metabolism.

Conclusion: This clinical trial demonstrated that THD is effective in improving pain, lumbar spine function and serum levels of inflammation in patients with LSS. Moreover, its mechanism of action is related to the regulation of purine metabolism, steroid hormone biosynthesis and the expression of key biomarkers in the metabolic pathway of amino acid metabolism.

KEYWORDS

Tongdu Huoxue Decoction, lumbar spinal stenosis, metabolomics, pain, inflammation

1 Introduction

Lumbar spinal stenosis (LSS) is a degenerative disease of the lumbar spine. It can lead to increased pressure in the spinal canal, causing cauda equina ischaemia or compression of the nerve roots, resulting in low back pain. The pain may be confined to the lower limbs or span multiple dermatomes, as well as impaired movement or sensation during walking, intermittent claudication and other clinical symptoms that seriously impact people's productivity and quality of life (Deer et al., 2022). Studies have reported an 11% prevalence of symptomatic LSS in the general population, with almost half of those over 60 years experiencing symptomatic LSS. The number of people with disabilities due to LSS is expected to increase globally as the population ages rapidly (Young et al., 2020). Surgical intervention is common, but postoperative pain and disability might persist, and studies have noted that no significant benefit has been observed with surgical treatment compared to non-surgical treatment (Zaina et al., 2016). The 2nd edition of the North American Spine Surgery Society (NASS) Guidelines for the Management of Degenerative Lumbar Spinal Stenosis recommends that patients with mild to moderate lumbar spinal stenosis be considered for conservative treatment with medication, physical therapy and functional exercise (Kreiner et al., 2013). Therefore, non-surgery management is urgently needed for patients, and previous studies have shown that Chinese medicine has clear advantages in treating LSS, with the holistic concept and evidence-based treatment being its main philosophy (Zhao et al., 2019).

Tongdu Huoxue Decoction (THD) is an experienced formula for treating degenerative spinal stenosis and consists of *Cervus elaphus Linnaeus* (Lu Jiao), *Cibotium barometz* (L.), *J.Sm.* (Jinmao Gouji), *Eucommia ulmoides Oliv.* (Du Zhong), *Astragalus membranaceus* (Fisch.) *Bge.var.mongholicus* (Bge.) *Hsiao* (Huang Qi), *Angelica sinensis* (Oliv.) *Diels* (Dang Gui), *Caesalpinia sappan L.* (Su Mu), *Lycopus lucidus Turcz. var. hirtus Regel* (Ze Lan Ye), *Pheretima aspergillum* (E.Perrier) (Di Long), *Paeonia lactiflora Pall.*(Chi Shao), and *Salvia miltiorrhiza Bge.* (Dan Shen). These substances have good anti-inflammatory and analgesic effects and can effectively reduce patients' clinical symptoms and improve the quality of life (Shu et al., 2005; Wu and Dong, 2016). THD was created by Chinese orthopaedic specialist Li Tongsheng and is mentionedin his book "*Famous Doctors' Remedies for Experimentation*". It has been reported that THD can improve the microcirculatory perfusion of the spinal stenosis lesion, improve local nerve root ischemia and hypoxia, accelerate the action of local inflammatory mediators and pain-causing factors, thereby reducing the patient's back pain and improve the function of the lower limbs (Li and Li, 1991). Some studies found that THD-containing serum can slow down the degeneration of the intervertebral disc annulus by reducing the expression of NLRP3 inflammatory vesicle-mediated caspase-1 signalling pathway-related cytokines, inhibiting lipopolysaccharide/ATP-induced cell scorching, and controlling the release of inflammatory factors (Wu et al., 2021). This might be the pharmacodynamic basis for THD's anti-inflammatory and analgesic effects. However, the effects of metabolites in treating LSS with THD are unclear. Alterations in metabolites can regulate gene transcription, and gene remodelling occurs when abnormal expression of some proteins is corrected, suggesting that changes in certain metabolic processes occur at the epigenetic level (Gao et al., 2022).

Metabolomics is capable of qualitative and quantitative analysis of metabolites in organisms. It can be used to study the changes in biomarkers and interference pathways in the body after Traditional Chinese Medicine (TCM) interventions and to scientifically interpret the efficacy of TCM interventions in diseases and their mechanisms of action (Wu et al., 2022). One study demonstrated tissue metabolism during intervertebral disc degeneration by correlating rat and human metabolomics and found that the degenerative process was associated with changes in carbohydrate utilisation patterns in the Gly-Ser-Thr metabolic axis and reduced antioxidant capacity in the *in-vitro* diagnostic environment. This process ultimately leads to the disintegration of the fibrous ring and the loss of water fixation groups (Wu et al, 2021). Moreover, metabolite changes in both serum and disc tissue of patients with disc degeneration are associated with amino acid metabolism, with increased glycine levels in both (Swank et al., 2020). This may provide ideas for treating patients with lumbar disc herniation or lumbar spinal stenosis. In addition, a broadly targeted metabolomic serum analysis using UPLC revealed that the Chinese medicine Zuojin pill was able to act as an inflammatory inhibitor, inhibiting levels of the inflammatory factors COX-2, IL-4 and IL-17, thereby regulating the combined metabolic disorders in patients with chronic non-atrophic gastritis (Ma et al., 2022). These studies offer the possibility of technical applications of THD in LSS. Therefore, we conducted a clinical trial to validate THD's analgesic and anti-inflammatory effects in LSS and explore the underlying mechanisms using metabolomics to provide a scientific basis for clinical treatment.

2 Methods and design

2.1 Patients and methods

We recruited patients attending the Department of Spine Surgery, Hubei 672 Orthopaedic Hospital of Integrated Traditional Chinese and Western Medicine, from January 2022 to June 2022. The ethical approval was granted by the Ethics Committee of Hubei 672 Orthopaedic Hospital of Integrated Traditional Chinese and Western Medicine (672HREC20220115A).

The inclusion criteria were as follows:1) the diagnostic criteria for LSS were met, and the clinical diagnosis of LSS was determined by a combination of clinical symptoms and radiological findings of LSS on computed tomography (CT) or magnetic resonance imaging (MRI). Computed tomography or MRI shows narrowing of the lumbar spinal canal with compression of the cauda equina by thickened posterior vertebral bodies, small joints, marginal bony bulges or soft tissue structures such as the ligamentum flavum or disc herniation (Alvarez and Hardy, 1998); 2) age 18–70 years; 3) no indication for the surgery; 4) voluntary signed informed consent form. Exclusion criteria are as follows: 1) patients with other severe orthopaedic conditions; 2) those with severe medical conditions; 3) psychiatric patients; 4) pregnant or lactating women, allergic patients or those who cannot

receive this treatment; 5) those who were already receiving other treatments that may affect the results of this study. The criteria for discontinuation/exclusion/withdrawal were as follows: 1) patients with severe adverse reactions during the study; 2) patients with poor compliance; 3) patients who were assessed to have difficulty tolerating the study protocol during the study. Discontinuation: In the event of withdrawal due to allergy or other adverse reactions to the study drug, the participant would be offered a specialist consultation and medication at no cost. All participants provided written informed consent and were screened by physical examination, medical history assessment and clinical laboratory tests.

Forty eligible patients were recruited to receive THD as the treatment. THD consisted of Lu Jiao 18 g, Jinmao Gouji 12 g, Du Zhong 9 g, Huang Qi 18 g, Dang Gui 9 g, Su Mu 9 g, Ze Lan Ye 9 g, Di Long 9 g, Chi Shao 9 g, and Dan Shen 18 g. All the above drugs were provided by the pharmacy of Hubei 672 Orthopaedic Hospital of Integrated Traditional Chinese and Western Medicine. Twenty general participants were used as the healthy group. The mean age of the patients was 50.83 ± 8.15 years, and the mean age of the normal group was 52.075 ± 7.82 years, and the difference in age between the two groups was not statistically significant ($p > 0.05$). Treatment: patients were given oral THD 150 mL/dose twice/day for 4 weeks. We collected 5 mL of fasting venous blood from the participants in the morning, rested at 4°C for 1 h, and centrifuged for 10 min (3000 r-min-1). Then, the supernatant was removed and stored frozen at −80 °C. Blood was collected from the patients in pre-treatment (A) and post-treatment (B) and once from the normal group (NC).

2.2 Efficacy evaluation

The patient's self-reported pain was scored pre- and post-treatment using a visual analogue scale (VAS), with higher scores indicating severe subjective pain. The patient's lumbar spine function was assessed pre- and post-treatment using the Japanese Orthopaedic Association (JOA) Assessment Treatment Score, with higher JOA scores indicating better recovery (Lyu et al., 2021).

2.3 Serum testing

Changes in serum interleukin-1-beta (IL-1β), tumour necrosis factor-alpha (TNF-α), and prostaglandin-E2 (PGE2) levels in the two groups of patients pre- and post-treatment were measured according to the method described in the ELISA kit for human use.

2.4 Metabolomics analysis

2.4.1 Sample preparation and extraction

The sample stored at −80 °C refrigerator was thawed on ice and vortexed for 10 s 50 μL of sample and 300 μL of 20% acetonitrile methanol internal standard extract were added into a 2 mL microcentrifugetube. The sample was vortexed for 3 min and then centrifuged at 12,000 rpm for 10 min (4 °C). 200 μL of the supernatant was collected and placed in −20 °C for 30 min, and then centrifuged at 12,000 rpm for 3 min (4 °C). A 180 μL aliquots of supernatant were transferred for LC-MS analysis.

2.4.2 UPLC conditions (T3)

All samples were acquired by Waters ACQUITY UPLC combined with the Xevo TQ-S Micro mass spectrometer system followed machine orders. The analytical conditions were as follows, UPLC: column, Waters ACQUITY UPLC HSS T3 C18 (1.8 μm, 2.1 mm*100 mm); column temperature, 40 °C; flow rate, 0.4 mL/min; injection volume, 2μL; solvent system, water (0.1% formic acid): acetonitrile (0.1% formic acid); gradient program, 95:5 V/V at 0 min, 10:90 V/V at 11.0 min, 10:90 V/V at 12.0 min, 95:5 V/V at 12.1 min, 95:5 V/V at 14.0 min.

2.4.3 Sample Quality Control analysis

Quality Control (QC) samples were prepared from a mixture of sample extracts and were used to analyse the reproducibility of the samples under the same processing method. During the instrumental analysis, one QC sample was inserted for every ten samples tested for analysis to monitor the reproducibility of the analytical process.

2.4.4 Differential metabolite and metabolic pathway analysis

The original data file acquisited by LC-MS was converted into mzML format by ProteoWizard software. Peak extraction, peak alignment and retention time correction were respectively performed by XCMS program. The "SVR" method was used to correct the peak area. The peaks with detetion rate lower than 50% in each group of samples were discarded. After that, metabolic identification information was obtained by searching the laboratory's self-built database, integrated public database, AI database and metDNA.

Principal component analysis (PCA) was performed by statistics function prcomp within R (www.r-project.org). The data was unit variance scaled before unsupervised PCA. For two-group analysis, differential metabolites were determined by VIP (VIP ≥1), p-value (p-value <0.05, Student's t test) and absolute Log2FC (|Log2FC| ≥ 1.0). VIP values were extracted from orthogonal partial least squares discriminant analysis (OPLS-DA) result, which also contain score plots and permutation plots, was generated using R package MetaboAnalystR. The data was log transform and mean centering before OPLS-DA. In order to avoid overfitting, a permutation test (200 permutations) was performed. Identified metabolites were annotated using KEGG Compound database (http://www.kegg.jp/kegg/compound/), annotated metabolites were then mapped to KEGG Pathway database (http://www.kegg.jp/kegg/pathway.html). Significantly enriched pathways are identified with a hypergeometric test's p-value for a given list of metabolites.

2.5 Statistical analysis

SPSS 24.0 was used to analyse the data. χ2 test was applied to compare the differences between groups, and the t-test was used to compare the measurement data at the test level of a = 0.05. All

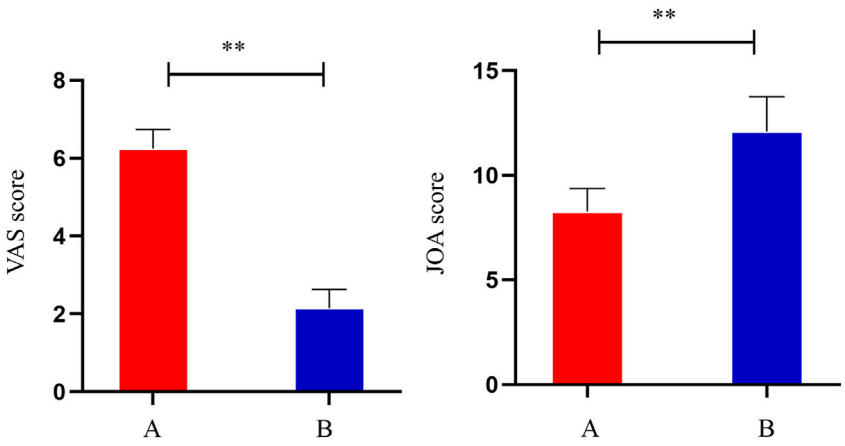

FIGURE 1
VAS scores and JOA scores of patients before and after treatment. **: $p < 0.01$.

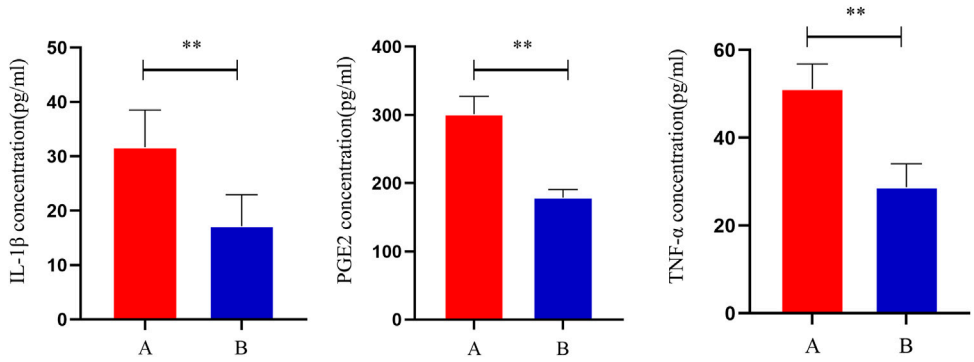

FIGURE 2
Changes in serum levels of IL-1β, TNF-α and PGE2 in patients before and after treatment. **: $p < 0.01$.

statistical tests were performed using a two-sided test, and $p < 0.05$ would be considered a statistically significant difference.

3 Results

3.1 Comparison of patients' VAS and JOA scores pre- and post-treatment

Compared to the pre-treatment period (A), the VAS scores of the patients decreased significantly after treatment (B) ($p < 0.05$), indicating that THD was able to reduce the pain of patients with LSS. Compared to the pre-treatment period (A), the JOA scores of the patients increased significantly after treatment (B) ($p < 0.05$). Thus, the results indicated that THD could improve the function of the lumbar spine in patients with LSS (Figure 1).

3.2 Comparison of serum inflammatory factors

Compared to group A, serum IL-1β, TNF-α, and PGE2 levels were significantly lower in group B ($p < 0.05$), indicating that THD could improve the inflammation level in the serum of LSS patients (Figure 2).

3.3 Metabolomic results

3.3.1 Metabolic routine analysis

This experiment selected 20 samples and divided them into three groups for metabolic studies. We detected 3412 metabolites. According to the analysis of metabolite composition, the main component was benzene and substituted derivatives, amino acid and its metabolites, heterocyclic compounds, and organic acid and its derivatives (Supplementary Figure S1). Overlap display analyses of total ion flow plots (TIC plots) were analysed using mass spectrometric detection. Different QC samples showed high overlap curves for metabolite detection of total ion flow, i.e., consistent retention times and peak intensities (Supplementary Figure S2), indicating good signal stability of the mass spectrometry for the same sample at different times. The coefficient of variation (CV) is the ratio of the standard deviation of the original data to the mean of the original data and reflects the degree of dispersion of the data. The empirical cumulative distribution function (ECDF) can be used to analyse the

10.3389/fmolb.2023.1074500

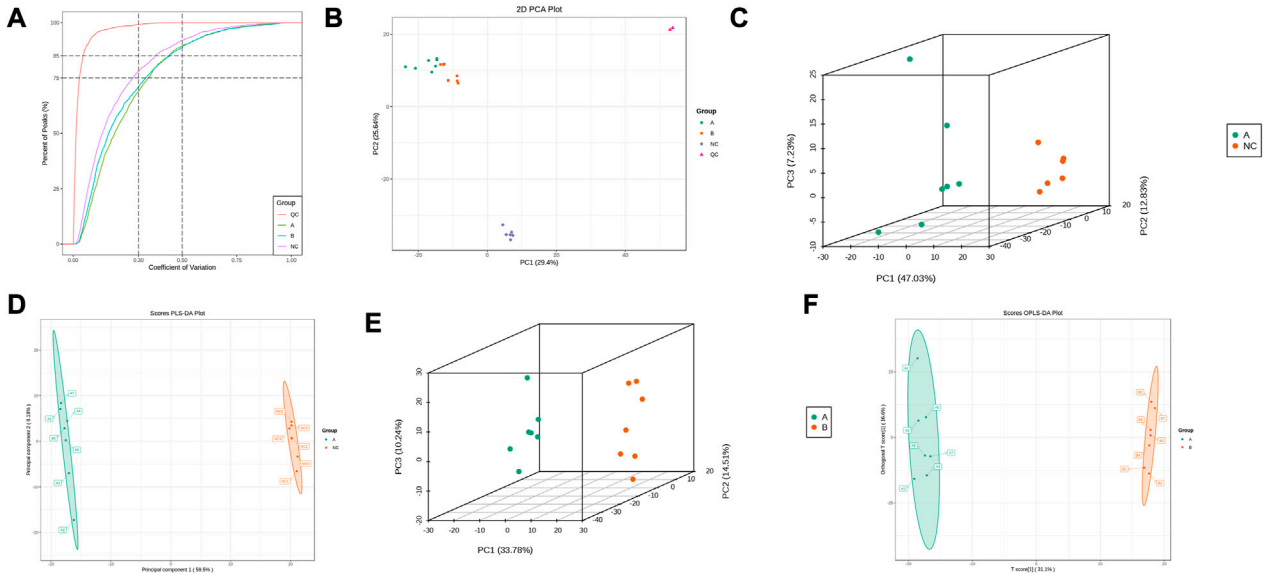

FIGURE 3
Metabolic Pulmonary Analysis. **(A)** CV distribution of each group of samples; **(B)** PCA score of each group of samples with mass spectral data of QC samples; **(C)** PCA score between A and NC; **(D)** OPLS-DA analysis between A and NC; **(E)** PCA score between A and B; **(F)** OPLS-DA analysis between A and B.

frequency of substances with CVs smaller than the reference value. In this study, the percentage of substances with CV values less than 0.3 was higher than 85%, indicating that the experimental data were very stable (Figure 3A).

PCA results showed trends in metabolome separation between groups and whether metabolomes differ within sample groups (Ho et al., 2013). The samples from the different groups in the PCA plot were clustered overall (Figure 3B), indicating good similarity within groups. Furthermore, QC samples were clustered and located in the middle of the other three groups, indicating good system stability, while the ability to separate the three groups indicated significant differences between groups. B lies between A and NC, suggesting that THD improved serum metabolism in patients with LSS. PLS-DA combined orthogonal signal correction and PLS-DA methods, with OPLS-DA maximising group differentiation and facilitating the search for differential metabolites compared to PCA. The characteristics between the NC and A, and A and B groups were well distinguished from each other in both the PCA and OPLS-DA score plots (Figures 3C–F). In the permutation test of OPLS-DA, R2X = 0.518, R2Y = 1, Q2 = 0.987 in NC and A group, R2X = 0.477, R2Y = 0.999, Q2 = 0.945 in A and B group, and $p < 0.05$, indicating that the OPLS-DA model has a high explanatory and predictive rate. In the permutation test of PLS-DA, R2X = 0.677, R2Y = 1, Q2 = 0.997 in NC and group A, R2X = 0.498, R2Y = 0.999, Q2 = 0.99 in A and B group, $p < 0.05$, indicating that the PLS-DA model has a high explanatory and predictive rate. (Supplementary Figure S3).

3.3.2 Screening for differential metabolites

Comparing the NC group with group A, there were 309 differential metabolites satisfying VIP >1, |Log2FC| ≥ 1.0 and $p < 0.05$, including 260 under anionic conditions, 98 upregulated and 162 downregulated; and 49 differential metabolites under cationic conditions, including 13 upregulated and 36 downregulated (Figures 4A, B). Moreover, heat maps were used to demonstrate the biomarkers between the groups and the differential expression of the biomarkers between the groups (Figures 4C, D). The top 20 potential biomarkers with VIP ≥1 included ursocholic acid, cephamycin C, ganolucidic acid C, ferulic acid dilactone, glycine deoxycholic acid caffeine, all-trans-13,14-Dihydroretinol, androstanedione, Arg-Tyr-Gln-Lys (Arginine-Tyrosine-Glutamine-Lysine), deoxycholic acid (Figures 5A, B). Based on the fold change values, the top 10 upregulated and downregulated biomarkers in the NC/A group comparison were mainly 2-Hydroxy-3-isopropyl-6-methyl benzoic acid, 3-Phosphoglyceric acid, Lys-Gln-Ile-Glu (lysine-glutamine-isoleucine-glutamic acid), taurohyodeoxycholic acid, 2-Methylnaphthalene 3alpha, 12alpha-Dihydroxy-5beta-chol-6-enoate, retinol, mitragynine (Figures 5C, D). In addition, the radar plot selectively shows ten representative biomarkers with variable scores, including Lys-Gln-Ile-Glu, 2-Hydroxy -3-isopropyl-6-methyl benzoic acid, taurohyodeoxycholic acid, 2-Methylnaphthalene, caffeine, mitragynine (Figures 5E, F). This suggests that amino acid metabolism and lipid metabolism abnormalities might be associated with developing LSS.

The sera from groups A and B were subjected to metabolomic analysis, and 309 differential metabolites satisfying VIP >1, Log2FC > 1 and $p < 0.05$, including 88 under anionic conditions, 48 upregulated and 40 downregulated, and 20 differential metabolites under cationic conditions, including 12 upregulated and 8 downregulated (Figures 6A, B). Heat maps were used to demonstrate the biomarkers in each group and differential expression between groups (Figures 6C, D). Of these, the top 20 potential biomarkers with VIP ≥1 were mainly ganolucidic acid C, chaetochromin, Leu-Asn-Arg-Glu, laminaribiose, N-(4-aminobutyl)-3-(4-hydroxy-3-methoxyphenyl) prop-2-enimidic acid, 8-Aminooctanoic

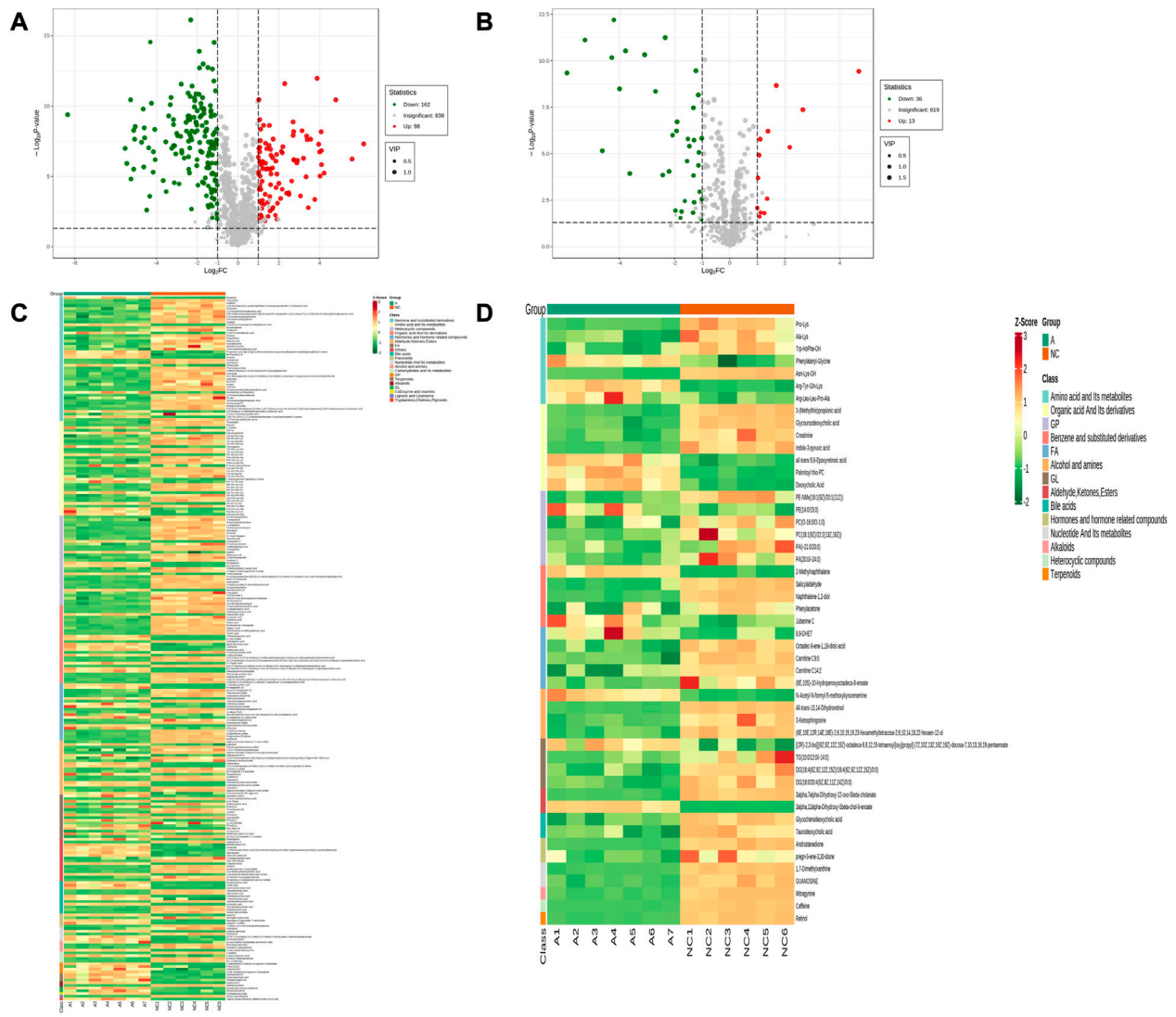

FIGURE 4
Expression of differential metabolites in NC vs. group A. **(A)** volcano plot of differential metabolites under anionic conditions; **(B)** volcano plot of differential metabolites under cationic conditions; **(C)** heat map of differential metabolite expression between samples under anionic conditions; **(D)** heat map of differential metabolite expression between samples under cationic conditions.

Acid, D-urobilinogen, Arg-Tyr-Gln-Lys (Figures 7A, B). The top ten upregulated and downregulated biomarkers in the A/B group comparison, based on the fold change values, contained Thiamine monophosphate, cholesteryl hemisuccinate, Leu-Asn-Arg-Glu (Leucine-Asparagine-Arginine- Glutamic acid), Ganolucidic acid C, D-Quinovose, 8-Aminooctanoic Acid, Arg-Tyr-Gln-Lys, D-urobilinogen, (S)-1-Phenylethanol, all-trans-5,6- Epoxyretinoic acid (Figures 7C, D). In addition, the radar plot selectively shows ten representative biomarkers with variable fractions of Leu-Asn-Arg-Glu, Phylloquinone oxide, Hydroxyecdysone, Arg-Tyr-Gln-Lys, D urobilinogen, and (S)-1-Phenylethanol (Figures 7E, F). The results suggested that THD could regulate amino acid and lipid metabolisms in the body of LSS patients, thus exerting its therapeutic effects.

Furthermore, Venn diagrams were used to identify the intersection between NC/A and A/B and identified 76 common biomarkers. Among those, 41 had significantly different levels in the normal group compared to pre-treatment and were significantly restored after THD treatment (Table 1). Most of those biomarkers belonged to amino acids and their metabolites, bile acids, organic acids and their derivatives, indicating that THD could regulate amino acid and lipid metabolisms in LSS patients.

3.3.3 Metabolite pathway analysis

Metabolites interact with the organism to form different pathways. Metabolic signalling in KEGG showed that bile secretion, vitamin digestion and absorption, ubiquinone and other terpenoid-quinone biosynthesis, primary bile acid biosynthesis, phenylalanine, tyrosine and tryptophan biosynthesis were altered compared to NC (Figure 8A). In contrast, metabolic pathways, biosynthesis of cofactors, and mannose-type O-glycan

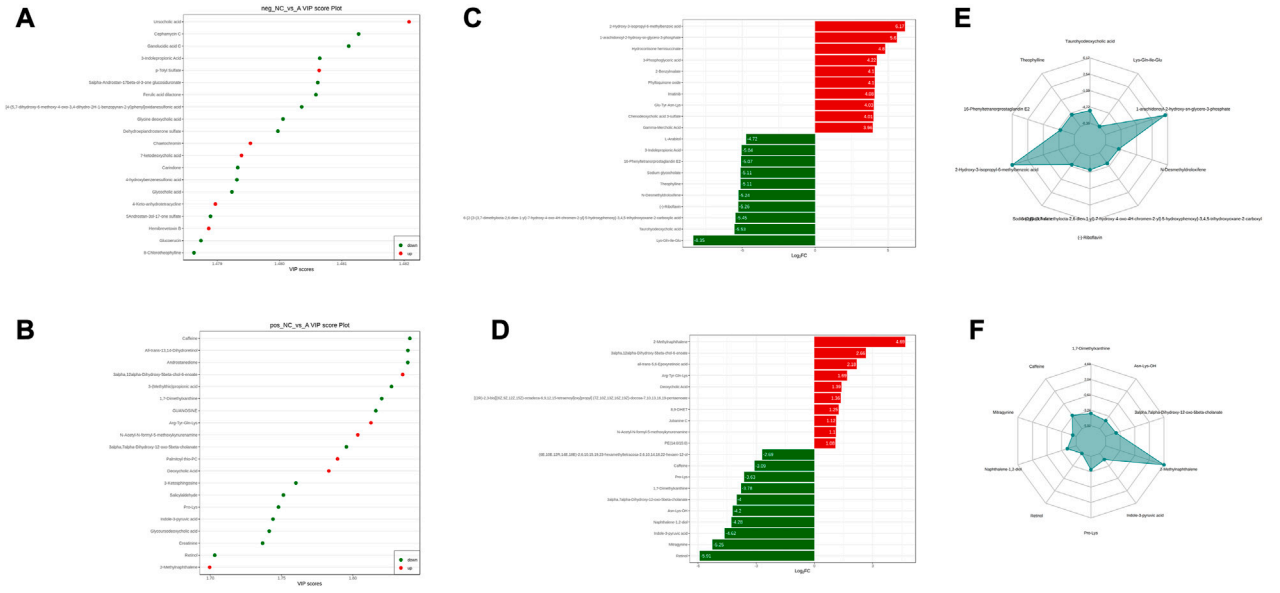

FIGURE 5
NC vs. group A differential metabolite screening. **(A)** top 20 potential differential metabolites with VIP ≥1 under anionic conditions; **(B)** top 20 potential differential metabolites with VIP ≥1 under cationic conditions; **(C)** top 10 differential metabolites with up- and downregulated ploidy change values under anionic conditions; **(D)** top 10 differential metabolites with up- and downregulated ploidy change values under cationic conditions; **(E)** radar plot under anionic conditions selectively showing ten representative differential metabolites with change fractions; **(F)** radar plot under cationic conditions selectively showing ten representative differential metabolites with change fractions.

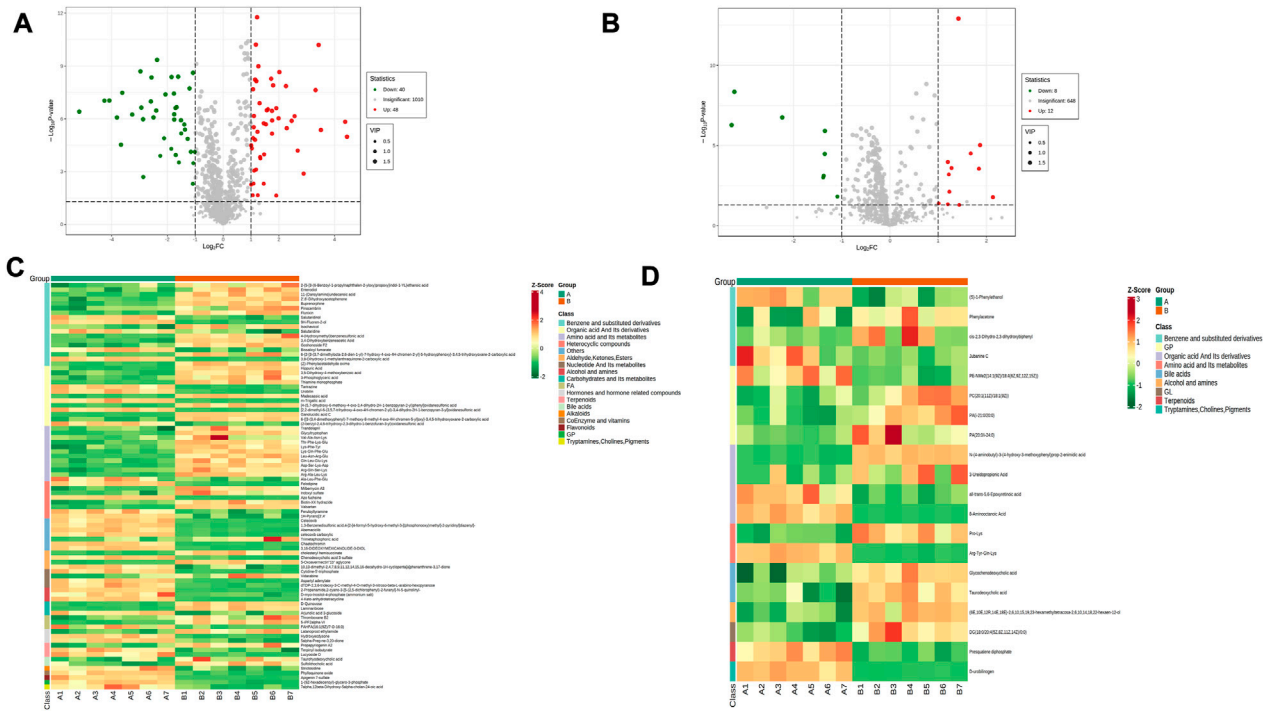

FIGURE 6
Expression of differential metabolites in groups A vs. B **(A)** volcano plot of differential metabolites under anionic conditions; **(B)** volcano plot of differential metabolites under cationic conditions; **(C)** heat map of differential metabolite expression between samples under anionic conditions; **(D)** heat map of differential metabolite expression between samples under cationic conditions.

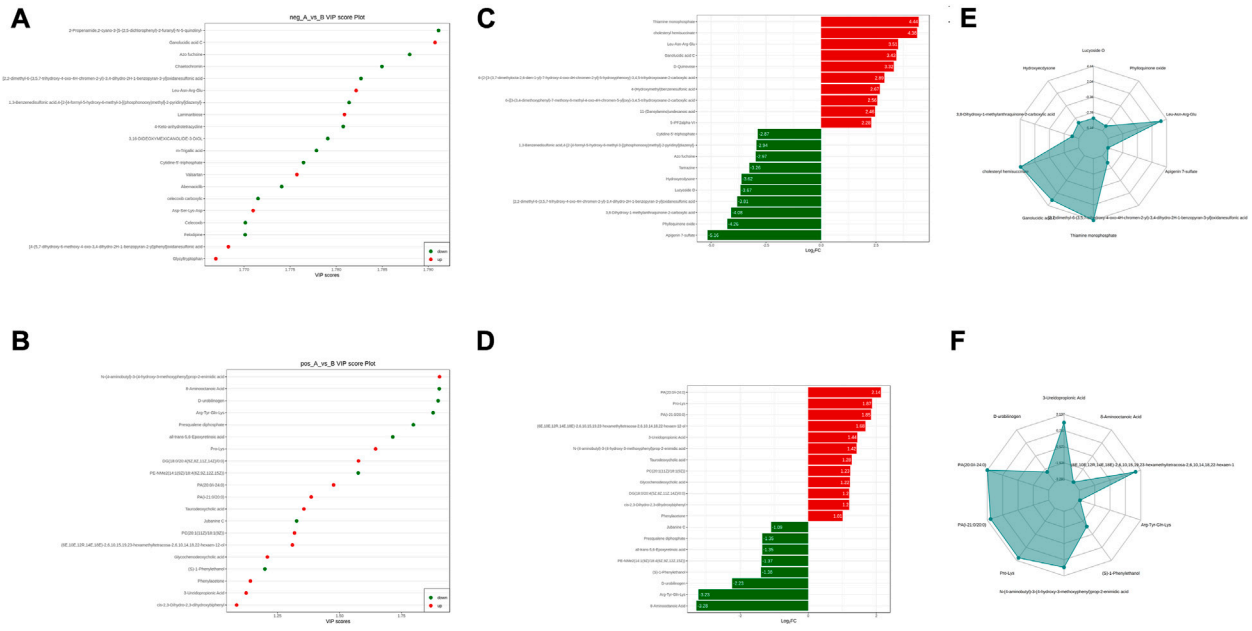

FIGURE 7
Groups A vs. B differential metabolite screening. **(A)** top 20 potential differential metabolites with VIP ≥1 under anionic conditions; **(B)** top 20 potential differential metabolites with VIP ≥1 under cationic conditions; **(C)** top ten differential metabolites with up- and downregulated ploidy change values under anionic conditions; **(D)** top ten differential metabolites with up- and downregulated ploidy change values under cationic conditions; **(E)** radar plot under anionic conditions selectively showing ten representative differential metabolites with change fractions; **(F)** radar plot under cationic conditions selectively showing ten representative differential metabolites with change fractions.

biosynthesis were regulated in the serum of patients before and after THD treatment, which might be an effective pathway for THD treatment of LSS (Figure 8B).

In addition, metabolic enrichment analysis (MSEA) does not require the specification of clear thresholds for differential metabolites and identifies significantly different metabolomes through a series of metabolic ensembles, each representing a biological function (Ma et al., 2022). The results showed that steroid hormone biosynthesis, biotin metabolism, one carbon pool by folate, tyrosine metabolism, and pyrimidine metabolism were the main pathways of metabolic differences between A and NC (Figure 9A). Purine metabolism, steroid hormone biosynthesis, tyrosine metabolism, one carbon pool by folate, and arginine biosynthesis had significant differences before and after THD treatment (groups A and B) (Figure 9B). This suggested a clear overlap between the therapeutic process of THD with LSS and its development. THD can potentially correct amino acid metabolism in patients with LSS and thus achieve therapeutic effects.

4 Discussion

Pain is the main symptom and reason for patients to seek medical attention, and low back pain is one of the common symptoms among LSS patients. Unbearable pain and severe functional impairment are the most common reasons patients with LSS undergo spinal surgery (Lurie and Tomkins-Lane, 2016). Treatment of THD is effective in relieving pain and improving the functional movement of the lumbar spine in patients with LSS. Moreover, the effective relief of pain is thought to be closely related to reducing local tissue inflammation in patients(Conaghan et al., 2019). In this study, serum levels of IL-1β, TNF-α and PGE2 decreased significantly after THD treatment compared with those before treatment. In contrast, levels of the pro-inflammatory cytokines IL-1β, TNF-α, and PGE2 were significantly elevated in the serum of surgically induced LSS rats, and it was noted that these inflammatory factors were closely related to pain (Park et al., 2019). Inhibition of the expression of key inflammatory mediators reduces LSS-induced chronic mechanical abnormalities in pain (Lee et al., 2019).

Activation of inflammation contributes to fibrosis and hypertrophy of the ligamentum flavum in the LSS (Sun et al., 2018). Macrophage migration inhibitory factor (MIF) promotes ligamentum flavum proliferation through the Src kinase signaling pathway and extracellular matrix changes through its pro-inflammatory effects. MIF and its mediated inflammatory response are the drivers of ligamentum flavum hypertrophy (Lu et al., 2022). The MIF content is positively correlated with the thickness of the ligamentum flavum, and it promotes fibroblast proliferation and collagen fibrillation which might be an important part of the ligamentum flavum scar repair leading to its hypertrophy. The inflammatory response, which includes both inflammatory damage and repair, is one of the main components of the blood stasis theory in TCM, and herbs with blood activation and blood stasis removal effects can effectively block the inflammatory and pro-proliferative effects of MIF on fibroblasts (Lu, 2020). Modern pharmacological studies have shown that tonifying the kidney and invigorating the blood can effectively reduce the expression of inflammatory factors and inhibit the degeneration of articular cartilage (Wang et al., 2022). THD is a clinically representative formula for tonifying the kidneys and invigorating the blood.

TABLE 1 Levels of 41 biomarkers were significantly restored by THD treatment.

	Formula	Compounds	Class I	VIP	*p*-value	Log2FC	Type
MW0109398	C11H21N3O3	Pro-Lys	Amino acid and Its metabolites	1.65	9.35E-06	1.87	up
MW0053750	C26H43NO5	Glycochenodeoxycholic acid	Bile acids	1.21	6.31E-04	1.22	up
MW0139070	C15H20O4	N-(4-aminobutyl)-3-(4-hydroxy-3-methoxyphenyl)prop-2-enimidic acid	Organic acid And Its derivatives	1.90	1.25E-13	1.42	up
MEDN0841	C4H8N2O3	3-Ureidopropionic Acid	Organic acid And Its derivatives	1.12	5.00E-02	1.44	up
MEDP1233	C33H42N4O6	D-urobilinogen	Tryptamines, Cholines,Pigments	1.90	1.76E-07	−2.23	down
MW0063749	C26H45NO6S	Taurodeoxycholic acid	Bile acids	1.36	2.51E-04	1.28	up
MW0140638	C8H10O	(S)-1-Phenylethanol	Benzene and substituted derivatives	1.20	9.83E-04	−1.38	down
MW0015647	C20H28O3	all-trans-5,6-Epoxyretinoic acid	Organic acid And Its derivatives	1.71	3.30E-05	−1.35	down
MW0155485	C9H10O	Phenylacetone	Benzene and substituted derivatives	1.14	4.03E-02	1.01	up
mws3144_N	C8H17NO2	8-Aminooctanoic Acid	Organic acid And Its derivatives	1.90	5.26E-07	−3.28	down
MW0147534	C12H12O2	cis-2,3-Dihydro-2,3-dihydroxybiphenyl	Benzene and substituted derivatives	1.09	4.51E-02	1.20	up
MW0155740	C30H52O7P2	Presqualene diphosphate	Terpenoids	1.80	1.21E-06	−1.35	down
MW0060196	C39H68NO8P	PE-NMe2(14:1(9Z)/18:4(6Z,9Z,12Z,15Z))	GP	1.58	7.68E-04	−1.37	down
MW0057219	C46H88NO8P	PC(20:1(11Z)/18:1(9Z))	GP	1.32	7.52E-03	1.23	up
MW0056644	C44H87O8P	PA(i-21:0/20:0)	GP	1.39	2.78E-04	1.85	up
MW0055921	C47H93O8P	PA(20:0/i-24:0)	GP	1.48	1.65E-02	2.14	up
MW0107606	C39H47N5O5	Jubanine C	Benzene and substituted derivatives	1.33	1.51E-02	−1.09	down
MW0050034	C41H72O5	DG(18:0/20:4(5Z,8Z,11Z,14Z)/0:0)	GL	1.58	1.05E-04	1.20	up
MW0145540	C26H43N9O7	Arg-Tyr-Gln-Lys	Amino acid and Its metabolites	1.88	4.48E-09	−3.23	down
MW0166423	C30H50O	(6E,10E,12R,14E,18E)-2,6,10,15,19,23-hexamethyltetracosa-2,6,10,14,18,22-hexaen-12-ol	Alcohol and amines	1.31	3.10E-05	1.68	up

Astragalus polysaccharide, the active ingredient of Huang Qi, can inhibit macrophage migration inhibitory factor(Liao et al., 2020). In addition, Huang Qi, Dang Gui and Dan Shen are involved in enhancing angiogenesis and osteogenesis in THD. Their positive effect on bone formation may be related to their ability to promote angiogenesis by acting on substances such as VEGF (Yang et al., 2014). Huang Qi and Dan Shen have been shown to promote the proliferation of bone marrow mesenchymal stem cells and TGF-β1-induced bone marrow mesenchymal stem cells *in vitro*(Cai et al., 2015). Tanshinone IIA is one of the main active phytochemicals isolated from Dan Shen, which has been reported to inhibit osteoclast differentiation and bone resorption by disrupting the actin ring, thereby inhibiting osteoclast formation and bone erosion(Kwak et al., 2008; Nicolin et al., 2010).

Based on the apparent clinical effects of THD on LSS, we explored its mechanism of action using metabolomics and showed that the levels of 41 potential metabolites were significantly restored by THD treatment, including Chenodeoxycholic acid 3-sulfate, Taurohyodeoxycholic acid, 3,5-Dihydroxy-4-methoxy benzoic acid, Pinocembrin. Bile acids have multiple biological functions and are involved in pathways, including lipid and glucose metabolism, energy expenditure and inflammation, thereby regulating metabolism-related diseases. By quantifying circulating levels of specific bile acids, Taurohyodeoxycholic acid was found to be negatively associated with diabetes(Choucair et al., 2020). The association between diabetes and LSS is a risk factor for developing LSS, and prolonged and poorly controlled hyperglycaemia can exacerbate disc degeneration(Asadian et al., 2016; Kakadiya et al., 2020). Upregulation of Chenodeoxycholic acid 3-sulfate levels is thought to disrupt the metabolic processes of the body's antioxidant defence (Wang et al., 2021). Similarly, 3,5-Dihydroxy-4-methoxybenzoic acid, a new antioxidant flavonoid, can effectively inhibit the level of reactive oxygen species and regulate the inflammatory process(Oladele Oladimeji et al., 2018; Gadallah et al., 2020). Pinocembrin attenuates

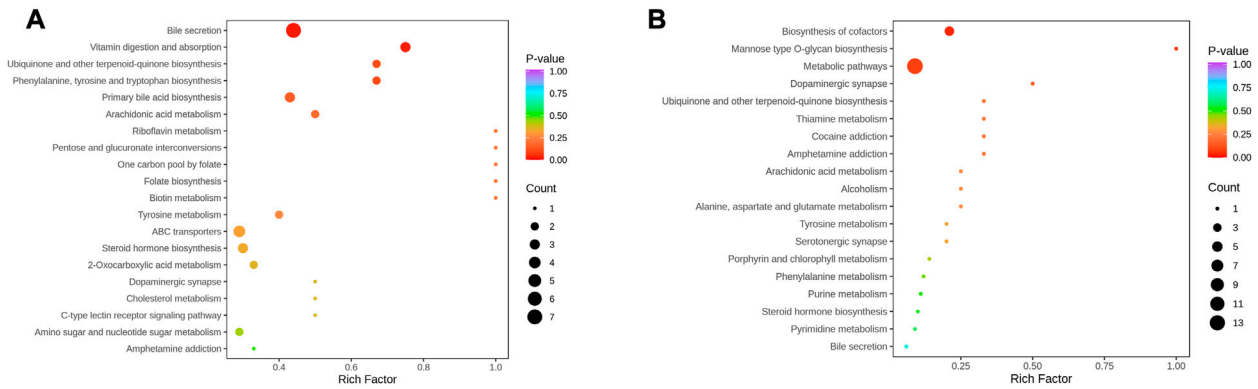

FIGURE 8
KEGG Enrichment analysis of differential metabolites. **(A)**: NC vs. A; **(B)** A vs. B; the dot's colour is the *p*-value. The redder it is, the more significant the enrichment is. The dot size represents the number of differential metabolites in the pathway enriched).

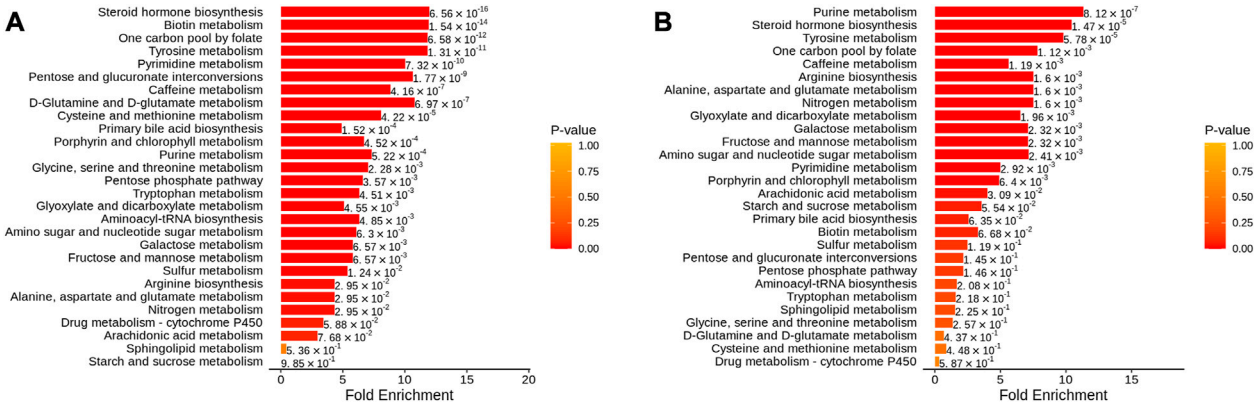

FIGURE 9
MSEA of differential metabolites. **(A)**: NC vs. A; **(B)** A vs. B; The dot's colour represents *p*-value).

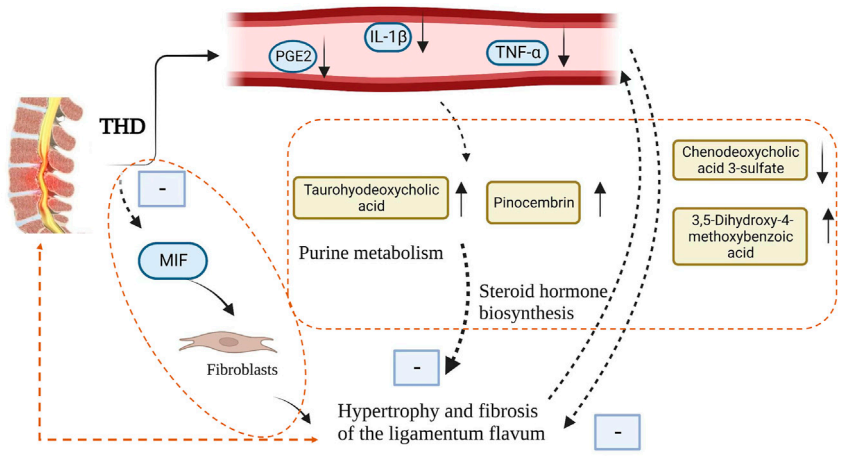

FIGURE 10
THD intervenes in LSS metabolic pathway mechanism map.

glucocorticoid-induced apoptosis in osteoblasts by inhibiting the PI3K/Akt/mTOR pathway to activate autophagy and may have a protective effect on osteocytes(Wang et al., 2020). The levels of these flavonoid molecules were significantly higher post-treatment compared to pre-treatment. Thus, THD might exert its anti-inflammatory mechanism by regulating the levels of flavonoid molecule metabolites.

The analysis of the different metabolites between patients in the NC group and group A found that it was mainly steroid hormone biosynthesis. Biotin metabolism, one carbon pool by Folate, Tyrosine metabolism, Pyrimidine metabolism and other pathways were related, while THD was related mainly through Purine Metabolism. Steroid hormone biosynthesis, Tyrosine metabolism, one carbon pool by Folate, Arginine biosynthesis, and other pathways regulate body metabolism and play a therapeutic role. A study using transcriptomic data found that purine metabolism significantly affected gene expression in patients with ligamentum flavum ossification, with xanthine dehydrogenase being a key regulator (Li et al., 2020). Whereas ligamentum flavum fibrosis and ossification be the primary pathology of ligamentum flavum hypertrophy, ligamentum flavum hypertrophy is the most crucial component of LSS (Yamada et al., 2021). The intervention of steroid hormone biosynthesis and amino acid metabolic pathways can effectively prevent bone loss (Xia et al., 2019). Epidural steroid injections improve serum monocyte chemotactic protein-1, biomarkers of nerve root injury and electromyography in patients with LSS (Lin et al., 2020).

5 Conclusion

THD can effectively improve pain and lumbar spine function in patients with LSS and reduce serum levels of IL-1β, TNF-α and PGE2-related inflammatory factors in patients. Its mechanism of action might be related to reducing the inflammatory response, improving amino acid metabolism and lipid metabolism, and relieving ligamentum flavum hypertrophy and fibrosis (Figure 10).

Data availability statement

The raw data supporting the conclusion of this article will be made available by the authors, without undue reservation.

Ethics statement

The studies involving human participants were reviewed and approved by Ethics Committee of Hubei 672 Orthopaedic Hospital of Integrated Traditional Chinese and Western Medicine. The patients/participants provided their written informed consent to participate in this study.

Author contributions

LJ designed experiments, performed the experiments of clinical efficacy, and wrote the manuscript. PH completed the analysis of metabolic data and wrote the manuscript. QW collection of patient data and designed experiments. YL and XL analyzed the efficacy and mechanism data.

Funding

This study was funded by the National Natural Science Foundation of China (grant no. 81903815).

Conflict of interest

The authors declare that the research was conducted in the absence of any commercial or financial relationships that could be construed as a potential conflict of interest.

Publisher's note

Supplementary material

The Supplementary Material for this article can be found online at: https://www.frontiersin.org/articles/10.3389/fmolb.2023.1074500/full#supplementary-material

SUPPLEMENTARY FIGURE S1
Metabolite Class Composition Ring Diagram. (Note: Each colour represents a metabolite category and the area of the colour block indicates the proportion of that category).

SUPPLEMENTARY FIGURE S2
TIC overlay for QC sample mass spectrometry.

References

Alvarez, J. A., and Hardy, R. H. (1998). Lumbar spine stenosis: A common cause of back and leg pain. *Am. Fam. Physician* 57 (8), 1839–1840.

Asadian, L., Haddadi, K., Aarabi, M., and Zare, A. (2016). Diabetes mellitus, a new risk factor for lumbar spinal stenosis: A case-control study. *Clin. Med. Insights Endocrinol. Diabetes* 9, 1–5. doi:10.4137/CMED.S39035

Cai, B., Zhang, A. G., Zhang, X., Ge, W. j., Dai, G. d., Tan, X. l., et al. (2015). Promoting effects on proliferation and chondrogenic differentiation of bone marrow-derived mesenchymal stem cells by four "Kidney-Tonifying" traditional Chinese herbs. *Biomed. Res. Int.* 2015, 792161. doi:10.1155/2015/792161

Choucair, I., Nemet, I., Li, L., Cole, M. A., Skye, S. M., Kirsop, J. D., et al. (2020). Quantification of bile acids: A mass spectrometry platform for studying gut microbe connection to metabolic diseases. *J. Lipid Res.* 61 (2), 159–177. doi:10.1194/jlr.RA119000311

Conaghan, P. G., Cook, A. D., Hamilton, J. A., and Tak, P. P. (2019). Therapeutic options for targeting inflammatory osteoarthritis pain. *Nat. Rev. Rheumatol.* 15 (6), 355–363. doi:10.1038/s41584-019-0221-y

Deer, T. R., Grider, J. S., Pope, J. E., Lamer, T. J., Wahezi, S. E., Hagedorn, J. M., et al. (2022). Best practices for minimally invasive lumbar spinal stenosis treatment 2.0

(MIST): Consensus guidance from the American society of pain and neuroscience (ASPN). *J. Pain Res.* 15, 1325–1354. doi:10.2147/JPR.S355285

Gadallah, A. S., Mujeeb Ur, R., Atta Ur, R., Yousuf, S., Tul-Wahab, A., Jabeen, A., et al. (2020). Anti-inflammatory principles from tamarix aphylla L.: A bioassay-guided fractionation study. *Molecules* 25 (13), 2994. doi:10.3390/molecules25132994

Gao, Z. W., Zhang, X., Zhuo, Q. Y., Chen, M. X., Yang, C., Chen, Z. J., et al. (2022). Metabolomics and integrated network pharmacology analysis reveal attenuates cardiac hypertrophic mechanisms of HuoXin pill. *J. Ethnopharmacol.* 292, 115150. doi:10.1016/j.jep.2022.115150

Ho, W. E., Xu, Y. J., Xu, F., Cheng, C., Peh, H. Y., Tannenbaum, S. R., et al. (2013). Metabolomics reveals altered metabolic pathways in experimental asthma. *Am. J. Respir. Cell. Mol. Biol.* 48 (2), 204–211. doi:10.1165/rcmb.2012-0246OC

Kakadiya, G., Gohil, K., Gandbhir, V., Shakya, A., and Soni, Y. (2020). Hyperglycemia and its influence on development of lumbar degenerative disc disease. *N. Am. Spine Soc. J.* 2, 100015. doi:10.1016/j.xnsj.2020.100015

Kreiner, D. S., Shaffer, W. O., Baisden, J. L., Gilbert, T. J., Summers, J. T., Toton, J. F., et al. (2013). An evidence-based clinical guideline for the diagnosis and treatment of degenerative lumbar spinal stenosis (update). *Spine J.* 13 (7), 734–743. doi:10.1016/j.spinee.2012.11.059

Kwak, H. B., Sun, H. M., Ha, H., Kim, H. N., Lee, J. H., Kim, H. H., et al. (2008). Tanshinone IIA suppresses inflammatory bone loss by inhibiting the synthesis of prostaglandin E2 in osteoblasts. *Eur. J. Pharmacol.* 601 (1-3), 30–37. doi:10.1016/j.ejphar.2008.10.034

Lee, J. Y., Choi, H. Y., Park, C. S., Jang, C., and Lee, K. T. (2019). Inhibition of COX-2 alleviates lumbar spinal stenosis-induced chronic mechanical allodynia in rats. *Int. Immunopharmacol.* 75, 105738. doi:10.1016/j.intimp.2019.105738

Li, J., Yu, L., Guo, S., and Zhao, Y. (2020). Identification of the molecular mechanism and diagnostic biomarkers in the thoracic ossification of the ligamentum flavum using metabolomics and transcriptomics. *BMC Mol. Cell. Biol.* 21 (1), 37. doi:10.1186/s12860-020-00280-3

Li, Q., and Li, T. S. (1991). Clinical and experimental study on the treatment of lumbar spinal stenosis with Tongdu Huoxue Decoction. *Chin. J. Orthop. Traumatology* 7, 18–20.

Liao, C. H., Yong, C. Y., Lai, G. M., Chow, J. M., Cheng, C. F., Fang, C. L., et al. (2020). Astragalus polysaccharide (PG2) suppresses macrophage migration inhibitory factor and aggressiveness of lung adenocarcinoma cells. *Am. J. Chin. Med.* 48 (6), 1491–1509. doi:10.1142/S0192415X20500731

Lin, C. K., Borresen, A., Kroll, M., and Annaswamy, T. M. (2020). Predicting response to epidural steroid injections for lumbar spinal stenosis with biomarkers and electromyography. *PM R.* 12 (7), 663–670. doi:10.1002/pmrj.12272

Lu, Q. L. (2020). *Inflammatory mechanism of hypertrophy of the ligamentum flavum in hyperglycemia with lumbar spinal stenosis and study of the intervention effect of curcumin*. Hubei University of Chinese Medicine. doi:10.27134/d.cnki.ghbzc.2020.000004

Lu, Q. L., Zheng, Z. X., Ye, Y. H., Lu, J. Y., Zhong, Y. Q., Sun, C., et al. (2022). Macrophage migration inhibitory factor takes part in the lumbar ligamentum flavum hypertrophy. *Mol. Med. Rep.* 26 (3), 289. doi:10.3892/mmr.2022.12805

Lurie, J., and Tomkins-Lane, C. (2016). Management of lumbar spinal stenosis. *BMJ* 352, h6234. doi:10.1136/bmj.h6234

Lyu, Z., Bai, J., Chen, S., Liu, J., and Yu, W. (2021). Efficacy of lumbar kinetic chain training for staged rehabilitation after percutaneous endoscopic lumbar discectomy. *BMC Musculoskelet. Disord.* 22 (1), 793. doi:10.1186/s12891-021-04674-y

Ma, X., Xie, S., Wang, R., Wang, Z., Jing, M., Li, H., et al. (2022). Metabolomics profiles associated with the treatment of Zuojin pill on patients with chronic nonatrophic gastritis. *Front. Pharmacol.* 13, 898680. doi:10.3389/fphar.2022.898680

Nicolin, V., Dal Piaz, F., Nori, S. L., Narducci, P., and De Tommasi, N. (2010). Inhibition of bone resorption by Tanshinone VI isolated from Salvia miltiorrhiza Bunge. *Eur. J. Histochem* 54 (2), e21. doi:10.4081/ejh.2010.e21

Oladele Oladimeji, A., Adebayo Oladosu, I., Shaiq Ali, M., and Lateef, M. (2018). Dioclins A and B, new antioxidant flavonoids from Dioclea reflexa. *Nat. Prod. Res.* 32 (17), 2017–2024. doi:10.1080/14786419.2017.1361949

Park, S. H., Hong, J. Y., Kim, W. K., Shin, J. S., Lee, J., Ha, I. H., et al. (2019) Effects of SHINBARO2 on rat models of lumbar spinal stenosis. *Mediat. Inflamm.* 2019, 7651470. doi:10.1155/2019/7651470

Shu, Q., Li, Q., and Li, T. S. (2005). Experience of 105 cases of lumbar spinal stenosis treated with Tongdu Huoxue Decoction. *Chin. J. Traditional Med. Traumatology Orthop.* 3, 26–27.

Sun, C., Wang, Z., Tian, J. W., and Wang, Y. H. (2018). Leptin-induced inflammation by activating IL-6 expression contributes to the fibrosis and hypertrophy of ligamentum flavum in lumbar spinal canal stenosis. *Biosci. Rep.* 38 (2), 214. doi:10.1042/BSR20171214

Swank, K. R., Furness, J. E., Baker, E. A., Gehrke, C. K., Biebelhausen, S. P., and Baker, K. C. (2020). Metabolomic profiling in the characterization of degenerative bone and joint diseases. *Metabolites* 10 (6), 223. doi:10.3390/metabo10060223

Wang, L. P., Ye, Y. T., and Zhang, J. E. (2022). Effect of Bushen Huoxue Decoction combined with minimally invasive decompression on lumbar spine function, pain and inflammatory factors in patients with degenerative lumbar spinal stenosis. *Liaoning J. Traditional Chin. Med.* 49 (08), 140–143. doi:10.13192/j.issn.1000-1719.2022.08.040

Wang, X., Tan, Z., Chen, S., Gui, L., Li, X., Ke, D., et al. (2021). Norethindrone causes cellular and hepatic injury in zebrafish by compromising the metabolic processes associated with antioxidant defence: Insights from metabolomics. *Chemosphere* 275, 130049. doi:10.1016/j.chemosphere.2021.130049

Wang, X. Y., Gong, L. J., Huang, J. M., Jiang, C., and Yan, Z. Q. (2020). Pinocembrin alleviates glucocorticoid-induced apoptosis by activating autophagy via suppressing the PI3K/Akt/mTOR pathway in osteocytes. *Eur. J. Pharmacol.* 880, 173212. doi:10.1016/j.ejphar.2020.173212

Wu, H., and Dong, Q. M. (2016). An experimental study on the anti-inflammatory and analgesic effects of Tongdu Huoxue Decoction. *Traditional Chin. Med. Res.* 29 (01), 63–65.

Wu, X., Liu, C., Yang, S., Shen, N., Wang, Y., Zhu, Y., et al. (2021a). Glycine-serine-threonine metabolic Axis delays intervertebral disc degeneration through antioxidant effects: An imaging and metabonomics study. *Oxid. Med. Cell. Longev.* 2021, 5579736. doi:10.1155/2021/5579736

Wu, Y., Gou, X. J., Yang, X. L., and Zhao, Y. (2022). Serum metabolomics study of Zihuapenyan Prescription retention enema in the treatment of patients with sequelae of pelvic inflammatory disease of damp-heat stasis type. *Chin. J. Hosp. Pharm. print* 2022, 1–12.

Wu, Z. J., Hu, Z. D., and Zhou, X. H. (2021b). Tongdu Huoxue Decoction-medicated serum inhibits pyroptosis in annulus fibrous cell of the intervertebral disc. *Chin. J. Tissue Eng. Res.* 25 (14), 2148–2154.

Xia, T., Dong, X., Jiang, Y., Lin, L., Dong, Z., Shen, Y., et al. (2019). Metabolomics profiling reveals rehmanniae radix preparata extract protects against glucocorticoid-induced osteoporosis mainly via intervening steroid hormone biosynthesis. *Molecules* 24 (2), 253. doi:10.3390/molecules24020253

Yamada, T., Horikawa, M., Sato, T., Kahyo, T., Takanashi, Y., Ushirozako, H., et al. (2021). Hypertrophy of the ligamentum flavum in lumbar spinal canal stenosis is associated with abnormal accumulation of specific lipids. *Sci. Rep.* 11 (1), 23515. doi:10.1038/s41598-021-02818-7

Yang, Y., Chin, A., Zhang, L., Lu, J., and Wong, R. W. (2014). The role of traditional Chinese medicines in osteogenesis and angiogenesis. *Phytother. Res.* 28 (1), 1–8. doi:10.1002/ptr.4959

Young, J. J., Hartvigsen, J., Jensen, R. K., Roos, E. M., Ammendolia, C., and Juhl, C. B. (2020). Prevalence of multimorbid degenerative lumbar spinal stenosis with knee and/or hip osteoarthritis: Protocol for a systematic review and meta-analysis. *Syst. Rev.* 9 (1), 232. doi:10.1186/s13643-020-01478-4

Zaina, F., Tomkins-Lane, C., Carragee, E., and Negrini, S. (2016). Surgical versus non-surgical treatment for lumbar spinal stenosis. *Cochrane Database Syst. Rev.* 1, CD010264. doi:10.1002/14651858.CD010264.pub2

Zhao, X. L., Liu, W., and Feng, J. (2019). "Treatment of 30 cases of lumbar spinal stenosis with the addition and subtraction of Tongdu Huoxue Decoction," in *2019 chutian orthopaedic summit and the 26th annual China orthopaedic and traumatology conference*. Wuhan, China: (Chinese Association of Integrative Medicine), 427–428. doi:10.26914/c.cnkihy.2019.019166

frontiers | Frontiers in Molecular Biosciences

TYPE Original Research
PUBLISHED 14 April 2023
DOI 10.3389/fmolb.2023.1166333

OPEN ACCESS

EDITED BY
Raúl González-Domínguez,
Universidad de Cádiz, Spain

REVIEWED BY
Francisco Jorquera,
Hospital de León, Spain
Sara Román-Sagüillo,
University of León, Spain

*CORRESPONDENCE
Hong-Wen Deng,
hdeng2@tulane.edu
Jie Shen,
sjiesy@smu.edu.cn

†These authors have contributed equally to this work and share first authorship

SPECIALTY SECTION
This article was submitted to Metabolomics, a section of the journal Frontiers in Molecular Biosciences

RECEIVED 15 February 2023
ACCEPTED 28 March 2023
PUBLISHED 14 April 2023

CITATION
Su K-J, Chen X-Y, Gong R, Zhao Q, Hu S-D, Feng M-C, Li Y, Lin X, Zhang Y-H, Greenbaum J, Tian Q, Shen H, Xiao H-M, Shen J and Deng H-W (2023), Systematic metabolomic studies identified adult adiposity biomarkers with acetylglycine associated with fat loss *in vivo*. *Front. Mol. Biosci.* 10:1166333. doi: 10.3389/fmolb.2023.1166333

Systematic metabolomic studies identified adult adiposity biomarkers with acetylglycine associated with fat loss *in vivo*

Kuan-Jui Su[1,2†], Xing-Ying Chen[3,4†], Rui Gong[1,3,5], Qi Zhao[6], Shi-Di Hu[4], Mei-Chen Feng[4], Ye Li[3], Xu Lin[1,3,4], Yin-Hua Zhang[3], Jonathan Greenbaum[1], Qing Tian[1], Hui Shen[1], Hong-Mei Xiao[7], Jie Shen[3,4*] and Hong-Wen Deng[1*]

[1]Tulane Center for Biomedical Informatics and Genomics, School of Medicine, Tulane University, New Orleans, LA, United States, [2]Department of Biostatistics and Data Science, School of Public Health and Tropical Medicine, Tulane University, New Orleans, LA, United States, [3]Shunde Hospital of Southern Medical University (The First People's Hospital of Shunde), Foshan, China, [4]Department of Endocrinology and Metabolism, The Third Affiliated Hospital of Southern Medical University, Guangzhou, China, [5]Department of Cadre Ward Endocrinology, Gansu Provincial Hospital, Lanzhou, China, [6]Department of Preventive Medicine, College of Medicine, University of Tennessee Health Science Center, Memphis, TN, United States, [7]Center of System Biology, Data Information and Reproductive Health, School of Basic Medical Science, Central South University, Changsha, China

Obesity is associated with various adverse health outcomes. Body fat (BF) distribution is recognized as an important factor of negative health consequences of obesity. Although metabolomics studies, mainly focused on body mass index (BMI) and waist circumference, have explored the biological mechanisms involved in the development of obesity, these proxy composite measures are not accurate and cannot reflect BF distribution, and thus may hinder accurate assessment of metabolic alterations and differential risk of metabolic disorders among individuals presenting adiposity differently throughout the body. Thus, the exact relations between metabolites and BF remain to be elucidated. Here, we aim to examine the associations of metabolites and metabolic pathways with BF traits which reflect BF distribution. We performed systematic untargeted serum metabolite profiling and dual-energy X-ray absorptiometry (DXA) whole body fat scan for 517 Chinese women. We jointly analyzed DXA-derived four BF phenotypes to detect cross-phenotype metabolite associations and to prioritize important metabolomic factors. Topology-based pathway analysis was used to identify important BF-related biological processes. Finally, we explored the relationships of the identified BF-related candidate metabolites with BF traits in different sex and ethnicity through two independent cohorts. Acetylglycine, the top distinguished finding, was validated for its obesity resistance effect through *in vivo* studies of various diet-induced obese (DIO) mice. Eighteen metabolites and fourteen pathways were discovered to be associated with BF phenotypes. Six of the metabolites were validated in varying sex and ethnicity. The obesity-resistant effects of acetylglycine were observed to be highly robust and generalizable in both human and DIO mice. These findings demonstrate the importance of metabolites associated with BF distribution patterns and several biological pathways that may contribute to obesity and obesity-related disease etiology, prevention, and intervention. Acetylglycine is highlighted as a potential therapeutic candidate for preventing excessive adiposity in future studies.

KEYWORDS
obesity, body fat, metabolomics, acetylglycine, biomarkers

1 Introduction

Obesity, defined as an excess of adiposity, is a global epidemic widely recognized as a leading cause of various metabolic disorders and cancers (Cirulli et al., 2019; Koenen et al., 2021; He et al., 2023). Excess central fat accumulation causing metabolic disturbance can exacerbate the risk of diabetes and cardiovascular diseases (Vasan et al., 2018; Marsh et al., 2023). Biomarkers reported to influence abdominal obesity have also been shown to be prognostic of early cardiometabolic risk independent of general obesity (Supriya et al., 2018). However, not all abdominal areas in which fat accumulates are associated with harm. It is known that android fat deposited around the waist increases the risk of metabolic disease, while gynoid fat deposited around the hips does not, and some studies suggest gynoid fat may have a beneficial effect (Vasan et al., 2018; Marsh et al., 2023). Therefore, uncovering novel biomarkers for fat distribution can provide more precise insight into fat accumulation and obesity-related diseases.

Metabolomics provides comprehensive profiling of distinct exogenous/endogenous small molecules functioning as intermediates or end products of cellular metabolism. Since metabolites represent the downstream expression of genomic, transcriptomic, and proteomic factors, their study can reveal biomarkers and pathways that link genotypes to phenotypes (Cirulli et al., 2019). Multiple studies have revealed crucial metabolites for obesity or regulating BF (Chen et al., 2015; Bogl et al., 2016; Ahmad et al., 2022; O'Keeffe et al., 2022), some of which were used as a basis for developing treatments and preventive interventions for obesity-related disorders (Okosun et al., 2015; Chen and Gerszten, 2020) and prediction models for visceral adipose tissue, an important prognostic factor that is difficult to measure in practice (Boone et al., 2022). Although there have been numerous efforts to identify metabolic biomarkers of obesity, these studies were largely limited by small sample sizes, the number of metabolites considered, and lack of replication/functional validation. Moreover, they primarily relied on proxy measures of body composition such as BMI and/or waist-to-hip ratio. These proxy measures may miss valuable information provided by the regional BF, and therefore hinder assessment of metabolic alterations and differential risk of metabolic disorders among individuals presenting adiposity differently throughout the body (Rangel-Huerta et al., 2019).

In the present study, we aim to identify shared and specific metabolites and their associated pathways related to various BF traits. The study has three main components: discovery, validation, and *in vivo* experiments. First, we analyzed untargeted liquid chromatography-mass spectrometry (LC-MS) metabolomics profiling on a sample of 517 Chinese women for discovery. Next, we verified the identified BF-related metabolites in two independent cohorts with various ethnicities and genders. Both the validated metabolites and those associated with all the studied BF traits were selected for more detailed examination of their biological functions and relevance as revealed in prior studies. One such metabolite, meeting both criteria, was chosen for *in vivo* experiments for further validation and functional significance in mice. Our study design and analytical approach are outlined in Supplementary Figure S1.

2 Materials and methods

2.1 Subjects and study design

A total of 517 unrelated peri-/post-menopausal Chinese women in the discovery cohort were recruited from the Third Affiliated Hospital of Southern Medical University (Guang Zhou, Guang Dong Province, China) between June 2014 and January 2018. The mean age was 52.9 years (standard deviation (SD) = 2.9). Two independent samples for validation were sampled from the Louisiana Osteoporosis Study (LOS) (Zhao et al., 2018). The first validation cohort consisted of 136 Caucasian women (mean aged 31.48 years (SD = 5.08)) sampled by a discordant phenotype design based on the top/bottom 20% of the hip bone mineral density Z-score (Zhao et al., 2018). The second validation cohort comprised 700 males (295 African Americans and 405 Caucasians) with mean age 37.8 (SD = 8.45) years overall. The study designs and sample characteristics are detailed in Supporting Material S1 and Supplementary Tables S1-S2, respectively. Signed consent forms were obtained from all participants. All clinical measurements and experiment procedures were subject to the Helsinki Declaration II and regulations of the Institutional Review Boards.

2.2 Clinical measurements

All respondents in the discovery and validation cohorts completed a questionnaire regarding demographics, lifestyle, dietary factors, and reproductive and medical history. Trained research staff collected clinical measurements with participants. The BF distribution phenotypes considered in this study were android fat/whole BF mass ratio (A/W ratio), gynoid fat/whole BF mass ratio (G/W ratio), android fat to gynoid fat ratio (A/G ratio), and whole BF percentage (W%) (Bogl et al., 2016). Daily calibrated DXA machines (discovery cohort: Lunar, GE Healthcare, Madison, WI, United States; validation cohorts: Hologic Inc., Bedford, MA, United States) were used to measure BF (Supplementary Figure S2). The detail of the region of interest is provided in Supporting Material S1.

2.3 Metabolite analysis

Untargeted LC-MS metabolite profiling was conducted on serum samples from all cohorts. The details of experimental protocols, which are in accordance with the suggestions of the Metabolomics Standards Initiative reporting standards (Sumner et al., 2007), have been previously described (Gong et al., 2021) and are provided in Supporting Material S2. A high-resolution tandem mass spectrometer TripleTOF5600plus (SCIEX, United Kingdom) at Lian-Chuan Biotechnology Co., Ltd

(Hangzhou, China) was used to detect metabolites eluted from the column in the discovery cohort. LC-MS metabolomics platforms were also used to perform the metabolomic analyses on serum samples for both validation cohorts. The experimental protocols for the validation cohorts have been previously described (Zhao et al., 2018) and are listed in Supporting Material S2. All metabolites profiling with a unique or high-confidence annotation were log-transformed and auto-scaled prior to the subsequent analyses.

2.4 *In vivo* validation study in mice for acetylglycine

Acetylglycine consistently demonstrated an anti-obesity association with observed BF traits across sex and ethnicity. We performed an *in vivo* study that extended the work of Harper et al. (Harper et al., 2010) by exploring the effect of acetylglycine on high-fat diet-induced obese mice for further validation. A total of 61 female C57BL/6 J mice were randomized into five groups: 1) standard chow diet with vehicle (control; n = 12), 2) high fat (60% kcal from fat; n = 12) diet with vehicle (HFD; n = 12), 3) HFD with low-dosage acetylglycine (HFD + ACE500; 500 mg/kg; n = 12), 4) HFD with medium-dosage acetylglycine (HFD + ACE1000; 1,000 mg/kg; n = 12), and 5) HFD with high-dosage acetylglycine (HFD + ACE1500; 1,500 mg/kg; n = 13). We administered drinking water or acetylglycine (treatment) to corresponding mice by oral gavage every day starting at 8 weeks of age. Experimental measurements were recorded weekly during the 16-week intervention. We used micro-computed tomography (μ-CT) to measure total abdominal fat (between L1 and L5 vertebrae), visceral BF, and subcutaneous BF (Luu et al., 2009). The biochemical analysis involved the measurement of fasting plasma glucose (FPG) after 6-h and 12-h fasting, total cholesterol (TC), triglyceride (TG), high-density lipoprotein cholesterol (HDL), low-density lipoprotein cholesterol (LDL), alanine transaminase (ALT), and aspartate aminotransferase (AST). All experimental procedures are provided in Supporting Material S3.

2.5 Statistical analysis

We investigated the relationship between the metabolites and BF traits using two complementary approaches, seemingly unrelated regression (SUR) and sparse partial least squares (sPLS) regression. The most important BF-related metabolites were identified as those with variable importance in projection (VIP) score >1 in sPLS and SUR false discovery rate (FDR) q-value ≤0.2. The selection of cutoffs for the FDR q-value and VIP score usually depends on the study objective. In this study, we aimed to provide a robust list of potential BF-related metabolites for future replication, and therefore chose not to apply highly stringent significance criteria since the analysis is exploratory in nature. A pathway analysis was performed to identify biological functions with p-score <0.05. The Spearman and partial Spearman correlation tests were conducted in the validation cohorts to examine the associations between the metabolites and traits after adjustment for age, height, physical activity for both cohorts, and ethnicity in the second cohort. We also performed the tests stratified by ethnicity. p-value ≤0.05 was considered statistically significant. All analyses were detailed in Supporting Material S4. The metabolites associated with all BF traits in the discovery cohort or replicated the associations in the validation cohorts will be further discussed in our study (Supporting Material S5).

The Generalized Estimating Equations (GEE) model was applied to investigate the associations between acetylglycine and the measure of weight and weight gain in the animal models. The covariates included baseline weight, treatment (water, low-, medium-, or high-dose acetylglycine), and diet (normal/HFD) in the weight model, and treatment and diet in the weight gain model. Tukey method was used to examine whether there were significant pairwise differences (p-value ≤0.05) in weight and weight gain. The Kruskal–Wallis test was used as a global test for a one-time measurement to compare biomedical indexes across different treatment groups. The null hypothesis of this test is that there is no significant difference in the biomedical measurement across all treatment groups, while the alternative hypothesis is that at least one group differs significantly from at least one other group. Following the Kruskal–Wallis test, Wilcoxon tests were conducted to examine whether acetylglycine had significant differences (FDR q-value ≤0.05) in pairwise comparisons for both the μ-CT and biochemical measurements.

3 Results

3.1 Relationships between BF traits and serum metabolites in discovery

Among 3,075 annotated metabolites with MS1 and MS2 confidence levels in our discovery cohort (Supplementary Table S3 and Supporting Material S3), we identified 18 statistically significant BF-metabolite associations with FDR q-values <0.2 in the SUR models and VIP scores >1 in sPLS (Figure 1 and Supplementary Table S4). Figure 1A illustrates how the metabolites relate to multiple traits: none of the 18 metabolites exclusively related to a single BF trait. All were significantly associated with G/W ratio. Overall, two metabolites had significant relationships with three traits (G/W, A/W, and A/G ratios) representing central BF and five with all four traits representing general and central BF.

Directions of coefficient effects on the four traits were consistent across the 18 metabolites; A/G ratio, A/W ratio, and W% were always affected in opposite directions as G/W ratio (Figure 1B). Those having positive relationships with A/G ratio, A/W ratio, and W% but a negative relation with G/W ratio were defined as obesity-risk metabolites, the others as protective metabolites. Among the six metabolites with VIP scores >2, the top three (austalide J, pyridinoline, and deoxycoformycin) are obesity-risk metabolites, while acetylglycine, creatinine, and cortisone are protective metabolites. The top six in the VIP score also had relatively large effect sizes on central BF compared with general BF (Supplementary Figure S3). Acetylglycine, for example, had stronger negative effect sizes on A/G ratio ($\beta = -0.19$, p-value = 1.09×10^{-5}) and A/W ratio

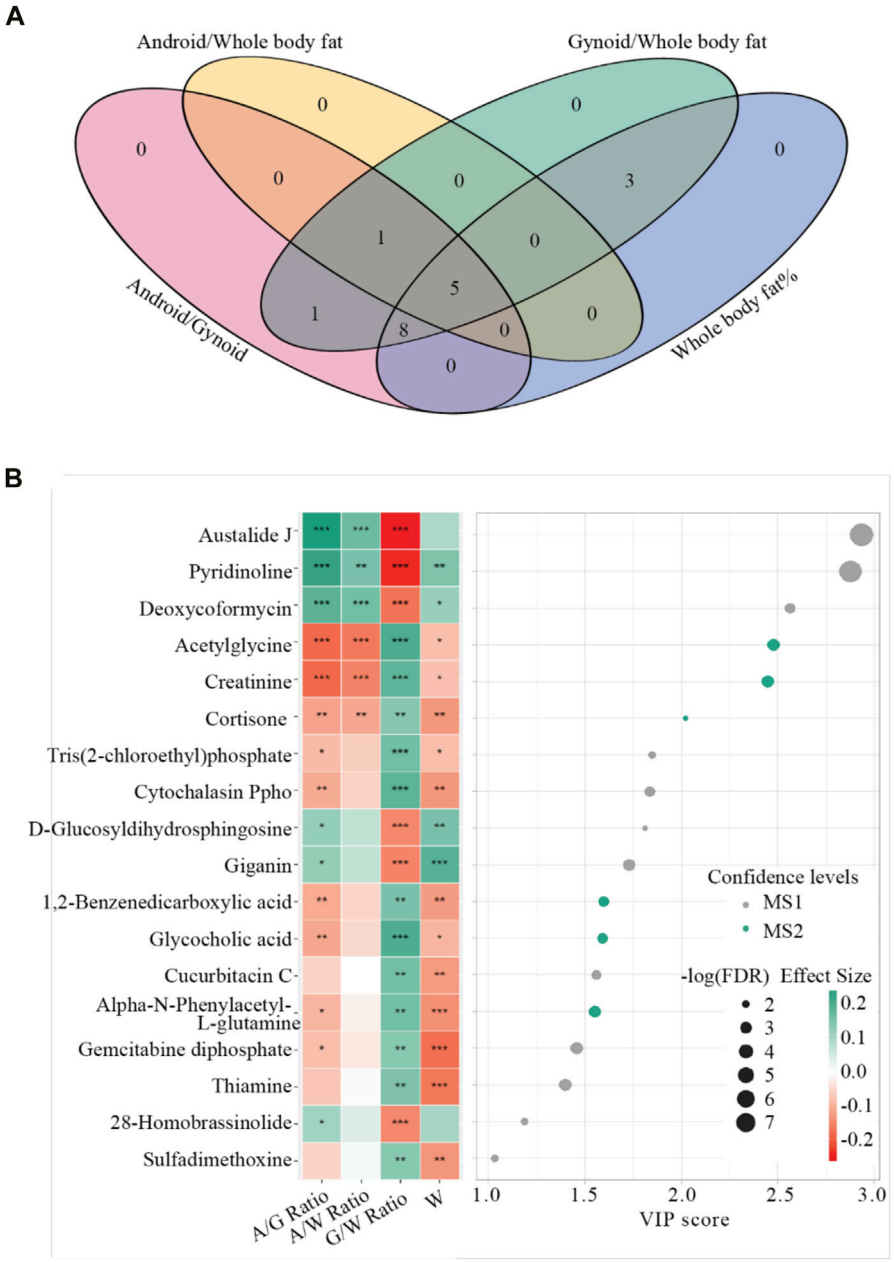

FIGURE 1
Summary results for the joint analysis in the discovery cohort. Panel **(A)** Venn diagram depicting metabolite sets that were significantly associated with body fat traits (FDR q-value <0.2 and VIP >1). Traits are represented by ovals of different colors. The number in each area represents the count of identified BF-associated metabolites associated with the given traits. Panel **(B)**. Important metabolites selected on the basis of VIP, score >1 and FDR q-value ≤0.2. Each tile represents the effect size of the metabolite on each trait. VIP: the variable importance in projection scores, FDR: false discovery rate, A/W ratio: Android fat/Whole body fat ratio, G/W ratio: Gynoid fat/Whole body fat ratio, A/G ratio: Android fat to gynoid fat ratio, and W: Whole body fat %. *: p-value <0.05; **: p-value <0.01; ***: p-value <0.001.

($\beta = -0.17$, p-value $= 6.23 \times 10^{-5}$) than on W% ($\beta = -0.09$, p-value $= 3.24 \times 10^{-3}$).

3.2 Functional topological pathway analysis in discovery

Six metabolites out of 18 could be mapped to the Kyoto Encyclopedia of Genes and Genomes (KEGG) database and used in the pathway analysis. We identified 14 significant pathways, three modules, 28 enzymes, 39 reactions, and 21 compounds (refer to Table 1 for an overview and Supplementary Table S6 for a comprehensive list). The topological results showed that thiamine had the highest connectivity at the compound level (degree = 10) and thiamine metabolism had the highest connectivity at the pathway level (degree = 9) in Supplementary Figure S4. The connectivity degree indicates the importance of thiamine for essential metabolic processes.

TABLE 1 Summary of topological attributes of the top 5% significant biological components at each biological level.

Level	KEGG ID	KEGG name	p Score	Betweenness centrality (B)	Closeness centrality (C)	Combined score (B)+(C)	Degree
Pathway[a]	hsa00330	Arginine and proline metabolism	1.80×10^{-3}	0.35	0.54	0.89	5
	hsa02010	ABC transporters	1.59×10^{-4}	0.39	0.26	0.64	8
Module[a]	hsa04979	Cholesterol metabolism	1.00×10^{-6}	0.31	0.25	0.56	5
	M00047	Creatine pathway	1.00×10^{-6}	0.37	0.56	0.93	5
Enzyme[b]	2.3.2.27	RING-type E3 ubiquitin transferase	1.54×10^{-3}	0.38	0.24	0.62	4
	2.7.3.2	Creatine kinase	1.00×10^{-6}	0.04	0.42	0.46	2
	2.1.1.2	Guanidinoacetate N-methyltransferase	1.00×10^{-6}	0.05	0.41	0.45	2
	3.1.3.2	Acid phosphatase	8.83×10^{-5}	0.15	0.23	0.37	4
	2.1.4.1	Glycine amidinotransferase	1.84×10^{-3}	0.00	0.37	0.37	1
	3.1.1.3	Triacylglycerol lipase	1.96×10^{-2}	0.08	0.24	0.32	2
Reaction[c]	R07420	Phosphocreatine ≤≥ Creatinine + Orthophosphate	1.00×10^{-6}	0.13	0.47	0.60	3
	R01884	Creatinine amidohydrolase	1.00×10^{-6}	0.10	0.47	0.57	3
	R02922	Creatinine iminohydrolase	1.00×10^{-6}	0.09	0.42	0.51	3
	R01566	Creatine amidinohydrolase	9.33×10^{-4}	0.04	0.43	0.47	2
	R01881	ATP:creatine N-phosphotransferase	2.01×10^{-6}	0.08	0.39	0.47	3
	R03720	Choloyl-CoA:glycine N-choloyltransferase	4.33×10^{-3}	0.18	0.25	0.44	8
	R03187	N-Methylimidazolidine-2,4-dione amidohydrolase	3.68×10^{-2}	0.04	0.38	0.42	2
Compound[d]	C00300	Creatine	9.93×10^{-5}	0.17	0.44	0.61	4
	C00378	**Thiamine**	**1.00×10^{-6}**	**0.27**	**0.26**	**0.53**	**10**
	C00791	**Creatinine**	**1.00×10^{-6}**	**0.08**	**0.44**	**0.52**	**3**
	C00037	Glycine	1.16×10^{-5}	0.22	0.26	0.48	5
	C01921	**Glycocholate**	**1.00×10^{-6}**	**0.21**	**0.24**	**0.46**	**3**
	C02305	Phosphocreatine	1.35×10^{-4}	0.02	0.38	0.41	2
	C01606	**Phthalate (1,2-Benzenedicarboxylic acid)**	**1.00×10^{-6}**	**0.09**	**0.21**	**0.30**	**4**
	C00762	**Cortisone**		**0.11**	**0.18**	**0.29**	**6**

(Continued on following page)

TABLE 1 (*Continued*) Summary of topological attributes of the top 5% significant biological components at each biological level.

Level	KEGG ID	KEGG name	p Score	Betweenness centrality (B)	Closeness centrality (C)	Combined score (B)+(C)	Degree
			1.00×10^{-6}				
	C04148	**Phenylacetylglutamine (Alpha-N-phenylacetyl-L-glutamine)**	**1.00×10^{-6}**	**0.00**	**0.18**	**0.18**	**1**

[a]Reported pathways and modules with combined score (B + C) > 0.5.
[b]Reported enzymes with combined score >0.3.
[c]Reported reactions with combined score >0.4.
[d]Reported compounds with combined score >0.4 or original input compounds; **Bold,** the original BF-related metabolites. The components were selected by the threshold of combined score greater than 0.3 or as the input metabolites. A comprehensive list can be found in Supplementary Table S6.

TABLE 2 Summary of body-fat associated metabolites in the validation cohorts.

Metabolite	Class	Ion	m/z	RT/RI[a]	Molecular	Trait	ρ	ρ *p*-value	ρ′	ρ′ *p*-value
Validation 1: Caucasian women (*n* = 136)										
Acetylglycine	Amino acids	Pos	140.03	1.17	$C_4H_7NO_3$	AG	−0.31	1.96×10^{-4}	−0.28	9.10×10^{-4}
						AW	−0.29	6.89×10^{-4}	−0.25	3.27×10^{-3}
						GW	0.29	5.88×10^{-4}	0.28	1.17×10^{-3}
						W%	−0.34	5.17×10^{-5}	−0.29	6.55×10^{-4}
Creatinine	Amino acids	Neg	112.05	0.98	$C_4H_7N_3O$	AW	−0.20	1.96×10^{-2}	−0.15	7.61×10^{-2}
Thiamine	Pyrimidines	Pos	265.11	1.13	$C12H_{16}N_4OS$	W%	−0.19	2.34×10^{-2}	−0.16	7.01×10^{-2}
Validation 2: African American and Caucasian men (n = 700)										
Acetylglycine	Amino acids	Polar	116.04	1,780	$C_4H_7NO_3$	AG	−0.26	7.22×10^{-12}	−0.24	1.47×10^{-10}
						AW	−0.28	6.48×10^{-14}	−0.26	1.97×10^{-12}
						GW	0.09	1.41×10^{-2}	0.09	1.32×10^{-2}
						W%	−0.27	6.34×10^{-13}	−0.24	5.28×10^{-11}
Cortisone	Lipid	Neg	359.19	4,575	$C_{21}H_{28}O_5$	AG	−0.11	2.67×10^{-3}	−0.10	1.12×10^{-2}
						AW	−0.11	2.38×10^{-3}	−0.10	8.97×10^{-2}
						W%	−0.11	5.02×10^{-3}	−0.09	1.22×10^{-2}
Creatinine	Amino acids	Pos Early	114.07	2,055	$C_4H_7N_3O$	AG	−0.09	2.20×10^{-2}	−0.05	ns
						AW	−0.09	1.84×10^{-2}	−0.03	ns
						W%	−0.16	1.24×10^{-5}	−0.13	6.69×10^{-4}
Glycocholic acid	Lipid	Neg	464.30	5,163	$C_{26}H_{43}NO_6$	AG	−0.10	8.16×10^{-3}	−0.07	ns
						AW	−0.13	5.96×10^{-4}	−0.10	8.13×10^{-3}
						W%	−0.12	1.96×10^{-3}	−0.09	1.38×10^{-2}
N-Phenylacetyl-L-Glutamine	Peptide	Pos Early	265.12	2,145	$C_{13}H_{16}N_2O_4$	AG	−0.02	ns	−0.11	4.17×10^{-3}
						AW	−0.04	ns	−0.12	1.34×10^{-3}
						W%	−0.08	2.81×10^{-2}	−0.14	2.60×10^{-4}

m/z: mass-to-chare ratio; a: RT (Retention time) and RI (Retention index); ρ: Spearman correlation coefficient; ρ': Partial Spearman correlation coefficient adjusted by age, height, and physical activity in Validation 1 and additional ethnicity in Validation 2; ns: not statistically significant; The directions of the correlation test in the validation studies are consistent with the findings in the Chinese women cohort. A/G: android to gynoid ratio; A/W: android fat to whole body total fat; G/W: gynoid fat to whole body total fat; W%: whole body total fat percentage.

3.3 Metabolite and BF trait relations validation in LOS cohorts

We examined the correlations of four metabolites in the female validation cohort and five in the male validation cohort, which resulted in 22 significant relations between the metabolites and traits (Table 2). The correlations between acetylglycine and the traits were significant in both cohorts, with the strongest negative association with W% and A/W ratio respectively in Caucasian women (Spearman correlation ρ) = −0.34, partial Spearman correlation

TABLE 3 Results of GEE models for the associations of acetylglycine on mouse weight and weight change.

Variable	Effect size	SE	Wald	*p*-value
Trait: Weight				
Water	REF			
TRT ACE 500	−0.29	0.28	1.08	0.30
TRT ACE 1000	−0.51	0.20	6.56	0.01
TRT ACE 1500	−1.03	0.20	26.78	2.30×10^{-7}
Normal Diet	REF			
HFD	1.35	0.19	48.23	3.80×10^{-12}
Baseline weight	0.98	0.10	92.78	$<2.00 \times 10^{-16}$
Trait: Weight change				
Water	REF			
TRT ACE 500	−0.38	0.32	1.44	0.2295
TRT ACE 1000	−0.65	0.22	8.61	0.0033
TRT ACE 1500	−1.41	0.23	39.10	3.90×10^{-10}
Normal Diet	REF			
HFD	1.61	0.21	58.00	2.70×10^{-14}

REF: Reference group. HFD: High fat diet. TRT ACE: Treatment group with acetylglycine (dose); SE: Standard error for the effect size.

(ρ') = −0.29, both *p*-value < 0.001) and African American and Caucasian men (ρ = −0.28, ρ' = −0.26, both *p*-value < 0.001). Glycocholic acid was negatively associated with A/G ratio, A/W ratio, and W% in African American and Caucasian men only, which may be attributed to the relatively small sample size of Caucasian women (Supplementary Tables S7-S14).

In the ethnicity-stratified analyses, we replicated the correlations of five metabolites related to at least one BF trait in African American or Caucasian men (Supplementary Table S5). Acetylglycine had the highest absolute correlation coefficients on the BF traits (except for the G/W ratio in the African American men). Cortisone had the significant negative correlations with A/G ratio, A/W ratio, and W% exclusively in the African American men; creatinine was also negatively related to W% in Caucasian men.

3.4 Relationship of acetylglycine with body weight, body weight gain, and abdominal fat mass in mice

The acetylglycine treatments with equivalent baseline weight and diet were significantly associated with an average decrease in body weight of 0.51 (*p*-value = 0.01) and 1.03 (*p*-value = 2.30×10^{-7}) grams, respectively, in ACE1000 and ACE1500 groups, compared with groups without the treatment. Similarly, we found negative marginal effect sizes on weight gain while adjusting for diet (Table 3). Body weight and weight gain were lower in all the acetylglycine treatment groups and the control group than the HFD-only group (Supplementary Figure S5). Overall food intake presented no differences between the HFD-only and HFD with treatment groups during the intervention period.

Among the acetylglycine treatment groups, we observed significant differences in the μ-CT measures: abdominal fat, visceral fat, subcutaneous fat, and fat/weight ratio (Figure 2 and Supplementary Tables S1-S15). The HFD groups had significantly higher measurements than the control group, indicating the success of the obesity model. Despite similar HFD consumption, we observed a decreasing trend in the four μ-CT measures as the treatment dosage increased, and statistically significant differences between the HFD-only group and the HFD with the medium and high-dose groups.

3.5 Association of acetylglycine with biochemical measurements in mice

The overall tests indicated significant differences in the levels of glucose, CHO, HDL, and LDL among the groups (Supplementary Table S16). The HFD-only group in the 6-h FPG test had significantly higher glucose level (mean = 8.57 mmol/L, SD = 1.49) than the control, HFD + ACE500, and HFD + ACE1000 groups (Figure 2). In the 12-h FPG test, there were significant differences between the HFD + ACE1000 and control/HFD-only groups. ALT and AST, two enzymes for testing liver toxicity or damage, were not significantly different across groups (Supplementary Figure S6). Lipid profiles were significantly higher in the treatment groups with HFD compared to those in the control group, and there were no differences in the cholesterol levels among the intervention groups (Supplementary Figure S7). Taken together, the HFD-only diet successfully induced obesity in the mice, as

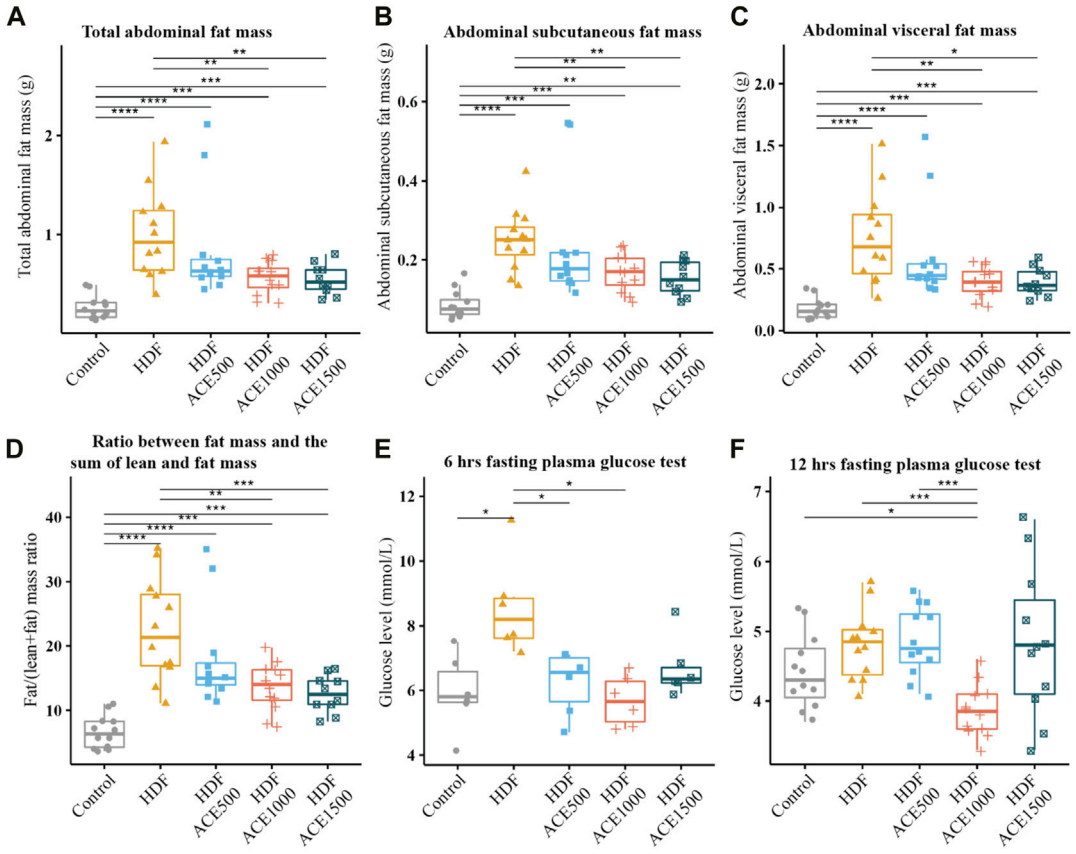

FIGURE 2
In vivo study with acetylglycine. Panels **(A–D)** show the pairwise comparisons for the μ-CT measures among different groups. The abdominal region was defined as between L1–L5 lumbar vertebrae. Panels **(E, F)** are the pairwise comparisons for the fasting plasma glucose test. FDR: false discovery rate; *: FDR q-value <0.05; **: FDR q-value <0.01; ***: FDR q-value <0.001; ****: FDR q-value <0.0001.

reflected by the higher weight, weight gain, abdominal fat mass, and glucose level observed in the study.

4 Discussion

We performed a joint analysis that revealed the relationships between the metabolites and four DXA-derived BF measures among Chinese women. In contrast to proxy phenotypes, such as BMI, BF measures provide a direct assessment of body adiposity distribution, enabling the identification of novel metabolites related to general or central BF. We identified 18 metabolites that demonstrated consistent associations with A/G ratio, A/W ratio, and W%, and opposing associations with G/W ratio. We further partially validated the consistent relationships of the metabolites on the BF traits in two independent samples with different ethnicity and sex characteristics. Lastly, we validated the protective effect of acetylglycine in the obese mouse experiments.

Pyridinoline, deoxycoformycin, acetylglycine, creatinine, and cortisone were robustly associated with general and central BF. Austalide J and 28-homobrassinolide were only associated with central BF, and austalide J had the highest VIP score, reflecting a strong contribution in distinguishing abdominal obesity. Interestingly, no metabolite was exclusively related to any single BF trait, implying that the identified metabolites simultaneously influence total and central region fat deposits with different effect sizes. As gynoid fat may reduce the risk of metabolic diseases (Fu et al., 2013; Okosun et al., 2015), our findings of 12 metabolites positively associated with G/W ratio suggest further replication and merit for future study in preventing obesity.

Pyridinoline and deoxycoformycin were observed as positive associations with general and central BF, except gynoid fat, in our study. These two metabolites have been recognized from exogenous sources and have close relationships with complex diseases. Pyridinoline, a well-known biomarker of bone resorption and formation (Delmas et al., 1991; Kuo and Chen, 2017), has been reported to be positively associated with weight, BMI, and bone mineral density at different skeletal sites (New et al., 2000; Wang et al., 2016). It is a cross-linked compound that provides chemical stabilization in cartilage, bone, ligaments, and blood vessels (Kuo and Chen, 2017). Next, deoxycoformycin is an inhibitor of adenosine deaminase and a common anticancer chemotherapeutic drug for leukemia and lymphoma treatment (Tusup et al., 2022). In addition, deoxycoformycin can be produced by fungi such as *C. militaris*, which is regarded as a

beneficial food supplement (Chen et al., 2020). However, it increases the susceptibility to toxic accumulation in kidney, liver, and central nervous system (Demain and Sanchez, 2009; Chen et al., 2020). The effect of the impaired tissue/organs by deoxycoformycin on the development of BF and its dose-dependent toxicity in humans is still unclear. Further research on the underlying mechanism of this relationship is warranted.

We demonstrated the potential anti-obesity effect of acetylglycine on both general and central body fat, which is consistent with previous findings of its association with lower BMI levels and fat percentages in population-based studies (Moore et al., 2014; Cirulli et al., 2019). However, a longitudinal study of Mexican American women aged 20–72 years reported that increased levels of acetylglycine elevated the risk of weight gain (Zhao et al., 2016). Further investigations into the long-term effect are needed to clarify these contradictory results. In addition to obesity-related traits, a study on the causal effect of metabolites on cardiovascular diseases found that acetylglycine is associated with a lower risk of diastolic blood pressure and is considered a potential cause (Qiao et al., 2021). The glycine N-acyltransferase (*GLYAT*) enzyme, linked with phenylalanine metabolism (Supplementary Figure S4), forms N-acylglycines (Westhuizen et al., 2000) and catalyzes glycine conjugation of acyl-Coa-species, producing intermediate products such as acetylglycine in amino acid and fatty acid metabolism (Badenhorst et al., 2013). A mice study showed that lower mRNA expression levels of GLYAT in adipose tissue were observed in a fat-susceptible group compared to a fat-resistant group (Fedry et al., 2016). The perturbation of *GLYAT* induces harmful disruption to CoA homeostasis (Badenhorst et al., 2013), musculoskeletal development (Badenhorst et al., 2013), and obesity-related metabolic disturbances (Fedry et al., 2016; Alves et al., 2019), suggesting that acetylglycine plays a role in the development of obesity-related diseases.

Creatinine, a breakdown product of creatine, reflects muscle metabolism and kidney function and plays a significant role in muscle energy production (Patel et al., 2013). Individuals with low muscle mass and body weight have low creatinine levels (Patel et al., 2013) and high glomerular hyperfiltration rates, which may increase the risk of metabolic diseases and diabetes (Hjelmesæth et al., 2010). The association between cortisone and general/central BF was consistent with a recent study reporting a negative association on BMI in European women (Cirulli et al., 2019). Interestingly, when assessing the relationship of cortisone in childhood obesity, cortisol and cortisone levels were significantly positively correlated with BMI and A/G ratio (Noppe et al., 2016).

The age-dependent differences in activities of 11β-hydroxysteroid dehydrogenases, an enzyme catalyzing the interconversion between cortisol and cortisone, may reverse the associations on BF deposition (Vierhapper et al., 2007; Chapman and Seckl, 2008). Cortisone participating in cortisol metabolism for generating steroid hormone is a known signature for obesity, type 2 diabetes (Gawlik et al., 2020), and other diseases (Supplementary Figure S4).

In our validation analyses, we observed the negative relationships for glycocholic acid, a key a bile acid regulator of fat absorption, cholesterol level, and energy homeostasis (Marco-Ramell et al., 2018). Glycocholic acid was only replicated in African American or Caucasian men but not in Caucasian women. This discrepancy could be attributed to aging-related decline in physiological functions, such as a decrease in female estrogen and hormone levels. A study reported a large difference in glycocholic acid levels between obese and lean women aged between 50 and 70 years old, and a relatively small difference in women aged 30–40 years old (Xie et al., 2015). This is consistent with the findings from our study samples. Further work is needed to understand the complex relationship between glycocholic acid and BF which may be mediated by age-related factors, estrogen, and hormone level.

The negative associations for N-Phenylacetyl-L-Glutamine and thiamine were validated in the men's and women's replication samples, respectively. A recent study reported that there are no sex differences in excretion of the amino acid N-Phenylacetyl-L-Glutamine (Zheng et al., 2014). The abnormal activity of N-Phenylacetyl-L-Glutamine could be attributed to the difference in phenylalanine metabolism and further reflect the development of obesity (Bogl et al., 2016). However, some studies also observed that the concentration was lower in obese men compared with normal-weight men (Yu et al., 2018). The mechanism through which N-Phenylacetyl-L-Glutamine may influence BF requires further investigation. Moreover, many studies support thiamine as an essential micronutrient in glucose metabolism that is negatively associated with obesity (Maguire et al., 2018). To the best of our knowledge, our study provided the first evidence of the relationship between thiamine and BF.

The arginine and proline metabolism pathway had a high closeness and betweenness centralities, which implies that the pathway has considerable influence on neighboring molecules/pathways. The pathway is known to be associated with obesity (Cirulli et al., 2019). Elevated arginine levels can reduce BF accretion in humans and animals (Wu et al., 2009). Further investigation of the identified biological components involved in the arginine and proline metabolism may reveal an important influence on obesity.

The ATP-binding cassette (ABC) transporter pathway, a pivotal connector pathway, regulates the import/export of membrane proteins, such as thiamine, phthalate, L-glutamine, and glycine *via* different enzymes or reactions for the overall BF-related network (Rees et al., 2009). The pathway may delineate associations between genes and physiologic changes before, during, and after the onset of obesity in mice (Donepudi et al., 2016) and beneficial influences on obese women (Teixeira et al., 2020). However, we observed that phthalate in ABC transporters was negatively associated with A/G, A/W, and W%, in accordance with the findings from Hatch et al.'s study of BMI and waist circumference (Hatch et al., 2008). Other studies found contradictory results, demonstrating that phthalate was an endocrine-disrupting chemical (Apau et al., 2020) and linked to adverse health outcomes such as obesity and diabetes (Hatch et al., 2008; Apau et al., 2020). The various characteristic of phthalates on obesity may depend upon endogenous hormone levels and vary across sex and age groups (Hatch et al., 2008). The influence on BF and other pathways *via* the ABC transporter pathway may warrant further investigation.

Additionally, our study suggested that impaired cholesterol metabolism may cause adverse health outcomes. The cholesterol

metabolism pathway was connected to pathways for aldosterone-regulated sodium reabsorption and prostate cancer. Cortisone and cortisol were closely connected to the disease pathway and may be diagnostic biomarkers for obesity. The impaired conversion of cortisone and cortisol has been reported as an important factor for insulin sensitivity and central obesity (Weaver et al., 1998).

Harper et al. observed no statistical differences in body weights and feed consumption between the acetylglycine treatment groups and the control group (Harper et al., 2010). Our animal model extended the prior research by exploring the effect of acetylglycine on HFD-induced obese mice. For the first time, we demonstrated a protective effect of mid and high doses of acetylglycine on body weight and fat in mice. The evidence has also been seen in a case of smoking-cessation-induced weight gain mice study that showed acetylglycine ameliorated weight gain rate compared with HFD control mice (Fluhr et al., 2021). The single-cell transcriptomics analysis of epididymal-adipose immune cells exemplified that acetylglycine is a potent signaling molecule that modulates modulated multiple adipose-tissue gene expressions in obesity-associated pathways such as immune response, lysosome function, and tissue remodeling (Fluhr et al., 2021).

Biochemical tests showed significant increases in the fasting glucose, total cholesterol, HDL, and LDL of the HFD groups, and unaltered triglycerides. This is consistent with what was reported in a previous HFD-induced obesity study in mice (Eisinger et al., 2014; Fluhr et al., 2021). The results of the FPG tests for the mid-dose group provided evidence for a reduction in the glucose levels, and the total and abdominal fat mass. Acetylglycine may ameliorate fat mass accumulation and further improve glucose metabolism since the decreased capacity for adipocyte differentiation and angiogenesis is reported to alleviate lipogenesis and lipolysis activities as well as insulin resistance (Patel and Abate, 2013). Elevated acetylglycine levels have been associated with decreased risk of impaired fasting glucose and onset of diabetes (Menni et al., 2013) and improved glucose tolerance (Fluhr et al., 2021). However, this evidence may not be applicable to all situations, such as high variations in glucose reduction in our high-dose group. Further investigations are needed to estimate the dose-response effects of acetylglycine on glucose.

Our study has several strengths. We had precise measures of BF mass from DXA scans to distinguish the association of metabolites with obesity. Our study systematically examined the BF-metabolites associations and partially validated them in two independent samples with different sex and ethnicities. We confirmed our novel finding with *in vivo* experiments showing that acetylglycine can significantly affect adiposity. One inherent limitation is the difficulty harmonizing metabolites from different metabolomics platforms. Although we partially replicated our findings in other sex and ethnicity groups, more research on obesity is still needed since metabolic responses affect or are affected by diverse lifestyles and diets. Second, we cannot draw causality in our findings due to the cross-sectional design. However, our validations from the independent replication cohort and *in vivo* mice studies may support the robustness of our findings to some extent.

Our investigation of adiposity phenotypes systematically identified BF metabolomic signatures and several relevant pathways. Our study provides evidence that acetylglycine, creatinine, and cortisone may have a protective role against body fat accumulation. External validation replicated six metabolites associated with BF in either Caucasian women or African American and Caucasian men. The protective effects of acetylglycine were consistent across different samples and were further validated *in vivo* in mice. The findings open new possibilities for utilizing acetylglycine as a potential diagnostic biomarker and therapeutic target of obesity or obesity-related diseases.

Data availability statement

The data that support the findings of this study are available from the corresponding author upon request and approval of the team and respective institutions. The Kyoto Encyclopedia of Genes and Genomes database and network documents for the topological pathway analysis have been deposited on the Mendeley data website: https://data.mendeley.com/datasets/rhm2b8hz75

Ethics statement

The studies involving human participants were reviewed and approved by Tulane University Institutional Review Board and Third Affiliated Hospital of Southern Medical University Institutional Review Board. The patients/participants provided their written informed consent to participate in this study.

Author contributions

The authors' responsibilities were as follows—H-WD: Supervision, Funding acquisition. JiS: Supervision, Funding acquisition. H-MX: Project administration, Funding acquisition. K-JS: Conceptualization, Methodology, Writing—Original Draft, Writing—Review and Editing, Visualization, Formal analysis, Investigation. X-YC: Validation, Resources, Investigation for the animal study. RG and XL: Data Curation, Conceptualization, Resources. QZ, JG, and HuS: Conceptualization, Writing—Review and Editing. S-DH, M-CF, YL, and Y-HZ: Resources. QT: Data Curation for the validation data. All authors provided critical feedback and helped shape the research, analysis, and manuscript.

Funding

H-WD and HuS were partially supported by grants from National Institutes of Health [R01AR069055, U19AG055373]. JiS was partially supported by grants from the Science and Technology Program of Guangzhou, China [201604020007], and the National Natural Science Foundation of China [81770878]. H-MX was partially supported by the National Key R&D Program of China (2016YFC1201805 and 2017YFC1001100). This research was supported in part using high-performance computing (HPC)

resources and services provided by Technology Services at Tulane University, New Orleans, LA.

Acknowledgments

The authors would like to acknowledge the English editing service from Loula Burton, Tulane Office of Research.

Conflict of interest

The authors declare that the research was conducted in the absence of any commercial or financial relationships that could be construed as a potential conflict of interest.

Publisher's note

Supplementary material

The Supplementary Material for this article can be found online at: https://www.frontiersin.org/articles/10.3389/fmolb.2023.1166333/full#supplementary-material

References

Ahmad, S., Hammar, U., Kennedy, B., Salihovic, S., Ganna, A., Lind, L., et al. (2022). Effect of general adiposity and central body fat distribution on the circulating metabolome: A multicohort nontargeted metabolomics observational and mendelian randomization study. *Diabetes* 71, 329–339. doi:10.2337/db20-1120

Alves, A., Bassot, A., Bulteau, A.-L. L., Pirola, L., and Morio, B. (2019). *Glycine metabolism and its alterations in obesity and metabolic diseases.* doi:10.3390/nu11061356

Apau, J., Sefah, W., and Adua, E. (2020). Human contact with phthalates during early life stages leads to weight gain and obesity. doi:10.1080/23312009.2020.1815273

Badenhorst, C. P. S., Van Der Sluis, R., Erasmus, E., and Van Dijk, A. A. (2013). Glycine conjugation: Importance in metabolism, the role of glycine N-acyltransferase, and factors that influence interindividual variation. *Expert Opin. Drug Metab. Toxicol.* 9, 1139–1153. doi:10.1517/17425255.2013.796929

Bogl, L. H., Kaye, S. M., Rämö, J. T., Kangas, A. J., Soininen, P., Hakkarainen, A., et al. (2016). Abdominal obesity and circulating metabolites: A twin study approach. *Metabolism* 65, 111–121. doi:10.1016/j.metabol.2015.10.027

Boone, S. C., van Smeden, M., Rosendaal, F. R., le Cessie, S., Groenwold, R. H. H., Jukema, J. W., et al. (2022). Evaluation of the value of waist circumference and metabolomics in the estimation of visceral adipose tissue. *Am. J. Epidemiol.* 191, 886–899. doi:10.1093/AJE/KWAB298

Chapman, K. E., and Seckl, J. R. (2008). 11beta-HSD1, inflammation, metabolic disease and age-related cognitive (dys)function. *Neurochem. Res.* 33, 624–636. doi:10.1007/s11064-007-9504-9

Chen, B., Sun, Y., Luo, F., and Wang, C. (2020). Bioactive metabolites and potential mycotoxins produced by cordyceps fungi: A review of safety. *Toxins (Basel)* 12, 410. doi:10.3390/TOXINS12060410

Chen, H. H., Tseng, Y. J., Wang, S. Y., Tsai, Y. S., Chang, C. S., Kuo, T. C., et al. (2015). The metabolome profiling and pathway analysis in metabolic healthy and abnormal obesity. *Int. J. Obes.* 39, 1241–1248. doi:10.1038/ijo.2015.65

Chen, Z.-Z., and Gerszten, R. E. (2020). Metabolomics and proteomics in type 2 diabetes. *Circ. Res.* 126, 1613–1627. doi:10.1161/CIRCRESAHA.120.315898

Cirulli, E. T., Guo, L., Leon Swisher, C., Shah, N., Huang, L., Napier, L. A., et al. (2019). Profound perturbation of the metabolome in obesity is associated with health risk. *Cell Metab.* 29, 488–500.e2. doi:10.1016/J.CMET.2018.09.022

Delmas, P. D., Schlemmer, A., Gineyts, E., Riis, B., and Christiansen, C. (1991). Urinary excretion of pyridinoline crosslinks correlates with bone turnover measured on iliac crest biopsy in patients with vertebral osteoporosis. *J. Bone Min. Res.* 6, 639–644. doi:10.1002/JBMR.5650060615

Demain, A. L., and Sanchez, S. (2009). Microbial drug discovery: 80 years of progress. *J. Antibiot.* 621 62, 5–16. doi:10.1038/ja.2008.16

Donepudi, A. C., Cheng, Q., Lu, Z. J., Cherrington, N. J., and Slitt, A. L. (2016). Hepatic transporter expression in metabolic syndrome: Phenotype, serum metabolic hormones, and transcription factor expression. *Drug Metab. Dispos.* 44, 518–526. doi:10.1124/dmd.115.066779

Eisinger, K., Liebisch, G., Schmitz, G., Aslanidis, C., Krautbauer, S., and Buechler, C. (2014). Lipidomic analysis of serum from high fat diet induced obese mice. *Int. J. Mol. Sci.* 15, 2991–3002. doi:10.3390/ijms15022991

Fedry, J., Blais, A., Even, P. C., Piedcoq, J., Fromentin, G., Gaudichon, C., et al. (2016). Urinary metabolic profile predicts high-fat diet sensitivity in the C57Bl6/J mouse. *J. Nutr. Biochem.* 31, 88–97. doi:10.1016/J.JNUTBIO.2015.12.015

Fluhr, L., Mor, U., Kolodziejczyk, A. A., Dori-Bachash, M., Leshem, A., Itav, S., et al. (2021). Gut microbiota modulates weight gain in mice after discontinued smoke exposure. *Nature* 600, 713–719. doi:10.1038/s41586-021-04194-8

Fu, X., Song, A., Zhou, Y., Xiaoguang, M., Jiao, J., Yang, M., et al. (2013). Association of regional body fat with metabolic risks in Chinese women. *Public Health Nutr.* 17, 2316–2324. doi:10.1017/S1368980013002668

Gawlik, A. M., Shmoish, M., Hartmann, M. F., Wudy, S. A., and Hochberg, Z. (2020). Steroid metabolomic signature of insulin resistance in childhood obesity. *Diabetes Care* 43, 405–410. doi:10.2337/DC19-1189

Gong, R., Xiao, H.-M., Zhang, Y.-H., Zhao, Q., Su, K.-J., Lin, X., et al. (2021). Identification and functional characterization of metabolites for bone mass in peri- and postmenopausal Chinese women. *J. Clin. Endocrinol. Metab.* 106, e3159–e3177. doi:10.1210/clinem/dgab146

Harper, M. S., Amanda Shen, Z., Barnett, J. F., Krsmanovic, L., Dakoulas, E. W., and Delaney, B. (2010). Toxicology studies with N-acetylglycine. *Food Chem. Toxicol.* 48, 1321–1327. doi:10.1016/j.fct.2010.02.031

Hatch, E. E., Nelson, J. W., Qureshi, M. M., Weinberg, J., Moore, L. L., Singer, M., et al. (2008). Association of urinary phthalate metabolite concentrations with body mass index and waist circumference: A cross-sectional study of nhanes data, 1999-2002. *Environ. Heal. A Glob. Access Sci. Source* 7, 27–15. doi:10.1186/1476-069X-7-27

He, X., Zhu, Z., Zang, J., Wang, Z., Liao, P., Wang, W., et al. (2023). Percent body fat, but not body mass index, is associated with cardiometabolic risk factors in children and adolescents. *Chronic Dis. Transl. Med.* doi:10.1002/CDT3.54

Hjelmesæth, J., Røislien, J., Nordstrand, N., Hofsø, D., Hager, H., and Hartmann, A. (2010). Low serum creatinine is associated with type 2 diabetes in morbidly obese women and men: A cross-sectional study. *BMC Endocr. Disord.* 10, 6. doi:10.1186/1472-6823-10-6

Koenen, M., Hill, M. A., Cohen, P., and Sowers, J. R. (2021). Obesity, adipose tissue and vascular dysfunction. *Circ. Res.* 128, 951–968. doi:10.1161/CIRCRESAHA.121.318093

Kuo, T. R., and Chen, C. H. (2017). Bone biomarker for the clinical assessment of osteoporosis: Recent developments and future perspectives. *Biomark. Res.* 5, 18–19. doi:10.1186/s40364-017-0097-4

Luu, Y. K., Lublinsky, S., Ozcivici, E., Capilla, E., Pessin, J. E., Rubin, C. T., et al. (2009). *In vivo* quantification of subcutaneous and visceral adiposity by micro-computed tomography in a small animal model. *Med. Eng. Phys.* 31, 34–41. doi:10.1016/j.medengphy.2008.03.006

Maguire, D., Talwar, D., Shiels, P. G., and McMillan, D. (2018). The role of thiamine dependent enzymes in obesity and obesity related chronic disease states: A systematic review. *Clin. Nutr. ESPEN* 25, 8–17. doi:10.1016/j.clnesp.2018.02.007

Marco-Ramell, A., Tulipani, S., Palau-Rodriguez, M., Gonzalez-Dominguez, R., Miñarro, A., Jauregui, O., et al. (2018). Untargeted profiling of concordant/discordant phenotypes of high insulin resistance and obesity to predict the risk of developing diabetes. *J. Proteome Res.* 17, 2307–2317. doi:10.1021/acs.jproteome.7b00855

Marsh, M. L., Oliveira, M. N., and Vieira-Potter, V. J. (2023). Adipocyte metabolism and health after the menopause: The role of exercise. *Nutr* 15, Page 444 15, 444. doi:10.3390/NU15020444

Menni, C., Fauman, E., Erte, I., Perry, J. R. B., Kastenmüller, G., Shin, S. Y., et al. (2013). Biomarkers for type 2 diabetes and impaired fasting glucose using a nontargeted metabolomics approach. *Diabetes* 62, 4270–4276. doi:10.2337/db13-0570

Moore, S. C., Matthews, C. E., Sampson, J. N., Stolzenberg-Solomon, R. Z., Zheng, W., Cai, Q., et al. (2014). Human metabolic correlates of body mass index. *Metabolomics* 10, 259–269. doi:10.1007/s11306-013-0574-1

New, S. A., Robins, S. P., Campbell, M. K., Martin, J. C., Garton, M. J., Bolton-Smith, C., et al. (2000). Dietary influences on bone mass and bone metabolism: Further evidence of a positive link between fruit and vegetable consumption and bone health? *Am. J. Clin. Nutr.* 71, 142–151. doi:10.1093/AJCN/71.1.142

Noppe, G., Van Den Akker, E. L. T., De Rijke, Y. B., Koper, J. W., Jaddoe, V. W., and Van Rossum, E. F. C. (2016). Long-term glucocorticoid concentrations as a risk factor for childhood obesity and adverse body-fat distribution. *Int. J. Obes.* 40, 1503–1509. doi:10.1038/ijo.2016.113

O'Keeffe, L. M., Bell, J. A., O'Neill, K. N., Lee, M. A., Woodward, M., Peters, S. A. E., et al. (2022). Sex-specific associations of adiposity with cardiometabolic traits in the UK: A multi-life stage cohort study with repeat metabolomics. *Plos Med.* 19, e1003636. doi:10.1371/JOURNAL.PMED.1003636

Okosun, I. S., Seale, J. P., and Lyn, R. (2015). Commingling effect of gynoid and android fat patterns on cardiometabolic dysregulation in normal weight American adults. *Nutr. Diabetes* 5, e155. doi:10.1038/nutd.2015.5

Patel, P., and Abate, N. (2013). Body fat distribution and insulin resistance. *Nutrients* 5, 2019–2027. doi:10.3390/nu5062019

Patel, S. S., Molnar, M. Z., Tayek, J. A., Ix, J. H., Noori, N., Benner, D., et al. (2013). Serum creatinine as a marker of muscle mass in chronic kidney disease: Results of a cross-sectional study and review of literature. *J. Cachexia. Sarcopenia Muscle* 4, 19–29. doi:10.1007/s13539-012-0079-1

Qiao, J., Zhang, M., Wang, T., Huang, S., Zeng, P., Tang, J., et al. (2021). Evaluating causal relationship between metabolites and six cardiovascular diseases based on GWAS summary statistics 12. doi:10.3389/fgene.2021.746677

Rangel-Huerta, O. D., Pastor-Villaescusa, B., and Gil, A. (2019). Are we close to defining a metabolomic signature of human obesity? A systematic review of metabolomics studies. *Metabolomics* 15, 93. doi:10.1007/s11306-019-1553-y

Rees, D. C., Johnson, E., and Lewinson, O. (2009). ABC transporters: The power to change. *Nat. Rev. Mol. Cell Biol.* 10, 218–227. doi:10.1038/nrm2646

Sumner, L. W., Amberg, A., Barrett, D., Beale, M. H., Beger, R., Daykin, C. A., et al. (2007). Proposed minimum reporting standards for chemical analysis: Chemical analysis working group (CAWG) metabolomics standards initiative (MSI). *Metabolomics* 3, 211–221. doi:10.1007/s11306-007-0082-2

Supriya, R., Tam, B. T., Yu, A. P., Lee, P. H., Lai, C. W., Cheng, K. K., et al. (2018). Adipokines demonstrate the interacting influence of central obesity with other cardiometabolic risk factors of metabolic syndrome in Hong Kong Chinese adults. *PLoS One* 13, e0201585. doi:10.1371/JOURNAL.PONE.0201585

Teixeira, M. D., Tureck, L. V., Do Nascimento, G. A., de Souza, R. L. R., and Furtado-Alle, L. (2020). Is it possible abc transporters genetic variants influence the outcomes of a weight-loss diet in obese women? *Genet. Mol. Biol.* 43, e20190326. doi:10.1590/1678-4685-GMB-2019-0326

Tusup, M., Kündig, T. M., and Pascolo, S. (2022). Epitranscriptomics modifier pentostatin indirectly triggers Toll-like receptor 3 and can enhance immune infiltration in tumors. *Mol. Ther.* 30, 1163–1170. doi:10.1016/J.YMTHE.2021.09.022

Vasan, S. K., Osmond, C., Canoy, D., Christodoulides, C., Neville, M. J., Di Gravio, C., et al. (2018). Comparison of regional fat measurements by dual-energy X-ray absorptiometry and conventional anthropometry and their association with markers of diabetes and cardiovascular disease risk. *Int. J. Obes.* 42, 850–857. doi:10.1038/ijo.2017.289

Vierhapper, H., Heinze, G., and Nowotny, P. (2007). Sex-specific difference in the interconversion of cortisol and cortisone in men and women. *Obesity* 15, 820–824. doi:10.1038/oby.2007.592

Wang, Y., Liu, D., Li, Y., Guo, L., Cui, Y., Zhang, X., et al. (2016). Metabolomic analysis of serum from obese adults with hyperlipemia by UHPLC-Q-TOF MS/MS. *Biomed. Chromatogr.* 30, 48–54. doi:10.1002/bmc.3491

Weaver, J. U., Taylor, N. F., Monson, J. P., Wood, P. J., and Kelly, W. F. (1998). Sexual dimorphism in 11 β hydroxysteroid dehydrogenase activity and its relation to fat distribution and insulin sensitivity; a study in hypopituitary subjects. *Clin. Endocrinol. (Oxf).* 49, 13–20. doi:10.1046/j.1365-2265.1998.00494.x

Westhuizen, F. H. van der, Pretorius, P. J., and Erasmus, E. (2000). The utilization of alanine, glutamic acid, and serine as amino acid substrates for glycine N-acyltransferase. *J. Biochem. Mol. Toxicol.* 14, 102–109. Available at: https://onlinelibrary.wiley.com/doi/abs/10.1002/%28SICI%291099-0461%282000%2914%3A2%3C102%3A%3AAID-JBT6%3E3.0.CO%3B2-H?sid=nlm%3Apubmed (Accessed June 26, 2021).

Wu, G., Bazer, F. W., Davis, T. A., Kim, S. W., Li, P., Marc Rhoads, J., et al. (2009). Arginine metabolism and nutrition in growth, health and disease. *Amino Acids* 37, 153–168. doi:10.1007/s00726-008-0210-y

Xie, G., Wang, Y., Wang, X., Zhao, A., Chen, T., Ni, Y., et al. (2015). Profiling of serum bile acids in a healthy Chinese population using UPLC–MS/MS. *J. Proteome Res.* 14, 850–859. doi:10.1021/pr500920q

Yu, H. T., Fu, X. Y., Xu, B., Zuo, L. L., Ma, H. B., and Wang, S. R. (2018). Untargeted metabolomics approach (UPLC-Q-TOF-MS) explores the biomarkers of serum and urine in overweight/obese young men. *Asia Pac. J. Clin. Nutr.* 27, 1067–1076. doi:10.6133/apjcn.052018.07

Zhao, H., Shen, J., Djukovic, D., Daniel-MacDougall, C., Gu, H., Wu, X., et al. (2016). Metabolomics-identified metabolites associated with body mass index and prospective weight gain among Mexican American women. *Obes. Sci. Pract.* 2, 309–317. doi:10.1002/osp4.63

Zhao, Q., Shen, H., Su, K.-J. J., Zhang, J.-G. G., Tian, Q., Zhao, L.-J. J., et al. (2018). Metabolomic profiles associated with bone mineral density in US Caucasian women. *Nutr. Metab.* 15, 57. doi:10.1186/s12986-018-0296-5

Zheng, H., Yde, C. C., Arnberg, K., Mølgaard, C., Michaelsen, K. F., Larnkjær, A., et al. (2014). NMR-based metabolomic profiling of overweight adolescents: An elucidation of the effects of inter-/intraindividual differences, gender, and pubertal development. *Biomed. Res. Int.* 2014, 537157. doi:10.1155/2014/537157

frontiers | Frontiers in Molecular Biosciences

TYPE Original Research
PUBLISHED 23 June 2023
DOI 10.3389/fmolb.2023.1203208

OPEN ACCESS

EDITED BY
Ryszard Tomasz Smolenski,
Medical University of Gdansk, Poland

REVIEWED BY
Wanling Xuan,
University of South Florida, United States
Xiao Li,
Shandong Provincial Qianfoshan Hospital, China

*CORRESPONDENCE
Yunfei Li,
liyunfei@tjutcm.edu.cn
Yubo Li,
yaowufenxi001@sina.com

†These authors have contributed equally to this work and share first authorship

RECEIVED 10 April 2023
ACCEPTED 12 June 2023
PUBLISHED 23 June 2023

CITATION
Wang Y, Li X, Qi M, Li X, Zhang F, Wang Y, Wu J, Shu L, Fan S, Li Y and Li Y (2023), Pharmacological effects and mechanisms of YiYiFuZi powder in chronic heart disease revealed by metabolomics and network pharmacology. *Front. Mol. Biosci.* 10:1203208. doi: 10.3389/fmolb.2023.1203208

Pharmacological effects and mechanisms of YiYiFuZi powder in chronic heart disease revealed by metabolomics and network pharmacology

Yuming Wang[1†], Xue Li[1†], Min Qi[2], Xiaokai Li[1], Fangfang Zhang[1], Yuyu Wang[1], Junke Wu[1], Lexin Shu[1], Simiao Fan[1], Yunfei Li[1*] and Yubo Li[1*]

[1]School of Chinese Materia, Tianjin University of Traditional Chinese Medicine, Tianjin, China, [2]TIPRHUYA Advancing Innovative Medicines Ltd., Tianjin, China

Introduction: YiYiFuZi powder (YYFZ) is a classical formula in Chinese medicine, which is commonly used clinically for the treatment of Chronic Heart Disease (CHD), but it's pharmacological effects and mechanism of action are currently unclear.

Methods: An adriamycin-induced CHD model rat was established to evaluate the pharmacological effects of YYFZ on CHD by the results of inflammatory factor level, histopathology and echocardiography. Metabolomic studies were performed on rat plasma using UPLC-Q-TOF/MS to screen biomarkers and enrich metabolic pathways; network pharmacology analysis was also performed to obtain the potential targets and pathways of YYFZ for the treatment of CHD.

Results: The results showed that YYFZ significantly reduced the levels of TNF-α and BNP in the serum of rats, alleviated the disorder of cardiomyocyte arrangement and inflammatory cell infiltration, and improved the cardiac function of rats with CHD. The metabolomic analysis identified a total of 19 metabolites, related to amino acid metabolism, fatty acid metabolism, and other metabolic pathways. Network pharmacology showed that YYFZ acts through PI3K/Akt signaling pathway, MAPK signaling pathway and Ras signaling pathway.

Discussion: YYFZ treatment of CHD modulates blood metabolic pattern and several protein phosphorylation cascades but importance specific changes for therapeutic effect require further studies.

KEYWORDS

metabolomics, biomarker, chronic heart disease, YiYiFuZi powder, pathways

1 Introduction

Chronic heart disease (CHD) is a complex clinical syndrome in which structural or functional abnormalities of the heart cause a range of symptoms of diastolic and systolic dysfunction, such as dyspnea, ankle swelling, and fatigue. CHD is the end-stage of heart disease and a major cause of death from cardiovascular disease (Tsutsui, 2022). The

main drugs used to treat heart failure are diuretics, angiotensin-converting enzyme (ACE) inhibitors, angiotensin receptor blockers (ARBs), β-blockers, and salt corticosteroid receptor antagonists (MRAs), but the morbidity and mortality rates of the disease remain high (Roger, 2021). Traditional Chinese medicine (TCM) has been used for thousands of years for the treatment of CHD with good results and multi-target advantages, and many studies are showing the use of TCM for the improvement of CHD, which makes the clinical application of TCM in the treatment of CHD possible (Du et al., 2021; Leung et al., 2021; Meng et al., 2021; Liao et al., 2022; Liu et al., 2022).

In Chinese medicine, CHD belongs to the category of "heart paralysis" and "chest paralysis," and the main pathogenesis of CHD is a deficiency of positive energy and paralysis by cold and dampness. This formula is from the book "Jin Gui Yao Lve." Coix seed has multiple pharmacological effects such as anti-tumor, improving body immunity, hypoglycemia, anti-inflammatory and analgesic, and regulating lipid metabolism, and its important pharmacological activities in the treatment of cervical cancer, lung cancer, and gastrointestinal tract tumors have been confirmed in clinical practice (Ni et al., 2021; Zhou et al., 2021; Sui and Xu, 2022; Yang et al., 2022). In a related experimental study, Coix seed was found to improve Th1/Th2 cytokines in mice to restore immune homeostasis after administration (Wang H. et al., 2022). Fuzi is commonly used in clinical practice for the treatment of heart diseases such as heart failure, and its main chemical constituents are alkaloids with cardiac analgesic, anti-myocardial ischemic, anti-arrhythmic, and improving the energy metabolism of cardiomyocytes (Zhang et al., 2017; Yan et al., 2020; Chen et al., 2022; Tai et al., 2022).

Metabolomics and network pharmacology are effective tools to elucidate the potential mechanisms of TCM compounding. In recent years, metabolomics has been widely used in biomedical research, and its target is endogenous metabolites with small molecular weight in the organism, and by detecting the changes of endogenous metabolites after the disturbance of the organism, the differential metabolites associated with the disturbance can be identified, and the metabolic pathways can be elucidated in combination with bioinformatics analysis, and then the biological metabolic mechanism can be analyzed (Li et al., 2020; Cui et al., 2021; Nicholson, 2021; Sun C. et al., 2021; Buergel et al., 2022; Santos-Gallego et al., 2022). Network pharmacology is a joint application of bioinformatics, systems biology and multidirectional pharmacology to study drugs. The "multi-target" and "synergistic mechanism" emphasized by cyber pharmacology are in line with the "holistic concept" and "diagnosis and treatment" emphasized by TCM theory. "Through the analysis of genes, proteins, diseases, drugs and other real data obtained from databases and experiments, the intrinsic relationship between multi-component and multi-target effects of TCM on the body can be explored from a systematic and holistic perspective, which is important for explaining the potential mechanisms of TCM treatment (Li et al., 2019; Yao et al., 2020; Li et al., 2021; Shi et al., 2022; Zhou et al., 2022). The combination of network pharmacology and metabolomics can complement each other to reveal the biological significance and mechanism of drug action more comprehensively.

In this study, we first established a rat model of CHD suitable for testing of pharmacological effects and metabolomic analysis on plasma samples to reveal potential biomarkers and metabolic pathways; secondly, we performed network pharmacological analysis on the *in vivo* components of YYFZ to predict the targets and pathways of action as well as allowing the in-depth study of the material basis and mechanism of action of YYFZ in the treatment of CHD.

2 Materials and methods

2.1 Instruments and reagents

Adriamycin hydrochloride was purchased from Solarbio (China). Purified water was purchased from Watson's (China). Isoflurane was purchased from Rwd Life Science Co., Ltd. (China). Saline for injection was purchased from SSY Group Limited. Captopril was purchased from Shanghai Xudong Haipu Pharmaceutical Co., Ltd. (China). Coix Seed was purchased from Hunan Yaoshengtang Traditional Chinese Medicine Technology Co., Ltd. (China). Fuzi was purchased from Hebei Meiwei Pharmaceutical Co., Ltd. (China).

Vevo small animal ultrasound imager was purchased from Visualsonics Co., Ltd. (United States). ALLLEGRATM-64R high-speed frozen centrifuge was purchased from Beckman Co., Ltd. (United States). TecanInfiniteF50 enzyme labeler was purchased from Tecan, Co., Ltd. (Switzerland). UPLC/Q-TOF/MS was purchased from Waters Corporation Co., Ltd. (United States). The rat TNF-α kit and rat BNP kit were purchased from Nanjing Jiancheng Biotechnology Co., Ltd. (China). The pathological sections of heart tissue were processed by Hunan Fenghui Biotechnology Co., Ltd. (China).

2.2 Preparation of YYFZ decoction

Weighed coix seeds and Fuzi, mixed in the ratio of 5:3, placed in a round bottom flask, added 10 times the amount of water and soak for 45 min. The extract was then extracted by reflux extraction method for 1 h. The extract was filtered through 3 layers of gauze. The remaining drug residue was added with 8 times the amount of water and extracted for 45 min. The two filtrates were combined and concentrated to a viscous infusion (concentration of 1 g/mL in terms of raw drug). The samples were stored in a refrigerator at 4°C and set aside.

2.3 Animals

Sixty SPF-grade male Wistar rats (190–220 g, purchased from Beijing Spelford Biotechnology Co., Ltd., license number: SCXK (Beijing) 2019–0010) were selected, and the rats were acclimatized and fed at a temperature of 20°C–26°C, relative humidity of 40%–70%, ventilation of 10–15 times/h, and light of 12 h light/dark for 7 days, and all animals The feeding process

was carried out by the operating procedures for clean grade laboratory animals. The study was approved by the Animal Ethics Committee of Tianjin University of Traditional Chinese Medicine (TCM-LAEC2021241), and ethical norms were followed in handling animals during the experiment to minimize animal numbers and suffering.

2.4 Establishment of CHD rat models and grouping

After 1 week of acclimatization feeding, 10 rats were randomly selected as the NS group (control group), and the remaining rats were injected intraperitoneally with 1.25 mg/mL aqueous solution of adriamycin hydrochloride at a dose of 1.25 mg/kg twice a week for 8 weeks, with a cumulative dose of 18 mg/kg; the NS group was injected with the same dose of saline. After the end of modeling, the rats were randomly divided into 5 groups: Model group, Captopril group, YYFZ-H group, YYFZ-M group, YYFZ-L group, 10 rats in each group and treated according to the dosing. YYFZ-H, YYFZ-M, and YYFZ-L groups were treated with 5.25 g/kg, 2.63 g/kg and 1.31 g/kg by gavage. The Captopril group was given 6.75 mg/kg by gavage. The NS and Model groups were given the same volume of pure water as a control and administered once a day for a treatment period of 30 days.

2.5 Observation and detection of indicators

2.5.1 General morphological observation

From the beginning of the modeling, the experimental animals were closely observed and recorded for weight, coat condition, mental status, respiratory system condition and survival.

2.5.2 Evaluation of rat CHD model

At the end of the modeling, all rats fasted for 12 h. Ten rats were randomly selected from the NS group and the model group, anesthetized with isoflurane. Cardiac function was measured using a vevo small animal ultrasound imager, with cardiac ejection fraction (EF) less than 55% as the modeling criterion. At the same time, blood was taken from the inner canthus of the rat's eye, placed at room temperature for 30 min, and then centrifuged for 10 min at 4°C and 3,500 rpm/min in a freezing centrifuge for the detection of BNP and TNF-α.

2.5.3 Detection of cardiac function indexes

The rats were anesthetized with a VMR small animal respiratory anesthesia machine, skin was prepared on the chest using hair removal cream, coupling agent was applied, and an ultrasound probe was used to perform ultrasound examination of the rat's heart from the long axis of the parasternal bone. In M ultrasound mode, and the rat's EF, fractional shortening (FS), left ventricular posterior wall end-systolic thickness (LVPW; s), left ventricular posterior wall end-diastolic thickness (LVPW; d), left ventricular end-systolic internal diameter (LVID; s), left ventricular internal diameter end-diastolic internal diameter (LVID; d), left ventricular end-systolic septal thickness (IVS; s), Left ventricular end-diastolic septal thickness (IVS; d), and the average of 3 cardiac cycles were taken for each sample.

2.6 Observation and detection of indicators

At the end of day 30 dosing, all rats fasted without water for 12 h. After anesthetizing the rats, the cardiac function indexes were first tested using VMR, and then subsequent operations were performed under anesthesia.

2.6.1 Collection of blood samples

Blood was collected from rats through the abdominal aorta to the maximum extent possible, and half of the whole blood samples were placed in heparin anticoagulation tubes and the other half in EP tubes, which were left for 30 min and then pretreated. The plasma samples in the anticoagulation tubes were centrifuged at 4°C, 3,500 rpm for 10 min, and the supernatant was frozen in a −80°C refrigerator for subsequent metabolomic analysis; the blood samples in the EP tubes were centrifuged at 4°C, 3,500 rpm for 10 min, and the supernatant was frozen in a −80°C refrigerator for subsequent serum biochemical analysis.

2.6.2 Heart index

The hearts of rats were removed and weighed after blood sampling from the abdominal aorta, and the organ index was calculated: organ index = organ (g)/body weight (kg).

2.6.3 Detection of serum biochemical indexes

The levels of BNP and TNF-α in rat serum were measured by ELISA kits.

2.6.4 Cardiac histopathology

The rat heart was taken and placed in a 4% tissue fixating solution for 24 h, then dehydrated, paraffin-embedded wax blocks were made, which were successively sliced, dissected, baked, and stained by HE. Morphological changes in rat cardiomyocytes were observed under a light microscope.

2.7 Metabolomics analysis

2.7.1 Sample preparation

Frozen rat plasma samples were removed from the −80°C refrigerator and thawed first in a 4°C refrigerator. 100 μL of plasma was pipetted from the samples, 300 μL of chromatographically pure acetonitrile was added at a volume ratio of 1:3, vortexed and mixed for 5 min, then centrifuged in a refrigerated centrifuge at 13,000 rpm/min for 15 min, and the supernatant was aspirated for UPLC-Q-TOF/MS analysis.

2.7.2 Preparation of QC sample

10 μL of each plasma sample was taken in an EP tube, vortexed for 1 min, and then centrifuged at 4°C at 13,200*g for 15 min, and the supernatant was aspirated for methodological investigation.

2.7.3 Instrument conditions

In this experiment, UPLC-Q-TOF/MS was used to characterize metabolites. UPLC separation was performed on an ACQUITY UPLC BEH C_{18} column (2.1 mm × 100 mm, 1.7 μm, Waters Co., United States) at 45°C. The mobile phase consists of water (A) and acetonitrile (B) (both containing 0.1% formic acid). The gradient elution procedure is as follows: 0–0.5 min, 1%B; 0.5–2 min, 1%-50%B; 2–9 min, 50%-99%B; 9–10 min, 99%B; 10–10.5 min, 99%-1%B; 10.5–12 min, 1% B, the flow rate was 0.3 mL/min. The injection volume was 5 μL.

After separation, mass spectra were detected and analyzed using an electrospray ion source (ESI) in positive and negative ionization modes. Ion source parameters are set as follows: The capillary voltage is 3.0 kV, the drying gas temperature is 325°C, the atomized gas pressure is 310 kPa, the drying gas flow is 0.26 mL/min, the desorption gas flow is 600 L/h, the source temperature is 120°C, the desorption temperature is 350°C, and the cone gas flow is 50 L/h.

2.7.4 Data processing

Raw data were exported by Masslynx4.1 (Waters, United States) software, after which the data were imported into SIMCA 14.1 statistical software (Umetrics Corporation, Sweden) for multivariate statistical analysis. Subsequently, SPSS 26.0 was applied for statistical tests and the appropriate test was selected to determine whether metabolites changed significantly ($p < 0.05$) in the statistical analysis. The metabolites screened by the above analysis are input into the MetaboAnalyst platform(https://www.metaboanalyst.ca/) for cluster analysis and Mate-Pa analysis.

2.8 Network pharmacology

2.8.1 Blood-inlet-components in YYFZ

Based on the incoming components of YYFZ identified in our previous study (Supplementary Material), the information on these components was retrieved in TCMSP (http://lsp.nwsuaf.edu.cn/tcmsp.php) for relevant target information. On the other hand, the molecular structure formula was drawn in Chemdraw, saved in. sdf format and uploaded to PharmaMapper (http://lilab-ecust.cn/pharmmapper/index.html) for predicting potential targets, and SwissTargetPrediction (http://www.swisstargetprediction.ch/) for predicting the results. As a supplement, the targets of all components were combined and de-weighted after conversion to Genename by UniProt (https://www.UniProt.org/) (UniProt Consortium, 2013).

2.8.2 Establishment of CHD disease target library

Search by Genecards (https://www.genecards.org/), TTD data (http://bidd.nus.edu.sg/group/cjttd/) (Wang et al., 2020), OMIM (https://omim.org/) (Amberger and Hamosh, 2017) databases The targets related to the pathogenesis of "chronic heart disease" were combined by removing duplicate targets from several databases.

2.8.3 Visualization and analysis of active ingredient-target-disease network

PPI (protein-protein interaction) maps were created through protein interaction analysis via STRING database and imported into Cytoscape 3.8.2 for intra-network visualization of PPI data between potential therapeutic targets of diseases and mapping of active ingredient-target-disease networks.

KEGG pathway enrichment analysis was performed on the network nodes using DAVID database to obtain the functional pathways involved in disease modulation by each component-acting target of YYFZ bulk, and the enriched pathways were visualized using the advanced bubble map function of the Omicshare platform.

3 Results

3.1 Pharmacodynamic study of YYFZ on CHD rat model

3.1.1 General conditions of rats

During the modeling of CHD rats, the rats in the NS group grew naturally, fed and drank normally, and were in good condition, and there was no death. During the modeling process, the rats' body weight growth slowed down significantly, and they lost their body weight and hair. After the fourth week, the rats gradually appeared ascites, abdominal distension, panting and shortness of breath, and individual rats lost their hair in flakes; until the seventh week, the rats had obvious abdominal distension, diarrhea, watery stool, filthy perianal area, shortness of breath, vertical hair, loose fur, lack of blood in the feet and paws and ears, mental inactivity, and increased secretion around the eyes and nose. After the start of administration, the condition of the rats in the Captopril group, YYFZ-H, YYFZ-M, and YYFZ-L improved, while no improvement was observed in the Model group. In addition, hepatomegaly was seen in the Model group at autopsy, and some of them had renal edema with mesenteric adhesions.

3.1.2 Weight gain of rats

After the beginning of modeling, it can be seen from (Figure 1A) that the weight gain of rats in the model group slowed down significantly, and there was a significant difference in body weight after the second injection ($p < 0.01$) until the end of the experiment. During the modeling period, the body weight of the NS group was stable, while that of the model group was slow, and occasionally fluctuated in the later period, but there was almost no obvious increase. The rats in the administration group showed no significant difference in body weight during the modeling period compared to NS ($p < 0.05$) and showed a significant increase after administration ($p < 0.05$). At the late stage of the experiment, the weight changes of rats were difficult to directly reflect the drug effect because of the severe abdominal ascites of some rats. Therefore, in this study, the therapeutic effect of the drug was reflected by calculating the body weight growth rate of rats, and the body weight growth rate % = (body weight without ascites—body weight before modeling)/body weight before modeling * 100%. It can be seen from Figure 1C that the body weight growth rate of the Model group and drug administration group was significantly different from that of the NS group ($p < 0.05$), while compared with the Model group, the body weight of Captopril group, YYFZ-H group and YYFZ-M group was significantly increased ($p < 0.05$).

10.3389/fmolb.2023.1203208

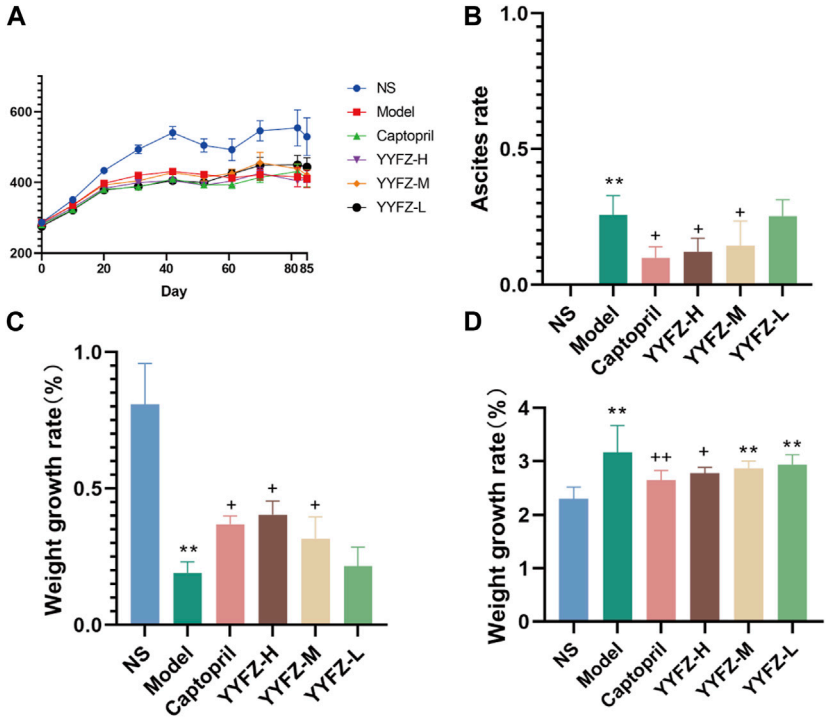

FIGURE 1
(A) Weight change trend of rats; **(B)** Ascites of rats in each group; **(C)** Weight growth of rats in each group; **(D)** Heart index of rats in each group.

TABLE 1 Comparison of cardiac structural and functional indices between modeled rats and blank rats.

Indicators	NS	Model
EF(%)	67.12 ± 1.59	49.23 ± 1.54**
FS(%)	38.53 ± 1.24	25.79 ± 0.98**
LVPW; s (mm)	2.95 ± 0.14	2.45 ± 0.14*
LVPW; d (mm)	1.96 ± 0.11	2.19 ± 0.15
LVID; s (mm)	4.52 ± 0.18	5.38 ± 0.23*
LVID; d (mm)	7.36 ± 0.31	7.27 ± 0.33
IVS; s (mm)	2.93 ± 0.15	2.92 ± 0.19
IVS; d (mm)	1.99 ± 0.15	2.14 ± 0.15

*$p < 0.05$, **$p < 0.01$.

(Compared with NS group, $n = 10$, $\bar{x} \pm SD$ *: $p<0.05$, **: $p < 0.01$; compared with Model group, $^{+}$: $p < 0.05$, $^{++}$: $p < 0.01$)

3.1.3 Ascites in rats

At the late stage of modeling, some rats showed significant signs of ascites; the ascites condition of the rats in the administered group did not continue to worsen as the administration treatment began. As seen in Figure 1B, the ascites of rats in Captopril, YYFZ-H and YYFZ-M groups appeared significantly different from the Model group ($p< 0.05$), and there was no significant difference in the low-dose group, suggesting that Captopril and high and medium doses of YYFZ have better efficacy.

3.1.4 Rat heart function

At the end of modeling, to determine the success of the model, we performed cardiac function tests on the rats. As seen in Table 1, the EF and FS in the Model group were significantly lower than those in the NS group ($p < 0.05$), indicating the success of the model. The rats were grouped after modeling, and cardiac function tests were performed after grouping. As seen in Table 2, compared with the NS group, LVPW; s and LVPW; d was significantly lower in the Model and drug administration groups ($p < 0.05$), with LVPW; d significantly higher in the Captopril group than in the Model group ($p < 0.05$). IVSs and IVSd in the Model group and YYFZ-H, YYFZ-M and YYFZ-L groups were significantly lower than those in the NS group ($p < 0.05$), with significant differences between IVSs in the YYFZ-H and YYFZ-M groups and the Model group ($p < 0.05$). The IVSs and IVSd in the Captopril group were not statistically different from those in the NS group and were significantly higher than those in the Model group ($p < 0.05$).

Cardiac function tests were performed on the rats at the end of the dosing. As shown in Table 3 and Figure 2. The EF and FS in the Model group were significantly lower than those in the NS group ($p < 0.05$), indicating that the systolic-diastolic function of the heart was reduced in the Model group. The EF and FS in the Captopril and YYFZ-H groups were significantly higher than those in the Model group. Compared with the NS group, LVID;d was significantly lower ($p < 0.05$) and LVID;s was significantly higher ($p < 0.05$) in the Model group. LVID;d, LVID;s in the YYFZ-M and YYFZ-L groups were significantly lower than those in the NS and Model groups ($p < 0.05$). LVID;d, LVID;s in the Captopril and YYFZ-H groups were

TABLE 2 Cardiac indexes (LVPW;s, LVPW;d, IVSs, IVSd) of rats in each group before drug administration.

Group	LVPW;s(mm)	LVPW;d(mm)	IVSs(mm)	IVSd(mm)
NS	3.68 ± 0.17	2.46 ± 0.08	3.30 ± 0.10	2.31 ± 0.09
Model	2.28 ± 0.11**	1.73 ± 0.10**	2.48 ± 0.12**	1.84 ± 0.09**
Captoril	2.63 ± 0.08**	2.12 ± 0.09**$^{+}$	2.85 ± 0.19^{+}	2.19 ± 0.13^{+}
YYFZ-H	2.60 ± 0.14**	2.04 ± 0.11**	2.81 ± 0.14^{+}	2.04 ± 0.06*
YYFZ-M	2.44 ± 0.09**	1.98 ± 0.07**	2.68 ± 0.10**$^{+}$	1.94 ± 0.06**$^{-}$
YYFZ-L	2.32 ± 0.13**	1.84 ± 0.06**$^{-}$	2.58 ± 0.13**	1.88 ± 0.13**$^{-}$

Compared to the NS group.*$p < 0.05$, ** $p < 0.01$; Compared with the Model group. $^{+}p<0.05$, $^{++}$ $p < 0.01$; Compared with the Captoptil group, Compared with the Captoptil group, $^{-}p < 0.05$, $^{--}p < 0.01$.

TABLE 3 Comparison of cardiac function indices (FS, EF, LVID;s, LVID;d) in rats in each group after drug administration.

Group	FS(%)	EF(%)	LVID;s(mm)	LVID;d(mm)
NS	44.96 ± 2.08	72.61 ± 2.13	4.60 ± 0.14	8.45 ± 0.14
Model	26.64 ± 0.86**	48.51 ± 1.93**	5.58 ± 0.11**	6.89 ± 0.11**
Captopril	35.52 ± 1.59**$^{++}$	59.29 ± 2.61**$^{++}$	4.98 ± 0.18^{+}	7.8 ± 0.25^{++}
YYFZ-H	33.11 ± 1.74**$^{++}$	56.42 ± 0.99**$^{++}$	5.01 ± 0.13^{++}	8.09 ± 0.16^{++}
YYFZ-M	30.35 ± 1.73**	53.18 ± 2.16**	5.24 ± 0.15**	7.7 ± 0.19**$^{++}$
YYFZ-L	28.95 ± 1.91**	51.96 ± 3.00**	5.42 ± 0.19**	7.48 ± 0.17**$^{++}$

Compared to the NS group.*$p < 0.05$, **$p < 0.01$; Compared with the Model group. $^{+}p < 0.05$,$^{++}$ $p < 0.01$; Compared with the Captoptil group, $^{-}p < 0.05$, $^{--}p < 0.01$.

not significantly different from the NS group, but were significantly different from the Model group ($p < 0.05$).

3.1.5 Rat cardiac index

After weighing and comparing, we found that there was no significant difference in the heart weight of the rats in each group, presumably related to the larger size of the rats in the NS group. After conversion into the cardiac index, it can be seen from Figure 1D that the cardiac index of the Model group and each dosing group was significantly higher than that of the NS group ($p < 0.05$), and the mean value of the cardiac index of each dosing group was lower than that of Model group, but only Captopril group and YYFZ-H group were significantly lower than that of Model group ($p < 0.05$), and the difference between the cardiac index of the remaining dosing groups and Model group was not The difference between the cardiac index of the remaining administration groups and the Model group was not statistically significant.

3.1.6 Detection of serum BNP and TNF-α in rats

To assess the rat modeling situation, this study used Elisa kits to detect BNP and TNF-α contents in rat serum, as shown in Figure 3C, there was a significant increase in BNP content in the serum of model rats about 2.16 times higher than that of NS group, and the difference was statistically significant ($p < 0.01$); TNF-α in model rats was about 1.6 times higher than that of NS rats, and the difference was statistically significant ($p< 0.01$).

After the administration, the serum BNP and TNF-α levels in each group are shown in Figures 3A, B. The serum BNP levels in the Model, YYFZ-M and YYFZ-L groups were significantly higher than those in the NS group ($p < 0.05$), with the serum BNP in the YYFZ-M group being significantly lower than that in the Model group ($p < 0.05$) and the YYFZ-L group not significantly different from that in the Model group. The differences between the Captopril and YYFZ-H groups were statistically significantly lower than those in the Model group ($p < 0.05$) and the NS group ($p < 0.05$). The TNF-α levels in the Captopril, YYFZ-H and YYFZ-M groups were significantly lower than those in the Model group ($p < 0.05$), and there was no significant difference with the NS group. (Compared with the NS group, $n = 10$, $\bar{x} \pm$ SD *: $p <0.05$, **: $p<0.01$; compared with the Model group, $^{+}$: $p<0.05$, $^{++}$: $p<0.01$).

3.1.7 Pathological results of myocardial tissue in rats

The results of histopathological HE (hematoxylin-eosin) staining of rat myocardium are shown in Figure 4: In the NS group, myocardial cells were clearly arranged and tightly packed, with a few myocardial transverse breaks, and vascular proliferation and inflammatory cell infiltration were not obvious. The myocardial cells in the Model group were unevenly stained, with relatively blurred transverse lines, reduced volume of some cells, and deepened staining of the envelope; the myocardial interstitium was obviously edematous, with loosely arranged cells and fat vacuoles within the cells (yellow arrows), an increased number of small blood vessels between the myocardium (red arrows), and a small number of lymphocytes between the myocardium. Captopril group and YYFZ-H group: myocardial cell transverse lines were clear, there was a small amount of edema in myocardial

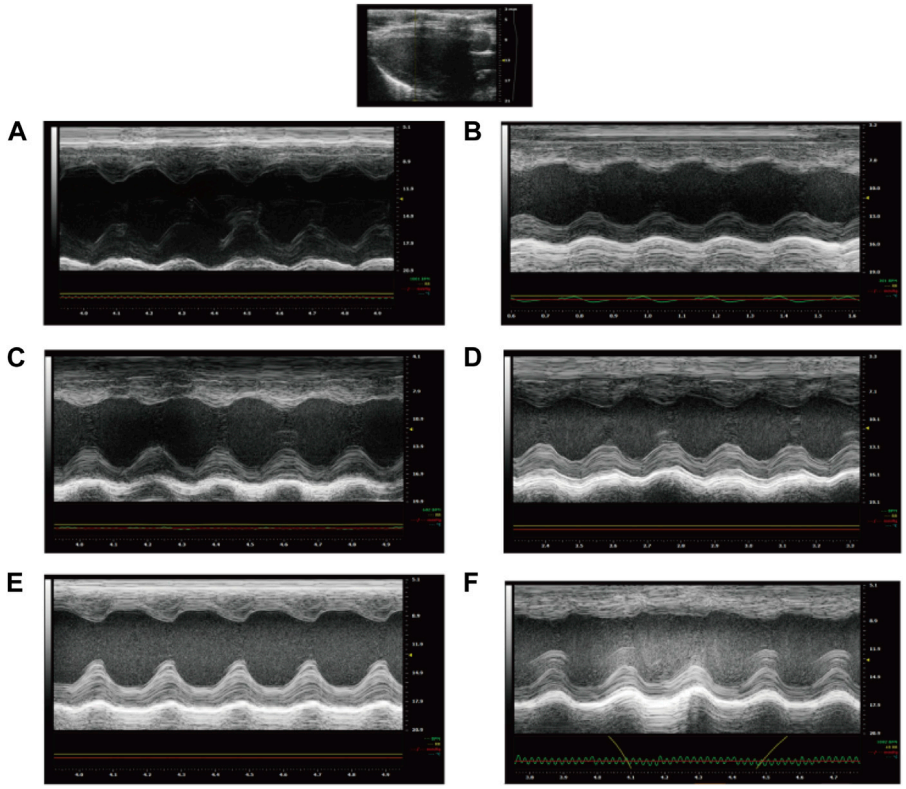

FIGURE 2
Echocardiography of rats after treatment ((**A**): NS group; **(B)** Model group; **(C)** Captopril group; **(D)**YYFZ-H group; **(E)** YYFZ-M group; **(F)** YYFZ-L group).

interstitium, and the area of lax cell arrangement was reduced compared with the model group. YYFZ-M group and YYFZ-L group: myocardial cell transverse lines were clear, the cell volume was reduced, the arrangement was more laxer, there was edema in the cell interstitium, and the number of blood vessels was increased.

3.2 Metabolomics analysis results

3.2.1 Methodological investigation

After collecting the data by UPLC-Q-TOF/MS analysis, we randomly selected 20 peaks from the obtained QC sample profiles (as shown in Figure 5A) and calculated the RSD values of their peak areas and retention times. RSD<16.17%, retention time RSD<0.92%; sample stability study in the sample at 0 h, 6 h, 12 h, 18 h, 24 h time points in the peak area RSD<12.45%, retention time RSD<0.59%. The above indicates that the instrument precision, method precision and sample stability are good, indicating that the method is reliable and can be followed up.

3.2.2 Metabolomics data pre-processing and multivariate statistical analysis

The raw data were exported from Masslynx4.1 software, and the data were subjected to a normality test and chi-square test after 80% modification, and suitable methods were selected to compare the NS and Model groups between groups, and *p*-values and fold change (FC) were calculated, and the substances and *p*-values and log2 (FC) values were entered into the Wukong data analysis cloud platform for volcano plot analysis to visually display the NS and Model groups group in the different substances. As shown in Figure 5C, the horizontal coordinate is log2 (FC), the greater the difference the more distant the metabolite is distributed, and the vertical coordinate is the *p*-value, the greater the difference the more distant the substance is from the horizontal axis, so the substance distributed in the upper left right corner is usually considered as a potential difference marker. Each of these points represents data, and the gray color is for substances with no significant changes, while the red and blue colors are for substances with significant elevated changes, which are potential differential substances that we need to pay attention to in the subsequent processing.

Multivariate statistical analysis was used to discriminate the changes of metabolites within the plasma of healthy and model rats. For this, we first set up an unsupervised PCA model as shown in Figure 6C. Each point in the figure represents a sample, respectively, and the color is used to distinguish the rat groups, and the farther the distance between the points of different groups indicates the greater difference. We can see that there is a certain convergence in the distribution of NS and Model groups, and Model and drug administration groups in the PCA model. Therefore, to further differentiate, we further established a supervised OPLS-DA model

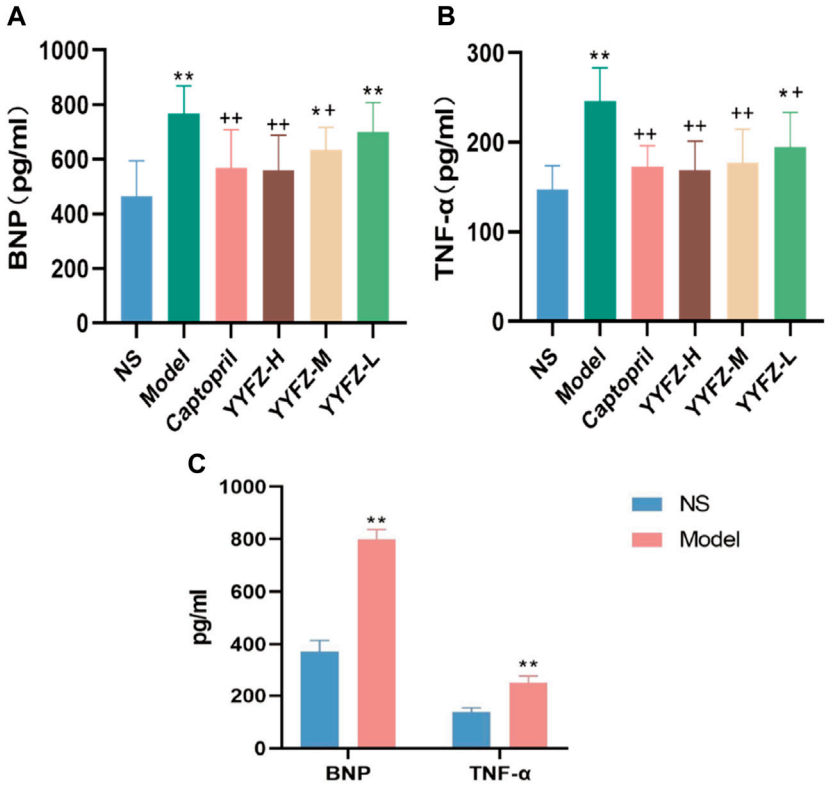

FIGURE 3
(A) Reduction of BNP after treatment; **(B)** Reduction of TNF after treatment; **(C)** BNP and TNF-α before treament.

(Figure 6A), and we can see that the NS group and Model group are distributed on both sides in the OPLS-DA model, with obvious distinction.

3.2.3 Identification of CHD biomarkers

The SPSS26.0 software was used to test for normality and the chi-square test for the differential substances. *t*-test and Mann-Whitney *u*-test were selected to test for significance according to whether the data distribution was normal and chi-square, and the differential substances with significant changes ($p < 0.05$) were considered as differential markers of heterogeneous disease and treatment. Finally, we obtained 732 NS-CHD differential substances, respectively. We entered m/z values in the HMDB database to search, selected $[M + H]^+$, $[M + K]^+$, $[M + Na]^+$ in ion addition mode, and identified metabolites by MS/MS analysis, metabolite database information, and literature information. We finally identified 19 markers, which were leukotriene F4, arachidonic acid, lysoSM(d18:0), tryptophan, phenylpyruvic acid, S-lactoylglutathione, phenylalanine, ornithine, nicotinamide-N-oxide, fumaric acid, adipic acid, D-pantothenic acid, PC(14:1/18:4), tetradecanedioic acid, 3-deoxy glucosone, α-linolenic acid, L-octanoylcarnitine, lysoPE (20:1(11Z)/0:0), lysoPC (17:0/0:0), see Table 4 for specific information. 16 markers were upregulated and 3 markers were downregulated in the Model group.

3.2.4 Hierarchical clustering analysis of CHD biomarkers

To observe the changes of markers in each group more intuitively, this study used hierarchical clustering analysis as shown in Figure 7, which can see the distribution of biomarkers in each group. The shades of color in the figure respond to the magnitude of the values, each row represents a metabolite, and each column represents the content of the whole group of samples; the left bifurcation is the cluster analysis of the substances, where the more clustering levels of the substances indicate the higher similarity of the substances, and there may be similar variations in the source and metabolic pathways. We can observe a significant change in plasma marker content in the Model group compared to the NS group, suggesting that the markers have some discriminatory ability. Metabolite levels in the captopril and YYFZ-H groups were closer to those in the NS group, and metabolite trends were more consistent, suggesting that high-dose YYFZ significantly modulates CHD disease-related markers.

3.2.5 CHD biomarker ROC analysis

ROC curves are widely used for the evaluation of the sensitivity and specificity of markers and can screen for more diagnostic biomarkers. After the above study, we identified markers with diagnostic potential by ROC analysis of the above 19 biomarkers by SPSS 26.0, and the area under the curve was used to evaluate the diagnostic ability of the markers. Usually, an area under the curve>0.5 indicates good discriminatory ability. As shown in Figure 6B, we can see that each

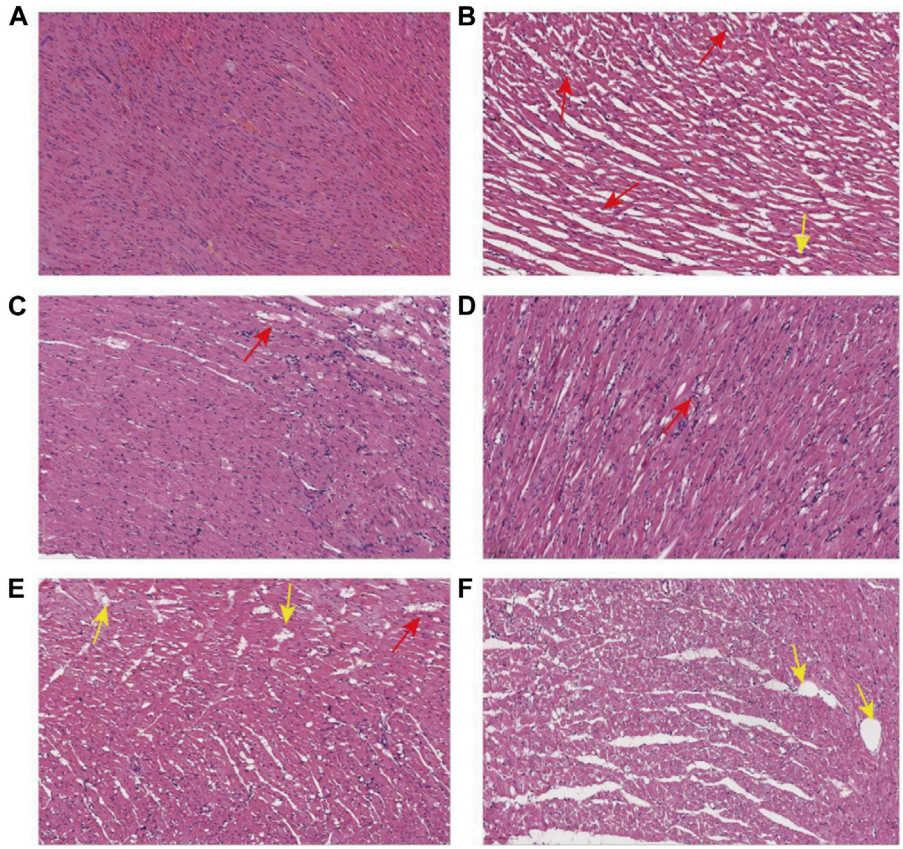

FIGURE 4
Pathological sections of myocardial tissue of rats in each group ((**A**): NS group; **(B)** Model group; **(C)** Captopril group; **(D)** YYFZ-H group; **(E)** YYFZ-M group; **(F)** YYFZ-L group).

curve represents a substance and the area under the curve is distributed between 1 and 0.87 (95% confidence interval), indicating that the 19 markers have the diagnostic ability.

3.2.6 CHD biomarker pathway analysis

To further speculate on the mechanism of CHD metabolic disorders, this study performed metabolic pathway analysis (MetPA) on 19 markers. The MetPA database is a visual metabolic pathway analysis database (www.metaboanalyst.ca), which combines pathway enrichment analysis and topological analysis to assist in screening relevant metabolic pathways. We obtained 16 metabolic pathways (Figure 5B), including phenylalanine, tyrosine and tryptophan biosynthesis, alpha-linolenic acid metabolism, phenylalanine metabolism, and arachidonic acid metabolism are the main metabolic pathways involved, suggesting that lipid metabolism and amino acid metabolism are the pathways to focus on in CHD.

3.3 Network pharmacology

3.3.1 YYFZ blood entry components and CHD targets

The database was used to predict the YYFZ inlet component targets, and finally, 228 YYFZ component targets were obtained. 1488 CHD disease targets were obtained. Venny enrichment analysis was performed between CHD inlet component targets and disease targets, as shown in Figure 8A, and 44 YYFZ targets for CHD was obtained.

3.3.2 Visualization and analysis of active ingredient-target-disease network

The potential targets of CHD and YYFZ were imported into the String database for protein interaction analysis and the PPI network was constructed, and the results showed 42 nodes with 176 edges (Figure 8B). The results in.tsv format were imported into Cytoscape 3.8.2 software for network analysis, MAPK14, EGFR, HSP90AA1, MTOR, ESR1, and IGF1 had high Dgree values, which might be the key targets of YYFZ for CHD treatment.

The Cytoscape software was used to construct the drug-active-ingredient-target network (Figure 8C). The network contains 70 nodes and 90 edges, and the larger the node degree value, the more important it is in the network. The core nodes were selected based on the network topological features such as node degree values. Among them, senbusine B, sitosterol, hypaconitine, phenylalanine, and deoxyaconitine may be the pharmacodynamic components of YYFZ for CHD.

To further discover the mechanism of action of YYFZ in the treatment of CHD, GO enrichment analysis was performed using

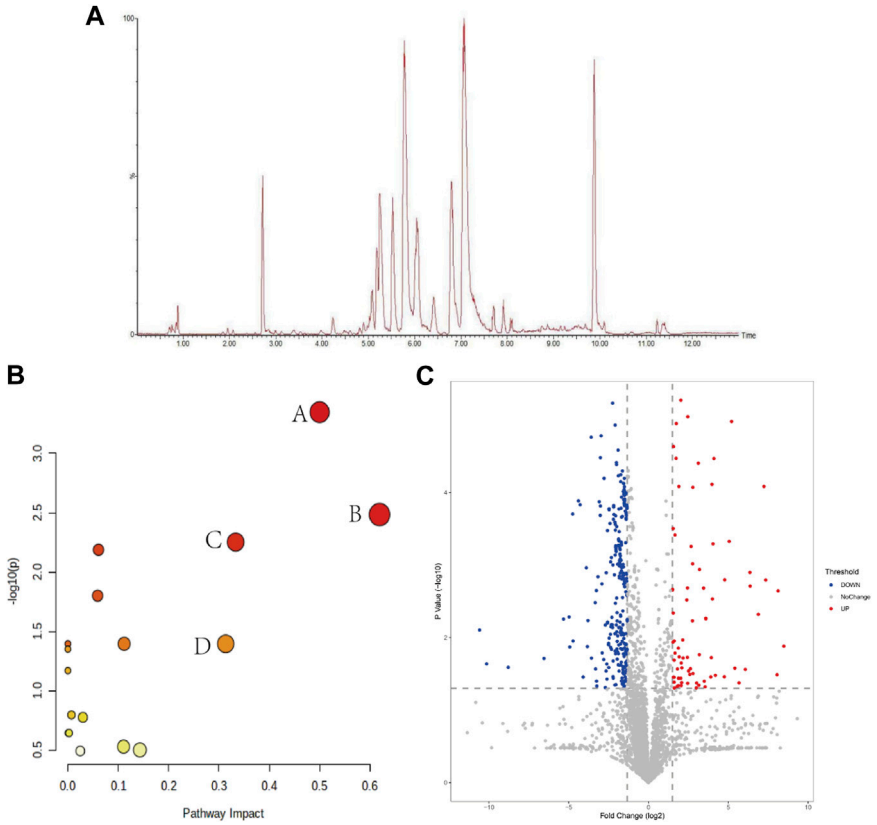

FIGURE 5
(A) BPI plots of QC samples; **(B)** Marker metabolic pathway analysis (A: phenylalanine, tyrosine and tryptophan biosynthesis; B: linolenic acid metabolism; C: phenylalanine metabolism; D: arachidonic acid metabolism); **(C)** intergroup volcano plot analysis between NS and Model groups.

the DAVID database for the common targets obtained above (Figure 9), and a total of 162 enrichment results were obtained for biological process (BP) screening at $p < 0.05$, mainly involving positive regulation of protein kinase B signaling, positive regulation of smooth muscle cell proliferation, phosphatidylinositol 3-kinase signaling. Cellular component (CC) obtained 36 enrichment results, mainly involving the extracellular region, lysosomal lumen, perinuclear region of cytoplasm, etc.; molecular function (MF) obtained 37 enrichment results, mainly involving identical protein binding, Enzyme binding, Protein homodimerization activity, etc. The KEGG pathway analysis is shown in Figure 10, excluding the pathways unrelated to CHD. signaling pathway, PI3K-Akt signaling pathway, MAPK signaling pathway, etc.

4 Discussion

In this experiment, the CHD model of rats was established by intraperitoneal injection of adriamycin, and the rats were treated with captopril and different doses of YYFZ, and the efficacy of YYFZ was comprehensively evaluated by observing the biochemical indexes and cardiac function indexes of rats and myocardial histopathological sections. Adriamycin belongs to anthracycline antibiotics, which are widely used in clinical practice for the treatment of various malignant tumors (Sabatino et al., 2020; Younis et al., 2021; Xu et al., 2022). Cardiotoxicity is one of its main side effects, which can be manifested as irreversible dose-dependent cardiomyopathy and CHD, so a heart failure model was prepared using this side effect. TNF-α is an inflammatory factor that plays an important role in promoting myocardial remodeling and inhibiting myocardial contraction, as well as in increasing endothelial and myocardial apoptosis, and there is abundant evidence that inhibition or reduction has a protective effect in heart failure models (Lee et al., 2019; Reina-Couto et al., 2021; Szabo et al., 2021; Zhong et al., 2022). BNP is a marker of cardiac insufficiency, and many studies have shown that plasma BNP levels are significantly elevated in heart failure patients, which can be used for the diagnosis of heart failure (Ichiki et al., 2013; McDonald et al., 2018; Rørth et al., 2020). We found that the YYFZ-H group had a better therapeutic effect from the perspective of biochemical indexes, significantly regulating serum BNP and TNF-α and improving cardiac function ($p < 0.05$). The pathological results showed that the YYFZ dose groups could improve myocardial cell disorder and reduce inflammatory cell infiltration. Echocardiographic determination of cardiac function in rats has been widely accepted because it provides a convenient, reliable, and non-invasive method (Zeng et al., 2019; Quagliariello et al., 2021; Wang X. et al., 2022). Generally, EF is measured as an indicator of cardiac function, FS is also one of the commonly used indicators,

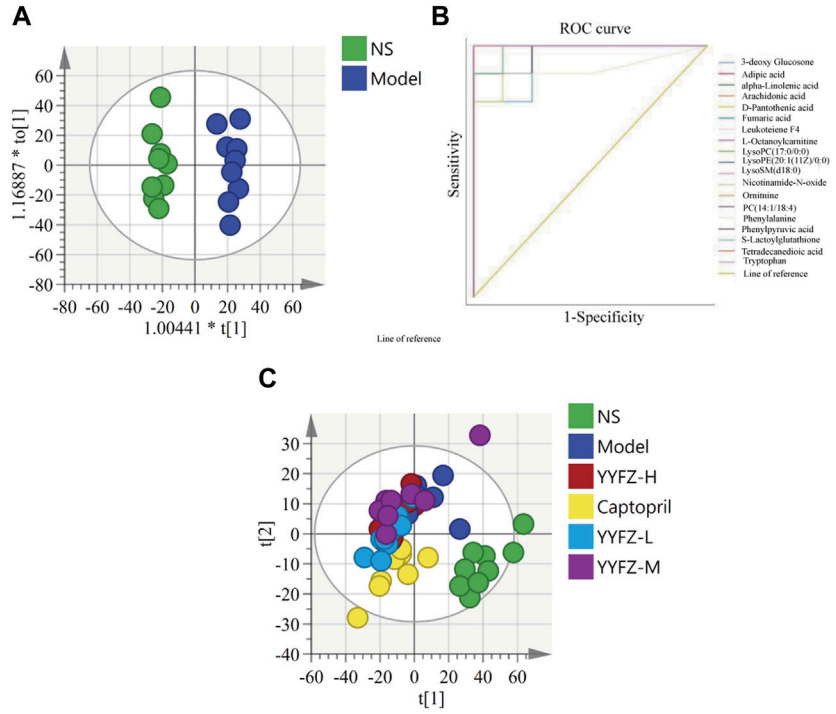

FIGURE 6
(A) OPLS-DA; **(B)** CHD marker ROC analysis **(C)** PCA.

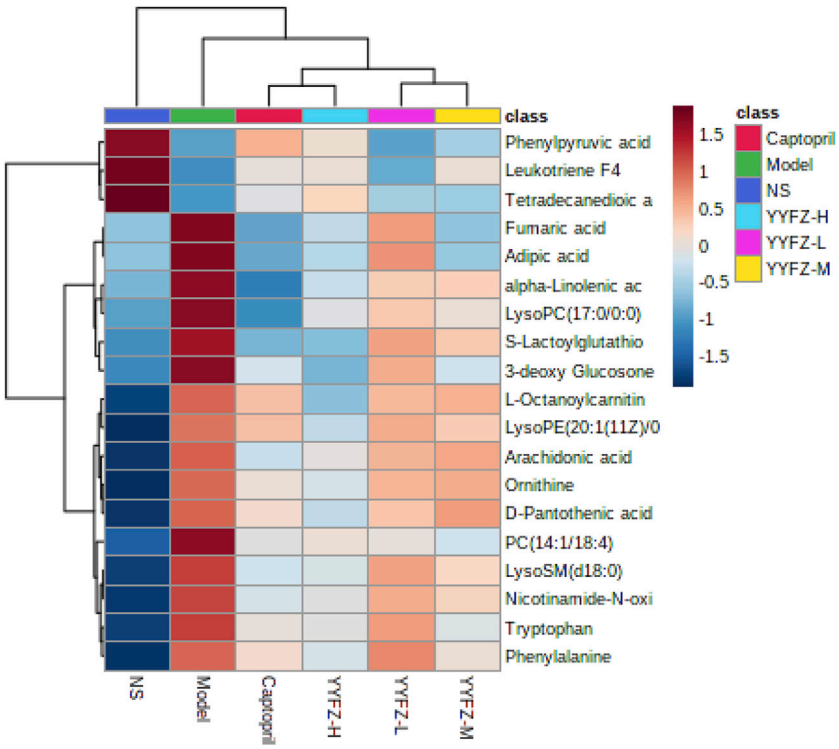

FIGURE 7
Heat map of serum metabolite changes from minimum (dark blue) to maximum (dark red) in NS, Model, YYFZ-H, YYFZ-M, YYFZ-L and Captopril groups.

TABLE 4 Differential metabolite information.

No.	tR/ min	Metabolite	Formula	Parent ion	Theoretical value	Measured value	ppm	Model/ NS	Captopril/ Model	YYFZ-H/ Model	YYFZ-M/ Model	YYFZ-L/ Model
1	5.47	Leukoteiene F4	$C_{28}H_{44}N_2O_8S$	M + K	607.2416	607.2443	4.45	↓**	↑*	↑*	↑*	↑
2	6.6	Arachidonic acid	$C_{20}H_{32}O_2$	M + K	343.2006	343.2029	6.70	↑**	↓**	↓*	↓*	↓
3	4.59	LysoSM(d18:0)	$C_{23}H_{51}N_2O_5P$	M + K	505.3174	505.3201	5.34	↑**	↓*	↓**	↓*	↓*
4	0.91	Tryptophan	$C_{11}H_{12}N_2O_2$	M + Na	227.0796	227.0784	−5.28	↑**	↓*	↓*	↓*	↓
5	0.89	Phenylpyruvic acid	$C_9H_8O_3$	M + H	165.0552	165.0547	−3.02	↓**	↑**	↑*	↑	↑
6	8.09	S-Lactoylglutathione	$C_{13}H_{21}N_3O_8S$	M + H	379.1049	379.1054	1.32	↑**	↓**	↓**	↓*	↓*
7	1.72	Phenylalanine	$C_9H_{11}NO_2$	M + H	166.0827	166.0831	2.41	↑**	↓*	↓**	↓*	↓*
8	3.09	Ornithine	$C_5H_{12}N_2O_2$	M + H	133.0991	133.0968	−17.28	↑**	↓*	↓*	↓*	↓
9	0.84	Nicotinamide-N-oxide	$C_6H_6N_2O_2$	M + Na	161.0359	161.0376	10.56	↑**	↓**	↓**	↓*	↓
10	6.79	Fumaric acid	$C_4H_4O_4$	M + Na	139.0007	139.0029	15.83	↑**	↓**	↓*	↓*	↓*
11	2.23	Adipic acid	$C_6H_{10}O_4$	M + H	147.0657	147.0636	−14.28	↑**	↓*	↓**	↓*	↓*
12	1.71	D-Pantothenic acid	$C_9H_{17}NO_5$	M + H	220.1144	220.1153	4.09	↑**	↓*	↓*	↓	↓
13	5.48	PC(14:1/18:4)	$C_{40}H_{70}NO_8P$	M + K	762.4469	762.4483	1.84	↑**	↓**	↓**	↓*	↓
14	6.06	Tetradecanedioic acid	$C_{14}H_{26}O_4$	M + K	297.1468	297.1501	11.11	↓**	↑*	↑**	↑*	↑*
15	5.89	3-deoxy Glucosone	$C_{27}H_{42}O_{11}$	M + Na	565.2661	565.2638	−4.69	↑**	↓*	↓*	↓*	↓
16	5.66	α-Linolenic acid	$C_{18}H_{30}O_2$	M + H	279.2324	279.2361	13.25	↑**	↓**	↓**	↓*	↓*
17	2.82	L-Octanoylcarnitine	$C_{15}H_{29}NO_4$	M + H	288.2169	288.2142	−9.37	↑**	↓*	↓*	↓*	↓
18	5.09	LysoPE(20:1(11Z)/0:0)	$C_{25}H_{50}NO_7P$	M + Na	530.3216	530.3247	5.84	↑**	↓*	↓*	↓*	↓*
19	6.11	LysoPC(17:0/0:0)	$C_{25}H_{52}NO_7P$	M + H	510.3641	510.3567	−14.5	↑**	↓*	↓**	↓*	↓

*p<0.05. **p<0.01.

10.3389/fmolb.2023.1203208

and the magnitude of the two values shows a correlation. In the present study, we observed the long axis of the sternum in rats and used EF as an indicator to determine the modeling status of rats and the effect of YYFZ treatment. We found that EF and FS were significantly retraced in the administered group, and there were some differences in the mean values of other functional indicators LVPW;s, LVPW;d, LVID;s, LVID;d, IVS;s, IVS;d, etc. Moreover, the cardiac index of rats in the YYFZ-H and YYFZ-M groups was lower than that of the model group, and ascites were also significantly reduced, suggesting that YYFZ could improve cardiac function and alleviate the symptoms of CHD in rats with CHD.

In this study, we used non-targeted metabolomics techniques to study serum metabolites in CHD rats and identified 19 CHD-related metabolites, seven of which were regulated by YYFZ including S-lactoylglutathione, phenylalanine, fumaric acid, adipic acid, tetradecanedioic acid, α-linolenic acid, and lysoPE (20:1(11Z)/0:0), and the metabolic pathways involved mainly include four categories: amino acid metabolism (phenylalanine, tyrosine and tryptophan biosynthesis; phenylalanine metabolism; arginine biosynthesis; alanine, aspartate and glutamate metabolism; arginine and proline metabolism; tryptophan metabolism; tyrosine metabolism), lipid metabolism (α-linolenic acid metabolism, arachidonic acid metabolism, biosynthesis of unsaturated fatty acids, glycerophospholipid metabolism), energy metabolism (pyruvate metabolism, pantothenate and CoA biosynthesis, citrate cycle (TCA cycle)), glutathione metabolism.

It has been confirmed that myocardial infarction and heart failure can lead to abnormalities in amino acid metabolism such as branched-chain amino acids, taurine or glutamine, and abnormalities in the metabolism of certain amino acids, such as branched-chain amino acids, can activate the mTOR signaling pathway, which accelerates myocardial remodeling and leads to the development of heart failure after myocardial infarction. In addition, elevated leucine levels may activate mTOR, and inhibition of mTOR in a heart failure model improves cardiac function. When mitochondrial dysfunction and phenylalanine are increased in the heart failure state, tetrahydrobiopterin consumption is increased, resulting in decreased nitric oxide production and causing heart failure (Nishijima et al., 2011; Hong et al., 2019). Phenylalanine may also be associated with increased aromatic amino acids, and increased protein breakdown in muscle and impaired liver function can cause accumulation of aromatic group amino acids. Dysregulation of the hepatic urea cycle can lead to a further increase in ornithine, a precursor to the formation of polyamines. Polyamines are also involved in the development of cardiac disease processes, and in models of myocardial hypertrophy (Chen et al., 2019). This further reflects the regulatory role of amino acid metabolism in heart failure, but the exact

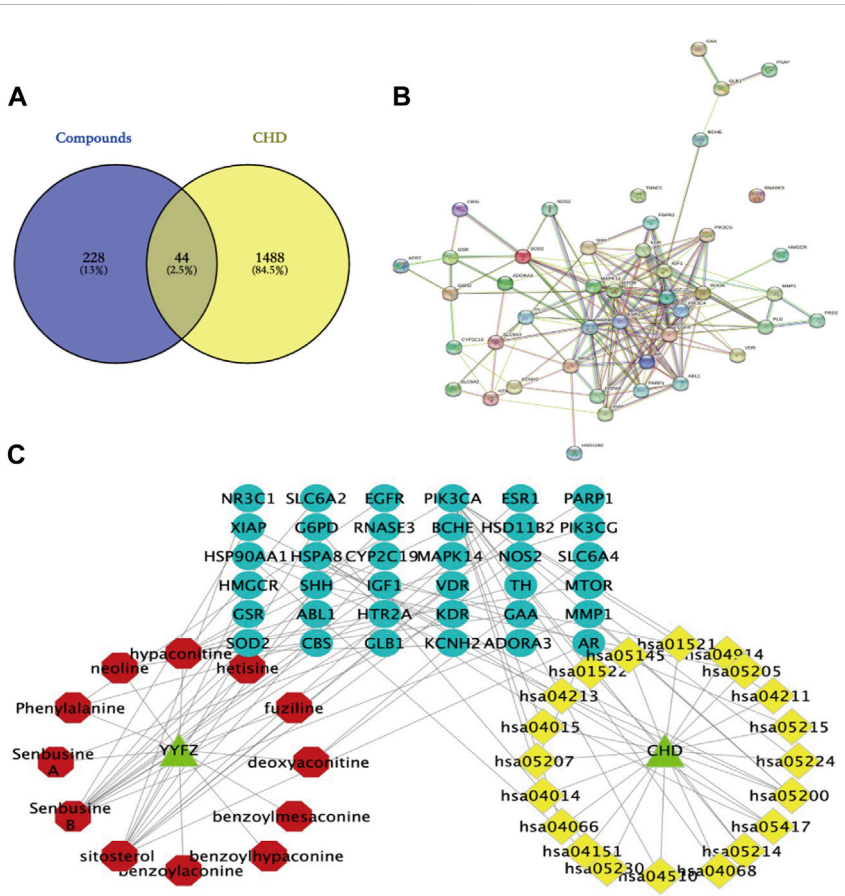

FIGURE 8
(A) Venn diagram of YYFZ component and CHD target; **(B)** PPI diagram; **(C)** Drug-active component-target network expressing the interaction between YYFZ inlet component, protein target and CHD pathway (red-inlet component, blue-target, yellow-pathway).

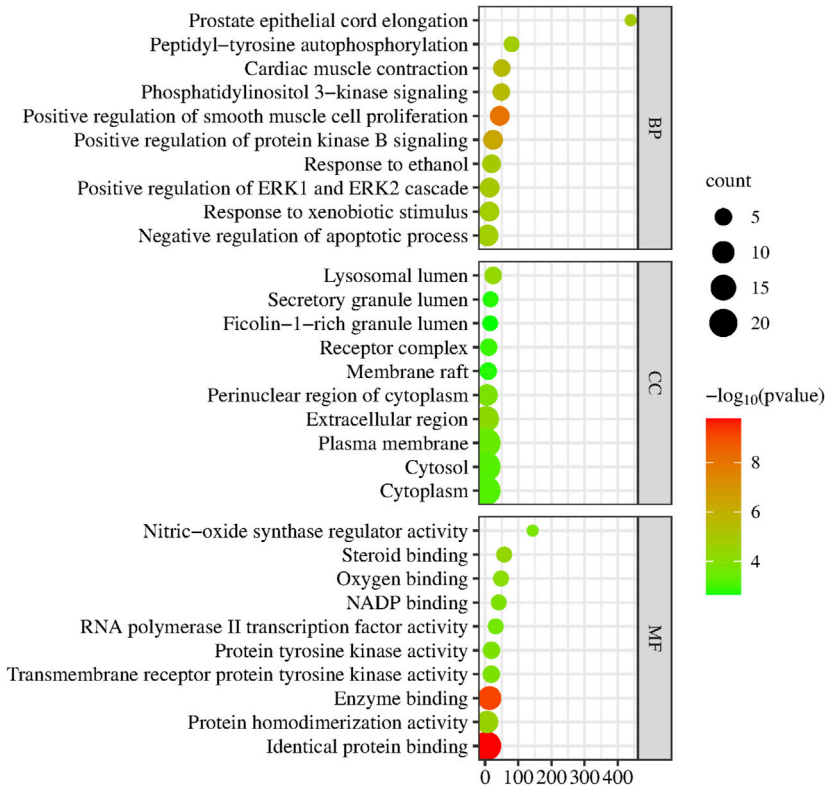

FIGURE 9
GO function enrichment map.

mechanisms still need to be investigated in depth (Wang et al., 2016; Dimou et al., 2022).

Disorders of lipid metabolism play an extremely important role in the process of CHD. It has been shown that patients with CHD often have abnormal lipid levels, and that disorders of lipid metabolism further contribute to the development of CHD. In this experiment, linoleic acid was significantly elevated in the model group compared to the blank group, and the molecular structure of linoleic acid contains double bonds that are susceptible to oxidative stress, causing vasodilator dysfunction and endothelial damage (Asselin et al., 2013; Djuricic and Calder, 2021). Phospholipids are the main constituent molecules of biological membrane structure and assist in the function of the organism at the cellular level. Arachidonic acid is a widely distributed unsaturated fatty acid in living organisms, and in pathological states, it is broken down into biologically active derivatives that are involved in inflammatory responses, apoptosis, and other biological processes (Sonnweber et al., 2018). Prostaglandins (PGs) are produced by the metabolism of arachidonic acid through the COX pathway and are further metabolized to produce a variety of active substances that regulate the process of vascular remodeling and generation and can control vascular tone and influence the course of CHD (Mitchell et al., 2021; Wan et al., 2021).

The heart is the organ of the body with the greatest energy demand, and the diastolic and contractile movements of the heart muscle depend on the energy produced by the cells. Under normal conditions, 60%–80% of the heart's energy is derived from fatty acid oxidation and 10%–20% from glucose metabolism. In contrast, when cardiac function is abnormal, the metabolic substrate is changed from glucose to fatty acids, resulting in increased levels of free fatty acids in serum and myocardial tissue. It has been shown that lipid deposition is observed in rat myocardium high in free fatty acids and that free fatty acids may contribute to impaired cardiac function via PI3K-Akt-GLUT4 and AMPK-eNOS pathways (Han et al., 2018). Acylcarnitine is mainly found in muscle tissues such as cardiac muscle and is involved in fatty acid metabolism and amino acid metabolism. Short-chain acylcarnitines are associated with branched-chain and aromatic amino acid metabolism, and the buildup of long-chain acylcarnitines results from impaired fatty acid oxidation (Roussel et al., 2015). One study found that acylcarnitine decreased in a guinea pig model of compensatory hypertrophy, while fatty acids gradually increased during the process. Long-chain acyl CoA dehydrogenase knockout mice were cardiac hypertrophy accompanied by elevated triglyceride levels, and after carnitine administration, triglyceride levels returned to normal in the myocardium of long-chain acyl CoA dehydrogenase knockout mice (Foster et al., 2016). The above suggests that amino acid metabolism, lipid metabolism and energy metabolism are closely related to the pathogenesis of CHD and that YYFZ acts to inhibit inflammation and reduce intravascular lipid accumulation by regressing lipid and amino acid metabolism.

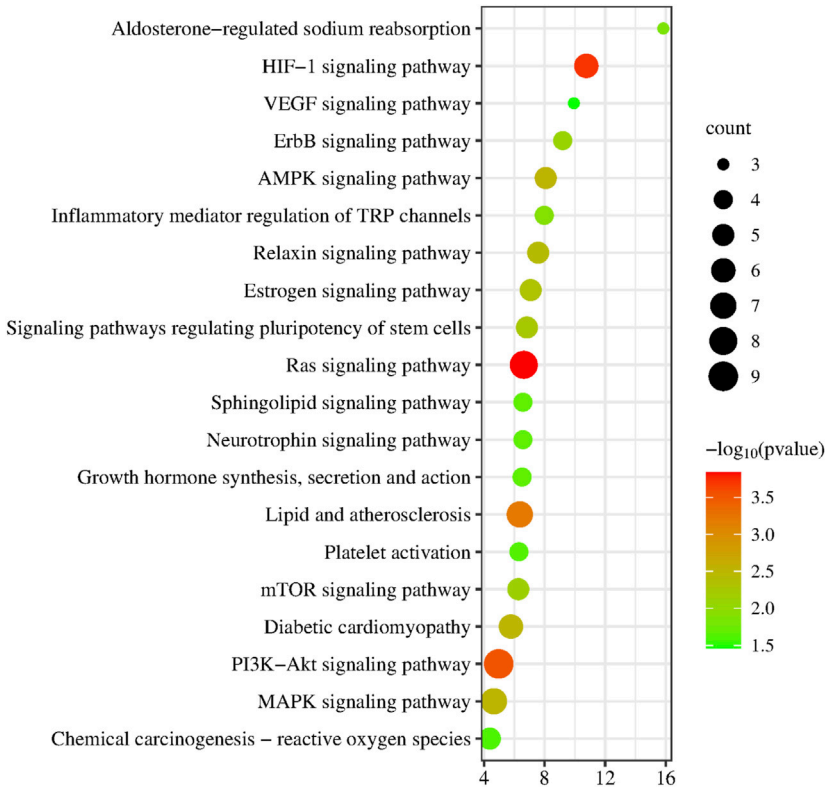

FIGURE 10
KEGG pathway enrichment analysis.

Hypaconitine, deoxyaconitine and senbusine B are all diterpenoid diester alkaloids with analgesic, anti-inflammatory and antipyretic effects (Zhang et al., 2022). YYFZ is composed of aconitum and Coicis seed. Aconitoid alkaloids in aconitum aconitine are the main active components of YYFZ, while aconitine alkaloids can be hydrolyzed under heating conditions. It is speculated that hypaconitine, deoxyaconitine and senbusine B are the hydrolyzed alkaloids that play a role. Sitosterol is the most abundant sterol in Coix seed, which can interfere with a variety of cell signaling pathways, including cell cycle, cell apoptosis, survival, invasion, proliferation, metastasis, anti-inflammatory, angiogenesis, and cardiac protection (Khan et al., 2022).MAPK14 (p38α), a member of the mitogen-activated protein kinase (MAPK) family, is the most abundant and well-characterized of the four isoforms of p38MAPK and plays a central role in the initiation of stress-activated pro-inflammatory responses (Cuenda and Rousseau, 2007). p38MAPK14 acts downstream on transcription factors and protein kinases to regulate cellular stress and inflammatory responses. It has been demonstrated that p38MAPK plays an important role in myocarditis and myocardial remodeling (Niu et al., 2017; Turner and Blythe, 2019). EGFR is a receptor-type tyrosine kinase, which is important for embryonic heart development and maintenance of adult heart function. EGFR signaling pathway is a complex network system, including three main pathways: Ras/Raf/MAPK pathway, PI3K/AKT pathway, JAK pathway, and STAT pathway (Iwamoto and Mekada, 2006). mTOR is an atypical serine/threonine protein kinase, which can participate in gene transcription and protein expression by phosphorylating its downstream target proteins, and then affect biological activities such as apoptosis. mTOR signaling pathway is one of the effective ways to treat heart failure (Shi et al., 2020). IGF1 is a key hormone that regulates the growth of cardiomyocytes and physiological cardiac hypertrophy. IGF1 is closely related to cardiac hypertrophy and heart failure. In cardiomyocytes, after IGF1 binds to its receptor, the receptor itself is phosphorylated and further activates the MAPK pathway and PI3K pathway (Tao et al., 2017). The Ras family of small guanosine triphosphate (GTP)-binding proteins (G proteins) is one of the major components of intracellular signaling required for normal heart growth and also plays a key role in the development of heart failure. Ras regulates multiple downstream signaling pathways mainly involving MAPK as well as the PI3K/Akt/mTOR pathway (Ramos-Kuri et al., 2021). Overactivation of the JNK and p38 signaling pathways play a key role in the CHD Ras can activate the JNK and p38 signaling pathways through the PI3K/AKT/mTOR pathway. The PI3K-Akt signaling pathway has an important role in the pathogenesis of heart disease, not only regulating the survival and function of cardiomyocytes, but also influencing the proliferation, migration, and apoptosis of vascular smooth muscle cells through the regulation of the pathogenesis and development of CHD (Magaye et al., 2021; Qin et al., 2021; Sun G. et al., 2021). These studies suggest that Ras/MEK/ERK and PI3K/Akt/mTOR signaling control the interconnection of several levels of protein

synthesis, cardiomyocyte growth, and remodeling. Ras and its downstream pathways (MAPK pathway, PI3K pathway) may be important pathways for CHD treatment by YYFZ.

5 Conclusion

In this study, the pharmacological effects and pharmacodynamic mechanisms of YYFZ in the treatment of adriamycin-induced CHD rats were investigated based on metabolomics combined with network pharmacology. The YYFZ group was able to improve the disorder of cardiomyocyte arrangement and reduce inflammatory cell infiltration, and the cardiac index of rats in the YYFZ-H and YYFZ-M groups was lower than that of the Model group, suggesting that YYFZ was able to improve the cardiac function and alleviate the symptoms of CHD in CHD rats. Metabolomics identified 19 biomarkers related to the pathogenesis of CHD, mainly involving the improvement of amino acid metabolic pathways, fatty acid metabolism, and energy metabolism. In addition, network pharmacology analysis showed that YYFZ may act through MAPK14, EGFR, HSP90AA1, MTOR, ESR1, IGF1, and other protein targets in the treatment of CHD. Combining the results of metabolomics and network pharmacology pathway enrichment analysis suggested that YYFZ may further regulate PI3K/Akt pathway and MAPK pathway by modulating amino acid metabolism and fatty acid metabolism. YYFZ, as a classical TCM formula, has been used to treat CHD from multiple links and targets.

Data availability statement

The raw data supporting the conclusion of this article will be made available by the authors, without undue reservation.

Ethics statement

The animal study was reviewed and approved by the Animal Ethics Committee of Tianjin University of Traditional Chinese Medicine.

Author contributions

YmW and XL conceived, designed the experiments. XL carried out the experiments and wrote the manuscript. MQ, XkL, FZ, YyW, JW, LS, and SF participated in the experiments. YfL and YbL reviewed and edited the manuscript. All authors contributed to the article and approved the submitted version.

Funding

This work was supported by the National Natural Science Foundation of China (No. 81903938) and Tianjin Development Program for Innovation.

Conflict of interest

Author MQ was employed by TIPRHUYA Advancing Innovative Medicines Ltd.

The remaining authors declare that the research was conducted in the absence of any commercial or financial relationships that could be construed as a potential conflict of interest.

Publisher's note

All claims expressed in this article are solely those of the authors and do not necessarily represent those of their affiliated organizations, or those of the publisher, the editors and the reviewers. Any product that may be evaluated in this article, or claim that may be made by its manufacturer, is not guaranteed or endorsed by the publisher.

Supplementary material

The Supplementary Material for this article can be found online at: https://www.frontiersin.org/articles/10.3389/fmolb.2023.1203208/full#supplementary-material

References

Amberger, J. S., and Hamosh, A. (2017). Searching online mendelian inheritance in man (OMIM): A knowledgebase of human genes and genetic phenotypes. *Curr. Protoc. Bioinforma.* 58, 1. doi:10.1002/cpbi.27-1.2.12

Asselin, C., Ducharme, A., Ntimbane, T., Ruiz, M., Fortier, A., Guertin, M. C., et al. (2013). Circulating levels of linoleic acid and HDL-cholesterol are major determinants of 4-hydroxynonenal protein adducts in patients with heart failure. *Redox Biol.* 2, 148–155. doi:10.1016/j.redox.2013.12.009

Buergel, T., Steinfeldt, J., Ruyoga, G., Pietzner, M., Bizzarri, D., Vojinovic, D., et al. (2022). Metabolomic profiles predict individual multidisease outcomes. *Metabolomic profiles predict Individ. multidisease outcomes* 28 (11), 2309–2320. doi:10.1038/s41591-022-01980-3

Chen, H. Y., Jia, X. L., Zhao, S. Q., Zheng, W. H., Mei, Z. G., Yang, H. W., et al. (2019). Dual role of polyamines in heart ischemia/reperfusion injury through regulation of mitochondrial permeability transition pore. *Sheng Li Xue Bao* 71 (5), 681–688. doi:10.13294/j.aps.2019.0057

Chen, X., Chen, Y., Xie, S., Wang, X., Wu, Y., Zhang, H., et al. (2022). The mechanism of Renshen-Fuzi herb pair for treating heart failure-Integrating a cardiovascular pharmacological assessment with serum metabolomics. *Front. Pharmacol.* 13, 995796. doi:10.3389/fphar.2022.995796

Cuenda, A., and Rousseau, S. (2007). p38 MAP-kinases pathway regulation, function and role in human diseases. *Biochim. Biophys. Acta* 1773 (8), 1358–1375. doi:10.1016/j.bbamcr.2007.03.010

Cui, H., Chen, Y., Li, K., Zhan, R., Zhao, M., Xu, Y., et al. (2021). Untargeted metabolomics identifies succinate as a biomarker and therapeutic target in aortic aneurysm and dissection. *Eur. Heart J.* 42 (42), 4373–4385. doi:10.1093/eurheartj/ehab605

Dimou, A., Tsimihodimos, V., and Bairaktari, E. (2022). The critical role of the branched chain amino acids (BCAAs) catabolism-regulating enzymes, branched-chain aminotransferase (BCAT) and branched-chain α-keto acid dehydrogenase (BCKD), in human pathophysiology. *Int. J. Mol. Sci.* 23 (7), 4022. doi:10.3390/ijms23074022

Djuricic, I., and Calder, P. C. (2021). Beneficial outcomes of omega-6 and omega-3 polyunsaturated fatty acids on human health: An update for 2021. *Nutrients* 13 (7), 2421. doi:10.3390/nu13072421

Du, Z. Y., Shu, Z. L., Li, C., Song, X. M., Ma, X. L., Liao, L. X., et al. (2021). Baoyuan decoction alleviates myocardial infarction through the regulation of metabolic dysfunction and the mitochondria-dependent caspase-9/3 pathway. *Acupunct. Herb. Med.* 1 (1), 49–58. doi:10.1097/hm9.0000000000000003

Foster, D. B., Liu, T., Kammers, K., O'Meally, R., Yang, N., Papanicolaou, K. N., et al. (2016). Integrated omic analysis of a Guinea pig model of heart failure and sudden cardiac death. *J. Proteome Res.* 15 (9), 3009–3028. doi:10.1021/acs.jproteome.6b00149

Han, L., Liu, J., Zhu, L., Tan, F., Qin, Y., Huang, H., et al. (2018). Free fatty acid can induce cardiac dysfunction and alter insulin signaling pathways in the heart. *Lipids Health Dis.* 17 (1), 185. doi:10.1186/s12944-018-0834-1

Hong, F. F., Liang, X. Y., Liu, W., Lv, S., He, S. J., Kuang, H. B., et al. (2019). Roles of eNOS in atherosclerosis treatment. *Inflamm. Res.* 68 (6), 429–441. doi:10.1007/s00011-019-01229-9

Ichiki, T., Huntley, B. K., and Burnett, J. C., Jr. (2013). BNP molecular forms and processing by the cardiac serine protease corin. *Adv. Clin. Chem.* 61, 1–31. doi:10.1016/b978-0-12-407680-8.00001-4

Iwamoto, R., and Mekada, E. (2006). ErbB and HB-EGF signaling in heart development and function. *Cell. Struct. Funct.* 31 (1), 1–14. doi:10.1247/csf.31.1

Khan, Z., Nath, N., Rauf, A., Emran, T. B., Mitra S, etc., Islam, F., et al. (2022). Multifunctional roles and pharmacological potential of β-sitosterol: Emerging evidence toward clinical applications. *Chem. Biol. Interact.* 365, 110117. doi:10.1016/j.cbi.2022.110117

Lee, H. C., Shiou, Y. L., Jhuo, S. J., Chang, C. Y., Liu, P. L., Jhuang, W. J., et al. (2019). The sodium-glucose co-transporter 2 inhibitor empagliflozin attenuates cardiac fibrosis and improves ventricular hemodynamics in hypertensive heart failure rats. *Cardiovasc Diabetol.* 18 (1), 45. doi:10.1186/s12933-019-0849-6

Leung, A. Y. L., Chen, H., Jia, Z., Li, X., and Shen, J. (2021). Study protocol: Traditional Chinese Medicine (TCM) syndrome differentiation for heart failure patients and its implication for long-term therapeutic outcomes of the Qiliqiangxin capsules. *Chin. Med.* 16 (1), 103. doi:10.1186/s13020-021-00515-1

Li, J., Guasch-Ferré, M., Chung, W., Ruiz-Canela, M., Toledo, E., Corella, D., et al. (2020). The Mediterranean diet, plasma metabolome, and cardiovascular disease risk. *Eur. Heart J.* 41 (28), 2645–2656. doi:10.1093/eurheartj/ehaa209

Li, L., Li, S. H., Jiang, J. P., Liu, C., and Ji, L. L. (2021). Investigating pharmacological mechanisms of andrographolide on non-alcoholic steatohepatitis (nash): A bioinformatics approach of network pharmacology. *Chin. Herb. Med.* 13 (3), 342–350. doi:10.1016/j.chmed.2021.05.001

Li, P., Chen, J., Zhang, W., Li, H., Wang, W., and Chen, J. (2019). Network pharmacology based investigation of the effects of herbal ingredients on the immune dysfunction in heart disease. *Pharmacol. Res.* 141, 104–113. doi:10.1016/j.phrs.2018.12.016

Liao, M., Xie, Q., Zhao, Y., Yang, C., Lin, C., Wang, G., et al. (2022). Main active components of Si-Miao-Yong-An decoction (SMYAD) attenuate autophagy and apoptosis via the PDE5A-AKT and TLR4-NOX4 pathways in isoproterenol (ISO)-induced heart failure models. *Pharmacol. Res.* 176, 106077. doi:10.1016/j.phrs.2022.106077

Liu, Y. J., Li, Z., Wang, X., Ni, T. Y., Ma, M., He, Y. Y., et al. (2022). Effects of adjuvant Chinese patent medicine therapy on major adverse cardiovascular events in patients with coronary heart disease angina pectoris: A population-based retrospective cohort study. *Acupunct. Herb. Med.* 2 (2), 109–117. doi:10.1097/hm9.0000000000000028

Magaye, R. R., Savira, F., Hua, Y., Xiong, X., Huang, L., Reid, C., et al. (2021). Attenuating PI3K/Akt-mTOR pathway reduces dihydrosphingosine 1 phosphate mediated collagen synthesis and hypertrophy in primary cardiac cells. *Int. J. Biochem. Cell. Biol.* 134, 105952. doi:10.1016/j.biocel.2021.105952

McDonald, K., Troughton, R., Dahlström, U., Dargie, H., Krum, H., van der Meer, P., et al. (2018). Daily home BNP monitoring in heart failure for prediction of impending clinical deterioration: Results from the HOME HF study. *Eur. J. Heart Fail* 20 (3), 474–480. doi:10.1002/ejhf.1053

Meng, H., Du, Z., Lu, W., Wang, Q., Sun, X., Jiang, Y., et al. (2021). Baoyuan decoction (BYD) attenuates cardiac hypertrophy through ANKRD1-ERK/GATA4 pathway in heart failure after acute myocardial infarction. *Phytomedicine* 89, 153617. doi:10.1016/j.phymed.2021.153617

Mitchell, J. A., Kirkby, N. S., Ahmetaj-Shala, B., Armstrong, P. C., Crescente, M., Ferreira, P., et al. (2021). Cyclooxygenases and the cardiovascular system. *Pharmacol. Ther.* 217, 107624. doi:10.1016/j.pharmthera.2020.107624

Ni, C., Li, B., Ding, Y., Wu, Y., Wang, Q., Wang, J., et al. (2021). Anti-cancer properties of coix seed oil against HT-29 colon cells through regulation of the PI3K/AKT signaling pathway. *Foods* 10 (11), 2833. doi:10.3390/foods10112833

Nicholson, J. K. (2021). Molecular phenomic approaches to deconvolving the systemic effects of SARS-CoV-2 infection and post-acute COVID-19 syndrome. *Phenomics* 1 (4), 143–150. doi:10.1007/s43657-021-00020-3

Nishijima, Y., Sridhar, A., Bonilla, I., Velayutham, M., Khan, M., Terentyeva, R., et al. (2011). Tetrahydrobiopterin depletion and NOS2 uncoupling contribute to heart failure-induced alterations in atrial electrophysiology. *Cardiovasc Res.* 91 (1), 71–79. doi:10.1093/cvr/cvr087

Niu, L., Li, C., Wang, Z., Xu, H., and An, X. (2017). Effects of the MAPK pathway and the expression of CAR in a murine model of viral myocarditis. *Exp. Ther. Med.* 13 (1), 230–234. doi:10.3892/etm.2016.3909

Qin, W., Cao, L., and Massey, I. Y. (2021). Role of PI3K/Akt signaling pathway in cardiac fibrosis. *Mol. Cell. Biochem.* 476 (11), 4045–4059. doi:10.1007/s11010-021-04219-w

Quagliariello, V., De Laurentiis, M., Rea, D., Barbieri, A., Monti, M. G., Carbone, A., et al. (2021). The SGLT-2 inhibitor empagliflozin improves myocardial strain, reduces cardiac fibrosis and pro-inflammatory cytokines in non-diabetic mice treated with doxorubicin. *Cardiovasc Diabetol.* 20 (1), 150. doi:10.1186/s12933-021-01346-y

Ramos-Kuri, M., Meka, S. H., Salamanca-Buentello, F., Hajjar, R. J., Lipskaia, L., and Chemaly, E. R. (2021). Molecules linked to Ras signaling as therapeutic targets in cardiac pathologies. *Biol. Res.* 4 (1), 23. doi:10.1186/s40659-021-00342-6

Reina-Couto, M., Pereira-Terra, P., Quelhas-Santos, J., Silva-Pereira, C., Albino-Teixeira, A., and Sousa, T. (2021). Inflammation in human heart failure: Major mediators and therapeutic targets. *Front. Physiol.* 12, 746494. doi:10.3389/fphys.2021.746494

Roger, V. L. (2021). Epidemiology of heart failure: A contemporary perspective. *Circ. Res.* 128 (10), 1421–1434. doi:10.1161/CIRCRESAHA.121.318172

Rørth, R., Jhund, P. S., Yilmaz, M. B., Kristensen, S. L., Welsh, P., Desai, A. S., et al. (2020). Comparison of BNP and NT-proBNP in patients with heart failure and reduced ejection fraction. *Circ. Heart Fail* 13 (2), e006541. doi:10.1161/CIRCHEARTFAILURE.119.006541

Roussel, J., Thireau, J., Brenner, C., Saint, N., Scheuermann, V., Lacampagne, A., et al. (2015). Palmitoyl-carnitine increases RyR2 oxidation and sarcoplasmic reticulum Ca2+ leak in cardiomyocytes: Role of adenine nucleotide translocase. *Biochim. Biophys. Acta* 1852 (5), 749–758. doi:10.1016/j.bbadis.2015.01.011

Sabatino, J., De Rosa, S., Tammè, L., Iaconetti, C., Sorrentino, S., Polimeni, A., et al. (2020). Empagliflozin prevents doxorubicin-induced myocardial dysfunction. *Cardiovasc Diabetol.* 19 (1), 66. doi:10.1186/s12933-020-01040-5

Santos-Gallego, C. G., Mayr, M., and Badimon, J. (2022). SGLT2 inhibitors in heart failure: Targeted metabolomics and energetic metabolism. *Circulation* 146 (11), 819–821. doi:10.1161/CIRCULATIONAHA.122.060805

Shi, B., Huang, Y., Ni, J., Chen, J., Wei, J., Gao, H., et al. (2020). Qi Dan Li Xin pill improves chronic heart failure by regulating mTOR/p70S6k-mediated autophagy and inhibiting apoptosis. *Sci. Rep.* 10 (1), 6105. doi:10.1038/s41598-020-63090-9

Shi, D., Liu, L., Li, H., Pan, D., Yao, X., Xiao, W., et al. (2022). Identifying the molecular basis of Jinhong tablets against chronic superficial gastritis via chemical profile identification and symptom-guided network pharmacology analysis. *J. Pharm. Anal.* 12 (1), 65–76. doi:10.1016/j.jpha.2021.01.005

Sonnweber, T., Pizzini, A., Nairz, M., Weiss, G., and Tancevski, I. (2018). Arachidonic acid metabolites in cardiovascular and metabolic diseases. *Int. J. Mol. Sci.* 19 (11), 3285. doi:10.3390/ijms19113285

Sui, Y., and Xu, D. (2022). Isolation and identification of anti-inflammatory and analgesic polysaccharides from Coix seed (Coix lacryma-jobi L.var. Ma-yuen (Roman) Stapf). *Nat. Prod. Res.* 30, 1–10. doi:10.1080/14786419.2022.2162896

Sun, C., Zeng, G., Wang, T., Ren, H., An, H., Lian, C., et al. (2021). Astragaloside IV ameliorates myocardial infarction induced apoptosis and restores cardiac function. *Front. Cell. Dev. Biol.* 9, 671255. doi:10.3389/fcell.2021.671255

Sun, G., Li, X., Wei, J., Zhang, T., Li, B., Chen, M., et al. (2021). Pharmacodynamic substances in Salvia miltiorrhiza for prevention and treatment of hyperlipidemia and coronary heart disease based on lipidomics technology and network pharmacology analysis. *Biomed. Pharmacother.* 141, 111846. doi:10.1016/j.biopha.2021.111846

Szabo, T. M., Frigy, A., and Nagy, E. E. (2021). Targeting mediators of inflammation in heart failure: A short synthesis of experimental and clinical results. *Int. J. Mol. Sci.* 22 (23), 13053. doi:10.3390/ijms222313053

Tai, C. J., El-Shazly, M., Yang, Y. H., Tsai, Y. H., Csupor, D., Hohmann, J., et al. (2022). The effectiveness of Fuzi in combination with routine heart failure treatment on chronic heart failure patients. *J. Ethnopharmacol.* 289, 115040. doi:10.1016/j.jep.2022.115040

Tao, L., Jia, L., Li, Y., Song, C., and Chen, Z. (2017). Recent advances of adapter proteins in the regulation of heart diseases. *Heart Fail Rev.* 22 (1), 99–107. doi:10.1007/s10741-016-9582-3

Tsutsui, H. (2022). Recent advances in the pharmacological therapy of chronic heart failure: Evidence and guidelines. *Pharmacol. Ther.* 238, 108185. doi:10.1016/j.pharmthera.2022.108185

Turner, N. A., and Blythe, N. M. (2019). Cardiac fibroblast p38 MAPK: A critical regulator of myocardial remodeling. *J. Cardiovasc Dev. Dis.* 6 (3), 27. doi:10.3390/jcdd6030027

UniProt Consortium (2013). Activities at the universal protein resource (UniProt). *Nucleic Acids Res.* 42, D191–D198. doi:10.1093/nar/gkt1140

Wan, Q., Kong, D., Liu, Q., Guo, S., Wang, C., Zhao, Y., et al. (2021). Congestive heart failure in COX2 deficient rats. *Sci. China Life Sci.* 64 (7), 1068–1076. doi:10.1007/s11427-020-1792-5

Wang, H., Yin, H., Zhong, Y., Hu, J., Xia, S., Wang, Z., et al. (2022). Polysaccharides from fermented coix seed modulates circulating nitrogen and immune function by altering gut microbiota. *Curr. Res. Food Sci.* 5, 1994–2003. doi:10.1016/j.crfs.2022.10.007

Wang, W., Zhang, F., Xia, Y., Zhao, S., Yan, W., Wang, H., et al. (2016). Defective branched chain amino acid catabolism contributes to cardiac dysfunction and remodeling following myocardial infarction. *Am. J. Physiol. Heart Circ. Physiol.* 311 (5), H1160–H1169. doi:10.1152/ajpheart.00114.2016

Wang, X., Simayi, A., Fu, J., Zhao, X., and Xu, G. (2022). Resveratrol mediates the miR-149/HMGB1 axis and regulates the ferroptosis pathway to protect myocardium in endotoxemia mice. *Am. J. Physiol. Endocrinol. Metab.* 323 (1), E21–E32. doi:10.1152/ajpendo.00227.2021

Wang, Y., Zhang, S., Li, F., Zhou, Y., Zhang, Y., Wang, Z., et al. (2020). Therapeutic target database 2020: Enriched resource for facilitating research and early development of targeted therapeutics. *Nucleic Acids Res.* 48 (1), D1031–D1041. doi:10.1093/nar/gkz981

Xu, L., He, D., Wu, Y., Shen, L., Wang, Y., and Xu, Y. (2022). Tanshinone IIA inhibits cardiomyocyte apoptosis and rescues cardiac function during doxorubicin-induced cardiotoxicity by activating the DAXX/MEK/ERK1/2 pathway. *Phytomedicine* 107, 154471. doi:10.1016/j.phymed.2022.154471

Yan, P., Mao, W., Jin, L., Fang, M., Liu, X., Lang, J., et al. (2020). Crude radix aconiti lateralis preparata (Fuzi) with Glycyrrhiza reduces inflammation and ventricular remodeling in mice through the TLR4/NF-κB pathway. *Mediat. Inflamm.* 2020, 5270508. doi:10.1155/2020/5270508

Yang, J., Liu, Y., Lu, S., Sun, X., Yin, Y., Wang, K., et al. (2022). Coix seed oil regulates mitochondrial functional damage to induce apoptosis of human pancreatic cancer cells via the PTEN/PI3K/AKT signaling pathway. *Mol. Biol. Rep.* 9 (7), 5897–5909. doi:10.1007/s11033-022-07371-8

Yao, Y. X., Xu, Y. L., Liu, B. W., Yang, H., Li, S. Y., Zhazo, L. L., et al. (2020). Identification and verification of effective components of Huanghuai for dysfunctional uterine bleeding based on network pharmacology and molecular docking. *Chin. Herb. Med.* 13 (2), 177–188. doi:10.1016/j.chmed.2020.08.003

Younis, N. N., Salama, A., Shaheen, M. A., and Eissa, R. G. (2021). Pachymic acid attenuated doxorubicin-induced heart failure by suppressing miR-24 and preserving cardiac junctophilin-2 in rats. *Int. J. Mol. Sci.* 22 (19), 10710. doi:10.3390/ijms221910710

Zeng, Z., Wang, Q., Yang, X., Ren, Y., Jiao, S., Zhu, Q., et al. (2019). Qishen granule attenuates cardiac fibrosis by regulating TGF-β/Smad3 and GSK-3β pathway. *Phytomedicine* 62, 152949. doi:10.1016/j.phymed.2019.152949

Zhang, J., Li, D., Zhong, D., Zhou, Q., Yin, Y., Gao, J., et al. (2022). Processed lateral root of aconitum carmichaelii debx.: A review of cardiotonic effects and cardiotoxicity on molecular mechanisms. *Front. Pharmacol.* 13, 1026219. doi:10.3389/fphar.2022.1026219

Zhang, L., Lu, X., Wang, J., Li, P., Li, H., Wei, S., et al. (2017). Zingiberis rhizoma mediated enhancement of the pharmacological effect of aconiti lateralis radix praeparata against acute heart failure and the underlying biological mechanisms. *Biomed. Pharmacother.* 96, 246–255. doi:10.1016/j.biopha.2017.09.145

Zhong, Y., Chen, L., Li, M., Chen, L., Qian, Y., Chen, C., et al. (2022). Dangshen erling decoction ameliorates myocardial hypertrophy via inhibiting myocardial inflammation. *Front. Pharmacol.* 12, 725186. doi:10.3389/fphar.2021.725186

Zhou, J., Qian, M., Li, C., Zhou, W., Yao, L., Chen, Y., et al. (2022). Metabolomics and integrated network pharmacology analysis reveal that ginkgolides act as potential active anticancer components by regulating one-carbon metabolism. *J. Ethnopharmacol.* 298, 115609. doi:10.1016/j.jep.2022.115609

Zhou, Q., Yu, R., Liu, T., Li, Y., Zhong, J., Zhang, T., et al. (2021). Coix seed diet ameliorates immune function disorders in experimental colitis mice. *Nutrients* 14 (1), 123. doi:10.3390/nu14010123

frontiers | Frontiers in Molecular Biosciences

TYPE Mini Review
PUBLISHED 04 August 2023
DOI 10.3389/fmolb.2023.1230282

OPEN ACCESS

EDITED BY
Michael Anton Witting,
Helmholtz Association of German Research Centres (HZ), Germany

REVIEWED BY
Maria Monge,
Consejo Nacional de Investigaciones Científicas y Técnicas, Argentina
Giuseppe Paglia,
University of Milano Bicocca, Italy

*CORRESPONDENCE
Karl Burgess,
karl.burgess@ed.ac.uk

RECEIVED 28 May 2023
ACCEPTED 27 July 2023
PUBLISHED 04 August 2023

CITATION
Moses T and Burgess K (2023), Right in two: capabilities of ion mobility spectrometry for untargeted metabolomics. *Front. Mol. Biosci.* 10:1230282. doi: 10.3389/fmolb.2023.1230282

Right in two: capabilities of ion mobility spectrometry for untargeted metabolomics

Tessa Moses[1] and Karl Burgess[2]*

[1]EdinOmics, RRID:SCR_021838, University of Edinburgh, Max Born Crescent, Edinburgh, United Kingdom, [2]Institute of Quantitative Biology, Biochemistry and Biotechnology, School of Biological Sciences, University of Edinburgh, Edinburgh, United Kingdom

This mini review focuses on the opportunities provided by current and emerging separation techniques for mass spectrometry metabolomics. The purpose of separation technologies in metabolomics is primarily to reduce complexity of the heterogeneous systems studied, and to provide concentration enrichment by increasing sensitivity towards the quantification of low abundance metabolites. For this reason, a wide variety of separation systems, from column chemistries to solvent compositions and multidimensional separations, have been applied in the field. Multidimensional separations are a common method in both proteomics applications and gas chromatography mass spectrometry, allowing orthogonal separations to further reduce analytical complexity and expand peak capacity. These applications contribute to exponential increases in run times concomitant with first dimension fractionation followed by second dimension separations. Multidimensional liquid chromatography to increase peak capacity in metabolomics, when compared to the potential of running additional samples or replicates and increasing statistical confidence, mean that uptake of these methods has been minimal. In contrast, in the last 15 years there have been significant advances in the resolution and sensitivity of ion mobility spectrometry, to the point where high-resolution separation of analytes based on their collision cross section approaches chromatographic separation, with minimal loss in sensitivity. Additionally, ion mobility separations can be performed on a chromatographic timescale with little reduction in instrument duty cycle. In this review, we compare ion mobility separation to liquid chromatographic separation, highlight the history of the use of ion mobility separations in metabolomics, outline the current state-of-the-art in the field, and discuss the future outlook of the technology. "Where there is one, you're bound to divide it. Right in two", James Maynard Keenan.

KEYWORDS

chromatography, separation, drift time, drift tube, travelling wave, trapped, high-field asymmetric

1 Introduction

Global untargeted metabolomics aims at facilitating our understanding of the dynamics of the chemical composition of biological systems. Metabolites in heterogenous systems are chemically diverse and vary in their abundances, with many endogenous metabolites existing at very low concentrations. The primary goal of metabolomics is the unbiased relative quantification of each metabolite in a biological

system. For comprehensive metabolite coverage of biological systems to be successful, multiple separation techniques are needed.

In this review, we outline the principles of separation systems as applied to mass spectrometry based metabolomics. We focus on the capabilities of the increasingly commonly used technique of ion mobility, hyphenated (or not) to liquid chromatography. We evaluate the current state-of-the-art of ion mobility metabolomics in its various guises and provide a forward-looking summary of where we can expect the technology to move in future.

2 Liquid chromatography

The term liquid chromatography was originally described by Michael Tswett in 1906 (Tswett, 1968). The method initially used to separate plant pigments (hence the name) has now become a powerful and ubiquitous technique routinely applied to separate and purify complex mixtures of molecules. Briefly, analytes are dissolved in a solvent and then passed through a column filled with a stationary phase. The stationary phase can be made of various materials, such as silica or polymer beads, which are packed uniformly into the column. As the analytes pass through the column, different molecules interact with the stationary phase, depending on their physicochemical properties. This interaction causes the molecules to separate and travel through the column at different rates, creating peaks.

There are many different stationary phases, allowing separations to be tailored depending on the particular characteristics of the analytes in question. A detailed analysis of stationary phases is beyond the scope of this article, and there are already many excellent reviews on the subject (Zou et al., 2002; Zhang, 2008; West et al., 2010; Sobańska, 2021), but the most commonly applicable phases in metabolomics in general are reversed phase (RP, which separates on the basis of hydrophobicity) and hydrophilic interaction liquid chromatography (HILIC, which separates on the basis of hydrophilicity).

2.1 Advantages of liquid chromatography separation

While there have been many excellent studies in the metabolomics discipline conducted using direct infusion mass spectrometry (Maleki et al., 2018; Dou et al., 2023; Sun et al., 2023; Wolthuis et al., 2023) and flow injection mass spectrometry (Zang et al., 2018), chromatographic separations are commonly hyphenated to mass spectrometry. This coupling adds a further dimension of separation, beyond mass spectrometry itself, which in essence is a separation.

The main aim of applying chromatographic separations up-front of a mass spectral analysis is to reduce the complexity of highly complex biological samples, in an effort to ameliorate the effects of dynamic range (Want et al., 2005) and ion suppression (Furey et al., 2013). Furthermore, chromatography provides a very valuable concentration of each analyte as it leaves the column as a peak, substantially improving its signal-to-noise ratio and making it more likely to be detected and quantified, as opposed to direct infusion mass spectrometry.

2.2 Limitations of liquid chromatography for global metabolomics

One of the main limitations of chromatography is its lack of reproducibility and its heavy reliance on a few common stationary phases. Reversed-phase chromatography, for example, is now the most well-developed and ubiquitous separation medium in analytical chromatography, and rather than use a different column, it is common to use ion-pairing reagents to adapt the chemistry of an analyte to a reversed-phase system (Gong, 2015). Unfortunately, the vast majority of ion-pairing reagents are not mass spectrometry compatible, comprising (as many do) inorganic salts or highly ionizable organic compounds in millimolar concentrations that overwhelm the detection of less abundant endogenous compounds in the system being studied. Various powerful metabolomics methods exploit these properties to perform more targeted analyses, but for broad-based untargeted metabolomics, analysts are typically limited to RP or HILIC with volatile organic acids, bases and salts used as separation systems. Thus, a major limitation of liquid chromatography, as applied to mass spectrometry is that the separation gradient is responsible for much of the selectivity of the system, which can lead to situations where global separations are poorly suited to the separation of closely related compounds.

3 Ion mobility spectrometry

Ion mobility spectrometry (IMS), also known as gaseous electrophoresis, plasma chromatography (Revercomb and Mason, 1975), or ion chromatography (Helden et al., 1995), is an electrophoretic technique that separates ions based on their mobility in gas phase when subjected to an electric field. Traditional IMS measurements determine the drift velocities of gaseous ions in a weak electric field at a constant temperature. The applied electrical field accelerates ions through the drift region, which is counteracted by the drift gas that impedes ion progress. The speed of ion movement or drift velocity (v_d) is therefore proportional to the strength of the applied electric field (E), with mobility (K) of the ion being the constant of proportionality. The mobility of an ion is determined by its shape, size, and charge in the given drift gas. As a result, ions traverse the drift region at a velocity that is proportional to the inverse of their collision cross section (CCS), a physical property that reflects the geometric shape of the ion in the specific gas (Borsdorf and Eiceman, 2006). More compact structural conformations undergo fewer collisions with the drift gas and therefore have smaller CCS values, than extended planar structures. Thus, the CCS feature provides insight into the overall shape of the molecule, while ion mobility allows rapid separation of mixtures, including isobaric ions, typically within milliseconds.

3.1 Types of ion mobility spectrometry

There are four major types of ion mobility spectrometry (Figure 1). The most common and oldest ion mobility analysers consist of a drift tube containing an inert gas, typically dubbed ‘drift tube ion mobility spectrometry or DTIMS’ (Kirk et al., 2019), as

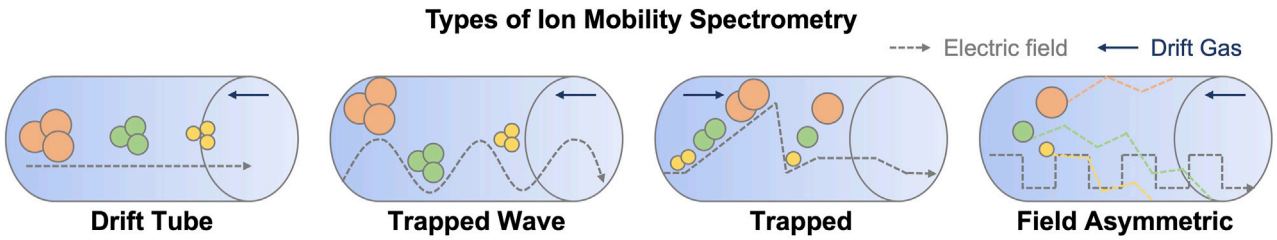

FIGURE 1
Schematic representation of the different types of ion mobility and the principles of separation. The direction of drift gas flow and electric field are indicated with dark blue and grey arrows, respectively.

described above. Travelling wave ion mobility spectrometry (TWIMS) is a more recent modification of the traditional drift tube on similar hardware, with the addition of an electrostatic pulse waveform that propagates along the tube, allowing nonlinear resolution of ions at the expense of ion heating (Shvartsburg and Smith, 2008). Ion heating is one of the more significant limitations of TWIMS as ion temperatures can reach 551–774 K (Merenbloom et al., 2012) and can lead to dissociation in small molecules (Morsa et al., 2011). More recent developments in this technology include structures for lossless ion manipulation (SLIM) and cyclic ion mobility (Giles et al., 2019). The SLIM architecture consists of a sandwich structure, with parallel, mirror image electrode arrays that can be configured for either conventional or travelling wave ion mobility (Ibrahim et al., 2017). Currently, available commercial instruments based on the technology configure the system in a serpentine array, significantly extending the ion mobility path length to a total of 13 m utilizing 44 U-turns. Resolving power varies depending on the configuration of the ion optics and the voltages applied, but resolutions of around 300 are available (May et al., 2021). The cyclic IMS instrument incorporates a doughnut-shaped cyclic ion mobility (cIM) device that allows ions to be separated via a user-designated number of repetitive 98 cm paths. The drawback to the instrument is that faster, lighter ions eventually end up 'lapping' slower ones, and to this end the instrument brackets the cIM with ion traps, allowing isolation and selection of pre-and post-separation ions. This allows some unprecedented and complex ion mobility experiments, such as the one described by (Sisley et al., 2020), to be performed.

Another type of ion mobility analyser is high-field asymmetric ion mobility spectrometry (FAIMS). This relies on the use of a changing compensation voltage as a filter across a gas flow counter to the direction of the ions. FAIMS was originally published by Buryakov et al. (1993), and has since found its way into several commercial instruments. It is generally employed as a filter (Canterbury et al., 2008), rather than a separation device and has therefore been sparsely used in liquid chromatography coupled to ion mobility multidimensional separations.

Recently, the Park group introduced the trapped ion mobility spectrometry (TIMS) device (Ridgeway et al., 2016). Unlike the previous systems, in TIMS the ions are held in a trapping device and exposed to a moving column of gas, based typically on a modification of ion funnel technology. This trap and release substantially reduce the dimensions of the ion mobility device. Ions are separated based on their physicochemical properties as in conventional drift tube ion mobility, however, the movement of the gas and ions are reversed. In TIMS, ramping the electric field gradient (E) releases ions in descending order of their mobility (K). For an excellent review of TIMS, see (Ridgeway et al., 2018). Parallel accumulation, serial fragmentation (PASEF) is an experimental methodology available on TIMS instruments that uses the unique capabilities of the ion mobility trapping device to accumulate ions, and then sequentially pulse them into a quadrupole for isolation and fragmentation (Meier et al., 2018). Thus, in a single drift spectrum, fragment patterns for each MSMS spectrum are resolved via ion mobility. This dramatically increases the acquisition rate of data dependent acquisition experiments (Meier et al., 2015). It has recently been modified to support data-independent acquisition (dia-PASEF) for proteomics applications (Demichev et al., 2022), which provides an intriguing possibility for improving metabolomics analysis.

3.2 Advantages of ion mobility as a separation technology

Regardless of the specific type of ion mobility device, there are two main advantages of ion mobility spectrometry. Firstly, it allows the separation of isomeric analytes. As discussed in Section 2.2, one of the major limitations of chromatography is that while an optimal liquid chromatography gradient can separate closely related ions, the generally applicable rapid gradients used with untargeted analysis often preclude the separation of isomeric compounds with closely related structures. While this is an issue for chromatography, modern ion mobility instruments with resolutions greater than 100 can now separate many isomeric ions within milliseconds. By coupling ion mobility to chromatography, multidimensional separation can be performed, allowing unprecedented resolution of complex mixtures without extending separation times or employing complex fractionation strategies.

Similar to the first, the second advantage of ion mobility comes from the modern high-resolution IM instruments. Collisional cross section is a fundamental property of an ion, and it can therefore be calculated with greater accuracy than predicting retention times on columns. While ion mobility devices measure 'drift times' rather than CCS directly, all modern instruments can calculate CCS from drift times, and this directly addresses one of the biggest challenges in metabolomics—the unambiguous identification of metabolites.

This latter poses an important challenge for the application of IMS to metabolomics. CCSs are able to be determined from experimental parameters via the Mason-Schamp equation (Siems et al., 2012) in DTIMS instruments, while for other types of IMS, calibration standards with known CCS values (derived from DTIMS experiments) must be used (Dodds and Baker, 2019). In practice, even on DTIMS instruments, a typical use for metabolomics, e.g., single field multiplexed analysis, require calibration standards derived from slower, more complex stepped-field methodologies (Dodds and Baker, 2019). Due to the development of large-scale, experimentally determined libraries (Zheng et al., 2017; Picache et al., 2019), as well as appropriate calibration, CCS features provide an additional criterion for metabolite annotation.

3.3 Limitations of ion mobility

Sensitivity has been the perennial issue with ion mobility mass spectrometry. In standard ion mobility analysis, analytes are introduced to the ion mobility device as a packet, followed by ion separation and concomitant detection in the mass spectrometer. Before the next packet of ions can be introduced to the ion mobility device, the slowest ion in the current packet must pass through and exit the IM device. This means that during ion mobility separation, all ions that would otherwise be analysed are lost. Furthermore, due to imperfect electronics, ions of interest can also be lost during the ion mobility separation itself. There have been many attempts to improve sensitivity, such as improving overall instrument design as outlined in 3.1 (Deng et al., 2016), advances in the construction of the instrument with improved lens designs and electric field generation, and the use of multiplexing. Multiplexing is a technique used to decrease ion packet losses in ion mobility mass spectrometry. Multiple ion packets are pulsed into a single ion mobility device in a pseudo-random order. This creates a patterning effect in the ion mobility analysis that can be deconvoluted by the use of a sliding window algorithm during data analysis. This technique has been reported to reduce sensitivity losses from 99% to 50% (Reinecke et al., 2019).

Current, commercially available ion mobility instruments possess resolving power in the hundreds, compared to the tens of thousands of theoretical plates typical in chromatography (for a fascinating discussion on the relationship between resolution parameters for chromatography and spectrometry see (Rokushika et al., 1985)). Consequently, reproducibility is a key parameter to confidently assign collisional cross sections to analytes. Interlaboratory studies have been performed, demonstrating RSDs of 0.14% and ~1.5% in TWIMS-based devices (Hernández-Mesa et al., 2020; Righetti et al., 2020) and 0.29% for DTIMS-based devices (Stow et al., 2017), which compares favourably to chromatography retention time RSD of 5%–20% depending on analyte (Madji Hounoum et al., 2015).

A further limitation to ion mobility is that it does not get around the problem of matrix effect, a somewhat complex term in 'omics disciplines, particularly metabolomics. Typically, the "matrix" corresponds to all of the components of a sample one does not want to analyse, while the "analytes" are the components one wants to detect. While all sample preparation methodologies are biased, a good 'targeted' analysis aims to strip out the vast majority of the "matrix" while leaving the "analytes" in place. In untargeted metabolomics one does not have this luxury, and the "matrix" and the analytes are (apart from contaminants, buffers, salts, etc.) mostly the same thing. The interaction between these contaminants, as well as the more abundant analytes within the ion mobility device can result in ion suppression (or ion enhancement).

Ion suppression is commonly associated with electrospray ionization, although matrix effects and suppression of ionization are also found in electron ionization used with gas chromatography (Yarita et al., 2015) and nanoelectrospray ionization (Kourtchev et al., 2020). Ion suppression occurs in the ion source, but matrix effects such as ion-ion interactions and space charging can occur in trapping instruments (Hohenester et al., 2020). Thus, ion mobility separations, occurring as they do, after ionization, provide no reduction on in-source ion suppression. Consequently, suppression resulting from, flow injection or direct infusion mass spectrometry will not be ameliorated by the use of IMS, and could result in additional artifacts in measurement (Levin et al., 2014).

4 Hyphenating ion mobility to mass spectrometry reduces sample complexity

As previously stated, the primary purpose of separation in mass spectrometry studies is the reduction in sample complexity and reduction of matrix effects. The human metabolome database currently contains 217,920 compounds (Wishart et al., 2022), demonstrating the scale of metabolomics researchers' analytical challenge. Of these, 8,369 metabolites are currently listed as 'detected' in human tissues, with the remainder either predicted or derived from other sources, such as the microbiome and the diet. With the impact of ion suppression (see 3.3) and the limited dynamic range of mass spectrometers (Want et al., 2005), it is very common to perform some separation of analytes before they are presented to the mass spectrometer.

An exception to this is mass spectrometry imaging (MSI), a technique where mass spectrometry is used to raster across a tissue or other spatially resolved sample, providing a spectrum per pixel. Individual ions can be collated to generate images of the distribution of a molecular species to, for example, a tissue structure or feature. Of course, a typical matrix-assisted laser desorption ionization (MALDI) (Tanaka et al., 1988) or desorption electrospray ionization (DESI) (Takáts et al., 2004) process is extremely challenging to hyphenate to chromatography as extraction of analytes and ionization are performed directly from the sample. Therefore, MSI sees considerable benefits from the incorporation of ion mobility separation prior to mass spectrometry (Spraggins et al., 2019), regardless of any impact of matrix effects, as high-resolution IMS can separate isobaric compounds without prior chromatographic separation, while also maintaining acquisition speed.

TABLE 1 Typical workflows in liquid chromatography ion mobility mass spectrometry utilizing multidimensional separation principles.

Type of ion mobility	Instrument used	Separation pre-ion mobility	Run length (min)	Sample	Comments	Reference
TWIMS	Waters Synapt G2S	Metabolites: BEH Amide Lipids: C18	30	Not listed		Paglia and Astarita (2017)
DTIMS	Agilent 6560	Waters Atlantis HSS T3 RPLC	21	*Pichia pastoris*		Feuerstein et al. (2021)
TIMS	Bruker timsTOF fleX	Matrix-assisted laser desorption ionization (MALDI)	N/A	Human kidney	IM separation only, mass spectrometry imaging	Neumann et al. (2020)
DTIMS	Agilent 6560	LC-MS: Atlantis T3 C18 Heart cutting: Hypercarb porous graphetised carbon	20	*Pichia pastoris*	Combines conventional LC-IMMS and heart cutting 2D LC-IMMS	Causon et al. (2019)
DTIMS	Agilent 6560	Capillary electrophoresis	Not listed	Mass Spectrometry Metabolite Library of Standards (Sigma)		Drouin et al. (2021)
TWIMS	Waters Synapt G2-S	Flow injection	3	Serum (prostate cancer)	No chromatographic separation	Zang et al. (2018)
DTIMS	Modified Agilent 6538	Laser ablation electrospray ionization (LAESI)	Not listed	*Allium cepa*	IM separation only, single-cell mass spectrometry	Taylor et al. (2021)
DTIMS	Agilent 6560	Agilent Zorbax Eclipse Plus C18	22.5	Human serum (xenobiotics)		Foster et al. (2022)
TWIMS	Waters Synapt G2-S	Waters HSS T3 RPLC	26	Human serum		Tebani et al. (2016)
DTIMS	Modified Agilent 6560	Waters BEH C18	5	*Pichia pastoris*	Data independent MS/MS	Mairinger et al. (2019)
TIMS	Bruker timsTOF Pro	Bruker Solo C18	23	Olive oil		Drakopoulou et al. (2021)
TWIMS	Waters Vion IM-QToF	Waters HSS T3	29	Ginseng root, leaf, bud		Li et al. (2021)
TWIMS	Waters Vion IM-QToF	Waters CORTECS C18	18	Human plasma (orange metabolites)		Lacalle-Bergeron et al. (2020)
DTIMS	Agilent 6560	Not listed	Not listed	Not listed	Protocol paper	Reisdorph et al. (2019)
DTIMS	Modified Thermo LTQ-Velos	Direct infusion	Not listed	Standards and bovine heart extract		Maleki et al. (2018)
DTIMS	Custom Ionwerks	Direct infusion	Not listed	Rat lymph		Kaplan et al. (2013b)
DTIMS	Tofwerk Resistive Glass Ion Mobility-ToF MS	Direct infusion	20	Rat brain tissue after cocaine administration		Kaplan et al. (2013a)
TWIMS	Waters Vion IM-QToF	Waters BEH Amide (HILIC) and Waters BEH C18 (RP)	HILIC: 12 RP: 17	Saposhnikoviae Radix		Wang et al. (2020)

(Continued on following page)

TABLE 1 (*Continued*) Typical workflows in liquid chromatography ion mobility mass spectrometry utilizing multidimensional separation principles.

Type of ion mobility	Instrument used	Separation pre-ion mobility	Run length (min)	Sample	Comments	Reference
FAIMS	Owlstone FAIMS with Agilent 6230	Agilent Poroshell 120 HILIC	13	Human urine		Szykuła et al. (2019)
TWIMS	Waters Synapt G2-S	Direct infusion	2	Exhaled human breath condensate (cystic fibrosis patients)		Zang et al. (2017)
TWIMS	Waters Vion IM-QToF	Phenomenex Kinetex C18 and CORTECS HILIC	18	Herbal cigarettes (14 herbs plus tobacco)		Gil-Solsona et al. (2021)
TWIMS	Waters Synapt G2-S	Inertsyl Phenyl-3	47	Zucker rat plasma (high fat diet)		Wickramasekara et al. (2013)
TWIMS	Waters Synapt G2-S	Waters HSS T3 C18	30	Mouse feces (bile diversion surgery)		Poland et al. (2019)
TWIMS	Waters Synapt G2-S	LAESI	Not listed	Human neuroblasts	IM separation only—single cell mass spectrometry	Stopka and Vertes (2019)
FAIMS	Sciex SelexION QTRAP 5500	Single cell microsampling	Not listed	*Raphanus sativus* single cells	IM separation only—single cell mass spectrometry	Fujii et al. (2015)
TWIMS	Waters Vion IMS-QToF	Waters HSS T3 C18	25	*Vangueria agrestis* glycosides and terpenoids		Avula et al. (2020)
DTIMS	Agilent 6560	Agilent HILIC-Z	4	*Bacillus* sp. Plant growth promoting rhizobacteria		Pičmanová et al. (2022)
TWIMS	Waters Synapt G2-S	Waters BEH Amide	3.3	Rat urine (tienilic acid study)		King et al. (2019)

Outside the world of MSI, hyphenation of chromatography to mass spectrometry has been used to ameliorate ion suppression and the effects of limited dynamic range for decades, and the recent advances in ion mobility peak capacities have made this a viable addition, or alternative, to chromatography separations.

5 The use of multidimensional separation and best practices

Typical multidimensional separation workflows consist of coupling multiple liquid chromatography-based separation chemistries and hyphenating to mass spectrometry. A full overview of metabolomics applications with liquid chromatography is beyond the scope of this article. For a comprehensive review of recent methods please read (Lv et al., 2019).

Many examples of ion mobility used as a separation method for metabolomics studies appear in the literature (see Table 1). Of the 28 tabulated articles, nine perform no prior separation to analysis via ion mobility-mass spectrometry. Of these, four are single-cell studies using a variety of methods (laser ablation electrospray ionization, matrix-assisted laser desorption ionization, microsampling), where the addition of chromatography would be challenging, if not impossible. For the remainder, a variety of chromatography methods are hyphenated. The most common remains the use of RP chromatography employing C18 columns, but a growing number of HILIC chromatography methods are beginning to be applied. A single method by Causon et al. incorporates heart-cutting two-dimensional liquid chromatography into a metabolomics workflow, while an additional two methods incorporate both HILIC and RP chromatography, performed separately, into their analyses.

Liquid chromatography hyphenated with ion mobility mass spectrometry has become a powerful technique for reducing complexity in untargeted metabolomics. Publications should, of course, adhere to the most appropriate rigorous standards for reporting, the most recent of which is currently (Kirwan et al., 2022), but ion mobility mass spectrometry is a relatively recent development and standards are still evolving. At minimum, the parameters for the ion mobility device should be recorded along with those for the mass spectrometer it is hyphenated to. This is relatively straightforward for dedicated hybrid instruments, but can be more complex for aftermarket or less intrinsically-linked hardware. Additionally, calibration standards should be noted and the parameters of the calibration should be recorded. Typically these are performed before every batch, but IM

calibration samples at both the beginning and the end of a run would provide good evidence that the system was working to appropriate parameters during sample acquisition. CCS libraries, both predicted (Zhou et al., 2020) and experimentally determined (Nichols et al., 2018) are now commonly used in ion mobility mass spectrometry analyses. Both are useful but which library and what criteria (typically a 1%–2% window is used to match CCS) were used is critically important information in the quality assessment of identifications, and should be rigorously reported.

Of course, libraries are not valuable without software to support their use, and academic software that supports the diversity of ion mobility datasets has been relatively slow in development in comparison to the advances in instrumentation. The three most commonly used packages in the field are MS-Dial (Tsugawa et al., 2015), Skyline (MacLean et al., 2010) and MzMine (Schmid et al., 2023). All three are graphical applications that provide peak picking, metabolite annotation and statistics, with Skyline being more closely aimed at targeted applications and MS-Dial having the benefit of integrated large-scale libraries. Ideally, the development of modular tools accessible via R and/or Python would support rapid advancement in terms of new features, that could then be backported into more attractive GUI applications while allowing the possibility of building pipelines into interfaces such as Workflow4Metabolomics (Giacomoni et al., 2015).

6 Conclusion and prospects

Ion mobility spectrometry hyphenated to mass spectrometry has seen rapid technological advancement in the previous 10 years. Initially confined to a few specialists, it is finding itself now routinely applied in proteomics and metabolomics studies for the valuable additional information it provides. Given its capacity for extremely rapid separations, we anticipate a great future for the technology and expect to see further developments to improvements in resolution for the technology.

Author contributions

TM and KB: writing original draft, preparation of figures and tables, conceptualisation and revision of the manuscript. All authors contributed to the article and approved the submitted version.

Funding

This work was funded by the Biotechnology and Biological Sciences Research Council grant BB/W020270/1 and the Engineering and Physical Sciences Research Council grant EP/V038095/1.

Conflict of interest

The authors declare that the research was conducted in the absence of any commercial or financial relationships that could be construed as a potential conflict of interest.

Publisher's note

References

Avula, B., Bae, J. Y., Wang, Y. H., Wang, M., Osman, A. G., Smith, K., et al. (2020). Chemical profiling and characterization of phenolic acids, flavonoids, terpene glycosides from Vangueria agrestis using ultra-high-performance liquid chromatography/ion mobility quadrupole time-of-flight mass spectrometry and metabolomics approach. *Biomed. Chromatogr.* 34, e4840. doi:10.1002/bmc.4840

Borsdorf, H., and Eiceman, G. A. (2006). Ion mobility spectrometry: Principles and applications. *Appl. Spectrosc. Rev.* 41, 323–375. doi:10.1080/05704920600663469

Buryakov, I. A., Krylov, E. V., Nazarov, E. G., and Rasulev, U. Kh. (1993). A new method of separation of multi-atomic ions by mobility at atmospheric pressure using a high-frequency amplitude-asymmetric strong electric field. *Int. J. Mass Spectrom. Ion. Process* 128, 143–148. doi:10.1016/0168-1176(93)87062-w

Canterbury, J. D., Yi, X., Hoopmann, M. R., and MacCoss, M. J. (2008). Assessing the dynamic range and peak capacity of nanoflow LC-FAIMS-MS on an ion trap mass spectrometer for proteomics. *Anal. Chem.* 80, 6888–6897. doi:10.1021/ac8004988

Causon, T. J., Si-Hung, L., Newton, K., Kurulugama, R. T., Fjeldsted, J., and Hann, S. (2019). Fundamental study of ion trapping and multiplexing using drift tube-ion mobility time-of-flight mass spectrometry for non-targeted metabolomics. *Anal. Bioanal. Chem.* 411, 6265–6274. doi:10.1007/s00216-019-02021-8

Demichev, V., Szyrwiel, L., Yu, F., Teo, G. C., Rosenberger, G., Niewienda, A., et al. (2022). dia-PASEF data analysis using FragPipe and DIA-NN for deep proteomics of low sample amounts. *Nat. Commun.* 13, 3944. doi:10.1038/s41467-022-31492-0

Deng, L., Ibrahim, Y. M., Baker, E. S., Aly, N. A., Hamid, A. M., Zhang, X., et al. (2016). Ion mobility separations of isomers based upon long path length structures for lossless ion manipulations combined with mass spectrometry. *Anal. Chem.* 1, 2396–2399. doi:10.1002/slct.201600460

Dodds, J. N., and Baker, E. S. (2019). Ion mobility spectrometry: Fundamental concepts, instrumentation, applications, and the road ahead. *J. Am. Soc. Mass Spectrom.* 30, 2185–2195. doi:10.1007/s13361-019-02288-2

Dou, Y., Mäkinen, M., and Jänis, J. (2023). Analysis of volatile and nonvolatile constituents in gin by direct-infusion ultrahigh-resolution ESI/APPI FT-ICR mass spectrometry. *J. Agric. Food Chem.* 71, 7082–7089. doi:10.1021/acs.jafc.3c00707

Drakopoulou, S. K., Damalas, D. E., Baessmann, C., and Thomaidis, N. S. (2021). Trapped ion mobility incorporated in LC-HRMS workflows as an integral analytical platform of high sensitivity: Targeted and untargeted 4D-metabolomics in extra virgin olive oil. *J. Agric. Food Chem.* 69, 15728–15737. doi:10.1021/acs.jafc.1c04789

Drouin, N., Mielcarek, A., Wenz, C., and Rudaz, S. (2021). Evaluation of ion mobility in capillary electrophoresis coupled to mass spectrometry for the identification in metabolomics. *Electrophoresis* 42, 342–349. doi:10.1002/elps.202000120

Feuerstein, M. L., Kurulugama, R. T., Hann, S., and Causon, T. (2021). Novel acquisition strategies for metabolomics using drift tube ion mobility-quadrupole resolved all ions time-of-flight mass spectrometry (IM-QRAI-TOFMS). *Anal. Chim. Acta* 1163, 338508. doi:10.1016/j.aca.2021.338508

Foster, M., Rainey, M., Watson, C., Dodds, J. N., Kirkwood, K. I., Fernández, F. M., et al. (2022). Uncovering PFAS and other xenobiotics in the dark metabolome using ion mobility spectrometry, mass defect analysis, and machine learning. *Environ. Sci. Technol.* 56, 9133–9143. doi:10.1021/acs.est.2c00201

Fujii, T., Matsuda, S., Tejedor, M. L., Esaki, T., Sakane, I., Mizuno, H., et al. (2015). Direct metabolomics for plant cells by live single-cell mass spectrometry. *Nat. Protoc.* 10, 1445–1456. doi:10.1038/nprot.2015.084

Furey, A., Moriarty, M., Bane, V., Kinsella, B., and Lehane, M. (2013). Ion suppression; A critical review on causes, evaluation, prevention and applications. *Talanta* 115, 104–122. doi:10.1016/j.talanta.2013.03.048

Giacomoni, F., Le Corguillé, G., Monsoor, M., Landi, M., Pericard, P., Pétéra, M., et al. (2015). Workflow4Metabolomics: A collaborative research infrastructure for computational metabolomics. *Bioinformatics* 31, 1493–1495. doi:10.1093/bioinformatics/btu813

Gil-Solsona, R., Sancho, J. V., Gassner, A. L., Weyermann, C., Hernández, F., Delémont, O., et al. (2021). Use of ion mobility-high resolution mass spectrometry in metabolomics studies to provide near MS/MS quality data in a single injection. *J. Mass Spectrom.* 56, e4718. doi:10.1002/jms.4718

Giles, K., Ujma, J., Wildgoose, J., Pringle, S., Richardson, K., Langridge, D., et al. (2019). A cyclic ion mobility-mass spectrometry system. *Anal. Chem.* 91, 8564–8573. doi:10.1021/acs.analchem.9b01838

Gong, L. (2015). Comparing ion-pairing reagents and counter anions for ion-pair reversed-phase liquid chromatography/electrospray ionization mass spectrometry analysis of synthetic oligonucleotides. *Rapid Commun. Mass Spectrom.* 29, 2402–2410. doi:10.1002/rcm.7409

Helden, G. Von, Bowers, M. T., and Wyttenbach, T. (1995). Inclusion of a MALDI ion source in the ion chromatography technique: Conformational information on polymer and biomolecular ions. *Int. J. Mass Spectrom. Ion. Process* 147, 349–364. doi:10.1016/0168-1176(95)04211-3

Hernández-Mesa, M., D'Atri, V., Barknowitz, G., Fanuel, M., Pezzatti, J., Dreolin, N., et al. (2020). Interlaboratory and interplatform study of steroids collision cross section by traveling wave ion mobility spectrometry. *Anal. Chem.* 92, 5013–5022. doi:10.1021/acs.analchem.9b05247

Hohenester, U. M., Barbier Saint-Hilaire, P., Fenaille, F., and Cole, R. B. (2020). Investigation of space charge effects and ion trapping capacity on direct introduction ultra-high-resolution mass spectrometry workflows for metabolomics. *J. Mass Spectrom.* 55, e4613. doi:10.1002/jms.4613

Ibrahim, Y. M., Hamid, A. M., Deng, L., Garimella, S. V. B., Webb, I. K., Baker, E. S., et al. (2017). New frontiers for mass spectrometry based upon structures for lossless ion manipulations. *Analyst* 142, 1010–1021. doi:10.1039/c7an00031f

Kaplan, K. A., Chiu, V. M., Lukus, P. A., Zhang, X., Siems, W. F., Schenk, J. O., et al. (2013a). Neuronal metabolomics by ion mobility mass spectrometry: Cocaine effects on glucose and selected biogenic amine metabolites in the frontal cortex, striatum, and thalamus of the rat. *Anal. Bioanal. Chem.* 405, 1959–1968. doi:10.1007/s00216-012-6638-7

Kaplan, K., Jackson, S., Dwivedi, P., Davidson, W. S., Yang, Q., Tso, P., et al. (2013b). Monitoring dynamic changes in lymph metabolome of fasting and fed rats by matrix-assisted laser desorption/ionization-ion mobility mass spectrometry (MALDI-IMMS). *Int. J. Ion Mobil. Spectrom.* 16, 177–184. doi:10.1007/s12127-012-0102-4

King, A. M., Mullin, L. G., Wilson, I. D., Coen, M., Rainville, P. D., Plumb, R. S., et al. (2019). Development of a rapid profiling method for the analysis of polar analytes in urine using HILIC–MS and ion mobility enabled HILIC–MS. *Metabolomics* 15, 17–11. doi:10.1007/s11306-019-1474-9

Kirk, A. T., Bohnhorst, A., Raddatz, C. R., Allers, M., and Zimmermann, S. (2019). Ultra-high-resolution ion mobility spectrometry — Current instrumentation, limitations, and future developments. *Anal. Bioanal. Chem.* 411, 6229–6246. doi:10.1007/s00216-019-01807-0

Kirwan, J. A., Gika, H., Beger, R. D., Bearden, D., Dunn, W. B., Goodacre, R., et al. (2022). Quality assurance and quality control reporting in untargeted metabolic phenotyping: mQACC recommendations for analytical quality management. *Metabolomics* 18, 70–16. doi:10.1007/s11306-022-01926-3

Kourtchev, I., Szeto, P., O'Connor, I., Popoola, O. A. M., Maenhaut, W., Wenger, J., et al. (2020). Comparison of heated electrospray ionization and nanoelectrospray ionization sources coupled to ultra-high-resolution mass spectrometry for analysis of highly complex atmospheric aerosol samples. *Anal. Chem.* 92, 8396–8403. doi:10.1021/acs.analchem.0c00971

Lacalle-Bergeron, L., Portolés, T., López, F. J., Sancho, J. V., Ortega-Azorín, C., Asensio, E. M., et al. (2020). Ultra-Performance liquid chromatography-ion mobility separation-quadruple time-of-flight ms (UHPLC-IMS-QTOF ms) metabolomics for short-term biomarker discovery of orange intake: A randomized, controlled crossover study. *Nutrients* 12, 1916. doi:10.3390/nu12071916

Levin, M., Krisilov, A., Zon, B., and Eiceman, G. (2014). The effect of space charge in ion mobility spectrometry. *Int. J. Ion Mobil. Spectrom.* 17, 73–77. doi:10.1007/s12127-014-0151-y

Li, W., Yang, X., Chen, B., Zhao, D., Wang, H., Sun, M., et al. (2021). Ultra-high performance liquid chromatography/ion mobility time-of-flight mass spectrometry-based untargeted metabolomics combined with quantitative assay unveiled the metabolic difference among the root, leaf, and flower bud of Panax notoginseng. *Arabian J. Chem.* 14, 103409. doi:10.1016/j.arabjc.2021.103409

Lv, W., Shi, X., Wang, S., and Xu, G. (2019). Multidimensional liquid chromatography-mass spectrometry for metabolomic and lipidomic analyses. *Trends Anal. Chem.* 120, 115302. doi:10.1016/j.trac.2018.11.001

MacLean, B., Tomazela, D. M., Shulman, N., Chambers, M., Finney, G. L., Frewen, B., et al. (2010). Skyline: An open source document editor for creating and analyzing targeted proteomics experiments. *Bioinformatics* 26, 966–968. doi:10.1093/bioinformatics/btq054

Madji Hounoum, B., Blasco, H., Nadal-Desbarats, L., Diémé, B., Montigny, F., Andres, C. R., et al. (2015). Analytical methodology for metabolomics study of adherent mammalian cells using NMR, GC-MS and LC-HRMS. *Anal. Bioanal. Chem.* 407, 8861–8872. doi:10.1007/s00216-015-9047-x

Mairinger, T., Kurulugama, R., Causon, T. J., Stafford, G., Fjeldsted, J., and Hann, S. (2019). Rapid screening methods for yeast sub-metabolome analysis with a high-resolution ion mobility quadrupole time-of-flight mass spectrometer. *Rapid Commun. Mass Spectrom.* 33, 66–74. doi:10.1002/rcm.8420

Maleki, H., Karanji, A. K., Majuta, S., Maurer, M. M., and Valentine, S. J. (2018). Ion mobility spectrometry-mass spectrometry coupled with gas-phase hydrogen/deuterium exchange for metabolomics analyses. *J. Am. Soc. Mass Spectrom.* 29, 230–241. doi:10.1007/s13361-017-1798-5

May, J. C., Leaptrot, K. L., Rose, B. S., Moser, K. L. W., Deng, L., Maxon, L., et al. (2021). Resolving power and collision cross section measurement accuracy of a prototype high-resolution ion mobility platform incorporating structures for lossless ion manipulation. *J. Am. Soc. Mass Spectrom.* 32, 1126–1137. doi:10.1021/jasms.1c00056

Meier, F., Beck, S., Grassl, N., Lubeck, M., Park, M. A., Raether, O., et al. (2015). Parallel accumulation-serial fragmentation (PASEF): Multiplying sequencing speed and sensitivity by synchronized scans in a trapped ion mobility device. *J. Proteome Res.* 14, 5378–5387. doi:10.1021/acs.jproteome.5b00932

Meier, F., Brunner, A. D., Koch, S., Koch, H., Lubeck, M., Krause, M., et al. (2018). Online parallel accumulation–serial fragmentation (PASEF) with a novel trapped ion mobility mass spectrometer. *Mol. Cell. Proteomics* 17, 2534–2545. doi:10.1074/mcp.TIR118.000900

Merenbloom, S. I., Flick, T. G., and Williams, E. R. (2012). How hot are your ions in TWAVE ion mobility spectrometry? *J. Am. Soc. Mass Spectrom.* 23, 553–562. doi:10.1007/s13361-011-0313-7

Morsa, D., Gabelica, V., and De Pauw, E. (2011). Effective temperature of ions in traveling wave ion mobility spectrometry. *Anal. Chem.* 83, 5775–5782. doi:10.1021/ac201509p

Neumann, E. K., Migas, L. G., Allen, J. L., Caprioli, R. M., Van De Plas, R., and Spraggins, J. M. (2020). Spatial metabolomics of the human kidney using MALDI trapped ion mobility imaging mass spectrometry. *Anal. Chem.* 92, 13084–13091. doi:10.1021/acs.analchem.0c02051

Nichols, C. M., Dodds, J. N., Rose, B. S., Picache, J. A., Morris, C. B., Codreanu, S. G., et al. (2018). Untargeted molecular discovery in primary metabolism: Collision cross section as a molecular descriptor in ion mobility-mass spectrometry. *Anal. Chem.* 90, 14484–14492. doi:10.1021/acs.analchem.8b04322

Paglia, G., and Astarita, G. (2017). Metabolomics and lipidomics using traveling-wave ion mobility mass spectrometry. *Nat. Protoc.* 12, 797–813. doi:10.1038/nprot.2017.013

Picache, J. A., Rose, B. S., Balinski, A., Leaptrot, K. L., Sherrod, S. D., May, J. C., et al. (2019). Collision cross section compendium to annotate and predict multi-omic compound identities. *Chem. Sci.* 10, 983–993. doi:10.1039/c8sc04396e

Pičmanová, M., Moses, T., Cortada-Garcia, J., Barrett, G., Florance, H., Pandor, S., et al. (2022). Rapid HILIC-Z ion mobility mass spectrometry (RHIMMS) method for untargeted metabolomics of complex biological samples. *Metabolomics* 18, 16–12. doi:10.1007/s11306-022-01871-1

Poland, J. C., Schrimpe-Rutledge, A. C., Sherrod, S. D., Flynn, C. R., and McLean, J. A. (2019). Utilizing untargeted ion mobility-mass spectrometry to profile changes in the gut metabolome following biliary diversion Surgery. *Anal. Chem.* 91, 14417–14423. doi:10.1021/acs.analchem.9b02924

Reinecke, T., Naylor, C. N., and Clowers, B. H. (2019). Ion multiplexing: Maximizing throughput and signal to noise ratio for ion mobility spectrometry. *Trends Anal. Chem.* 116, 340–345. doi:10.1016/j.trac.2019.03.014

Reisdorph, R., Michel, C., Quinn, K., Doenges, K., and Reisdorph, N. (2019). Untargeted differential metabolomics analysis using drift tube ion mobility-mass spectrometry. *Methods Mol. Biol.* 2084, 55–78. doi:10.1007/978-1-0716-0030-6_3

Revercomb, H. E., and Mason, E. A. (1975). Theory of plasma chromatography/gaseous electrophoresis. Review. *Anal. Chem.* 47, 970–983. doi:10.1021/ac60357a043

Ridgeway, M. E., Lubeck, M., Jordens, J., Mann, M., and Park, M. A. (2018). Trapped ion mobility spectrometry: A short review. *Int. J. Mass Spectrom.* 425, 22–35. doi:10.1016/j.ijms.2018.01.006

Ridgeway, M. E., Wolff, J. J., Silveira, J. A., Lin, C., Costello, C. E., and Park, M. A. (2016). Gated trapped ion mobility spectrometry coupled to fourier transform ion cyclotron resonance mass spectrometry. *Int. J. Ion Mobil. Spectrom.* 19, 77–85. doi:10.1007/s12127-016-0197-0

Righetti, L., Dreolin, N., Celma, A., McCullagh, M., Barknowitz, G., Sancho, J. V., et al. (2020). Travelling wave ion mobility-derived collision cross section for mycotoxins: Investigating interlaboratory and interplatform reproducibility. *J. Agric. Food Chem.* 68, 10937–10943. doi:10.1021/acs.jafc.0c04498

Rokushika, S., Hatano, H., Bairn, M. A., and Hill, H. H. (1985). Resolution measurement for ion mobility spectrometry. *Anal. Chem.* 57, 1902–1907. doi:10.1021/ac00286a023

Schmid, R., Heuckeroth, S., Korf, A., Smirnov, A., Myers, O., Dyrlund, T. S., et al. (2023). Integrative analysis of multimodal mass spectrometry data in MZmine 3. *Nat. Biotechnol.* 41, 447–449. doi:10.1038/s41587-023-01690-2

Shvartsburg, A. A., and Smith, R. D. (2008). Fundamentals of traveling wave ion mobility spectrometry. *Anal. Chem.* 80, 9689–9699. doi:10.1021/ac8016295

Siems, W. F., Viehland, L. A., and Hill, H. H. (2012). Improved momentum-transfer theory for ion mobility. 1. Derivation of the fundamental equation. *Anal. Chem.* 84, 9782–9791. doi:10.1021/ac301779s

Sisley, E. K., Ujma, J., Palmer, M., Giles, K., Fernandez-Lima, F. A., and Cooper, H. J. (2020). LESA cyclic ion mobility mass spectrometry of intact proteins from thin tissue sections. *Anal. Chem.* 92, 6321–6326. doi:10.1021/acs.analchem.9b05169

Sobańska, A. W. (2021). Emerging or underestimated silica-based stationary phases in liquid chromatography. *Crit. Rev. Anal. Chem.* 51, 631–725. doi:10.1080/10408347.2020.1760782

Spraggins, J. M., Djambazova, K. V., Rivera, E. S., Migas, L. G., Neumann, E. K., Fuetterer, A., et al. (2019). High-Performance molecular imaging with MALDI trapped ion-mobility time-of-flight (timsTOF) mass spectrometry. *Anal. Chem.* 91, 14552–14560. doi:10.1021/acs.analchem.9b03612

Stopka, S. A., and Vertes, A. (2019). Metabolomic profiling of adherent mammalian cells *in situ* by LAESI-MS with ion mobility separation. *Methods Mol. Biol.* 2084, 235–244. doi:10.1007/978-1-0716-0030-6_15

Stow, S. M., Causon, T. J., Zheng, X., Kurulugama, R. T., Mairinger, T., May, J. C., et al. (2017). An interlaboratory evaluation of drift tube ion mobility-mass spectrometry collision cross section measurements. *Anal. Chem.* 89, 9048–9055. doi:10.1021/acs.analchem.7b01729

Sun, X., Jia, Z., Zhang, Y., Zhao, X., Zhao, C., Lu, X., et al. (2023). A strategy for uncovering the serum metabolome by direct-infusion high-resolution mass spectrometry. *Metabolites* 13, 460. doi:10.3390/metabo13030460

Szykuła, K. M., Meurs, J., Turner, M. A., Creaser, C. S., and Reynolds, J. C. (2019). Combined hydrophilic interaction liquid chromatography-scanning field asymmetric waveform ion mobility spectrometry-time-of-flight mass spectrometry for untargeted metabolomics. *Anal. Bioanal. Chem.* 411, 6309–6317. doi:10.1007/s00216-019-01790-6

Takáts, Z., Wiseman, J. M., Gologan, B., and Cooks, R. G. (2004). Mass spectrometry sampling under ambient conditions with desorption electrospray ionization. *Sci. (1979)* 306, 471–473. doi:10.1126/science.1104404

Tanaka, K., Waki, H., Ido, Y., Akita, S., Yoshida, Y., Yoshida, T., et al. (1988). Protein and polymer analyses up to m/z 100 000 by laser ionization time-of-flight mass spectrometry. *Rapid Commun. Mass Spectrom.* 2, 151–153. doi:10.1002/rcm.1290020802

Taylor, M. J., Mattson, S., Liyu, A., Stopka, S. A., Ibrahim, Y. M., Vertes, A., et al. (2021). Optical microscopy-guided laser ablation electrospray ionization ion mobility mass spectrometry: Ambient single cell metabolomics with increased confidence in molecular identification. *Metabolites* 11, 200. doi:10.3390/metabo11040200

Tebani, A., Schmitz-Afonso, I., Rutledge, D. N., Gonzalez, B. J., Bekri, S., and Afonso, C. (2016). Optimization of a liquid chromatography ion mobility-mass spectrometry method for untargeted metabolomics using experimental design and multivariate data analysis. *Anal. Chim. Acta* 913, 55–62. doi:10.1016/j.aca.2016.02.011

Tsugawa, H., Cajka, T., Kind, T., Ma, Y., Higgins, B., Ikeda, K., et al. (2015). MS-DIAL: Data-independent MS/MS deconvolution for comprehensive metabolome analysis. *Nat. Methods* 12, 523–526. doi:10.1038/nmeth.3393

Tswett, M. (1968). Physical chemical studies on chlorophyll adsorptions. *A Source Book Chem.* 1900-1950, 23–28.

Wang, S., Qian, Y., Sun, M., Jia, L., Hu, Y., Li, X., et al. (2020). Holistic quality evaluation of Saposhnikoviae Radix (Saposhnikovia divaricata) by reversed-phase ultra-high performance liquid chromatography and hydrophilic interaction chromatography coupled with ion mobility quadrupole time-of-flight mass spectrometry-based untargeted metabolomics. *Arabian J. Chem.* 13, 8835–8847. doi:10.1016/j.arabjc.2020.10.013

Want, E. J., Cravatt, B. F., and Siuzdak, G. (2005). The expanding role of mass spectrometry in metabolite profiling and characterization. *ChemBioChem* 6, 1941–1951. doi:10.1002/cbic.200500151

West, C., Elfakir, C., and Lafosse, M. (2010). Porous graphitic carbon: A versatile stationary phase for liquid chromatography. *J. Chromatogr. A* 1217, 3201–3216. doi:10.1016/j.chroma.2009.09.052

Wickramasekara, S., Zandkarimi, F., Morré, J., Kirkwood, J., Legette, L., Jiang, Y., et al. (2013). Electrospray quadrupole travelling wave ion mobility time-of-flight mass spectrometry for the detection of plasma metabolome changes caused by xanthohumol in obese zucker (fa/fa) rats. *Metabolites* 3, 701–717. doi:10.3390/metabo3030701

Wishart, D. S., Guo, A. C., Oler, E., Wang, F., Anjum, A., Peters, H., et al. (2022). Hmdb 5.0: The human metabolome database for 2022. *Nucleic Acids Res.* 50, D622–D631. doi:10.1093/nar/gkab1062

Wolthuis, J. C., Magnúsdóttir, S., Stigter, E., Tang, Y. F., Jans, J., Gilbert, M., et al. (2023). Multi-country metabolic signature discovery for chicken health classification. *Metabolomics* 19, 9–14. doi:10.1007/s11306-023-01973-4

Yarita, T., Aoyagi, Y., and Otake, T. (2015). Evaluation of the impact of matrix effect on quantification of pesticides in foods by gas chromatography-mass spectrometry using isotope-labeled internal standards. *J. Chromatogr. A* 1396, 109–116. doi:10.1016/j.chroma.2015.03.075

Zang, X., Monge, M. E., Gaul, D. A., and Fernández, F. M. (2018). Flow injection-traveling-wave ion mobility-mass spectrometry for prostate-cancer metabolomics. *Anal. Chem.* 90, 13767–13774. doi:10.1021/acs.analchem.8b04259

Zang, X., Pérez, J. J., Jones, C. M., Monge, M. E., McCarty, N. A., Stecenko, A. A., et al. (2017). Comparison of ambient and atmospheric pressure ion sources for cystic fibrosis exhaled breath condensate ion mobility-mass spectrometry metabolomics. *J. Am. Soc. Mass Spectrom.* 28, 1489–1496. doi:10.1007/s13361-017-1660-9

Zhang, W. (2008). Fluorocarbon stationary phases for liquid chromatography applications. *J. Fluor Chem.* 129, 910–919. doi:10.1016/j.jfluchem.2008.07.001

Zheng, X., Aly, N. A., Zhou, Y., Dupuis, K. T., Bilbao, A., Paurus, V. L., et al. (2017). A structural examination and collision cross section database for over 500 metabolites and xenobiotics using drift tube ion mobility spectrometry. *Chem. Sci.* 8, 7724–7736. doi:10.1039/c7sc03464d

Zhou, Z., Luo, M., Chen, X., Yin, Y., Xiong, X., Wang, R., et al. (2020). Ion mobility collision cross-section atlas for known and unknown metabolite annotation in untargeted metabolomics. *Nat. Commun.* 11, 4334–4413. doi:10.1038/s41467-020-18171-8

Zou, H., Huang, X., Ye, M., and Luo, Q. (2002). Monolithic stationary phases for liquid chromatography and capillary electrochromatography. *J. Chromatogr. A* 954, 5–32. doi:10.1016/S0021-9673(02)00072-9

frontiers | Frontiers in Molecular Biosciences

TYPE Original Research
PUBLISHED 15 March 2024
DOI 10.3389/fmolb.2024.1253983

OPEN ACCESS

EDITED BY
Marianna Caterino,
University of Naples Federico II, Italy

REVIEWED BY
Luis G. Gonçalves,
Universidade Nova de Lisboa, Portugal
Michele Costanzo,
University of Naples Federico II, Italy

*CORRESPONDENCE
Shayne Mason,
nmr.nwu@gmail.com

†These authors share last authorship

RECEIVED 16 October 2023
ACCEPTED 20 February 2024
PUBLISHED 15 March 2024

CITATION
Isaiah S, Loots DT, van Reenen M, Solomons R, van Elsland S, Tutu van Furth AM, van der Kuip M and Mason S (2024), Urinary metabolic characterization of advanced tuberculous meningitis cases in a South African paediatric population.
Front. Mol. Biosci. 11:1253983.
doi: 10.3389/fmolb.2024.1253983

Urinary metabolic characterization of advanced tuberculous meningitis cases in a South African paediatric population

Simon Isaiah[1], Du Toit Loots[1], Mari van Reenen[1], Regan Solomons[2], Sabine van Elsland[2,3], A. Marceline Tutu van Furth[4], Martijn van der Kuip[4†] and Shayne Mason[1*†]

[1]Human Metabolomics, Faculty of Natural and Agricultural Sciences, North-West University, Potchefstroom, South Africa, [2]Department of Paediatrics and Child Health, Faculty of Medicine and Health Sciences, Stellenbosch University, Cape Town, South Africa, [3]MRC Centre for Global Infectious Disease Analysis, Imperial College London, London, United Kingdom, [4]Vrije Universiteit, Pediatric Infectious Diseases and Immunology, Amsterdam University Medical Centers, Emma Children's Hospital, Amsterdam, Netherlands

Tuberculous meningitis (TBM) is a severe form of tuberculosis with high neuro-morbidity and mortality, especially among the paediatric population (aged ≤12 years). Little is known of the associated metabolic changes. This study aimed to identify characteristic metabolic markers that differentiate severe cases of paediatric TBM from controls, through non-invasive urine collection. Urine samples selected for this study were from two paediatric groups. Group 1: controls (n = 44): children without meningitis, no neurological symptoms and from the same geographical region as group 2. Group 2: TBM cases (n = 13): collected from paediatric patients that were admitted to Tygerberg Hospital in South Africa on the suspicion of TBM, mostly severely ill; with a later confirmation of TBM. Untargeted 1H NMR-based metabolomics data of urine were generated, followed by statistical analyses via MetaboAnalyst (v5.0), and the identification of important metabolites. Twenty nine urinary metabolites were identified as characteristic of advanced TBM and categorized in terms of six dysregulated metabolic pathways: 1) upregulated tryptophan catabolism linked to an altered vitamin B metabolism; 2) perturbation of amino acid metabolism; 3) increased energy production–metabolic burst; 4) disrupted gut microbiota metabolism; 5) ketoacidosis; 6) increased nitrogen excretion. We also provide original biological insights into this biosignature of urinary metabolites that can be used to characterize paediatric TBM patients in a South African cohort.

KEYWORDS

urine, metabolic, paediatric, tuberculous meningitis (TBM), untargeted metabolomics, Proton nuclear magnetic resonance (^{1}H NMR) spectroscopy

1 Introduction

The most lethal form of extra-pulmonary tuberculosis (TB)–tuberculous meningitis (TBM)–affects 1%–5% of TB infected individuals globally (Donovan et al., 2020). The pediatric age group (aged ≤12 years) are the most at risk for contracting the disease, and account for 12% of all TBM cases, with one in five affected children dying and only one in three surviving without long-term neurological sequelae (WHO, 2020; Basu Roy et al., 2021). According to the World Health Organization, South Africa is among the eight countries that account for two-thirds of the global total TB burden (WHO, 2020). In the Western Cape province of South Africa, TBM is the most common form of paediatric meningitis detected (Donald et al., 1996; Wolzak et al., 2012). Early diagnosis and timely introduction of appropriate therapy can potentiate a positive treatment outcome (Donovan et al., 2020). However, the timely and accurate diagnosis of TBM is challenging, since the early symptoms are usually nonspecific (van Toorn and Solomons, 2014).

There is a pressing need to improve current TBM diagnostic strategies (Hasbun et al., 2018). Stand-alone methods currently used to diagnose TBM in children are unreliable (Manyelo et al., 2021). Existing diagnostic techniques for TBM are invasive, complex and time-consuming, subsequently delaying treatment, and putting patients at a high risk of mortality. Recently, efforts have been made to better understand the pathophysiology through new research focused on finding novel TBM biomarker signatures (Rohlwink et al., 2017; Manyelo et al., 2019). Yet, there are still no clear biomarker(s), nor biosignature(s), for TBM in the cerebrospinal fluid (CSF), let alone one from patient samples collected non-invasively, such as from urine. Urine is rich in metabolic information that describes the systematic state of an individual and is a relatively unexplored biofluid in TBM research. Urinary metabolomics profiling in pulmonary TB patients has been an efficient means of diagnosing and monitoring an individual's response to treatment (Luies et al., 2017). Mason *et al.* (2016b) holistically illustrated the metabolic complexity of TBM and provided proof-of-concept that a putative biosignature of urinary metabolites (methylcitric, 2-ketoglutaric, quinolinic and 4-hydroxyhippuric acids) can be defined with the potential to be used for the non-invasive metabolomics diagnosis and prognosis of paediatric TBM patients. In another metabolomics study, Chatterji *et al.* (2016) observed reduced malonic acid and elevated 2-hydroxybutyric acid, acetic acid, creatine and glycerophosphocholine, in the urine of TBM adults. These pioneering metabolomics studies have provided proof-of-concept that urine provides a wealth of metabolic information in TBM cases and deserves further investigation.

Metabolomics provides analytical, chemical and physiological insights into metabolite interactions (Mason et al., 2016a). These metabolites are vital constituents of biological systems and are highly informative of their functional state, serving as biomarkers of disease and also reflective of therapeutic response (Goodacre, 2010). van der Greef *et al.* (2004) describe metabolomics as a prospective tool for clinical use in the early detection of a metabolic perturbation in a biological system, before the disease symptoms actually present themselves. Nuclear magnetic resonance (NMR) spectroscopy is one such technique commonly used for the metabolite profiling and analysis of complex biofluids (Nagana Gowda et al., 2008). Studying the molecular level shift in equilibrium in patient urine will improve the systematic understanding of TBM and may also help develop transformable solutions related to novel diagnostics (Blankley et al., 2014). The need for research, such as that reported here, in order to generate knowledge which can be used to develop timely and accurate diagnosis, improve treatment outcomes, and ultimately reduce the dire mortality and neuro-morbidity in paediatric TBM disease in children (and adults), has become a priority (Organization, 2018). Hence, this study aimed to identify metabolites in urine that characterize the metabolic profile of severe TBM in paediatric cases, using ^{1}H NMR metabolomics. Characterization here is defined as explaining the biochemistry underpinning TBM, in terms of altered metabolic pathways and increased/decreased metabolites.

2 Materials and methods

2.1 Sample origin and selection criteria

The sample population used in this study were infants and children (aged ≤12 years) from the Western Cape Province of South Africa, an area with high prevalence of TB (681 per 100,000), especially among children ≤12 years of age (100 per 966) (Donald et al., 1996; KANABUS, 2020). Participants were referred from primary and secondary level healthcare facilities to the paediatric department at Tygerberg Hospital, Stellenbosch University. The participants were divided into two groups (Group 1: control; n = 44) and (Group 2: TBM; n = 13). Criteria for collection of the controls (Group 1) were paediatric patients without meningitis, no neurological symptoms, and from the same geographical region as the TBM patients. Urine samples from the control group were requested from children undergoing routine follow up at Paediatric Outpatient Clinics, none of whom were acutely ill during sampling. The TBM urine samples (Group 2) used in this study were collected from pediatric patients (van Elsland et al., 2018) under initial treatment that were admitted to the hospital on suspicion of TBM, most of them severely sick; with a later confirmation of "definite TBM" according to the uniform research case definition for TBM (i.e., *M. tuberculosis* (*M.tb*) identified on CSF by microscopy, culture and/or detection by commercial nucleic-acid amplification test (Marais et al., 2010)) at an advanced stage (with or without focal neurological deficit) (Van Toorn et al., 2012). The urine sample used in this study was the first urine sample collected as an out-patient (discharged from hospital once stabilized) as a home-treatment program (van Elsland et al., 2018). Clinical information was recorded for all TBM cases (see Table 1). As per ethics requirements, all urine samples were collected after written informed consent from parent(s) and assent from the child, if older than 7 years and able to do so, was obtained, under the Health Research Ethics Committee (HREC) approval of Stellenbosch University (ethics approval no. N16/11/142 and N11/03/061 for group 1 and 2 respectively), the Western Cape provincial government, as well as by the HREC of the North-West University, Potchefstroom campus (ethics approval no. NWU-00063-18-A1-01). Participants with an unknown or positive HIV status were excluded from this

10.3389/fmolb.2024.1253983

TABLE 1 Demographic, clinical, laboratory and imaging findings of 13 paediatric patients diagnosed with advanced tuberculous meningitis.

CRITERIA	n (%)
Gender: male/female	6 (46.2)/7 (53.8)[a]
Age (months) (Median [range])	43 [22–140]
Clinical symptoms	
Fever	11/13 (84.6)
Night sweats	2/13 (15.4)
Poor feeding	5/13 (38.5)
Weight loss	5/13 (38.5)
Vomiting	4/13 (30.8)
Coughing	None
Headache	1/13 (7.7)
Seizures	4/13 (30.8)
Lethargy	2/13 (15.4)
Neurological signs	
GCS: (median [range])	10 [7–15]
Meningism	3/13 (23.1)
Focal motor deficit	4/13 (30.8)
Cranial nerve palsy	3/13 (23.1)
Raised ICP	4/13 (30.8)
Neuroimaging (CT brain)	
Hydrocephalus	11/13 (84.6)
Infarctions	1/13 (7.7)
Tuberculoma	2/13 (15.4)
Meningeal enhancement	7/13 (53.8)
VP shunt	4/13 (30.8)
Convulsions	1/13 (7.7)
Hemiparesis	4/13 (30.8)
CXR (signs of pulmonary TB)	1/13 (7.7)
Laboratory values	
Blood albumin (g/L) (median [range])	41 [40–52]
Blood sodium (mmol/L) (median [range])	131.5 [120–141]
Blood total protein (g/L) (median [range])	77.5 [75–80]
Blood glucose (mmol/L) (median [range])	7.1 [4.9–7.7]
Blood lipids (median)	3.9
CSF protein (g/L) (median [range])	0.84 [0.21–3.0]
CSF glucose (mmol/L) (median [range])	2.2 [0.2–4.8]
CSF pleocytosis (cells/μL) (median [range])	40 [3–129]
CSF lymphocytes (cells/μL) (median [range])	57 [3–148])
BCG positive status	3/13 (23.1)

[a]= so significant difference; ICP = intracranial pressure; VP = ventriculoperitoneal; BCG = *Bacillus* Calmette–Guérin vaccine; GCS = glasgow coma scale; CSF = cerebrospinal fluid; CXR = chest X-ray.

study because HIV co-infection further confounds an already complex metabolic profile.

2.2 Sample transport, storage and handling

Upon collection, urine samples were stored at −80°C in a dedicated freezer at the division of Molecular Biology and Human Genetics at Stellenbosch University. Once all samples were collected, they were collectively couriered overnight–frozen, on dry ice, to a dedicated freezer (−80°C) in a biosafety level 3 (BSL3) laboratory at the Centre for Human Metabolomics, situated on the Potchefstroom campus of North-West University. All urine samples were thawed in a biological safety cabinet, after which 600 µL of each sample was aliquoted into a separate tube for NMR analysis and an additional 50 µL for the purpose of making a pooled quality control (QC) sample. The pooled QC sample was then vortexed and re-aliquoted into 20 equal-volume quantities. All aliquoted samples (including QC samples) were kept at −80°C until NMR analysis.

2.3 Sample preparation and ^{1}H NMR analysis

All urine samples were thawed to room temperature prior to processing. A volume of 600 µL of urine was centrifuged at 12,000 *g* for 5 min to sediment any particulates and macromolecules. A volume of 540 µL of the supernatant was collected in a micro-centrifuge tube, with 60 µL of the NMR buffer solution [1.5 M potassium phosphate solution in deuterium oxide with internal standard TSP (trimethylsilyl-2,2,3,3-tetradeuteropropionic acid); pH 7.4]. The sample was briefly vortexed to ensure homogeneity before being centrifuged at 12,000 *g* for 5 min. For ^{1}H NMR analysis, 540 µL of the supernatant was transferred to a 5 mm NMR glass tube and analyzed using a Bruker Avance III HD NMR spectrometer with a triple-resonance inverse (TXI) ^{1}H (^{15}N,^{13}C) probe head and x, y, and z gradient coils, at 500 MHz, in a randomized sequence, with QC samples interweaved at regular intervals. With a spectral width of 12,000 Hz, ^{1}H spectra were recorded as 128 transients in 32 K data points. The sample temperature was kept constant at 300 K, and the H2O resonance was pre-saturated using single-frequency irradiation with a 4-s relaxation delay and an 8-µs excitation pulse, using the noesygppr1d water presaturation pulse program. Sample shimming was performed automatically based on the deuterium signal. TSP and metabolites had resonance line widths of <1 Hz. Fourier transformation, phase and baseline correction were performed automatically. Bruker Topspin (V3.5) was used to process the NMR data. For metabolite identification and quantification, Bruker AMIX (V3.9.14) was employed (Erasmus et al., 2019).

2.4 Data pre-processing and statistical analysis

The ^{1}H NMR spectral output was binned at 0.02 ppm widths, relative to creatinine, to create a data matrix of spectral intensity with the bins as the columns and samples as the rows. A t-test on the peak integral region of the creatinine peak between the control and TBM group revealed a *p*-value of 0.065. The noise level was identified as less than the limit of detection (LOD), calculated as: LOD = average of blank bins (bins with no discernible peaks) + 3.3 * standard deviation of blank bins (Westgard, 2008), and bins identified as noise were zeroed. All zeroes were replaced with 1/5 of the lowest value using MetaboAnalyst (V5.0). Bins around the suppressed water peak ~4.72 ppm were also removed. The final data matrix gave a total of 468 bins. Throughout the batch analysis, 20 aliquots of a pooled QC sample were processed at predefined intervals to ensure trustworthy data. Quality assurance was based on QC observations, with bins with a coefficient of variation (CV) value greater than 30% were removed from the spectral binned data matrix. Because spectral intensity does not always reflect biological significance, data were log transformed and Pareto scaled to account for skewed distributions and to put bins on an even footing when presented for multivariate analysis. Statistical analyses and identification of important metabolites were conducted using MetaboAnalyst (V5.0)–a comprehensive platform dedicated for metabolomics data analysis via a web-based interface that enables high-throughput analysis for both targeted and untargeted metabolomics (Pang et al., 2021); included univariate statistics (fold changes and t-tests, displayed using a volcano plot) and multivariate statistics, specifically principal component analysis (PCA), partial least squares–discriminant analysis (PLS-DA). To project the data onto fewer, more manageable dimensions and to highlight entirely data-driven connections between instances, unsupervised PCA analyses were used with a 95% confidence interval (CI) ellipsis to detect natural separation between group centroid, to remove outliers in the two experimental groups, and to examine QC distribution to assess overall method reliability. Hierarchical cluster analysis was also performed, based on Euclidean distance using Ward's linkage method. Quantitative statistical data were used to identify variables of importance: PLS-DA VIP of >1.0 for components 1 and 2, a t-test *p*-value ≤0.05, corrected for multiple testing (FDR, false discovery rate), and a fold change ≥2.0. Discriminatory metabolites were identified using pure compound 1D ^{1}H NMR spectral libraries and confirmed using 2D correlation spectroscopy (COSY) and J-resolved (JRES) ^{1}H–^{1}H NMR data. Important identified metabolites were quantified relative to the creatinine peak (µmol/mmol creatinine) and additional univariate measures, including t-test *p*-values (adjusted using Bonferroni–Holm) and Cohen's d-values, were calculated. Statistical significance ($p \leq 0.05$) was used to generalize findings, that is, what is the probability that we won't find a difference if we take another sample? On the other hand, practical significance (d > 0.6) indicates magnitude of difference and answers the "so what" question, namely, whether the effect is large enough to care about. A summary of the experimental design for this study is illustrated schematically in Figure 1. The use of online metabolite databases, such as the Human Metabolome Database (HMDB) and the Kyoto Encyclopedia of Genes and Genomes (KEGG), were used to assist in the biological interpretation of the results.

3 Results

Prior to statistical analysis, a quantitative quality assurance check was performed on all QC samples. A total of 24 bins

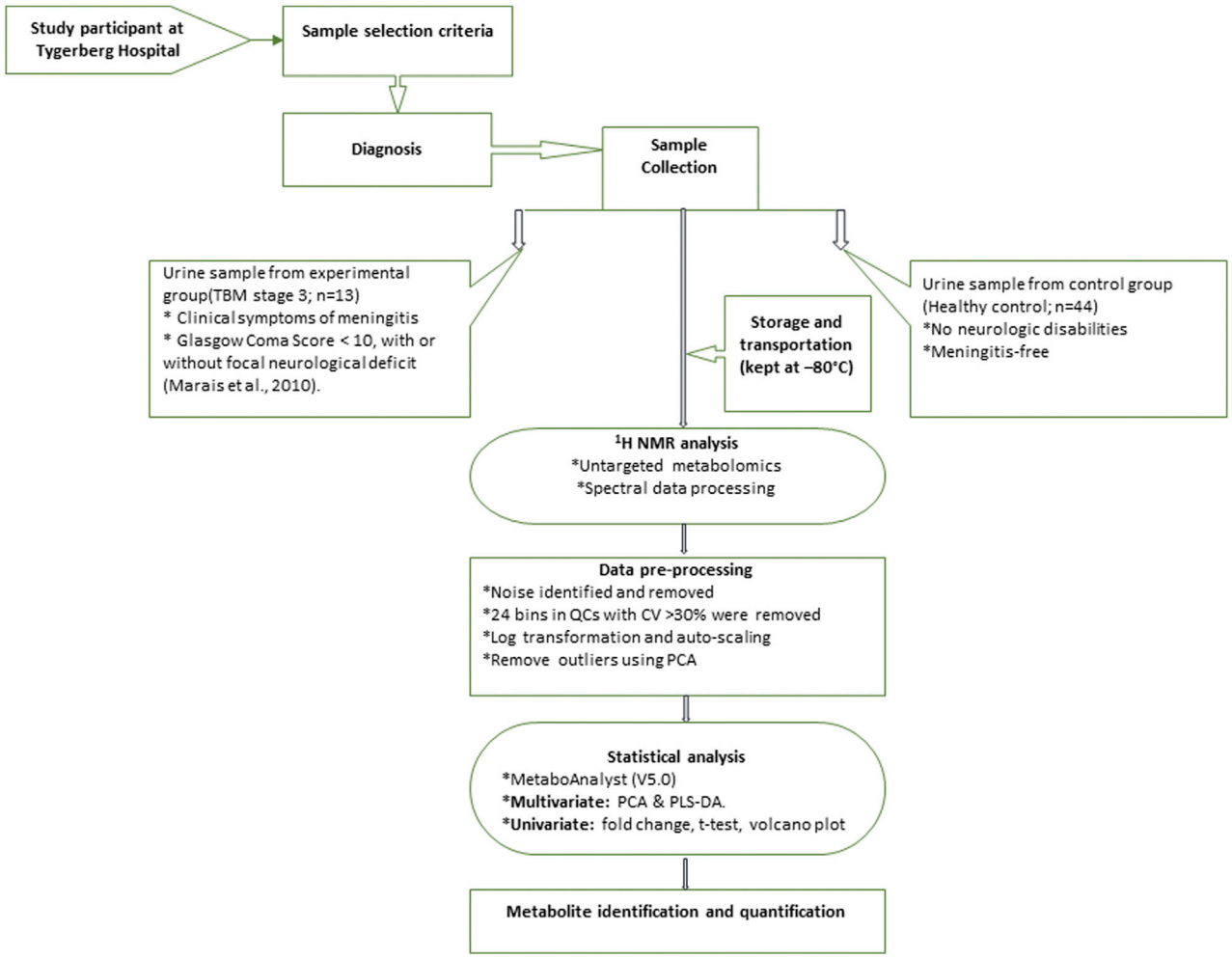

FIGURE 1
Schematic diagram indicating sequence of steps of experimental design of ^{1}H NMR metabolomics and statistical analyses performed.

across 20 QC samples had a CV greater than 30% and were removed from the spectral binned data matrix. This reduced the number of bins from 468 to 444. Hence, the variation exhibited across bins between the two groups can be attributed towards biological variation. A PCA of all cases, including the QC samples (Figure 2A), shows that the 20 QC samples cluster closely together, indicating overall method reliability (i.e., no batch or machine drift). An unsupervised PCA, excluding QC samples, was performed Supplementary Figure S1 and four outliers were identified in the control group and removed from further analysis; no outliers identified in the TBM group. Next, an unsupervised PCA analysis of the 40 controls against the 13 TBM cases was performed (Figure 2B), which yielded almost complete natural separation between the groups, with their 95% CI ellipses slightly overlapping as a result of two control samples. The results of the unsupervised PCA confirm that the two groups are indeed differentiated, providing confidence before using the supervised method of PLS-DA.

Subsequent hierarchical cluster analysis (Supplementary Figure S2) identified two clusters: one homogeneous cluster containing control cases (n = 38) at the top, with one TBM case, and the other (bottom) cluster containing 12 TBM cases and two control cases. The hierarchical cluster analysis further illustrates that there was some overlap between the two groups, but overall there was differentiation.

A supervised PLS-DA (Figure 3) was performed in order to detect differentiating bins and avoid false discoveries. The PLS-DA model generates meaningful information that can be used to identify important variables and assess the significance of class discrimination by performing a permutation test using the optimal number of components determined by cross validation. The supervised PLS-DA model for the data exhibited an R^2 of 96%, and was validated by a Q^2 of 81%, and a permutation p-value of 0.0004 (188/2000). Various bins differentiating the TBM and control groups were observed through loading plots for the PLS-DA and identified through a variable of importance in projection (VIPs) cut-off criteria of greater than 1.0 (VIP >1.0) for components 1 and 2.

Additionally, univariate statistics of fold change analysis and Wilcoxon t-tests are illustrated as a volcano plot in (Figure 4). Thresholds of absolute fold change ≥2.0 and an FDR p-value ≤0.05 were used to identify statistically significant bins.

Based upon the quantitative statistical data of the ^{1}H-NMR spectral bins, the important bins were identified using the following

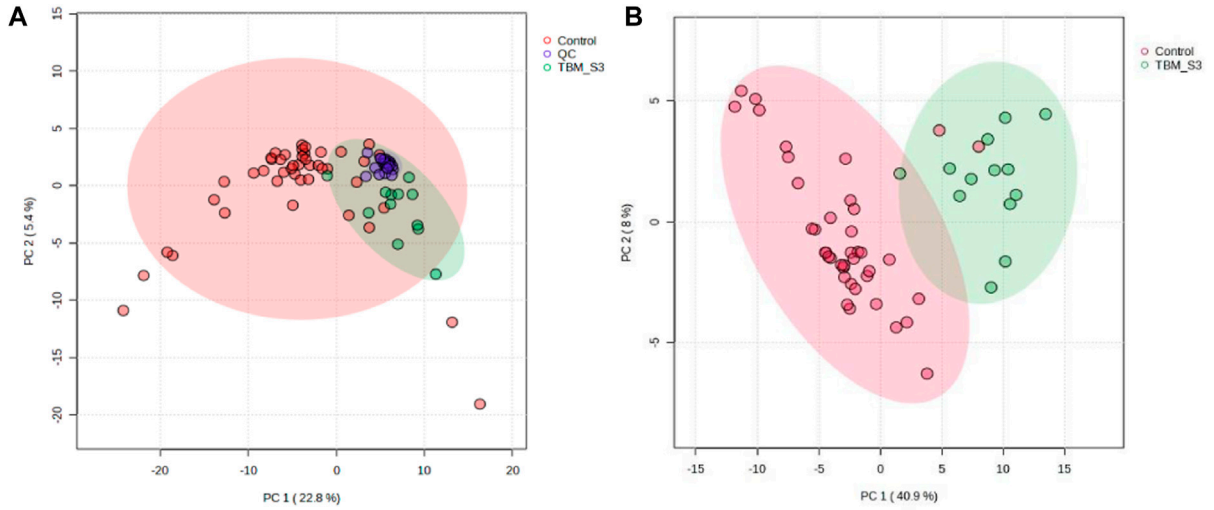

FIGURE 2
PCA scores plots. **(A)** (Left): Quality controls (QCs) and all cases–20 QCs, 44 controls and 13 TBM cases at initial treatment (TBM), with 95% CI ellipses. The total explained variance from PC1 and PC2 is 28.2%. **(B)** (Right): Reduced cases (without QCs)–40 controls and 13 TBM cases at initial treatment (TBM), with 95% CI ellipses. The total explained variance from PC1 and PC2 is 48.9%.

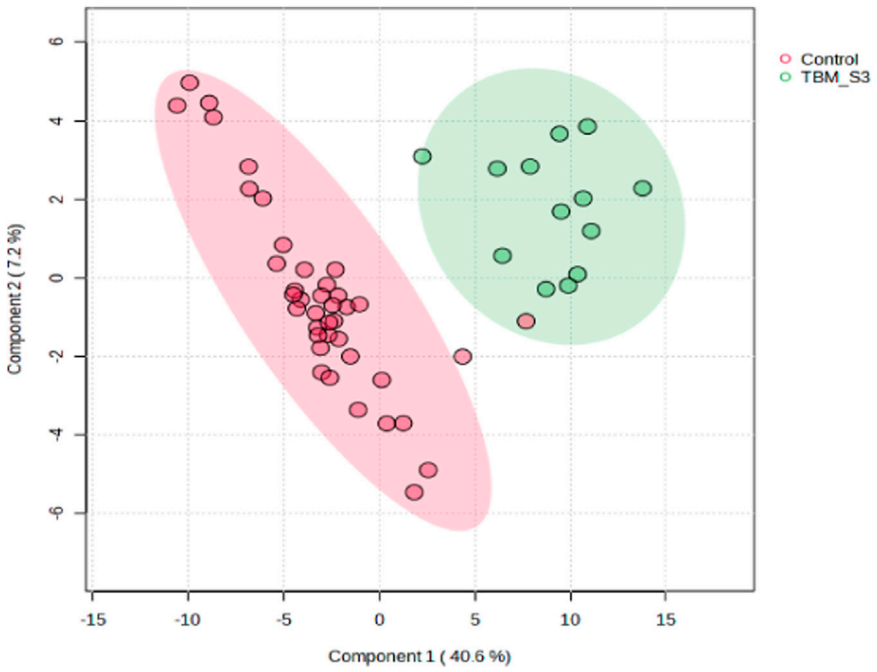

FIGURE 3
Supervised PLS-DA scores plot of 40 controls and 13 TBM cases at initial treatment (TBM), with 95% CI ellipses. The total explained variance from component 1 and component 2 is 47.8%.

rule: (VIP comp one and comp 2 > 1.0) OR (p-value FDR ≤0.05 and absolute fold change ≥2.0) (see Supplementary Table S1). Pure compound ^{1}H NMR spectral libraries were used to annotate most of the important bins that discriminated between the 40 controls and the 13 cases of TBM at initial treatment. Several important bins contained either pure forms of medications, or their metabolites: 1,2-propanediol, acetaminophen, isoniazid, isonicotinic acid, acetylisoniazid, pyrazine carboxamide, pyrazine carboxylic acid, 2-pyridin-4-formidoacetic acid, 5-hydroxy-2-pyrazine carboxylic acid. 1,2-Propanediol (or propylene glycol) is used as a solvent for the preparation of pharmaceuticals and is a common vehicle for some paediatric medication (Komoroski et al., 2000). Aspirin, or acetylsalicylic acid, is a medication in the family of salicylates and the derivative salicyluric acid (2-hydroxyhippuric

10.3389/fmolb.2024.1253983

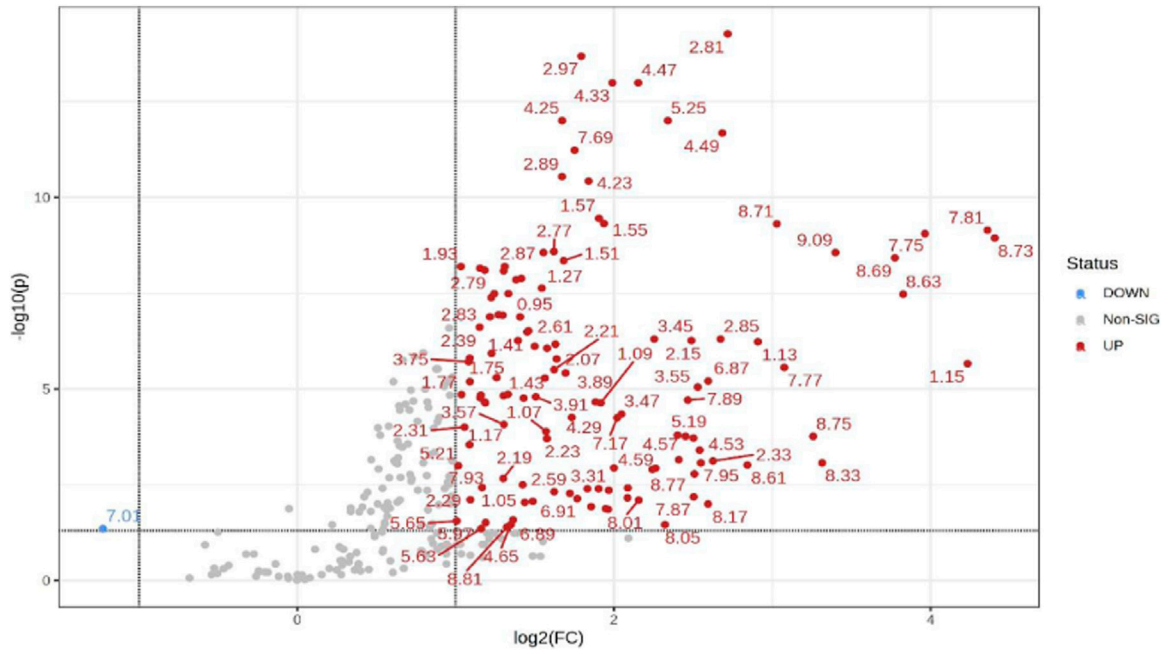

FIGURE 4
Volcano plot showing univariate statistically significant bins. Thresholds of absolute fold change ≥2.0 (log2) and *p*-value ≤0.05 (log10) are given as dotted lines. The red circles represent features above the threshold–notably, almost all significant bins are increased in TBM cases. Note that both fold changes and *p*-values are log transformed on the axes.

acid) is the glycine conjugation product (Erasmus et al., 2019). Isoniazid–a first-line TB treatment drug, was identified, along with two of its metabolites–isonicotinic acid, acetylisoniazid. Four metabolites (pyrazine carboxamide, pyrazine carboxylic acid, 2-pyridin-4-formidoacetic acid, 5-hydroxy-2-pyrazine carboxylic acid) of the first-line TB drug pyrazinamide were also identified. These medications are excluded from our discussion because they are of exogenous origin. A total of 29 metabolites were identified that characterize the urinary metabolic profile of the TBM cases in this cohort. The relative concentrations (μmol/mmol creatinine) of 28 metabolites were calculated (Figures 5–8) and the *p*-value and effects size were determined (Table 2). The resulting 28 metabolites were classified as: perturbed amino acid metabolism Figure 5: a) quinolinic acid, b) tyrosine, c) leucine, d) 3-hydroxyisobutyric acid, e) lysine, f) isoleucine, g) valine, h) glycine]; gut microbiota perturbation Figure 6: a) o-cresol, b) 4-hydroxyphenylacetic acid, c) m-cresol, d) formic acid, e) arabinose, f) hippuric acid, g) methylamine, h) methylguanidine]; perturbed energy metabolism Figure 7: a) myo-inositol, b) 3-hydroxyisovaleric acid, c) glucose, d) sucrose, e) mannose, f) pyruvic acid]; ketoacidosis [Figure 8: a) acetone, b) acetic acid, c) acetoacetic acid]; altered vitamin B metabolism Figure 8: d) 1-methylnicotinamide, e) trigonelline]; increased nitrogen excretion Figure 8: f) N-acetylglutamine, as well as increased urea–not quantified].

4 Discussion

The 29 significant urinary metabolites identified in this study can be categorized in terms of six dysregulated metabolic pathways. 1) Upregulated tryptophan catabolism (quinolinic acid) linked to an altered vitamin B3 metabolism (1-methylnicotinamide, trigonelline). 2) Perturbation of amino acid metabolism (leucine, lysine, isoleucine, glycine, tyrosine, valine). 3) Increased energy production–metabolic burst (3-hydroxyisobutyric acid, 3-hydroxyisovaleric acid, glucose, mannose, myo-inositol, pyruvic acid, sucrose). 4) Disrupted gut microbiota metabolism (4-hydroxyphenylacetic acid, arabinose, formic acid, hippuric acid, m-cresol, methylamine, methylguanidine, o-cresol). 5) Ketoacidosis (acetic acid, acetoacetic acid, acetone). 6) Increased nitrogen excretion (urea, N- acetylglutamine). We provide biological context by describing the characterization of the urinary metabolic profile of TBM in the discussion below.

4.1 Upregulated tryptophan catabolism

Quinolinic acid (Figure 5A) was significantly elevated in the urine of the TBM patients (71.57 ± 49.42 μmol/mmol creatinine) compared to the controls (0 μmol/mmol creatinine; $p < 0.001$, d = 2.9). Quinolinic acid was completely absent (or below the detection limit of the NMR spectrometer) in all control cases. This suggests that quinolinic acid would be an excellent candidate as a potential urinary diagnostic marker for TBM–to be tested in a future study.

Tryptophan is a key amino acid required for protein biosynthesis, and a precursor for the synthesis of a diversity of other metabolites (Davis et al., 2019); the most reported on, in the case of TB (Campbell et al., 2014; Manyelo et al., 2019), is the kynurenine pathway, via the *M. tb* infection-induced pro-inflammatory cytokines IL-6, TNF-α, and IFN-γ, upregulating

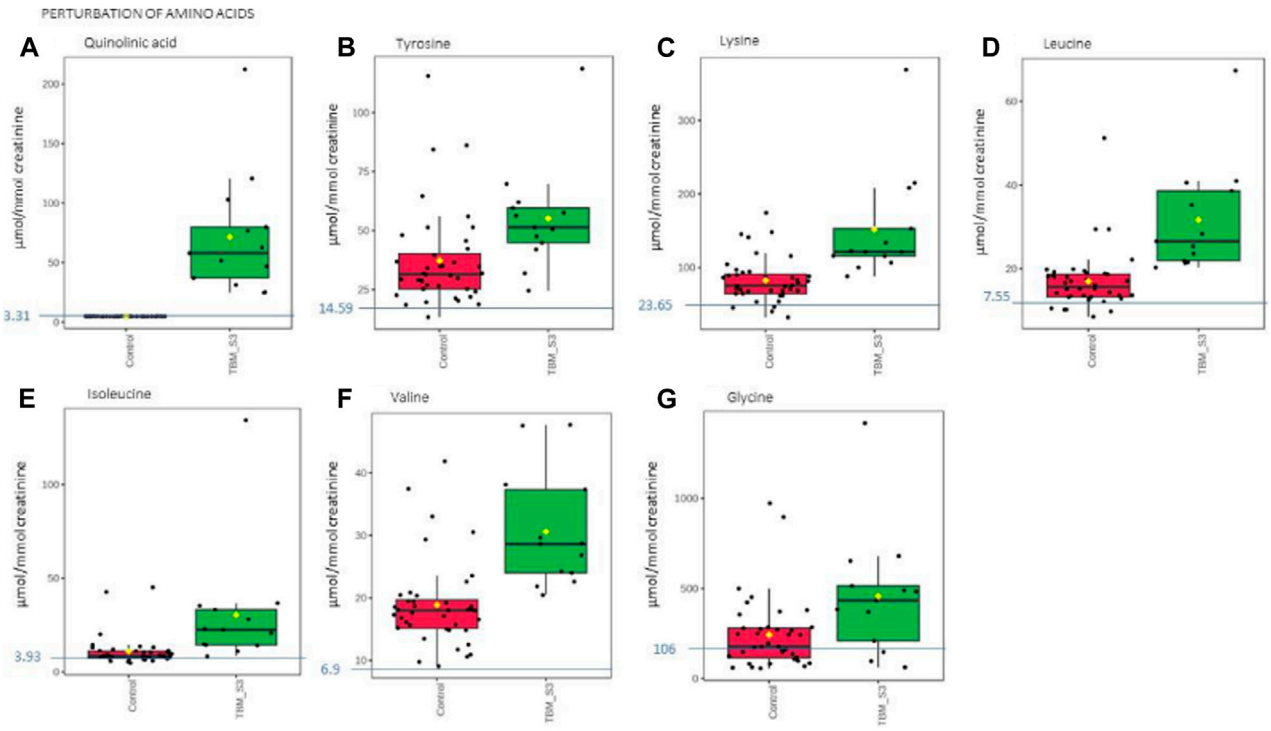

FIGURE 5
Box plots of the relative concentration (µmol/mmol creatinine) of seven urinary metabolites **(A)** quinolinic acid, **(B)** tyrosine, **(C)** lysine, **(D)** leucine, **(E)** isoleucine, **(F)** valine, **(G)** glycine] identified as being part of perturbation of amino acid metabolism in TBM. Green = TBM cases; red = controls. Blue line (and number) indicates normal reference value, based upon www.hmdb.ca and Bouatra *et al.* (2013).

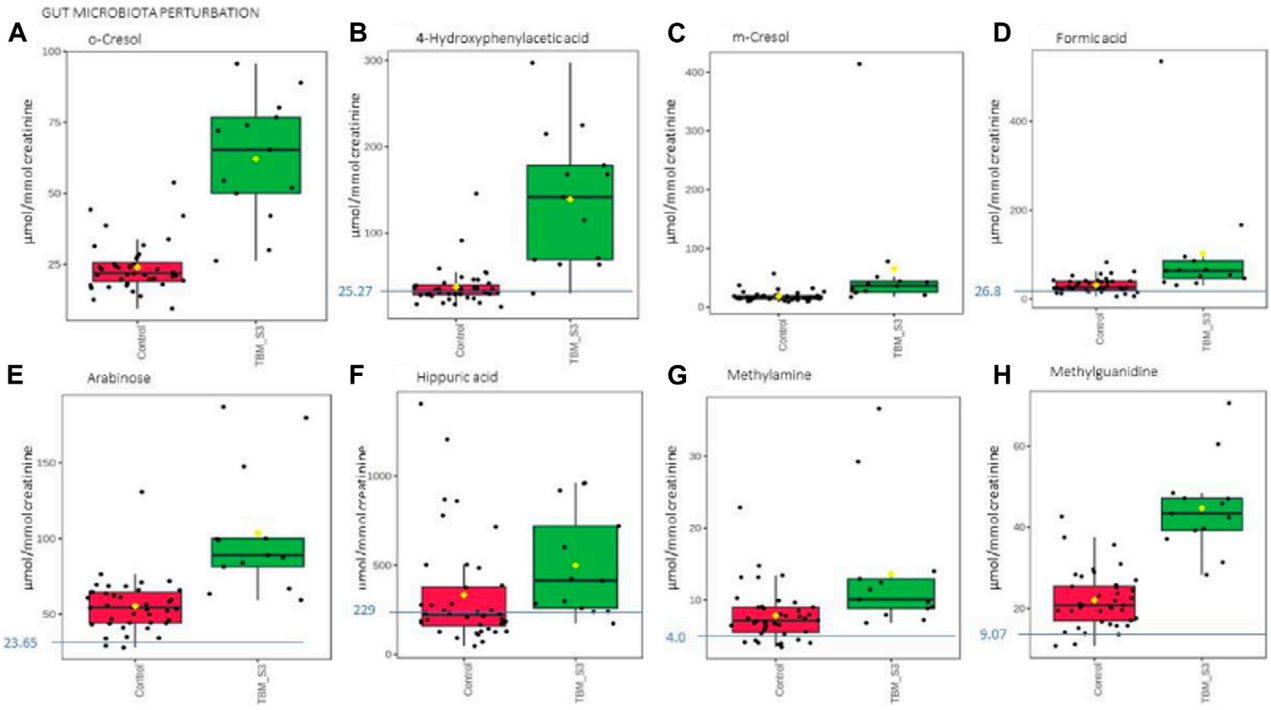

FIGURE 6
Box plots of the relative concentration (µmol/mmol creatinine) of eight urinary metabolites **(A)** o-cresol, **(B)** 4-hydroxyphenylacetic acid, **(C)** m-cresol, **(D)** formic acid, **(E)** arabinose, **(F)** hippuric acid, **(G)** methylamine, **(H)** methylguanidine] identified as being part of gut microbiota perturbation in TBM. Green = TBM cases; red = controls. Blue line (and number) indicates normal reference value, based upon www.hmdb.ca and Bouatra *et al.* (2013).

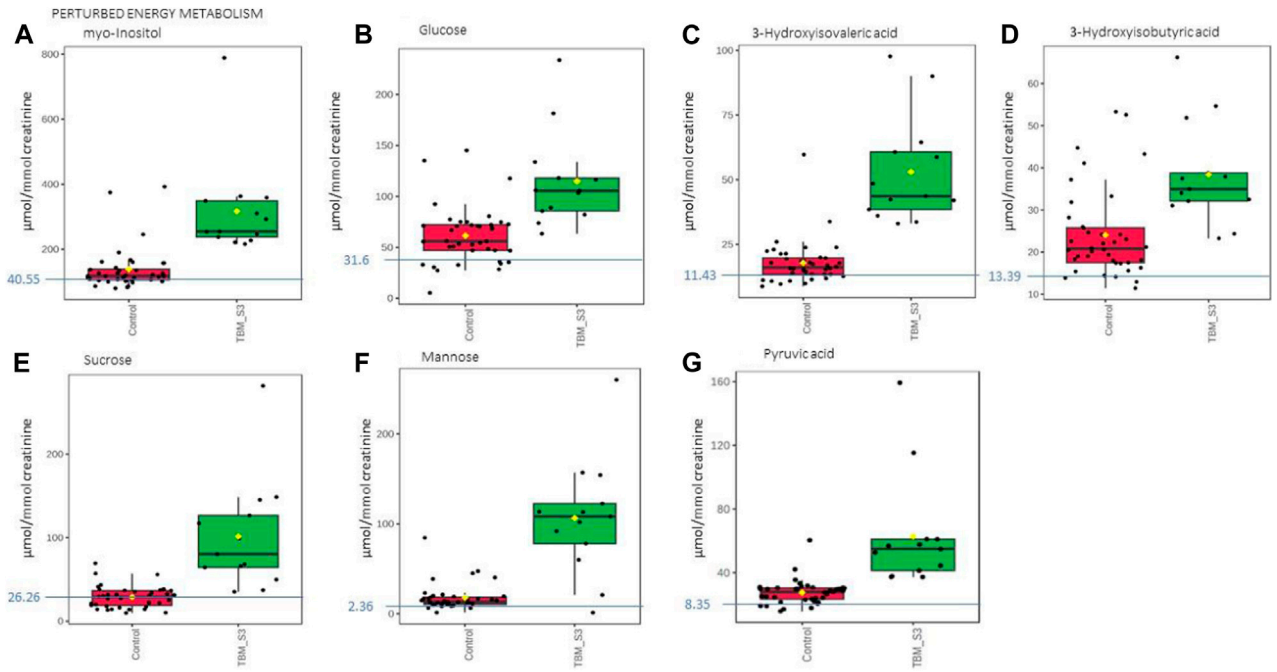

FIGURE 7
Box plots of the relative concentration (µmol/mmol creatinine) of seven urinary metabolites **(A)** myo-inositol, **(B)** glucose, **(C)** 3-hydroxyisovaleric acid. **(D)** 3-hydroxyisobutyric acid, **(E)** sucrose, **(F)** mannose, **(G)** pyruvic acid] identified as being part of perturbed energy metabolism in TBM. Green = TBM cases; red = controls. Blue line (and number) indicates normal reference value, based upon www.hmdb.ca and Bouatra *et al.* (2013).

indoleamine 2,3-dioxygenase (IDO) (Campbell et al., 2014). Quinolinic acid (a downstream metabolite of tryptophan), induced via IDO-1 (Heyes et al., 1992), has been associated with a variety of inflammatory disorders, elevated, and also detected in elevated concentrations in the CSF and brain tissue of patients with a wide range of infectious and other neurological diseases (Heyes et al., 2001), produced in large quantities by activated macrophages and microglia (Heyes et al., 1996). Of note, a study on the CSF collected from adult TBM cases done by van Laarhoven *et al.* (2018) identified tryptophan metabolism as one of the most upregulated metabolic pathways in TBM cases, with downstream upregulated tryptophan metabolism reflected by the kynurenine pathway. Their study examined an adult cohort of 33 TBM cases against 22 controls; with a further validation study of 101 TBM cases verses 17 controls. Of the metabolites identified in the initial study, 250 metabolites were increased and 18 decreased in TBM. Van Laarhoven *et al.* further examined the initial 33 TBM cases and identified 16 as survivors and 17 as non-survivors; 13 metabolites were shown to be increased in TBM survivors compared to controls and even higher in TBM non-survivors compared to TBM survivors. Of the 13 metabolites identified, three metabolites, including tryptophan, were found to be decreased in non-survivors compared to controls, and also decreased in TBM survivors *versus* TBM non-survivors. Van Laarhoven *et al.* then carried out a validation study on CSF tryptophan with 101 TBM cases *versus* 17 controls; that identified IDO-1 as having greater expression in TBM. However, in all of these investigation studies, there is no report of the metabolites that characterize TBM. In a study characterizing the CSF immunological signature of TBM in a cohort of 23 children (Manyelo et al., 2019), a 3-marker signature associated with neuroinflammation (VEGF, IFN-γ, and MPO) showed strong potential as a diagnostic tool for TBM in children with promising accuracy. We modelled the downstream metabolic effects expected from VEGF, IFN-γ, and MPO and predicted pivotal altered metabolic pathways that would be reflected in the urinary profiles of TBM subjects (Isaiah et al., 2020). Quinolinic acid was one of the major metabolic end-products that we predicted to come from this, within the *M. tb*-infected brain, induced by an increased IFN-γ. Urinary quinolinic acid was also observed in the TBM patients' urine samples in a similar untargeted urinary ^{1}H NMR metabolomics study carried out by Mason *et al.* (2016b). Quinolinic acid is not only expected in abundance in the *M. tb*-infected brain, but also produced by the enteric nervous system in the gut caused by dysbiosis, in conjunction with a perturbed gut–brain axis (Isaiah et al., 2020).

4.2 Altered vitamin B3 metabolism

Trigonelline (1-methylnicotinic acid) was significantly elevated (Figure 8E) in the urine of the TBM patients (18.65 ± 12.58 µmol/mmol creatinine) when compared to that of the controls (6.94 ± 7.96 µmol/mmol creatinine; $p = 0.008$, d = 1.14). 1-Methylnicotinamide, the methylated amide of nicotinic acid, was also significantly elevated (Figure 8D) in the urine of the TBM patients (45.30 ± 25.22 µmol/mmol creatinine) when compared to that of the controls (10.61 ± 12.83 µmol/mmol creatinine; $p < 0.001$, d = 1.82). Both 1-methylnicotinic acid and 1-methylnicotinamide are products of an upregulated kynurenine metabolism (Cazzullo et al., 1976), and, within

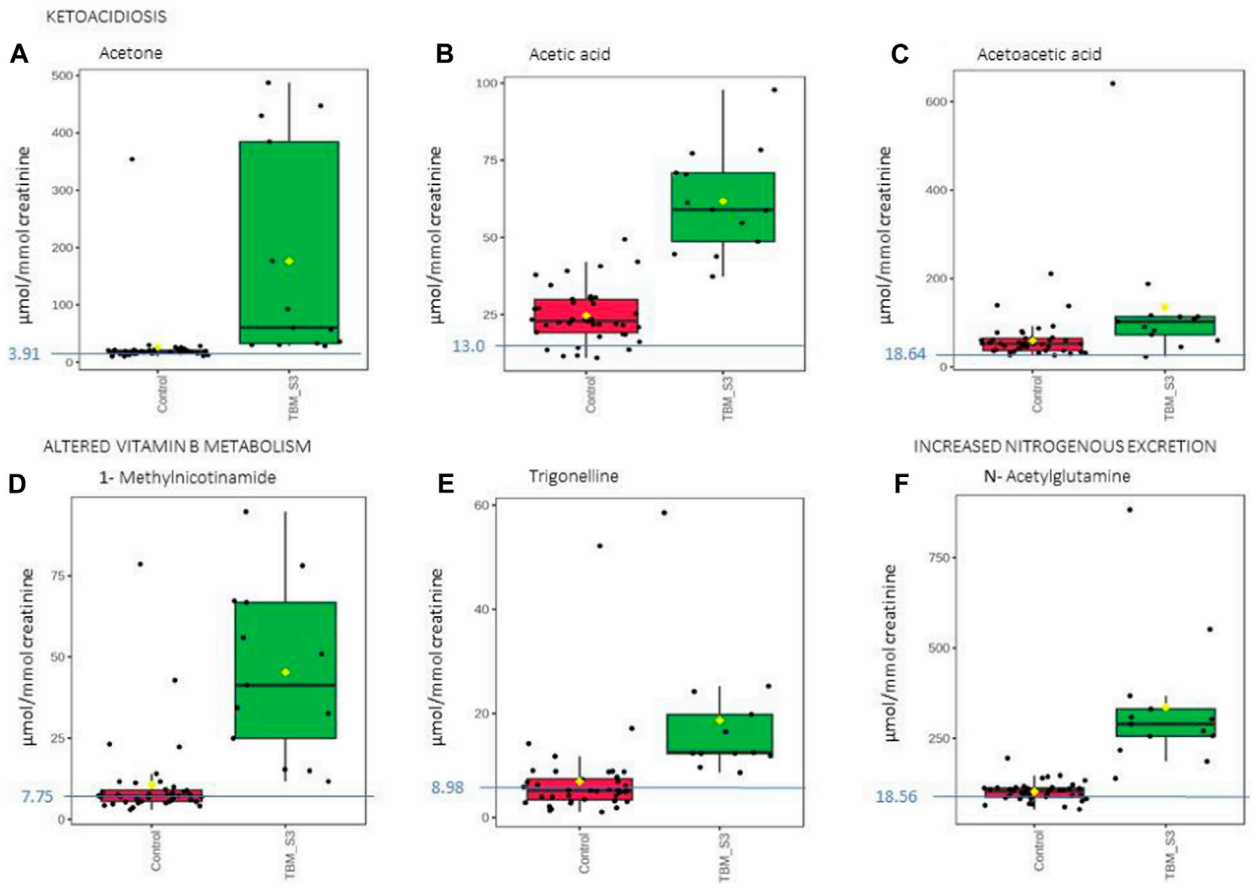

FIGURE 8
Box plots of the relative concentration (µmol/mmol creatinine) of six urinary metabolites identified as being part of ketoacidosis **(A)** acetone, **(B)** acetic acid, **(C)** acetoacetic acid], altered vitamin B metabolism **(D)** 1-methylnicotinamide, **(E)** trigonelline] and increased nitrogen excretion **(F)** N-acetylglutamine] in TBM. Green = TBM cases; red = controls. Blue line (and number) indicates normal reference value, based upon www.hmdb.ca and Bouatra *et al.* (2013).

the tryptophan–nicotinic acid metabolism, 1-methylnicotinamide is an end-product of nicotinamide (vitamin B3) metabolism. Nicotinamide is the precursor of the coenzymes β-nicotinamide adenine dinucleotide (NAD) and nicotinamide adenine dinucleotide phosphate (NADP), which are involved in a variety of enzyme-mediated oxidation and reduction reactions (Li et al., 2006; Zhou et al., 2009). Excess nicotinamide is methylated, oxidized or hydroxylated to 1-methylnicotinamide, nicotinamide-N-oxide or 6- hydroxynicotinamide, respectively, and then 1-methylnicotinamide is further oxidized to the pyridones 1-methyl-2-pyridone-5-carboxamide (2Py) and 1-methyl-4-pyridone-3-carboxamide by aldehyde oxidase (Zhou et al., 2009; Mayneris-Perxachs et al., 2016). 2Py and 1-methylnicotinamide are the major common nicotinamide metabolites found in human urine (Kitamura et al., 2008). A study by Zhou *et al.* (2009) showed that 1-methylnicotinamide clearance was delayed in diabetic patients, suggesting that 1-methylnicotinamide could cause oxidative stress and insulin resistance (discussed further below). 1-Methylnicotinamide may also play a role in the progression of Parkinson's disease, as a result of a superoxide anion formed by 1-methylnicotinamide via mitochondria (Fukushima et al., 2002; Williams et al., 2005), associated with elevated oxidative stress (Smeitink et al., 2004), and also with major depressive disorders (Zheng et al., 2013); hence, associating increased urinary 1-methylnicotinamide to several neurological and inflammatory conditions. In this study, the significantly elevated concentrations of 1-methylnicotinamide, is most likely due to the increased flux through the kunurenine pathway induced by INF-γ, and generation of reactive oxygen species (ROS) and reactive nitrogen species (RNS)–the consequences of severe oxidative stress and impaired redox status, associated with TB (Reddy et al., 2009; Miric et al., 2013).

4.3 Perturbation of amino acid metabolism

The urinary concentrations of tyrosine (Figure 5B) were significantly elevated in the TBM patients (55.09 ± 21.81 µmol/mmol creatinine) compared to the controls (37.2 ± 20.14 µmol/mmol creatinine; $p = 0.021$, d = 0.85). Phenylalanine and tyrosine are aromatic amino acids, synthesized from phosphoenolpyruvate and erythrose 4-phosphate–intermediates of glycolysis and the pentose phosphate pathway, respectively (Ferreira and Teixeira, 2003). Phenylalanine is catabolized into acetoacetic acid and fumaric

TABLE 2 Data of the quantified (concentration: μmol/mmol creatinine) important metabolites (n = 28) that characterize TBM. A *p*-value ≤0.05 indicates statistical significance, and a Cohen's d effect size ≥0.6 indicates practical significance.

Metabolites (chemical shift)	HMDB ID	*p*-value	Effect size
1-Methylnicotinamide (9.29)	HMDB0000699	<0.001	1.82
3-Hydroxyisobutyric acid (1.08)	HMDB0000023	0.001	1.3
3-Hydroxyisovaleric acid (1.27)	HMDB0000754	<0.001	2.48
4-Hydroxyphenylacetic acid (6.88)	HMDB0000020	<0.001	2.07
Acetic acid (1.92)	HMDB0000042	<0.001	2.97
Acetoacetic acid (2.29)	HMDB0000060	0.111	0.81
Acetone (2.33)	HMDB0001659	0.014	1.29
Arabinose (4.54)	HMDB0000646	0.001	1.67
Formic acid (8.46)	HMDB0000142	0.08	0.99
Glucose (4.67)	HMDB0000122	0.001	1.48
Glycine (3.57)	HMDB0000123	0.053	0.81
Hippuric acid (7.66)	HMDB0000714	0.096	0.57
Isoleucine (1.03)	HMDB0000172	0.052	0.99
Leucine (0.99)	HMDB0000687	0.002	1.49
Lysine (1.76)	HMDB0000182	0.007	1.34
Mannose (5.20)	HMDB0000169	<0.001	2.3
m-Cresol (2.31)	HMDB0002048	0.135	0.85
Methylamine (2.60)	HMDB0000164	0.043	0.93
Methylguanidine (2.83)	HMDB0001522	<0.001	2.56
myo-Inositol (4.09)	HMDB0000211	0.001	1.71
N-Acetylglutamine (2.08)	HMDB0006029	<0.001	2.21
o-Cresol (2.21)	HMDB0002055	<0.001	2.58
Pyruvic acid (2.39)	HMDB0000243	0.004	1.70
Quinolinic acid (8.03)	HMDB0000232	<0.001	2.9
Sucrose (5.42)	HMDB0000258	0.002	1.89
Trigonelline (9.13)	HMDB0000875	0.008	1.14
Tyrosine (6.91)	HMDB0000158	0.021	0.85
Valine (1.05)	HMDB0000687	<0.001	1.48

Note: chemical shifts (ppm) of metabolites are given in brackets. HMDB ID refers to the identity number assigned to the metabolite in the Human Metabolome Database (www.hmdb.ca).

acid via tyrosine (Komoda and Matsunaga, 2015). Tyrosine is formed by the hydroxylation of phenylalanine in the liver when the intake of tyrosine is low (Litwack, 2018). Both these amino acids serve as precursors for the synthesis of many biologically/neurologically active compounds that are essential for maintaining a variety of biological functions (Han et al., 2019). The neurotransmitters epinephrine and norepinephrine are synthesized from the tyrosine metabolite L-3,4-dihydroxyphenylalanine (L-DOPA). Parkinson's disease and schizophrenia are thought to be caused by, amongst other factors, a lack of these neurotransmitters (Komoda and Matsunaga, 2015). Hyperphenylalaninemia (HPA), a disorder resulting in levels of phenylalanine that are excessive, is caused by a deficiency of the hepatic phenylalanine-4-hydroxylase (PAH) or its cofactor tetrahydrobiopterin (BH4), and clinically presents with a number of neurological signs and symptoms, such as irritability, hyperkinesis, and severe cognitive deficiency, often associated with TBM (Blau et al., 2014). In TB patients, altered metabolism of phenylalanine and tyrosine was previously observed in a pilot study that compared the urine metabolic profiles of 21 adults [33]; this alteration was confirmed in *M. tb*-infected mice (Shin et al., 2011; Weiner et al., 2012). These studies support our findings of significantly elevated tyrosine in advanced TBM when compared to controls.

Glycine concentrations (Figure 5G) were elevated in the TBM patients (457.19 ± 336.45 μmol/mmol creatinine) when compared to

that of the controls (242.51 ± 194.75 μmol/mmol creatinine; p = 0.053, d = 0.81), at a practically significant level (d > 0.6). Glycine functions as a neurotransmitter in the brain, allowing neurons to communicate with one another, and subsequently regulates neuronal activity (Shahsavar et al., 2020). Many of the clinical signs and symptoms of TBM, such as low muscle tone, lethargy, seizures, coma, and apnea requiring ventilator support, are associated with glycine accumulation in the brain and neural tissue (DeArmond et al., 2017). Glycine transporters, both astrocytic GlyT1 and presynaptic neuronal GlyT2, are critical for proper glycine recycling at glutamatergic and glycinergic synapses. A number of key studies have shown that microglial activity is modulated by astrocyte-derived glycine and L-serine (Van Den Eynden et al., 2009). Glycine at micromolar concentrations changes the morphology of microglial cells and increases the secretion of nitrogen oxide, superoxide, acid phosphatase, and their metabolic activity when induced by lipopolysaccharides (LPS) (Van Den Eynden et al., 2009). LPS are also well-known for their ability to stimulate the production of proinflammatory cytokines (Jansky et al., 2003; Schildberger et al., 2013), especially IL-6 and IFN-γ, all of which (LPS and the associated cytokines) are also elevated in TB patient blood (Feruglio et al., 2013; Gallucci et al., 2021). Several of the clinical symptoms associated with HPA and an accumulation of glycine in the brain are similar to those clinical symptoms seen in TBM–e.g., altered consciousness and behavior. Thus, the treatment of these amino acid imbalances is a potential basis of therapy to alleviate the symptoms found in TBM cases–something that needs to be tested in a future study.

The branched chain amino acids were all increased in the TBM group–leucine (Figure 5D): 31.67 ± 12.64 μmol/mmol creatinine, isoleucine (Figure 5E): 30.5 ± 31.27 μmol/mmol creatinine and valine (Figure 5F): 31.67 ± 12.64 μmol/mmol creatinine, relative to the controls–leucine: 16.95 ± 7.05 μmol/mmol creatinine; p = 0.002, d = 1.49, isoleucine: 10.95 ± 8.08 μmol/mmol creatinine; p = 0.052, d = 0.99, valine: 18.88 ± 6.9 μmol/mmol creatinine; $p < 0.001$, d = 1.48. One of the most crucial building blocks for gluconeogenesis are free amino acids, which become elevated when protein synthesis is impaired. These findings are in line with other reports of wasting (cachexia) and malnutrition, also known as "anabolic block," in TB patients. Here, the term "anabolic block" describes a higher proportion of ingested amino acids being oxidized than being used for protein anabolism (MacAllan et al., 1998; Macallan, 1999; Schwenk and Macallan, 2000). Hence, the significant increase in BCAAs may likely be caused by the increased proteolysis needed to meet the elevated demand for amino acids that are used as fuel sources for energy production during infection (Levin et al., 1983). It is also well recognized that branched chain amino acids (BCAAs) contribute to important metabolic processes in the brain, such as the gluconeogenesis that occurs in activated microglia, as a source of energy during an activated immune response (Sweatt et al., 2004). Furthermore, numerous other pathological conditions are associated with changes to amino acid levels in body fluids (Binici et al., 2023). The level of total amino acids in CSF was measured and examined in a 1981 study on patients who had viral meningitis and TBM. Patients with TBM were found to have significantly higher concentrations of total amino acids, which included leucine, isoleucine and valine (Corston et al., 1981). In a recent investigation of the predictive value of amino acids for bacterial, aseptic, and tuberculous meningitis (n = 41, 41, and 21, respectively), against healthy controls (n = 64), carried out by Binici *et al.* (2023), all BCAAs were found to be significantly increased in TBM subjects, confirming the results. In a ^{1}H NMR-based metabolomics study, serum BCAAs were increased in *M. tb*-infected rats, as compared to control rats (Shin et al., 2011) giving support to what we are seeing in this paediatric study population. In conditions of perturbed energy metabolism, as reported by Mason *et al.* (2016b), as analyzed using urine from a similar pediatric TBM cohort, elevated concentrations of hydroxyl acids derived from BCAAs leucine (3-hydroxyisovaleric acid) isoleucine (2-methyl-3-hydroxybutyric acid) and valine (3- hydroxyisobutyric acid) were shown in a putative urinary biosignature. The present study also indicates a comparable metabolic increase in BCAAs to that observed in CSF of children with TBM by Mason *et al.* (2015).

Lastly, lysine, an important amino acid known to facilitate protein synthesis (Chang and Gao, 1995) (Figure 5C) was also significantly increased in the TBM cases (151.55 ± 72.73 μmol/mmol creatinine) when compared to that of the controls (82.59 ± 29.84 μmol/mmol creatinine; p = 0.007, d = 1.34). Via it's already well described neuroprotective and neurotrophic effects, lysine has been shown to enhance neurological function and cerebral blood flow in patients with ischemic stroke (Kondoh et al., 2010). According to reports, intellectual disability and other motor neuron impairment are associated with elevated levels of lysine in the CSF of TBM patients (Shaw et al., 1995a). Additionally, it has been demonstrated to form adducts with various substances, including acrolein-lysine, a marker of lipid peroxidation in pediatric meningitis (Tsukahara et al., 2002). Children with persistent atopic dermatitis have also been shown to exhibit considerably higher urine excretion of acrolein-lysine adducts than do healthy children (unpublished data) (Tsukahara et al., 2002). In this investigation, all TBM patients showed elevated lysine concentration, which is in support of the aforementioned reports, and that of Mason *et al.* (2017), who investigated the utilization of amino acids in CSF, in order to distinguish TBM from healthy controls.

4.4 Metabolic burst energy metabolites

In this study, urinary glucose (Figure 7A) was significantly elevated in the TBM patients (114.82 ± 44.86 μmol/mmol creatinine) compared to the controls (61.35 ± 27.63 μmol/mmol creatinine; p = 0.001, d = 1.48). Other significantly increased urinary saccharides in TBM included mannose (106.26 ± 62.42 μmol/mmol creatinine) and sucrose (101.48 ± 63.86 μmol/mmol creatinine) when compared to the controls, respectively (17.83 ± 14.63 μmol/mmol creatinine; $p < 0.001$, d = 2.3 and 28.83 ± 12.95 μmol/mmol creatinine; p = 0.002, d = 1.89). Myo-inositol (Figure 7A) and pyruvic acid (Figure 7G) were also identified by statistical analysis in this study as being significantly increased in TBM (317.02 ± 145.37 μmol/mmol creatinine and 62.79 ± 34.04 μmol/mmol creatinine, respectively) when compared to the controls (137.99 ± 64.29 μmol/mmol creatinine; p = 0.001, d = 1.71 and 27.41 ± 7.49 μmol/mmol creatinine; p = 0.004, d = 1.70, respectively).

These increased metabolites–glucose, mannose, sucrose, myo-inositol, pyruvic acid, 3- hydroxyisobutyric acid and 3-hydroxyisovaleric acid–can be linked to metabolic burst, associated with an increased need for energy production in the *M. tb*-infected brain (Mason et al., 2015; Mason, 2017; van Zyl et al., 2020). Glucose is the primary metabolite that is catabolized for neuroenergetics purposes. However, uncontrolled glucose utilization in the brain may subsequently lead to insulin resistance, and transitory glucose oxidation via glucose oxidase during unregulated glucose metabolism. According to a growing body of evidence, chronic neuroinflammatory diseases, such as TBM, are known to be linked to insulin resistance (Isaiah et al., 2020). The oxidation of glucose produces gluconolactone, an inflammatory marker previously observed in pulmonary TB (Preez et al., 2017), when insulin becomes depleted. Gluconolactone is siphoned into the pentose phosphate pathway and leads to elevated levels of hydrogen peroxide (Preez et al., 2017). Various studies (Hampton et al., 1998; Podrez et al., 2000; Klebanoff, 2005; Manyelo et al., 2019) have shown that myeloperoxidase, identified as an immunological marker of TBM, interacts with hydrogen peroxide and triggers a variety of oxidative stress pathways. In our previously published downstream metabolic model of TBM (Isaiah et al., 2020), we predicted end products of myeloperoxidase activation, namely, glutathione sulfonamide and 3- chlorotyrosine. Although we did not detect these two products in the urine of the TBM patients using ^{1}H-NMR, it is highly likely that other more sensitive analytical methods (e.g., liquid chromatography coupled to mass spectrometry) may detect these and this could be considered for a later study.

In the brain, lactate has neuroprotective properties, associated with a shuttling neuroenergetic mechanism (Mason, 2017). However, this shuttling role of lactate is compartmentalized within the brain during TBM, and urinary lactate levels do not significantly increase during such times. Systemically, lactate is converted to pyruvate, leading to significantly increased urinary levels of pyruvate in TBM, and an increased conversion of NAD + to NADH. This signals an increased levels of redox and oxidative stress, as previously described in the predictive urinary TBM model by Isaiah *et al.* (2020). This is evidenced when looking at the urinary lactate:pyruvate (Lac:Pyr) ratio, and TBM cases have a significantly lower ($p = 0.004$) Lac-Pyr ratio of 2.43, when compared to that of the controls (6.32). An additional measure of the redox status can be done by determining the ratio of 3-hydroxybutyric acid:acetoacetic acid (3HB:AAA), which is significantly lower ($p < 0.001$) in the TBM cases (1.12), than in the controls (1.93).

3-Hydroxyisobutyric acid, a downstream catabolite of valine metabolism (Ko et al., 1991) (Figure 7D), was significantly increased in the TBM group (38.41 ± 11.78 μmol/mmol creatinine), as well as was the leucine catabolite 3-hydroxyisovaleric acid (Figure 7C, 53. ± 20 μmol/mmol creatinine), when compared to the controls, respectively (24.06 ± 10.32 μmol/mmol creatinine; $p = 0.001$, d = 1.3 and 17.85 ± 8.39 μmol/mmol creatinine; $p < 0.001$, d = 2.48). Both of these hydroxy acids gave further support for the metabolites associated with a perturbed energy state in TBM (Mason et al., 2016b). The accumulation of 3-hydroxyisobutyric acid and 3-hydroxyisovaleric acid, subsequently feeds into the anaplerotic Krebs cycle, for primary energy production. Coincidently, the *M. tb* bacilli also utilize the TCA cycle for their own energy production (Savvi et al., 2008). An additional indicator of perturbed energy metabolism is the elevated myo-inositol detected in the paediatric TBM patients. Myo-inositol is mostly made from glucose (Hauser and Finelli, 1963) and is a key signaling molecule required for immunological responses, such as microglia activation. Myo-inositol has previously been linked to microglia and astrocyte activation, as well as a pathogenic response seen in neurodegenerative illness and neuroinflammation (Pears et al., 2005). Increased CSF myo-inositol in TBM patients has also been reported previously (van Zyl et al., 2020), and this study shows that this is a systemic condition in TBM that is likely linked to uncontrolled glucose utilization.

Mannose is interesting because it is described as being ubiquitous (i.e., it occurs everywhere). It is grouped under energy metabolism here since it is a sugar but mannose can also come from lipoarabinomannan (LAM), one of the key components of the *M. tb* cell wall (Van Toorn et al., 2014). In lab grown *M. tb*, LAM was shown to be composed of D-arabinose (55%–60%), D-mannose (36%–40%), and fatty acyls (1%–3%; palmitate C:16; tuberculostearate (TBSA) C:19:1) (Amin et al., 2021). Further examination of the role of mannose is however still needed.

4.5 Disrupted gut microbiota metabolism

Eight of the metabolites listed in Table 2 are urinary indicators of altered metabolism associated with the gut microbiota. A significant increase of 4-hydroxyphenylacetic acid (Figure 6B) was observed in TBM urine (138.78 ± 75.85 μmol/mmol creatinine) compared to the controls (37.45 ± 22 μmol/mmol creatinine; $p < 0.001$, d = 2.07). Elevated levels of o-cresol (Figure 6A) and m-cresol (Figure 6C) (62.15 ± 20.88 μmol/mmol creatinine and 65.57 ± 101.77 μmol/mmol creatinine, respectively) were found in TBM compared to the controls (24.02 ± 8.67 μmol/mmol creatinine; $p < 0.001$, d = 2.58 and 18.5 ± 8.7 μmol/mmol creatinine; $p = 0.135$, d = 0.85, respectively). Other elevated urinary gut microbiota metabolites were formic acid (Figure 6D), methylamine (Figure 6G) and methylguanidine (Figure 6H) (102.66 ± 129.4 μmol/mmol creatinine, 13.56 ± 8.65 μmol/mmol creatinine and 44.7 ± 10.8 μmol/mmol creatinine, respectively), when compared to the controls (31 ± 16.06 μmol/mmol creatinine; $p = 0.08$, d = 0.99, 7.82 ± 3.64 μmol/mmol creatinine; $p = 0.043$, d = 0.93 and 22.03 ± 6.9 μmol/mmol creatinine; $p < 0.001$, d = 2.56). Hippuric acid was identified by statistical analyses as significant based upon the ^{1}H NMR spectral data (Table 2). However, the concentration data (Figure 6F) of hippuric acid did not show statistical significance ($p = 0.096$, d = 0.57). Lastly, arabinose (Figure 6E) was identified from the untargeted ^{1}H-NMR data as being statistically significant in TBM cases (103.45 ± 40.2 μmol/mmol creatinine) compared to the controls (55.47 ± 17.21 μmol/mmol creatinine; $p = 0.001$, d = 1.67).

Arabinose is another ubiquitous metabolite that is produced by the host and gut microbiota, but is also a component of LAM (Amin et al., 2021). Previous studies have shown arabinose as a proxy for LAM in active TB (De et al., 2015). Hence, it's significantly elevated concentrations in this pediatric cohort of TBM cases, could be classified as a potential biomarker of *M. tb*–this requires further investigation. Arabinose has also been associated with other diseases. In a case of two autistic brothers, without any known metabolic disease, urinary arabinose concentrations were found to be six times greater than that in healthy children (Shaw et al., 1995b). Furthermore, increased

levels of arabinose have been reported to have an inhibitory effect on sucrase (Seri et al., 1996), which could account for the increased levels of urinary sucrose in TBM cases found in this study.

Some organic acids are produced, at least in part, by intestinal gut bacterial metabolism. Clinically, these organic acids can be used as an indirect indicator of dysbiosis (Chapman et al., 2020), and the higher the quantities of these bacterial metabolites in the urine, the greater the bacterial quantities and activity in the gastrointestinal tract (Chapman et al., 2020). Elevated urinary concentrations of gut microbiota metabolites. Chalmers *et al.* (1979) indicated that 4-hydroxyphenylacetic acid is synthesized when amino acids, such as phenylalanine and tyrosine–both elevated in TBM–are metabolized by intestinal bacteria. Tyrosine is degraded to tyramine, and then deaminated and oxidized eventually to form 4-hydroxyphenylacetic acid, which is then excreted unchanged and unconjugated in the urine (van Der Heiden et al., 1971; Fellaman et al., 1977). The latter occurs in children with small-bowel disease or in various bacterial overgrowth syndromes; Chalmers *et al.* (1979) subsequently concluded that urinary 4-hydroxyphenylacetic acid serves as a useful marker for the screening of gut disorders in children (Chalmers et al., 1979). It has also been determined that roughly 50% of cystic fibrosis patients, and some patients with confirmed or suspected TB, have elevated urinary concentrations of 4-hydroxyphenylacetic acid in both adults and children with different types of pulmonary disease (Garrettson et al., 1971; van Der Heiden et al., 1971). The occurrence of 4- hydroxyphenylacetic acid has also been linked to the breakdown of amino acids.

Hippuric acid, also known as benzoylglycine or benzoylamino-acetate, is the glycine conjugate of benzoic acid (Lees et al., 2013). Increased levels of urinary hippuric acid have been linked to several diseases, including dysbiosis. This supports its recognition as a biomarker for microbial changes in the gut (Williams et al., 2010; Chapman et al., 2020). In a gas chromatography–mass spectrometry (GC-MS) metabolomics study conducted on a similar paediatric cohort, Mason *et al.* (2016b) observed a significant increase of hippuric acid in the urine of TBM patients and attributed the observation to a drug-like phase II metabolic response of the host to products generated by the microbiota, indicating a highly active glycine-conjugated GLYAT-biotransformation system in TBM. Hence, the presence of increased urinary hippuric acid in TBM is supported by our previous metabolomics study, in which an alternative analytical platform was used.

Methylamine has been found in numerous tissues and bodily fluids, and it has been hypothesized that methylamine, and other closely similar short-chain aliphatic amines, may be involved in the abnormalities of the central nervous system seen during hepatic and renal disease, particularly when the blood-brain barrier is damaged. When compared to trimethylamine and dimethylamine, there is little information in the literature about the human urinary excretion of methylamine (Mitchell and Zhang, 2001; Pirisino et al., 2005; Guba et al., 2022). Methylguanidine is the immediate precursor to methylamine, thereby linking it to microbial metabolism, however, methylguanidine is also known to be an uremic (neuro)toxin (De Deyn et al., 2001) and an inhibitor of inducible nitric oxide synthase (iNOS), which is known to affect *M. tb* cerebral infection (Poh et al., 2022). Hence, methylguanidine is another metabolite of interest that is potentially produced directly by *M. tb*, and requires further investigation.

Formic acid is a common organic acid used and excreted by bacteria and no specific link has previously been made to TBM, however, formic acid has been associated as a potential biomarker of Alzheimer's disease, as a byproduct of the metabolism of formaldehyde (Wang et al., 2022). To our knowledge, no literature exists on the two cresols (o-cresol and m-cresol) detected as increased in TBM in this study, in relation to neuropathology.

Thus, these eight increased microbial metabolites originate almost exclusively from altered bacterial metabolism in the gut and are attributed to the severe TBM disease in this study. The occurrence of dysbiosis in TBM is supported by several studies and the results support further investigation of the gut–brain axis in TBM (Isaiah et al., 2020). A major limitation of this study is that we cannot account for treatment given to the TBM cases prior to admission to hospital, nor upon admission, and their effects on the gut microbiota.

4.6 Ketoacidosis

Ketoacidosis is a condition defined by increased ketone bodies, such as acetone, acetic acid and acetoacetic acid. Acetone (Figure 8A) and acetic acid (Figure 8B) were significantly elevated in the TBM cases (176.48 ± 179.09 μmol/mmol creatinine and 61.77 ± 16.25 μmol/mmol creatinine, respectively) compared to the controls (26.82 ± 52.59 μmol/mmol creatinine; $p = 0.014$, d = 1.29 and 24.73 ± 8.7 μmol/mmol creatinine; $p < 0.001$, d = 2.97, respectively). However, acetoacetic acid (Figure 8C) in the TBM group was not statistically different from the control group ($p = 0.111$), but were practically significant (d = 0.81).

Ketones are metabolic end-products of fatty acid metabolism that occurs in the liver (Dhillon and Gupta, 2021; Cruzat et al., 2018). During perturbed energy metabolism, or in the absence/diminished availability of carbohydrates, fats become the primary source of energy, and large levels of ketones are produced as a metabolic by-product. Hence, the occurrence of ketoacidosis also supports evidence for insulin resistance, as elevated glucose levels are found in TBM patients. The increased levels of ketone bodies indicate that this elevated glucose is not being used for energy production; instead, fatty acid metabolism has become the major source of energy production in TBM (Blau et al., 2014; Dhillon and Gupta, 2021).

Acetone, which may give the breath of ketotic patients a typical odor, is formed via the non-enzymatic decarboxylation of acetoacetate (Blau et al., 2014). The TBM group's urinary ketone values in this study are indicative of their poor clinical health. Ketoacidosis also supports the metabolic burst that we described previously. Several ketoacidosis markers were also identified in our previous GC-MS metabolomics study of TBM (Mason et al., 2016b), which included the ketosis markers 2- hydroxybutyric acid, 3-hydroxybutyric acid, 2-methyl-3-hydroxybutyric acid, and acetoacetic acid, in the urine of the TBM patients.

4.7 Increased nitrogen excretion

Urea was identified in the statistical analyses of the raw data as being significantly increased in the urine of the TBM cases compared to the controls. Increased urea is irrevocably linked to elevated

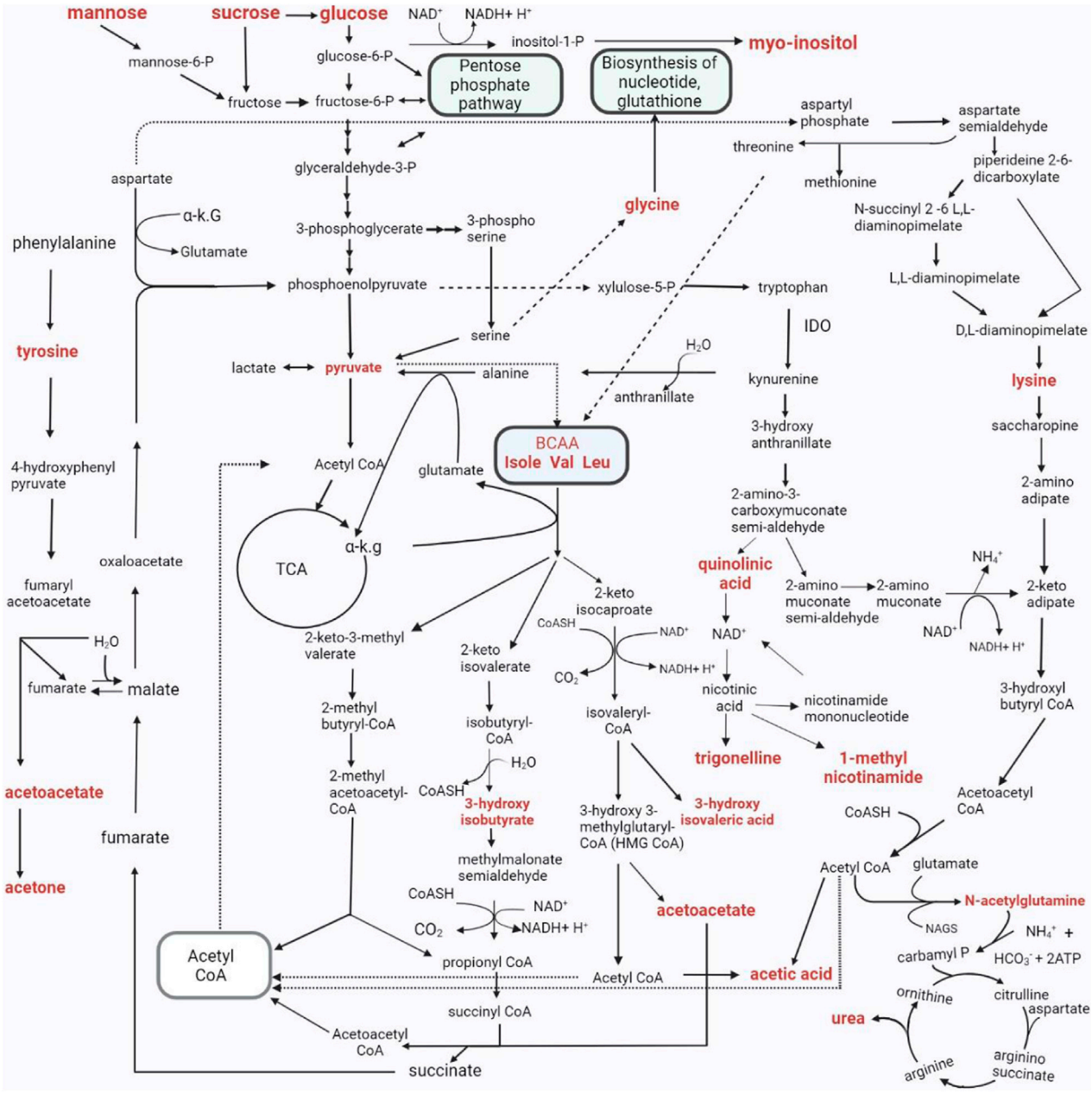

FIGURE 9
The metabolic pathways characterizing the changed urinary metabolic profiles in TBM stage 3 patients. The metabolites in bold denote those detected in significantly elevated concentrations in the TBM stage 3 patients when compared to the controls. As indicated in the pathway, P–phosphate; α K.G–alpha ketoglutarate; IDO - Indoleamine 2, 3-dioxygenase; Isole–isoleucine; Val–valine; Leu–leucine; CoA, CoASH–coenzyme A; TCA - tricarboxylic acid cycle; NH_4^+–ammonium; HCO_3^-–bicarbonate; ATP–adenosine triphosphate; NAD–nicotinamide adenine dinucleotide; BCAA–branched-chain amino acids.; H_2O–water; NAGS–N-acetyl glutamate synthase.

nitrogen excretion. Urea in a ^{1}H NMR spectrum presents as a very distinctive broad singlet near to the suppressed water signal. Owing to the width of the urea signal in the ^{1}H NMR spectra, and the known influence of water suppression on the urea peak, accurate quantification of urea was not possible.

N-Acetylglutamine (Figure 8F), another metabolite of increased nitrogen excretion, was significantly elevated in the TBM patients (335.45 ± 184.47 μmol/mmol creatinine) compared to the controls (102.43 ± 25.98 μmol/mmol creatinine; $p \leq 0.001$, d = 2.21). N-Acetylglutamine is an amino acid derivative, and the downstream metabolite of D-glutamine and D-glutamate metabolism (Zhou et al., 2018). N- acetylglutamine is used as a neurotransmitter in the brain, and perturbed N-acetylglutamine can be linked to altered neuronal stability and/or function. In a study that conducted RNA-sequencing on whole blood and CSF of ventricular and lumbar punctures of paediatric patients treated for TBM, Rohlwink *et al.* (2019) indicated immune responses and neural excitotoxicity which depicts the immunological events that occurs in the brain. Of the 389 differentially expressed genes, 45 genes are mainly associated with glutamate excitotoxicity, key

excitatory neurotransmitter in learning and memory also, mediator associated with several neurological diseases (Rohlwink et al., 2019). N-Acetylglutamine is also classified as a uremic toxin and increased urinary levels indicate severe neurological complications (typical in TBM), advanced catabolism and/or possible kidney damage. Glutamine supplementation is a well-known strategy to treat some critically ill patients, such as prematurely born infants (Darmaun et al., 2018), and could be considered in paediatric TBM.

4.8 Urinary metabolic map of TBM

We took all of the above described metabolic pathways characterizing the urinary profiles of advanced hospitalized TBM paediatric cases, and connected them into a metabolic map (Figure 9). Figure 9 illustrates how all these metabolic pathways connect with each other, providing new connections (information) of metabolic pathways, and their complexity, in advanced TBM in paediatric patients. With this new information, we offer new insights and approaches into future TBM research.

4.9 Limitations of the study and TB medications

The limitations in this study included: 1) a small sample size (no *a priori* sample size considerations were factored in because the samples were retrospectively selected from a previous study), 2) no validation sample cohort, 3) there was no information available on the timing and type of treatment regime administered to the undiagnosed TBM patients at the referral healthcare centers, before being taken to the hospital, 4) the controls were heterogenous and, due to ethical restrictions, the only information available for the controls were that they were pediatric patients without meningitis, no neurological symptoms, and from the same geographical region as the TBM patients. Upon inspection of the ^{1}H-NMR spectra, it was found that pyrazinamide (PZA), isoniazid (IZA) and ethionamide were detected in all the time zero stage three (T0) TBM cases urine samples, except for 2 cases (103 and 114) which had no IZA and no ethionamide. Rifampicin and its two metabolites–3- formylrifampicin and 25-deacetyl-rifampicin, were not detectable in the ^{1}H-NMR spectra in any of the urine samples. The inability to see rifampicin and its two known urinary metabolites could be that either the rifampicin has been detoxified in the body into a form that we do not know of, or, more likely, the NMR analytical platform lacks the sensitivity (i.e., below the detection limit of the NMR).

5 Conclusion

We consider the significant metabolites identified in this study as being the best urinary metabolic characterization of TBM, to date. The precise outcome of this study indicated that TBM under initial treatment could be well differentiated from controls, based upon urinary metabolic profiles analyzed by ^{1}H NMR spectroscopy. These results support metabolomics data produced in our previous GC-MS metabolomics study conducted using a similar paediatric cohort. Thus, these results support the use of ^{1}H NMR metabolomics in characterizing TBM, and in the pursuit of non-invasive metabolic markers of TBM to aid in the early differential diagnosis and subsequent treatment of TBM–something that is greatly needed in the paediatric population, the patient group most at risk of mortality.

Moreover, several clinical aspects of the studied cohort of advanced TBM were inferred from the urinary metabolomics data, which need to be confirmed from blood samples collected from TBM cases. The findings related to -illness induced-malnutrition can have therapeutic impact. Malnutrition can be subdivided in deficiency of micronutrients (e.g., vitamins) and macronutrients (e.g., proteins). We found (a) deficient vitamin B3 status expressed by increased urinary 1-methylnicotinamide–upregulated utilization of vitamin B3 from increased tryptophan catabolism, and increased urinary trigonelline; (b) increased nitrogen excretion, which reflects the elevated catabolic state of patients and their related malnutrition. For instance, shortage of the semi essential amino acid glutamine can lead to immune dysfunction (Cruzat et al., 2018). Thus, it is our recommendation that the nutritional status of TBM cases should be assessed with comparison made to pulmonary TB cases or controls, in order to determine whether the findings are specific to TB or TBM. Potentially, additional supplementation of vitamin B and glutamine may be a consideration in the nutritional component of the future overall management of TBM.

Data availability statement

The original contributions presented in the study are included in the article/Supplementary Material, further inquiries can be directed to the corresponding author.

Ethics statement

The studies involving humans were approved by the Health Research Ethics Committee (HREC) of Stellenbosch University (ethics approval no. N16/11/142 and N11/03/061 for group 1 and 2 respectively), as well as by the HREC of the North-West University, Potchefstroom campus (ethics approval no. NWU-00063-18-A1-01). The studies were conducted in accordance with the local legislation and institutional requirements. Written informed consent for participation in this study was provided by the participants' legal guardians/next of kin.

Author contributions

SI: Data curation, Formal Analysis, Investigation, Methodology, Software, Writing–original draft. DL: Formal Analysis, Investigation, Methodology, Supervision, Writing–review and editing. MR: Formal Analysis, Methodology, Writing–review and editing. RS: Data curation, Methodology, Resources, Writing–review and editing. SE: Data curation, Methodology, Writing–review and editing. AT: Funding acquisition, Project administration, Resources,

Supervision, Writing–review and editing. MK: Funding acquisition, Investigation, Methodology, Project administration, Supervision, Writing–review and editing. SM: Conceptualization, Formal Analysis, Investigation, Methodology, Project administration, Supervision, Writing–review and editing.

Funding

The author(s) declare financial support was received for the research, authorship, and/or publication of this article. This work was supported by funding from the Mr Willem Backhuys Roozeboomstichting in the Netherlands, the National Research foundation (NRF) of South Africa and the Dutch Organisation for Internationalisation in Education (NUFFIC) [grant number UID: 120209].

Acknowledgments

We wish to thank the Centre for Human Metabolomics for their assistance.

Conflict of interest

The authors declare that the research was conducted in the absence of any commercial or financial relationships that could be construed as a potential conflict of interest.

Publisher's note

Supplementary material

The Supplementary Material for this article can be found online at: https://www.frontiersin.org/articles/10.3389/fmolb.2024.1253983/full#supplementary-material

References

Amin, A. G., De, P., Graham, B., Calderon, R. I., Franke, M. F., and Chatterjee, D. (2021). Urine lipoarabinomannan in HIV uninfected, smear negative, symptomatic TB patients: effective sample pretreatment for a sensitive immunoassay and mass spectrometry. *Sci. Rep.* 11, 2922. doi:10.1038/s41598-021-82445-4

Basu Roy, R., Bakeera-Kitaka, S., Chabala, C., Gibb, D. M., Huynh, J., Mujuru, H., et al. (2021). Defeating paediatric tuberculous meningitis: applying the WHO "defeating meningitis by 2030: global roadmap". *Microorganisms* 9, 857. doi:10.3390/microorganisms9040857

Binici, I., Huyut, Z., Alp, H. H., Akbay, H. İ., Karsen, H., Parlak, M., et al. (2023). Investigation of the predictive value of amino acids for tuberculous meningitis, aseptic meningitis and bacterial meningitis. *East. J. Med.* 28, 185–194. doi:10.5505/ejm.2023.49404

Blankley, S., Berry, M. P. R., Graham, C. M., Bloom, C. I., Lipman, M., and O'Garra, A. (2014). The application of transcriptional blood signatures to enhance our understanding of the host response to infection: the example of tuberculosis. *Philos. Trans. R. Soc. Lond., B, Biol. Sci.* 369, 20130427. doi:10.1098/rstb.2013.0427

Blau, N., Duran, M., Gibson, K. M., and Dionisi-Vici, C. (2014). *Physician's guide to the diagnosis, treatment, and follow-up of inherited metabolic diseases*. Cham: Springer.

Bouatra, S., Aziat, F., Mandal, R., Guo, A. C., Wilson, M. R., Knox, C., et al. (2013). The human urine metabolome. *PloS one* 8, e73076. doi:10.1371/journal.pone.0073076

Campbell, B. M., Charych, E., Lee, A. W., and Möller, T. (2014). Kynurenines in CNS disease: regulation by inflammatory cytokines. *Front. Neurosci.* 8, 12. doi:10.3389/fnins.2014.00012

Cazzullo, C., Sacchetti, E., and Smeraldi, E. (1976). N-methylnicotinamide excretion and affective disorders. *Psychol. Med.* 6, 265–270. doi:10.1017/s0033291700013817

Chalmers, R., Valman, H., and Liberman, M. (1979). Measurement of 4-hydroxyphenylacetic aciduria as a screening test for small-bowel disease. *J. Clin. Chem.* 25, 1791–1794. doi:10.1093/clinchem/25.10.1791

Chang, Y.-F., and Gao, X.-M. (1995). L-lysine is a barbiturate-like anticonvulsant and modulator of the benzodiazepine receptor. *Neurochem. Res.* 20, 931–937. doi:10.1007/BF00970739

Chapman, M. J., Pollock, T. A., and Wallace, E. C. (2020). *Organic acid profiling*. Elsevier, 236–244. doi:10.1016/B978-0-323-43044-9.00029-7

Chatterji, T., Singh, S., Sen, M., Singh, A. K., Maurya, P. K., Husain, N., et al. (2016). Comprehensive 1 H NMR metabolic profiling of body fluids for differentiation of meningitis in adults. *Metabolomics* 12, 130–214. doi:10.1007/s11306-016-1073-y

Corston, R., Mcgale, E., Stonier, C., Hutchinson, E., and Aber, G. (1981). Cerebrospinal fluid amino acid concentrations in patients with viral and tuberculous meningitis. *J. Neurology, Neurosurg. Psychiatry* 44, 791–795. doi:10.1136/jnnp.44.9.791

Cruzat, V., Macedo Rogero, M., Noel Keane, K., Curi, R., and Newsholme, P. J. N. (2018). Glutamine: metabolism and immune function, supplementation and clinical translation. *Nutrients* 10, 1564. doi:10.3390/nu10111564

Darmaun, D., Lapillonne, A., Simeoni, U., Picaud, J.-C., Rozé, J.-C., Saliba, E., et al. (2018). Parenteral nutrition for preterm infants: issues and strategy. *Arch. Pediatr.* 25, 286–294. doi:10.1016/j.arcped.2018.02.005

Davis, A. G., Rohlwink, U. K., Proust, A., Figaji, A. A., and Wilkinson, R. J. (2019). The pathogenesis of tuberculous meningitis. *J. Leukoc. Biol.* 105, 267–280. doi:10.1002/JLB.MR0318-102R

Dearmond, P. D., Dietzen, D. J., and Pyle-Eilola, A. L. (2017). "Chapter 2 - amino acids disorders," in *Biomarkers in inborn errors of metabolism*. Editors U. GARG and L. D. SMITH (San Diego: Elsevier).

De Deyn, P. P., D'Hooge, R., Van Bogaert, P.-P., and Marescau, B. (2001). Endogenous guanidino compounds as uremic neurotoxins. *Kidney Int.* 59, S77–S83. doi:10.1046/j.1523-1755.2001.59780077.x

De, P., Amin, A. G., Valli, E., Perkins, M. D., Mcneil, M., and Chatterjee, D. (2015). Estimation of D-arabinose by gas chromatography/mass spectrometry as surrogate for mycobacterial lipoarabinomannan in human urine. *PLoS One* 10, e0144088. doi:10.1371/journal.pone.0144088

Dhillon, K. K., and Gupta, S. (2021). Biochemistry, ketogenesis. *Statpearls*. StatPearls Publishing.

Donald, P., Cotton, M., Hendricks, M., Schaaf, H., De Villiers, J. N., and Willemse, T. (1996). Pediatric meningitis in the Western cape province of South Africa. *J. Trop. Pediatr.* 42, 256–261. doi:10.1093/tropej/42.5.256

Donovan, J., Thwaites, G. E., and Huynh, J. (2020). Tuberculous meningitis: where to from here? *Curr. Opin. Infect. Dis.* 33, 259–266. PMID: 32324614; PMCID: PMC7259381. doi:10.1097/QCO.0000000000000648

Erasmus, E., Mason, S., Van Reenen, M., Steffens, F. E., Vorster, B. C., and Reinecke, C. J. (2019). A laboratory approach for characterizing chronic fatigue: what does metabolomics tell us? *Metabolomics* 15, 158–211. doi:10.1007/s11306-019-1620-4

Fellaman, J., Buist, N., and Kennaway, N. J. C. B. (1977). Pitfalls in metabolic studies: the origin of urinary p-tyramine. *Clin. Biochem.* 10, 168–170. doi:10.1016/s0009-9120(77)92494-8

Ferreira, R. M. B., and Teixeira, A. R. N. (2003). "AMINO ACIDS, metabolism," in *Encyclopedia of food sciences and nutrition*. Editor B CABALLERO. Second Edition (Oxford: Academic Press).

Feruglio, S. L., Trøseid, M., Damås, J. K., Kvale, D., and Dyrhol-Riise, A. M. (2013). Soluble markers of the Toll-like receptor 4 pathway differentiate between active and latent tuberculosis and are associated with treatment responses. *PLoS One* 8, e69896. doi:10.1371/journal.pone.0069896

Fukushima, T., Kaetsu, A., Lim, H., and Moriyama, M. (2002). Possible role of 1-methylnicotinamide in the pathogenesis of Parkinson's disease. *Exp. Toxicol. Pathol.* 53, 469–473. doi:10.1078/0940-2993-00214

Gallucci, G., Santucci, N., Díaz, A., Bongiovanni, B., Bértola, D., Gardeñez, W., et al. (2021). Increased levels of circulating LPS during Tuberculosis prevails in patients with advanced pulmonary involvement. *PLoS One* 16, e0257214. doi:10.1371/journal.pone.0257214

Garrettson, L. K., Turpin, D. L., Hvidberg, E. F., and Mellinger, T. J. (1971). Para-hydroxyphenylacetic and homovanillic acid excretion: variation during growth and in cystic fibrosis and other pulmonary diseases. *Am. J. Clin. Pathol.* 55, 318–324. doi:10.1093/ajcp/55.3.318

Goodacre, R. (2010). An overflow of. . . what else but metabolism!. *Metabolomics* 6, 1–2. doi:10.1007/s11306-010-0201-3

Guba, A., Bába, O., Tőzsér, J., Csősz, É., and Kalló, G. (2022). Fast and sensitive quantification of AccQ-Tag derivatized amino acids and biogenic amines by UHPLC-UV analysis from complex biological samples. *Metabolites* 12, 272. doi:10.3390/metabo12030272

Hampton, M. B., Kettle, A. J., and Winterbourn, C. C. (1998). Inside the neutrophil phagosome: oxidants, myeloperoxidase, and bacterial killing. *Blood, Am. J. Hematol.* 92, 3007–3017. doi:10.1182/blood.V92.9.3007

Han, Q., Phillips, R. S., and Li, J. (2019). Editorial: aromatic amino acid metabolism. *Front. Mol. Biosci.* 6, 22. doi:10.3389/fmolb.2019.00022

Hasbun, R., Hasbun, R., and PERSAUD (2018). *Meningitis and encephalitis*. Springer.

Hauser, G., and Finelli, V. N. (1963). The biosynthesis of free and phosphatide myo-inositol from glucose by mammalian tissue slices. *J. Biol. Chem.* 238, 3224–3228. doi:10.1016/s0021-9258(18)48650-4

Heyes, M. P., Achim, C. L., Wiley, C. A., Major, E. O., Saito, K., and Markey, S. P. (1996). Human microglia convert l-tryptophan into the neurotoxin quinolinic acid. *Biochem. J.* 320, 595–597. doi:10.1042/bj3200595

Heyes, M. P., Ellis, R. J., Ryan, L., Childers, M. E., Grant, I., Wolfson, T., et al. (2001). Elevated cerebrospinal fluid quinolinic acid levels are associated with region-specific cerebral volume loss in HIV infection. *Brain* 124, 1033–1042. doi:10.1093/brain/124.5.1033

Heyes, M. P., Saito, K., and Markey, S. P. (1992). Human macrophages convert L-tryptophan into the neurotoxin quinolinic acid. *Biochem. J.* 283, 633–635. doi:10.1042/bj2830633

Isaiah, S., Loots, D. T., Solomons, R., Van Der Kuip, M., Tutu Van Furth, A. M., and Mason, S. (2020). Overview of brain-to-gut Axis exposed to chronic CNS bacterial infection(s) and a predictive urinary metabolic profile of a brain infected by *Mycobacterium tuberculosis*. *Front. Neurosci.* 14, 296. doi:10.3389/fnins.2020.00296

Jansky, L., Reymanova, P., and Kopecky, J. (2003). Dynamics of cytokine production in human peripheral blood mononuclear cells stimulated by LPS, or infected by Borrelia. *Physiological Res.* 52, 593–598. doi:10.33549/physiolres.930372

Kanabus, A. (2020). *Information about tuberculosis*. GHE. Available at: https://www.tbfacts.org/about-us/.

Kitamura, S., Nitta, K., Tayama, Y., Tanoue, C., Sugihara, K., Inoue, T., et al. (2008). Aldehyde oxidase-catalyzed metabolism of N1-methylnicotinamide *in vivo* and *in vitro* in chimeric mice with humanized liver. *Drug Metab. Dispos.* 36, 1202–1205. doi:10.1124/dmd.107.019075

Klebanoff, S. J. (2005). Myeloperoxidase: friend and foe. *J. Leukoc. Biol.* 77, 598–625. doi:10.1189/jlb.1204697

Ko, F.-J., Nyhan, W. L., Wolff, J., Barshop, B., and Sweetman, L. J. P. R. (1991). 3-Hydroxyisobutyric aciduria: an inborn error of valine metabolism. *Pediatr. Res.* 30, 322–326. doi:10.1203/00006450-199110000-00006

Komoda, T., and Matsunaga, T. (2015). "Chapter 4 - metabolic pathways in the human body," in *Biochemistry for medical professionals*. Editors T. KOMODA and T. MATSUNAGA (Boston: Academic Press).

Komoroski, E. M., Komoroski, R. A., Valentine, J. L., Pearce, J. M., and Kearns, G. L. (2000). The use of nuclear magnetic resonance spectroscopy in the detection of drug intoxication. *J. Anal. Toxicol.* 24, 180–187. doi:10.1093/jat/24.3.180

Kondoh, T., Kameishi, M., Mallick, H. N., Ono, T., and Torii, K. (2010). Lysine and arginine reduce the effects of cerebral ischemic insults and inhibit glutamate-induced neuronal activity in rats. *Front. Integr. Neurosci.* 18. doi:10.3389/fnint.2010.00018

Lees, H. J., Swann, J. R., Wilson, I. D., Nicholson, J. K., and Holmes, E. J. J. O. P. R. (2013). Hippurate: the natural history of a mammalian–microbial cometabolite. *J. Proteome Res.* 12, 1527–1546. doi:10.1021/pr300900b

Levin, L., Gevers, W., Jardine, L., De Guel, F., and Duncan, E. (1983). Serum amino acids in weight-losing patients with cancer and tuberculosis. *Eur. J. Cancer Clin. Oncol.* 19, 711–715. doi:10.1016/0277-5379(83)90002-0

Li, F., Chong, Z. Z., and Maiese, K. J. C. M. C. (2006). Cell Life versus cell longevity: the mysteries surrounding the NAD+ precursor nicotinamide. *Curr. Med. Chem.* 13, 883–895. doi:10.2174/092986706776361058

Litwack, G. (2018). "Chapter 13 - metabolism of amino acids," in *Human biochemistry*. Editor G. LITWACK (Boston: Academic Press).

Luies, L., Mienie, J., Motshwane, C., Ronacher, K., Walzl, G., and Loots, D. T. (2017). Urinary metabolite markers characterizing tuberculosis treatment failure. *Metabolomics* 13, 124–210. doi:10.1007/s11306-017-1261-4

Macallan, D. C. (1999). Malnutrition in tuberculosis. *Diagnostic Microbiol. Infect. Dis.* 34, 153–157. doi:10.1016/s0732-8893(99)00007-3

Macallan, D. C., Mcnurlan, M. A., Kurpad, A. V., De Souza, G., Shetty, P. S., Calder, A. G., et al. (1998). Whole body protein metabolism in human pulmonary tuberculosis and undernutrition: evidence for anabolic block in tuberculosis. *Clin. Sci.* 94, 321–331. doi:10.1042/cs0940321

Manyelo, C. M., Solomons, R. S., Snyders, C. I., Manngo, P. M., Mutavhatsindi, H., Kriel, B., et al. (2019). Application of cerebrospinal fluid host protein biosignatures in the diagnosis of tuberculous meningitis in children from a high burden setting. *Mediat. Inflamm.* 2019, 7582948. doi:10.1155/2019/7582948

Manyelo, C. M., Solomons, R. S., Walzl, G., and Chegou, N. N. (2021). Tuberculous meningitis: pathogenesis, immune responses, diagnostic challenges, and the potential of biomarker-based approaches. *J. Clin. Microbiol.* 59, 017711–e1820. doi:10.1128/JCM.01771-20

Marais, S., Thwaites, G., Schoeman, J. F., Török, M. E., Misra, U. K., Prasad, K., et al. (2010). Tuberculous meningitis: a uniform case definition for use in clinical research. *Lancet Infect. Dis.* 10, 803–812. doi:10.1016/S1473-3099(10)70138-9

Mason, S. (2017). Lactate shuttles in neuroenergetics—homeostasis, allostasis and beyond. *Front. Neurosci.* 11, 43. doi:10.3389/fnins.2017.00043

Mason, S., Reinecke, C. J., and Solomons, R. (2017). Cerebrospinal fluid amino acid profiling of pediatric cases with tuberculous meningitis. *Front. Neurosci.* 11, 534. doi:10.3389/fnins.2017.00534

Mason, S., Reinecke, C. J., Solomons, R., and Van Furth, A. (2016a). Tuberculous meningitis in infants and children: insights from nuclear magnetic resonance metabolomics. *S. Afr. J. Sci.* 112, 8. doi:10.17159/sajs.2016/20150086

Mason, S., Van Furth, A. M., Mienie, L. J., Engelke, U. F. H., Wevers, R. A., Solomons, R., et al. (2015). A hypothetical astrocyte–microglia lactate shuttle derived from a 1H NMR metabolomics analysis of cerebrospinal fluid from a cohort of South African children with tuberculous meningitis. *Metabolomics* 11, 822–837. doi:10.1007/s11306-014-0741-z

Mason, S., Van Furth, A. M. T., Solomons, R., Wevers, R. A., Van Reenen, M., and Reinecke, C. J. (2016b). A putative urinary biosignature for diagnosis and follow-up of tuberculous meningitis in children: outcome of a metabolomics study disclosing host–pathogen responses. *Metabolomics* 12, 110–116. doi:10.1007/s11306-016-1053-2

Mayneris-Perxachs, J., Lima, A. A., Guerrant, R. L., Leite, Á. M., Moura, A. F., Lima, N. L., et al. (2016). Urinary N-methylnicotinamide and β-aminoisobutyric acid predict catch-up growth in undernourished Brazilian children. *Sci. Rep.* 6, 19780–19789. doi:10.1038/srep19780

Miric, D., Katanic, R., Miric, B., Kisic, B., Popovic-Katanic, N., Nestorovic, V., et al. (2013). Changes in vitamin C and oxidative stress status during the treatment of tuberculous meningitis. *Int. J. Tuberc. Lung Dis.* 17, 1495–1500. doi:10.5588/ijtld.13.0017

Mitchell, S. C., and Zhang, A. Q. (2001). Methylamine in human urine. *Clin. Chim. acta* 312, 107–114. doi:10.1016/s0009-8981(01)00608-8

Nagana Gowda, G., Zhang, S., Gu, H., Asiago, V., Shanaiah, N., and Raftery, D. (2008). Metabolomics-based methods for early disease diagnostics: a review. *Expert Rev. Mol. diagn.* 8, 617–633. doi:10.1586/14737159.8.5.617

Organization, W. H. (2018). Roadmap towards ending TB in children and adolescents. Geneva. Available online: http://www.who.int/tb/publications/2018/tb-childhoodroadmap/en/(Accessed October 6, 2018).

Pang, Z., Chong, J., Zhou, G., De Lima Morais, D. A., Chang, L., Barrette, M., et al. (2021). MetaboAnalyst 5.0: narrowing the gap between raw spectra and functional insights. *Nucleic Acids Res.* 49, W388–W396. doi:10.1093/nar/gkab382

Pears, M. R., Cooper, J. D., Mitchison, H. M., Mortishire-Smith, R. J., Pearce, D. A., and Griffin, J. L. (2005). High resolution 1H NMR-based metabolomics indicates a neurotransmitter cycling deficit in cerebral tissue from a mouse model of Batten disease. *J. Biol. Chem.* 280, 42508–42514. doi:10.1074/jbc.M507380200

Pirisino, R., Ghelardini, C., De Siena, G., Malmberg, P., Galeotti, N., Cioni, L., et al. (2005). Methylamine: a new endogenous modulator of neuron firing? *Med. Sci. Monit.* 11, RA257–RA261.

Podrez, E. A., Abu-Soud, H. M., and Hazen, S. L. (2000). Myeloperoxidase-generated oxidants and atherosclerosis. *Free Radic. Biol. Med.* 28, 1717–1725. doi:10.1016/S0891-5849(00)00229-X

Poh, X. Y., Hong, J. M., Bai, C., Miow, Q. H., Thong, P. M., Wang, Y., et al. (2022). Nos2−/− mice infected with *M. tuberculosis* develop neurobehavioral changes and immunopathology mimicking human central nervous system tuberculosis. *J. Neuroinflammation* 19, 21–15. doi:10.1186/s12974-022-02387-0

Preez, I. D., Luies, L., and Loots, D. T. (2017). Metabolomics biomarkers for tuberculosis diagnostics: current status and future objectives. *Biomark. Med.* 11, 179–194. doi:10.2217/bmm-2016-0287

Reddy, Y. N., Murthy, S. V., Krishna, D., Prabhakar, M. J., and Pharmacology, B. J. O. (2009). Oxidative metabolic changes in pleural fluid of tuberculosis patients. *Bangladesh J. Pharmacol.* 4, 69–72. doi:10.3329/bjp.v4i1.1443

Rohlwink, U. K., Figaji, A., Wilkinson, K. A., Horswell, S., Sesay, A. K., Deffur, A., et al. (2019). Tuberculous meningitis in children is characterized by compartmentalized immune responses and neural excitotoxicity. *Nat. Commun.* 10, 3767–3768. doi:10.1038/s41467-019-11783-9

Rohlwink, U. K., Mauff, K., Wilkinson, K. A., Enslin, N., Wegoye, E., Wilkinson, R. J., et al. (2017). Biomarkers of cerebral injury and inflammation in pediatric tuberculous meningitis. *Clin. Infect. Dis.* 65, 1298–1307. doi:10.1093/cid/cix540

Savvi, S., Warner, D. F., Kana, B. D., Mckinney, J. D., Mizrahi, V., and Dawes, S. S. (2008). Functional characterization of a vitamin B12-dependent methylmalonyl pathway in *Mycobacterium tuberculosis*: implications for propionate metabolism during growth on fatty acids. *J. Bacteriol.* 190, 3886–3895. doi:10.1128/JB.01767-07

Schildberger, A., Rossmanith, E., Eichhorn, T., Strassl, K., and Weber, V. (2013). Monocytes, peripheral blood mononuclear cells, and THP-1 cells exhibit different cytokine expression patterns following stimulation with lipopolysaccharide. *Mediat. Inflamm.* 10, 697972. doi:10.1155/2013/697972

Schwenk, A., and Macallan, D. C. (2000). Tuberculosis, malnutrition and wasting. *Curr. Opin. Clin. Nutr. Metabolic Care* 3, 285–291. doi:10.1097/00075197-200007000-00008

Seri, K., Sanai, K., Matsuo, N., Kawakubo, K., Xue, C., and Inoue, S. (1996). l-Arabinose selectively inhibits intestinal sucrase in an uncompetitive manner and suppresses glycemic response after sucrose ingestion in animals. *Metab* 45, 1368–1374. doi:10.1016/S0026-0495(96)90117-1

Shahsavar, A., Stohler, P., Bourenkov, G., Zimmermann, I., Siegrist, M., Guba, W., et al. (2020). Structural insights into glycine reuptake inhibition. bioRxiv., Availale at: https://doi.org/10.1101/2020.12.20.110478.

Shaw, P. J., Forrest, V., Ince, P. G., Richardson, J. P., and Wastell, H. J. (1995a). CSF and plasma amino acid levels in motor neuron disease: elevation of CSF glutamate in a subset of patients. *Neurodegeneration* 4, 209–216. doi:10.1006/neur.1995.0026

Shaw, W., Kassen, E., and Chaves, E. (1995b). Increased urinary excretion of analogs of Krebs cycle metabolites and arabinose in two brothers with autistic features. *Clin. Chem.* 41, 1094–1104. doi:10.1093/clinchem/41.8.1094

Shin, J.-H., Yang, J.-Y., Jeon, B.-Y., Yoon, Y. J., Cho, S.-N., Kang, Y.-H., et al. (2011). 1H NMR-based metabolomic profiling in mice infected with *Mycobacterium tuberculosis*. *J. Proteome Res.* 10, 2238–2247. doi:10.1021/pr101054m

Smeitink, J. A., Van Den Heuvel, L. W., Koopman, W. J., Nijtmans, L. G., Ugalde, C., and Willems, P. H. J. C. N. R. (2004). Cell biological consequences of mitochondrial NADH: ubiquinone oxidoreductase deficiency. *Curr. Neurovasc. Res.* 1, 29–40. doi:10.2174/1567202043480224

Sweatt, A. J., Wood, M., Suryawan, A., Wallin, R., Willingham, M. C., and Hutson, S. M. (2004). Branched-chain amino acid catabolism: unique segregation of pathway enzymes in organ systems and peripheral nerves. *Am. J. Physiology-Endocrinology Metabolism* 286, E64–E76. doi:10.1152/ajpendo.00276.2003

Tsukahara, H., Haruta, T., Todoroki, Y., Hiraoka, M., Noiri, E., Maeda, M., et al. (2002). Oxidant and antioxidant activities in childhood meningitis. *Life Sci.* 71, 2797–2806. doi:10.1016/s0024-3205(02)02137-9

Van Den Eynden, J., Sahebali, S., Horwood, N., Carmans, S., Brône, B., Hellings, N., et al. (2009). Glycine and glycine receptor signalling in non-neuronal cells. *Front. Mol. Neurosci.* 2, 9. doi:10.3389/neuro.02.009.2009

Van Der Greef, J., Stroobant, P., and Van Der Heijden, R. (2004). The role of analytical sciences in medical systems biology. *Curr. Opin. Chem. Biol.* 8, 559–565. doi:10.1016/j.cbpa.2004.08.013

Van Der Heiden, C., Wadman, S. K., Ketting, D., and De Bree, P. K. (1971). Urinary and faecal excretion of metabolites of tyrosine and phenylalanine in a patient with cystic fibrosis and severely impaired amino acid absorption. *Clin. Chim. Acta* 31, 133–141. doi:10.1016/0009-8981(71)90370-6

Van Elsland, S. L., Peters Rph Kok, M. O., Van Toorn, R., Springe, P., Cotton, M. F., Grobbelaar, C. J., et al. (2018). A treatment-support intervention evaluated in South African paediatric populations with HIV infection or tuberculous meningitis. *Trop. Med. Int. Health* 23 (10), 1129–1140. doi:10.1111/tmi.13134

Van Laarhoven, A., Dian, S., Aguirre-Gamboa, R., Avila-Pacheco, J., Ricaño-Ponce, I., Ruesen, C., et al. (2018). Cerebral tryptophan metabolism and outcome of tuberculous meningitis: an observational cohort study. *Lancet Infect. Dis.* 18, 526–535. doi:10.1016/S1473-3099(18)30053-7

Van Toorn, R., Schaaf, H. S., Laubscher, J. A., Van Elsland, S. L., Donald, P. R., and Schoeman, J. F. (2014). Short intensified treatment in children with drug-susceptible tuberculous meningitis. *Pediatr. Infect. Dis. J.* 33, 248–252. doi:10.1097/INF.0000000000000065

Van Toorn, R., and Solomons, R. (2014). Update on the diagnosis and management of tuberculous meningitis in children. *Semin. Pediatr. Neurol.* 21, 12–18. doi:10.1016/j.spen.2014.01.006

Van Toorn, R., Springer, P., Laubscher, J., and Schoeman, J. (2012). Value of different staging systems for predicting neurological outcome in childhood tuberculous meningitis. *Int. J. Tuberc. Lung Dis.* 16, 628–632. doi:10.5588/ijtld.11.0648

Van Zyl, C. D. W., Loots, D. T., Solomons, R., Van Reenen, M., and Mason, S. (2020). Metabolic characterization of tuberculous meningitis in a South African paediatric population using 1H NMR metabolomics. *J. Infect.* 81, 743–752. doi:10.1016/j.jinf.2020.06.078

Wang, Y., Wang, Y., Zhu, J., Guan, Y., Xie, F., Cai, X., et al. (2022). Systematic evaluation of urinary formic acid as a new potential biomarker for Alzheimer's disease. *Front. Aging Neurosci.* 14, 1364. doi:10.3389/fnagi.2022.1046066

Weiner, J., Parida, S. K., Maertzdorf, J., Black, G. F., Repsilber, D., Telaar, A., et al. (2012). Biomarkers of inflammation, immunosuppression and stress with active disease are revealed by metabolomic profiling of tuberculosis patients. *PloS one* 7, e40221. doi:10.1371/journal.pone.0040221

Westgard, J. (2008). *Basic method validation*. 3rd Edn. Westgard QC.

WHO (2020). *W.H.O global tuberculosis report 2020*. Geneva, Switzerland: World Health Organization.

Williams, H. R., Cox, I. J., Walker, D. G., Cobbold, J. F., Taylor-Robinson, S. D., Marshall, S. E., et al. (2010). Differences in gut microbial metabolism are responsible for reduced hippurate synthesis in Crohn's disease. *BMC Gastroenterol.* 10, 108–8. doi:10.1186/1471-230X-10-108

Williams, A., Ramsden, D. J. P., and Disorders, R. (2005). Nicotinamide: a double edged sword. *Park. Relat. Disord.* 11, 413–420. doi:10.1016/j.parkreldis.2005.05.011

Wolzak, N. K., Cooke, M. L., Orth, H., and Van Toorn, R. (2012). The changing profile of pediatric meningitis at a referral centre in Cape Town, South Africa. *J. Trop. Pediatr.* 58, 491–495. doi:10.1093/tropej/fms031

Zheng, P., Wang, Y., Chen, L., Yang, D., Meng, H., Zhou, D., et al. (2013). Identification and validation of urinary metabolite biomarkers for major depressive disorder. *Mol. Cell Proteomics* 12, 207–214. doi:10.1074/mcp.M112.021816

Zhou, S.-S., Da Li, W.-P. S., Guo, M., Lun, Y.-Z., Zhou, Y.-M., Xiao, F.-C., et al. (2009). Nicotinamide overload may play a role in the development of type 2 diabetes. *World J. Gastroenterol.* 15, 5674–5684. doi:10.3748/wjg.15.5674

Zhou, K., Ding, X., Yang, J., Hu, Y., Song, Y., Chen, M., et al. (2018). Metabolomics reveals metabolic changes caused by low-dose 4-Tert-Octylphenol in mice liver. *Int. J. Environ. Res. Public Health* 15, 2686. doi:10.3390/ijerph15122686

frontiers | Frontiers in Molecular Biosciences

TYPE Original Research
PUBLISHED 10 July 2024
DOI 10.3389/fmolb.2024.1338497

OPEN ACCESS

EDITED BY
Markus R. Meyer,
Saarland University, Germany

REVIEWED BY
Simone Schmitz-Spanke,
University of Erlangen Nuremberg, Germany
Wasan Katip,
Chiang Mai University, Thailand

*CORRESPONDENCE
E. Gikas,
vgikas@chem.uoa.gr

RECEIVED 14 November 2023
ACCEPTED 23 May 2024
PUBLISHED 10 July 2024

CITATION
Barla I, Dagla IV, Daskalopoulou A, Panagiotopoulou M, Kritikaki M, Dalezis P, Thomaidis N, Tsarbopoulos A, Trafalis D and Gikas E (2024), Metabolomics highlights biochemical perturbations occurring in the kidney and liver of mice administered a human dose of colistin.
Front. Mol. Biosci. 11:1338497.
doi: 10.3389/fmolb.2024.1338497

Metabolomics highlights biochemical perturbations occurring in the kidney and liver of mice administered a human dose of colistin

I. Barla[1], I. V. Dagla[2], A. Daskalopoulou[3], M. Panagiotopoulou[3], M. Kritikaki[3], P. Dalezis[4], N. Thomaidis[1], A. Tsarbopoulos[4], D. Trafalis[4] and E. Gikas[1]*

[1]Laboratory of Analytical Chemistry, Department of Chemistry, School of Science, National and Kapodistrian University of Athens, Athens, Greece, [2]GAIA Research Center, The Goulandris Natural History Museum, Kifissia, Greece, [3]Laboratory of Pharmaceutical Analysis, Department of Pharmacy, School of Health Science, National and Kapodistrian University of Athens, Athens, Greece, [4]Laboratory of Pharmacology, School of Medicine, National and Kapodistrian University of Athens, Athens, Greece

Introduction: Colistin (CMS) is used for the curation of infections caused by multidrug-resistant bacteria. CMS is constrained by toxicity, particularly in kidney and neuronal cells. The recommended human doses are 2.5–5 mg/kg/day, and the toxicity is linked to higher doses. So far, the *in vivo* toxicity studies have used doses even 10-fold higher than human doses. It is essential to investigate the impact of metabolic response of doses, that are comparable to human doses, to identify biomarkers of latent toxicity. The innovation of the current study is the *in vivo* stimulation of CMS's impact using a range of CMS doses that have never been investigated before, i.e., 1 and 1.5 mg/kg. The 1 and 1.5 mg/kg, administered in mice, correspond to the therapeutic and toxic human doses, based on previous expertise of our team, regarding the human exposure. The study mainly focused on the biochemical impact of CMS on the metabolome, and on the alterations provoked by 50%-fold of dose increase. The main objectives were i) the comprehension of the biochemical changes resulting after CMS administration and ii) from its dose increase; and iii) the determination of dose-related metabolites that could be considered as toxicity monitoring biomarkers.

Methods: The *in vivo* experiment employed two doses of CMS versus a control group treated with normal saline, and samples of plasma, kidney, and liver were analysed with a UPLC-MS-based metabolomics protocol. Both univariate and multivariate statistical approaches (PCA, OPLS-DA, PLS regression, ROC) and pathway analysis were combined for the data interpretation.

Results: The results pointed out six dose-responding metabolites (PAA, DA4S, 2,8-DHA, etc.), dysregulation of renal dopamine, and extended perturbations in renal purine metabolism. Also, the study determined altered levels of liver suberylglycine, a metabolite linked to hepatic steatosis. One of the most intriguing findings was the detection of elevated levels of renal xanthine and uric acid, that act as AChE activators, leading to the rapid degradation of

acetylcholine. This evidence provides a naïve hypothesis, for the potential association between the CMS induced nephrotoxicity and CMS induced 39 neurotoxicity, that should be further investigated.

KEYWORDS

metabolomics, colistin, drug toxicity, pathway analysis, dopamine metabolism, purine metabolism

1 Introduction

Colistin is typically used as a last resort antibiotic to treat infections caused by multidrug-resistant bacteria as it has a narrow therapeutic index and can cause significant toxicity, particularly to the kidneys and nervous system (Grégoire et al., 2017; Satlin et al., 2020; Mohapatra et al., 2021). It belongs to the class of antibiotics known as polymyxins, which have a unique mechanism of action that disrupts the bacterial cell membrane. This mechanism of action makes polymyxins effective against many Gram-negative bacteria that are resistant to other antibiotics, such as *Pseudomonas aeruginosa*, *Acinetobacter baumannii*, and *Klebsiella pneumoniae* (Falagas and Kasiakou, 2005). However, polymyxins are also toxic to human cells, particularly kidney cells and neuronal cells. The drug is usually given as colistimethate sodium (CMS), a prodrug of colistin (Bergen et al., 2006). The dosage regimen of CMS can vary depending on the patient's age, weight, the severity of infection, and the method of administration (injection or inhalation). For the treatment of infections caused by Gram-negative bacteria, the usual adult dose is 3 million units daily, administered intravenously in divided doses every 8 h (Plachouras et al., 2009). An average steady-state plasma colistin concentration of 2 mg/L seems to be a reasonable target value (Nation et al., 2015). A loading dose CMS is often recommended to achieve a therapeutic concentration quickly. The loading dose can vary depending on the patient's condition, but it is usually higher than the subsequent maintenance dose (Haseeb et al., 2021; Rychlíčková et al., 2023). The duration of treatment can also vary depending on the severity of infection and the patient's response to therapy. According to the prescribing information for CMS injection, the maximum daily dose should not exceed 5 mg/kg of body weight (https://www.accessdata.fda.gov/drugsatfda_docs/label/2009/050108s026lbl.pdf, accessed on 26 April 2023). It is important to note that the dosage regimen for CMS should be adjusted in patients with renal impairment as the drug is primarily eliminated by the kidneys (Garonzik et al., 2011). The use of CMS should always be monitored by a healthcare professional. An approach to increase the drug efficacy is the co-administration of CMS with other antibiotics such as fosfomycin (Katip et al., 2024).

CMS, like other antibiotics, can cause side effects and toxicities, i.e., brain dysfunction and neurotoxicity. The mechanism of CMS-induced neurotoxicity is not fully understood, but it is thought to involve the drug's ability to penetrate the blood–brain barrier and interact with neuronal cells (Inci et al., 2018; Dai et al., 2019; Ramezanzade et al., 2023). Furthermore, CMS can cause damage to the kidneys, especially if it is used for a long time or at high doses. This can lead to symptoms such as decrease in creatinine clearance, decreased urine output, proteinuria, cylinduria, swelling in the legs or feet, and shortness of breath (Gai et al., 2019; Eljaaly et al., 2021; Alotaibi et al., 2022).

In vivo studies of CMS nephrotoxicity have shown histological abnormalities, tubular dilation and cell necrosis, and epithelial cell vacuolation as well (Gai et al., 2019). Although CMS is primarily associated with kidney toxicity, there is some evidence to suggest that it may also have an effect on the liver (Long et al., 2022). It is important to note that the risk of toxicities may vary depending on the dose, duration of treatment, and individual patient factors. Therefore, the levels of CMS should be carefully monitored.

Despite these limitations, CMS remains a last-resort treatment against multidrug-resistant bacteria. There is limited literature on CMS toxicity; i.e., in PubMed (https://pubmed.ncbi.nlm.nih.gov/?term=colistin+induced+toxicity, last access in March 2024), the search *colistin induced toxicity* resulted in 178 published papers.

The majority of the CMS toxicity *in vivo* studies use doses even 10-folds higher than the human doses (Gai et al., 2019), to investigate the background of highly toxic conditions; therefore, our knowledge on the impact of low CMS doses is limited. In addition, metabolomics studies of colistin toxicity are limited, although *in vivo* metabolomics experiments could increase our knowledge on CMS impact, as the metabolites are molecules of universal structure and, thus, provide consistent interpretation of the evidence resulting from toxicological studies using animal-to-human translation. Until now, one metabolomics study has been conducted for the characterization of urinary metabolites as biomarkers of colistin-induced nephrotoxicity in rats (Jeong et al., 2016). Furthermore, Long et al. (2022) have studied the alteration of kidney and liver metabolome after the administration of a high CMS dose.

Based on the above, the objective of the current study is the evaluation of the biochemical impact resulting from realistic human-relevant CMS doses and from an increase of 50% that is perceived as pragmatistic . The main objectives of the study were 1) comprehension of the biochemical changes resulting from the mentioned doses; 2) determination of dose-related metabolites, as potential toxicity-monitoring biomarkers; and 3) estimation of early signs of hepatotoxicity. Therefore, an *in vivo* stimulation of CMS metabolic changes was performed by administering CMS to mice (1 and 1.5 mg/kg/day for 5 sequential days). Plasma, kidney, and liver were used for metabolomics profiling using a UPLS-MS-based platform. The doses were calculated by using the dose conversion from animals to humans (Nair and Jacob, 2016; Jacob et al., 2022). Based on the clinical experience of our team, these doses correspond to human exposure, representing the therapeutic and toxic dose.

2 Materials and methods

2.1 Animals and dosage regime

The study employed plasma, kidney, and liver samples of 15 C57Bl/6 (weight: 20–25 g; age: 8–10 weeks) mice. All *in vivo* experiments were carried out in accordance with the "Guide for the care and use of laboratory animals," and experiments were approved by the Ethics Committee (Approval No: 574234/20-07-2020). The mice were housed and maintained according to the ARRIVE guidelines. The number of animals needed to achieve statistical power >80% was calculated using GPower 3.1. The animals were randomized into three groups (n = 5 for each group) as follows: 1) control (NaCl 0.9%), 2) low dose (LD) (CMS 1 mg/kg/day), and 3) high dose (HD) (CMS 1.5 mg/kg/day). The drug and the normal saline, respectively, were injected intramuscularly (i.m.) to the thigh of each laboratory animal. The administration was repeated for 5 sequential days, and on the sixth day, the laboratory animals were sacrificed.

2.2 Metabolite extraction from plasma and tissues

For the plasma extraction, 200 µL of the sample was mixed with 600 µL of frozen MeOH, centrifuged using a Neya 16R centrifugation apparatus (REMI, Mumbai, India) at 10,000 rpm, 5 min, 4°C, and the supernatant was stored at −80°C. For the extraction of liver and kidney samples, 100 mg of the tissue was homogenized with 1 µL of MeOH–H_2O (1:1, v/v) solution. A Cryolys Evolution tissue homogenizer (Bertin Instruments, Rockville, MD, United States) and the homogenizing CKMix lysing kit (Bertin Corp., Rockville, MD, United States) were employed for a two-step procedure. At first, 500 µL of the solution was added in the falcon tube with the tissue, and the "hard" mode (9,600 rpm, three 20-s cycles followed by a 60-s pause) of the homogenizer was applied. Then, the blend was centrifuged, and the supernatant was obtained. For the second step, after removing the supernatant, the rest of the solution was added to the homogenizing tube with the remaining tissue and submitted to a second cycle of a "soft" mode (5,000 rpm, one 60-s cycle) homogenization. The blend was centrifuged, as before, and the supernatant was obtained and mixed with the supernatant obtained from the 1st homogenization cycle; 400 µL and 500 µL of plasma and tissue extract, respectively, were evaporated to dryness using a HyperVAC-LITE centrifugal vacuum concentrator (Hanil Scientific Inc., Gimpo, Korea), and the remaining solid was reconstituted with 150 µL of IS mix solution containing 1 ppm of yohimbine and reserpine in MeOH–H_2O (1:1, v/v). Yohimbine and reserpine are pharmaceutical compounds that are not normally detected in organisms and were used for multi-IS-based signal correction.

2.3 UPLC-MS analysis

The samples were analyzed using a Dionex UltiMate 3000 RSLC (Thermo Fisher Scientific, Dreieich, Germany) UPLC system, coupled to a maXis Impact QTOF mass spectrometer (Bruker Daltonics, Bremen, Germany) equipped with an electrospray ionization source. The chromatographic column used was Acclaim RSL C18 column (2.1 × 100 mm, 2.2 µm, Thermo Fisher Scientific), and elution of the analytes was performed with gradient conditions, by a ramp increase of the organic mobile phase. The DIA methodology (bbCID mode, in Bruker terminology) was selected for MS acquisition. A detailed description of the UPLC conditions and the parameters of ESI and MS are included in the Supplementary Material, § Experimental Condition.

2.4 Data processing

The MZmine 4.9 software was selected for untargeted peak-picking (Pluskal et al., 2010). The QCRLSC (Luan et al., 2018) algorithm (via the StatTarget platform) (Luan et al., 2018) and the NOMIS algorithm [via NOREVA 2.0 platform (Fu et al., 2022)] were employed for QC- and IS-based signal correction, respectively. RamClustR was used for the assignment of pseudo-MSMS clusters (Broeckling et al., 2014), and MCID (http://www.mycompoundid.org/mycompoundid_IsoMS/) (Huan et al., 2015) and HMDB (Wishart et al., 2018) online libraries were used for metabolite annotation. SIMCA 14.1 (Umetrics, Upsala, Sweden) and MetaboAnalyst 5.0 (https://www.metaboanalyst.ca) (Pang et al., 2021) platforms were used for statistical analysis. Moreover, TASQ Client 2.1 software (Bruker Daltonics, Bremen, Germany) was used for the screening of the raw MS data, for the determination of metabolites involved in purine metabolism. Further description of the pre-processing workflow is included in the Supplementary Material.

2.5 Statistical analysis design

The final feature tables were submitted to the following statistical tests. Initially, the groups were submitted to pairwise comparisons, i.e., C vs. LD and LD vs. HD, using PCA and OPLS-DA. Pairwise comparisons were selected as they provided several advantages:

- The comparison of C and LD provided an insight into the biochemical impact of CMS on the metabolome, and so far, to the best of our knowledge, this issue has not been addressed by the existing literature.
- The comparison of LD and HD provided an image of what happens when the CMS dose is 50% increased. It is worth mentioning that low-dose increases display a realistic scenario of clinical practice, and considering that CMS is nephrotoxic, increasing the circulating levels of CMS could result in latent or severe toxicity outcomes.
- The pairwise comparisons provide the ability to use ortho-based methodologies, i.e., OPLS-DA, and thus remove the impact of confounders on the metabolomics profiles, acquiring more interpretable results.
- Pairwise comparisons can be combined with methodologies such as SUS plot. The SUS plot compares two ortho-models

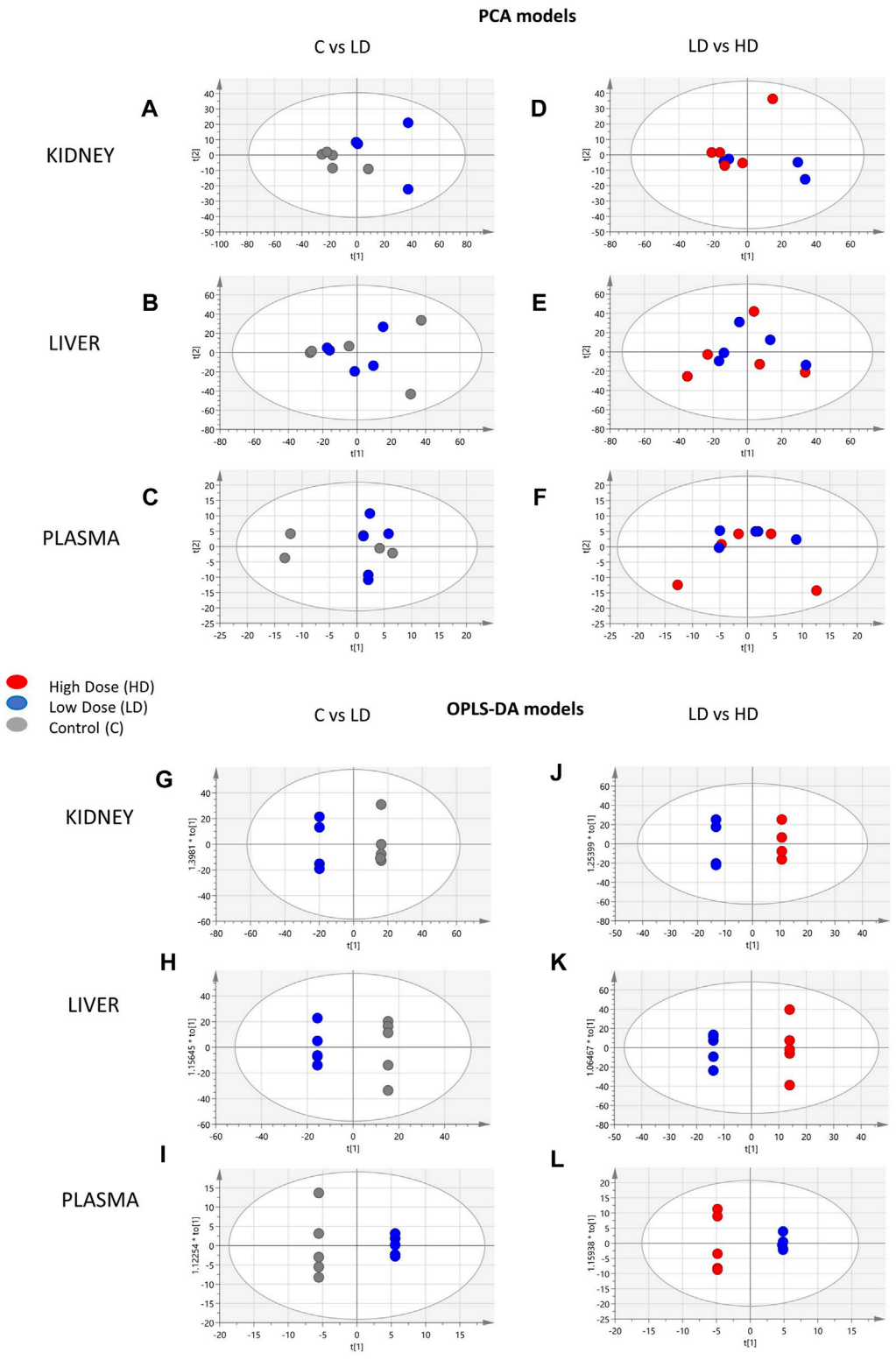

FIGURE 1
Summary of the PCA and OPLS-DA results of the ESI⁺ datasets. PCA scores' plots of the following: **(A)** kidney, C (n = 5)-LD (n = 5); **(B)** liver, C (n = 5)-LD (n = 5); **(C)** plasma, C (n = 5)-LD (n = 5); **(D)** kidney, LD (n = 5)-HD (n = 5); **(E)** liver, LD (n = 5)-HD (n = 5); **(F)** plasma, LD (n = 5)-HD (n = 5). OPLS-DA scores' plots: **(G)** kidney, C (n = 5)-LD (n = 4); **(H)** liver, C (n = 5)-LD (n = 5); **(I)** plasma, C (n = 5)-LD (n = 5); **(J)** kidney, LD (n = 5)-HD (n = 5); **(K)** liver, LD (n = 5)-HD (n = 5); **(L)** plasma, LD (n = 5)-HD (n = 5).

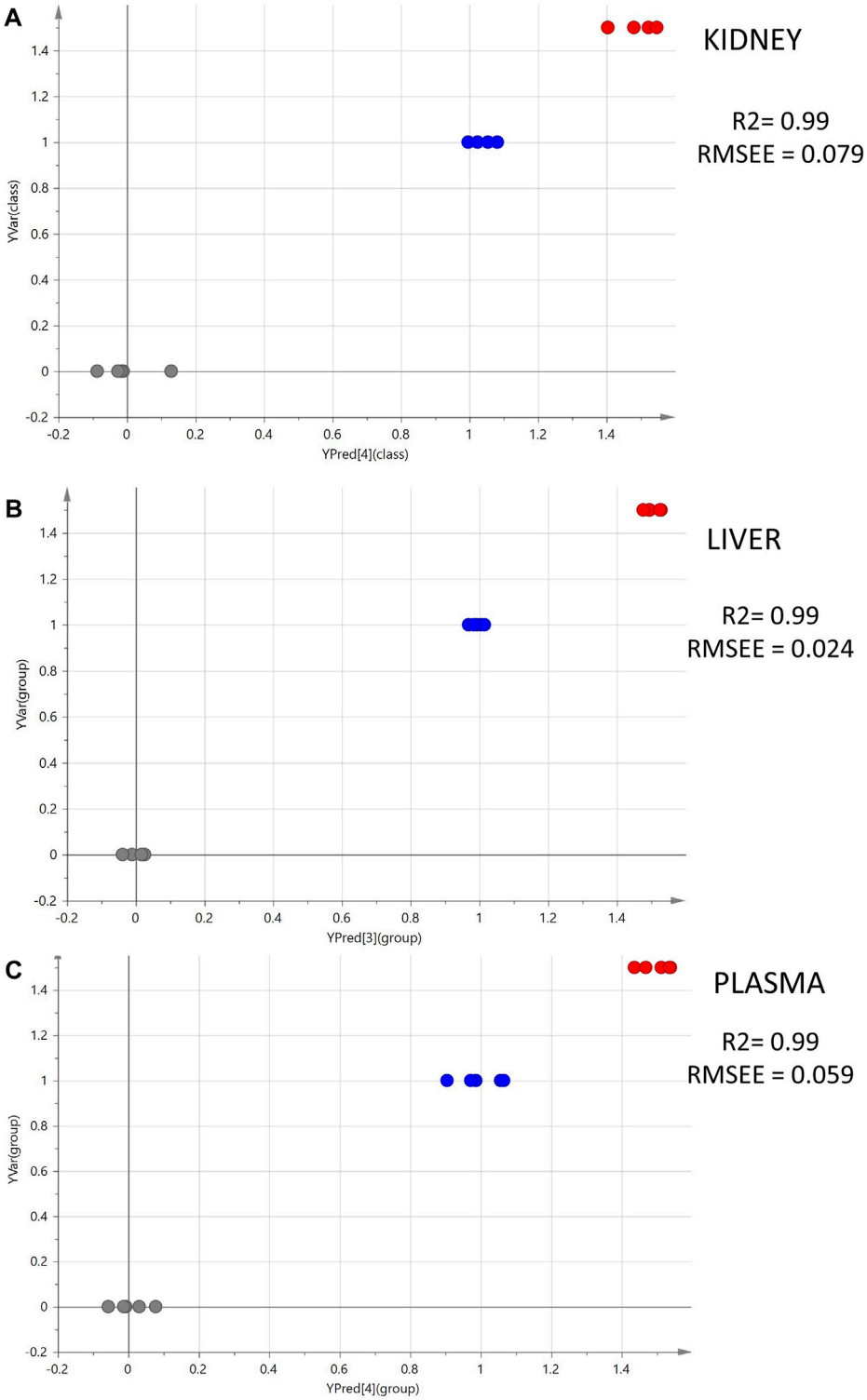

FIGURE 2
Summary of PLS analysis. Observed vs. predicted plots of ESI$^+$ datasets: **(A)** kidney; **(B)** liver; **(C)** plasma. The gray spots represent the C samples (CMS 0 mg/kg, *n* = 5); the blue spots represent the LD samples (CMS 1.0 mg/kg, *n* = 5); and the red spots represent the HD samples (CMS 1.5 mg/kg, *n* = 5).

simultaneously and provides information about their common and different trends, which is discussed in detail below.

Considering that the CMS nephrotoxicity is dose-related, based on the existing literature, the metabolites differentiated in LD and HD could reveal latent signs of toxicity and even facilitate toxicity

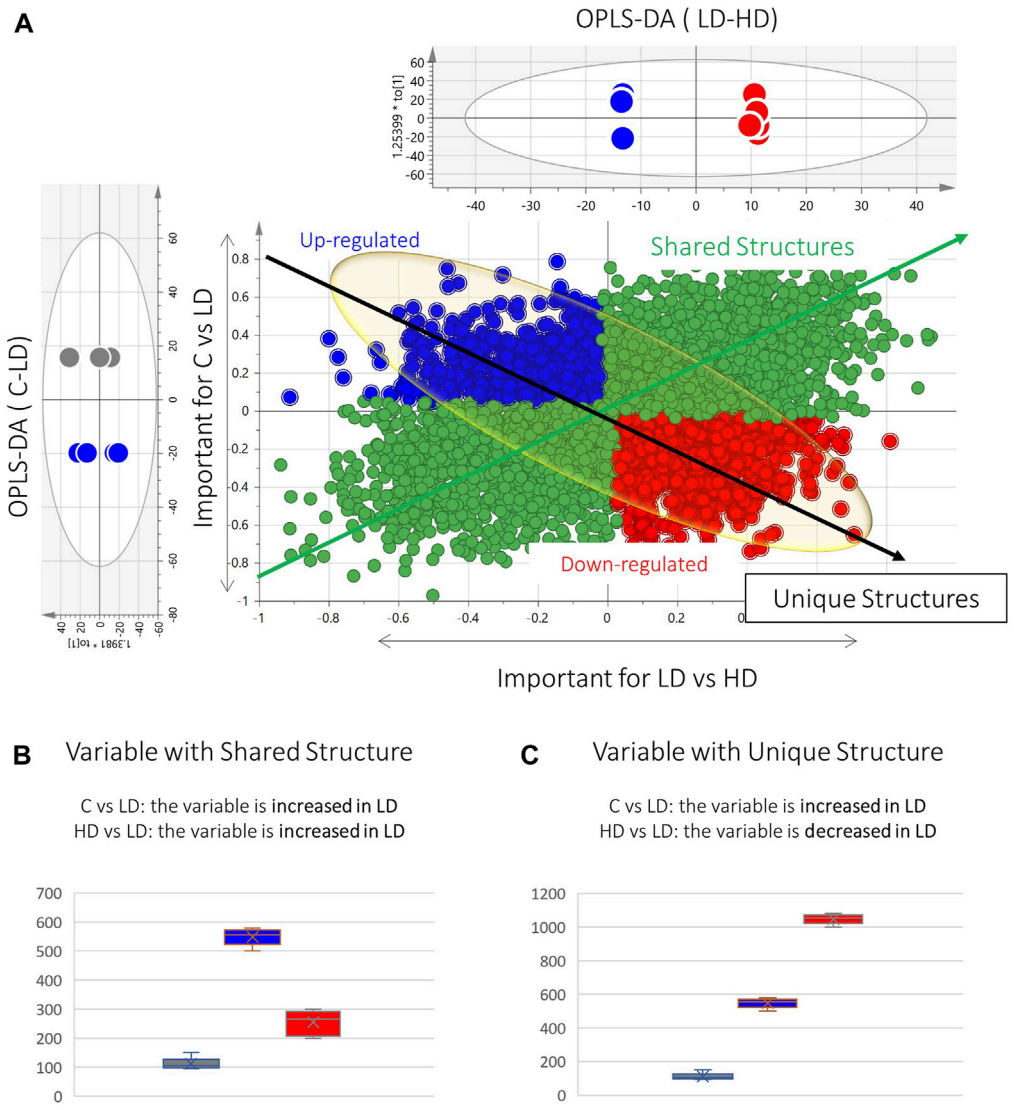

FIGURE 3
Graphical description of the SUS plot basic information. **(A)** SUS plot developed by the OPLS-DA models of C–LD and LD–HD of the kidney ESI$^+$ dataset. The green spotted area represents the variables of the shared structure. The blue and red spotted areas represent the variables of the unique structure. At the edges of the black arrow of unique structures exist the statistically significant dose–response variables (red: upregulated, blue: downregulated). **(B)** Box-plot representing a variable of the shared structure, which shows increased levels in LD (blue) but decreased levels in C (gray) and HD (red). **(C)** Box-plot representing an example of an upregulated unique structure variable, which is increased in LD (blue) compared with C (gray) and in parallel is decreased in LD, compared with HD (red).

monitoring. For further investigation, OPLS-DA was used to develop the SUS plot that allowed structure comparison of the two states.

PLS regression models were used to investigate if there is a linear correlation between the dose and the metabolomics alterations, as has been observed by Nguyen et al. (Gai et al., 2019) when administrating higher doses of CMS. Acknowledging that the linear correlations provide limited explanation of the dose–response phenomena, the study focused on the linearly dose-related metabolites as their alterations were more easily interpretable, and, most importantly, they could lead to monitoring biomarkers, i.e., metabolites whose their levels are altered by the dose increase in a consistent way and could betray the stage or the development of toxicity.

Finally, univariate Receiver Operating Characteristic (ROC) curve analysis was used for pairwise comparisons to validate the prediction ability of the variables that were statistically significant in the multivariate tests.

3 Results

3.1 Statistical analysis results

The control (C), the low dose (LD)-treated, and the high dose (HD)-treated mice were compared in pairs to detect classification trends correlated 1) with the drug administration (C vs. LD) and 2) with the drug dose (LD vs. HD). Initially, PCA exhibited clear

separation of C and LD mice in the kidney (Figure 1A) but there was no separation observed either in C–LD comparison, or in the plasma and liver (Figures 1B–F). The confidence and performance of the developed models were estimated through misclassification and permutation testing and model ROC analysis, and the results, along with the figures of merit, are presented in Supplementary Table S1.

The main objective of the study was to investigate the alterations occurring by dose increase, and thus, the study was focused on the differentially expressed variables acquired from the LD–HD comparisons. Those with Variable Importance in the Projection (VIP) > 1.2 were employed for univariate ROC curve analysis to detect the variables that responded to the dose increase. The number of variables with Area Under Curve (AUC) value >0.8 were as follows: 251 variables for kidneys (49 upregulated in the HD), 345 variables for the liver (136 upregulated in the HD), and 47 variables for plasma (28 upregulated in the HD).

Moreover, PLS models were employed to investigate the linear correlation between the three levels of administered CMS (0, 1, and 1.5 mg/kg) and the alteration occurring to the metabolomics profiles of the mice. The excellent linearity (R^2 > 0.99) and the low root means square error of estimation of the PLS models (Figure 2) prove that there is a linear correlation between the administered dose and the resulting metabolomics alterations.

To elaborate on this observation, the OPLS-DA models of C–LD and LD–HD comparisons were used to build shared and unique structure plots, known as SUS plots, aiming to highlight the most highly dose-correlated variables. The SUS plot describes the correlation of the predictive variables afforded by the two OPLS-DA models, by plotting the loadings of both against each other. In this case, the two OPLS-DA models share a common group, the LD group. The SUS plot in Figure 3A represents the loadings of C–LD and LD–HD for the dataset of kidney, ESI^+. The features at the edges of the y-axis are discriminant for the model C–LD, and those at the edges of the x-axis are discriminant for the model LD–HD. The features existing in the diagonal orientation from the lower left to the higher right (Figure 3A, green arrow) are those that present shared structures, whereas those existing in the diagonal orientation from the higher left to the lower right (Figure 3A, black arrow) present unique structures. As the LD is the common group in the two OPLS-DAs, the variables of the shared structure show the same regulation in the LD group, in both C–LD and LD–HD comparisons. For example, the variable in Figure 3B shows increased levels in LD samples and decreased levels in C and HD samples; so, as it is always increased in the LD group, it is considered a variable of shared structure. Conversely, the variable in Figure 3C shows increased levels in the LD group, compared with the C-group levels, and in parallel shows decreased levels in the LD group when compared with the HD group. Thus, it is considered to be a variable of unique structure. The features of the unique structure seem to express dose–response, whereas those of the shared structure do not provide meaningful information.

Aiming to determine variables showing linear correlation to the dose, a pipeline of three steps was followed: 1) at first, the variables existing at the edges of the shared-structure-diagonal (of the SUS plot) were selected; 2) then, they were submitted to pairwise (C–LD and LD–HD) univariate ROC curve analysis, and those having AUC > 0.8 in both comparisons were retained; and 3) they were used to develop regression curves, as shown in Supplementary Figures S1, S2. This procedure resulted in 16 dose–response variables, with R^2 > 0.7; nine of them were upregulated in correlation to the dose (Table 1).

3.2 Variable selection and identification

The identification was statistically driven by the results of the pairwise comparison of LD–HD and also by the results of the SUS plot procedure. The pipeline followed for the current metabolomics study is described in Figure 4. Thirty-four statistically important features were attributed to known metabolites, as shown in Table 2. The identified metabolites were submitted to pathway analysis, showing extended alteration of purine metabolism in the kidneys. Thus, an additional hypothesis-driven peak-picking, focusing on the metabolites involved in the purine metabolism pathway, was performed. The screening list of the investigated metabolites is provided in Supplementary Table S3. For this step, the C, LD, and HD groups of kidney samples were used, and 27 metabolites were finally identified.

3.3 Pathway analysis

The pathway analysis was performed in two steps, using the *Pathway Analysis* module of MetaboAnalyst 5.0. Initially, all the identified metabolites, despite the biosample that they were detected in, were submitted to a naïve pathway analysis. This step pointed out extended dysregulation in purine metabolism, as described in Figure 5. Therefore, the metabolites participating in purine metabolism were targeted and determined in the raw MS data of all samples (kidney, plasma, and liver) and all groups (C, LD, and HD). The list of metabolites that were searched is available in Supplementary Table S3.

A higher number (27) of purine metabolism metabolites were detected in the kidney dataset, and therefore, the pathway analysis focused on kidneys. The peak area signals of the detected metabolites were used instead of concentration in the corresponding module of the Pathway Analysis tool. As this module is capable of pairwise comparisons, C–LD and LD–HD were investigated separately. In the C–LD comparison, 17/65 metabolites were altered, providing a *p*-value (FDR) = 0.04, in contrast to the LD–HD comparison that showed 17/65 altered metabolites as well, but a *p*-value (FDR) = 0.37, indicating that purine metabolism was highly influenced by the LD, but there was no further impact by the dose increase.

4 Discussion

This study was designed to enrich the existing knowledge of the metabolic alterations related to CMS. So far, most of the *in vivo* studies have used significantly high CMS doses to invoke the drug's toxicity. For instance, the most recent experiment by Nguyen et al. induced *in vivo* CMS toxicity by administering 25 mg/kg and 50 mg/kg (Long et al., 2022) at low and high doses, respectively, which are 10-fold higher than the recommended human dose (2.5–5 mg/kg/day). The high-dosing approaches provide ample

10.3389/fmolb.2024.1338497

TABLE 1 Summary of information for the dose–response variables resulting from the SUS plot procedure.

Dataset	M/Z	RT	R2	VIP (HD–LD)	AUC (HD–LD)	*p*-value (HD-LD)	Regulation (HD)	VIP (C–LD)	AUC (C–LD)	*p*-value (C–LD)	Regulation (LD)
KIDNEY(−)	205.994	0.8	0.78	1.2	0.85	0.08	↑	1.1	1	0.02	↑
KIDNEY(+)	125.0185	3.6	0.79	1.2	1	0.02	↑	1.1	0.85	0.12	↑
KIDNEY(+)	175.0059	1.5	0.84	1.3	0.8	0.19	↓	1.0	0.9	0.03	↓
KIDNEY(+)	224.5468	6.9	0.79	1.4	0.95	0.03	↑	1.0	0.9	0.08	↑
KIDNEY(+)	262.0619	4.4	0.82	1.3	0.9	0.09	↑	1.1	1	0.03	↑
KIDNEY(+)	278.0401	3.6	0.77	1.3	0.85	0.24	↑	1.2	0.95	0.02	↑
LIVER(−)	239.0422	14.7	0.73	1.3	0.8	0.1	↓	1.2	0.8	0.16	↓
LIVER(+)	126.0923	5.2	0.71	1.7	1	0.01	↑	1.2	0.76	0.22	↑
LIVER(+)	195.1244	15.1	0.76	1.5	0.88	0.03	↑	0.9	0.8	0.48	↑
LIVER(+)	206.1408	8.9	0.75	1.6	0.88	0.10	↑	1.1	0.72	0.19	↑
LIVER(+)	222.1616	10.2	0.78	1.8	0.84	0.10	↑	1.2	0.76	0.18	↑
LIVER(+)	241.1771	15.4	0.87	1.5	0.88	0.12	↓	1.1	0.72	0.28	↓
LIVER(+)	254.0957	12.7	0.75	1.4	0.84	0.19	↓	1.1	0.72	0.26	↓
LIVER(+)	348.3154	7.5	0.84	1.3	0.88	0.09	↓	1.6	0.96	0.03	↓
LIVER(+)	359.3187	16.1	0.72	2.2	1	0.00	↓	1.4	0.80	0.12	↓
LIVER(+)	399.2547	7.4	0.76	1.6	0.84	0.05	↓	1.7	0.92	0.02	↓

The (R2) column includes the R2 factor of linearity resulting from the developed regression curves.

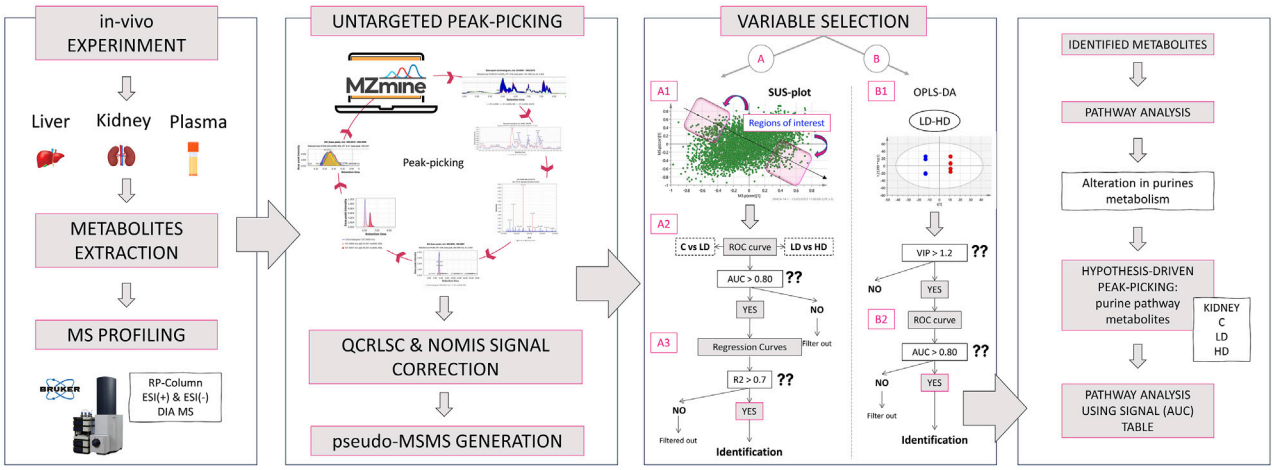

FIGURE 4
Graphical description of the applied metabolomics workflow: Initially, the *in vivo* experiment simulated the impact of 1-mg/kg and 1.5-mg/kg CMS in mice. The liver, kidney, and plasma samples were used for metabolite extraction, and the analysis was conducted with a Bruker maXis Impact QTOF MS, using RPLC and ESI$^{+/-}$ ionization. The MS was acquired with the DIA methodology. Then, the raw data were used for untargeted peak-picking, and the feature list was submitted to QC- and IS-based signal correction. RAMclustR was used for the generation of pseudo-MSMS. Then, the features were used for variable selection performed with two ways: i) extraction of dose–response variables using the SUS plot procedure and ii) extraction of dose-correlated variables combining multivariate (OPLS-DA) and univariate (ROC) models of the LD–HD comparison. The most discriminant variables were subjected to identification. The identified metabolites were used for a naïve pathway analysis. The results showed an alteration in renal purine metabolism, and thus, a targeted peak-picking of specific metabolites was applied to the raw data on kidneys. The results were used for a new semi-quantitative pathway analysis.

10.3389/fmolb.2024.1338497

TABLE 2 Summary of the identified metabolites.

mz_rt	Precursor	Common name	Mass error (Da)	Initial score	Fit score	Dataset	1reaction	AUC (LD−HD)	Regulation[a]
192.0526_4.06	[M−H]−	Glycolic acid	<0.001	1	0.675	KIDNEY	[+($C_5H_5N_5$ − H_2O)]	1	↓
211.9876_3.93	[M−H]−	L-Aspartyl-4-phosphate	−0.009	1	0.383	KIDNEY	-	1	↓
125.0185_3.57	[M+H]+	(R)-N-Methylsalsolinol	−0.002	1	0.931	KIDNEY	[+CO2]	0.85	↑ Dose-dependent
136.0652_1.76	[M+H]+	Adenine	0.003	1	0.458	KIDNEY	-	1	↓
159.0317_1.5	[M+Na]+	Hypoxanthine	0.004	1	0.494	KIDNEY	-	1	↑
175.006_1.51	[M+K]+	Phenylacetic acid	−0.010	1	0.302	KIDNEY	-	0.9	↓ Dose-dependent
194.0826_5.37	[M+H]+	2-Methylhippuric acid	0.001	1	0.707	KIDNEY	-	1	↓
232.0382_5.38	[M+K]+	2-Methylhippuric acid	0.001	1	0.627	KIDNEY	-	1	↓
256.122_5.57	[M+Na]+	Hydroxypropionylcarnitine	0.006	1	0.321	KIDNEY	-	1	↓
262.062_4.45	[M+H]+	2,8-Dihydroxyadenine	−0.006	1	0.508	KIDNEY	[+$C_4H_2N_2O$]	1	↑ Dose-dependent
269.0943_2.25	[M+H]+	Inosine	0.006	0.998	0.822	KIDNEY	-	1	↓
272.0946_5.57	[M+H]+	Deoxycytidine	0.007	1	0.858	KIDNEY	[+CO_2]	1	↓
273.0901_1.5	[M+Na]+	5-Methoxytryptophan	0.001	1	0.758	KIDNEY	[+O]	0.95	↓
278.0404_3.57	[M+H]+	Dopamine-4-sulfate	0.007	1	0.641	KIDNEY	[+CO_2]	0.95	↑ Dose-dependent
307.0513_2.24	[M+Na]+	D-Glucurono-6,3-lactone	−0.002	1	0.698	KIDNEY	[+$C_5H_4N_2O$]	0.95	↑
348.0774_1.6	[M+H]+	2′-Deoxyguanosine 5′-monophosphate	0.007	1	0.713	KIDNEY	-	1	↓
371.1139_1.84	[M+K]+	4-Hydroxynonenal	0.004	0.977	0.666	KIDNEY	[+$C_6H_8O_6$]	1	↓
520.3444_8.18	[M+H]+	LysoPC(18:2(9Z,12Z))	0.005	1	0.519	KIDNEY	-	1	↑
113.0361_1.09	[M+H]+	Dihydrouracil	0.002	1	0.122	LIVER	[−CH_2]	0.92	↓
145.0505_1.91	[M+H]+	3-Methylglutaconic acid	0.001	1	0.777	LIVER		0.92	↑
149.1182_5.93	[M+H]+	3-Hydroxyisoheptanoic acid	0.001	1	0.221	LIVER	[+H_2]	0.92	↓
188.0695_2.69	[M+H]+	Indoleacrylic acid	−0.001	1	0.725	LIVER	-	0.92	↑
241.1771_15.35	[M+K]+	Spermine	−0.002			LIVER	-	0.72	↓ dose-dependent
254.0957_12.56	[M+Na]+	Suberylglycine	−0.004	1	0.689	LIVER	-	0.72	↓ dose-dependent
256.0920_3.83	[M+K]+	Propionylcarnitine	−0.003	1	0.59	PLASMA	-	0.85	↑
278.0352_3.57	[M+H]+	L-DOPA sulfate	0.002	1	0.65	PLASMA	-	0.92	↑
254.0949_5.04	[M+H]+	Neopterin	0.006	1	0.75	PLASMA	-	0.88	↑
229.1555_1.65	[M+H]+	L-isoleucyl-L-proline	0.000	1	0.79	PLASMA	-	1	↑
222.0898_6.78	[M−H]−	5-Methyldeoxycytidine	1.000	1	0.69	PLASMA	[−H_2O]	0.98	↑
239.1498_4.34	[M+H]+	Homoanserine	−0.001	1	0.7	PLASMA	[−O]	1	↓
515.1538_6.72	[M−H]−	S-Adenosylhomocysteine	0.002	1	0.74	PLASMA	[+$C_5H_8O_4$]	1	↑
264.0569_3.23	[M+H]	N-acetyl-S-(3-oxo-3-carboxynpropyl) cysteine	0.006	1	1	LIVER	[−H_2]	1	↑

(Continued on following page)

TABLE 2 (*Continued*) Summary of the identified metabolites.

mz_rt	Precursor	Common name	Mass error (Da)	Initial score	Fit score	Dataset	1reaction	AUC (LD−HD)	Regulation[a]
154.0705	[M+H]+	Dopamine	0.002	1	0.77	LIVER	-	0.79	↑
206.1405_10.45	[M+NH4]+	Nonic acid	0.001	1	0.76	LIVER	-	1	↓

The (1reaction) column provides information for those metabolites that were identified as products of metabolite metabolism.
[a]The arrows (↑, ↓) refer to the levels of the metabolites in the HD group when it is compared with the LD group. ↑/↓ Dose-dependent refers to the metabolites that are dose-related and detected up (↑)/down (↓) regulated by the increase in the dose.

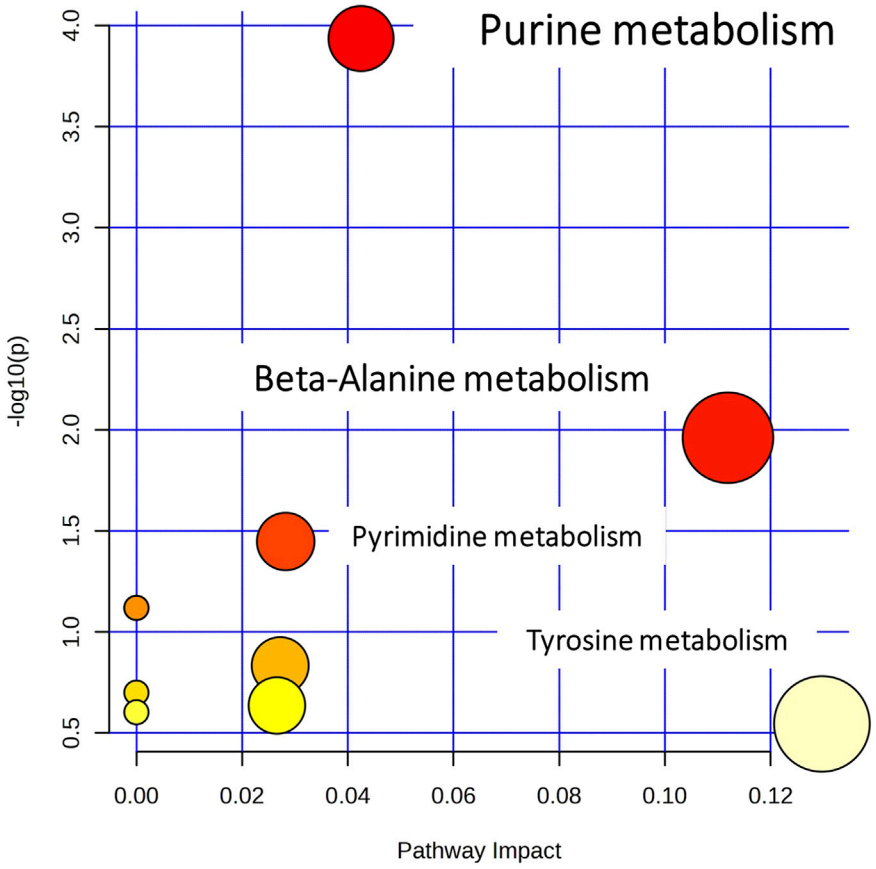

FIGURE 5
Overview of pathway analysis, showing all matched pathways according to the *p*-values from the pathway enrichment analysis and pathway impact values from the pathway topology analysis.

information on biochemical alterations occurring in extremely toxic conditions, offering clear evidence of the triggered pathways leading to the observed clinical symptoms. Conversely, such dosing regimens are never met in the clinical setting, where the administered drug levels are strictly regulated and immediately taken care of either by lowering or even by stopping the administration. However, CMS remains the last-resort antibiotic for patients infected by multidrug-resistant bacteria; thus, metabolic dysregulations caused even by the normal dosing schemes should be investigated.

Anticipating the early and frequently latent biochemical alterations provoked by the drug will provide the ability to adjust the curation protocol by reducing/stopping the administration. Under this notion, the current study attempted to simulate *in vivo* the metabolic alterations caused by the CMS doses that are comparable with those administered to humans. Thus, 15 mice were separated into three equal groups and received 0 mg/kg (C—the control group), 1 mg/kg (LD), and 1.5 mg/kg (HD) of CMS. The doses administered to mice were calculated based on the dose conversion between humans and animals. The study examined plasma, kidneys, and livers to investigate the latent background of colistin nephrotoxicity and the impact of the drug on the circulatory system and on the liver as well.

An Reversed Phase Liquid Chromatography—High Resolution Mass Spectrometry (RPLC-HRMS)-based metabolomics protocol was employed to analyze the samples, whereas an array of univariate

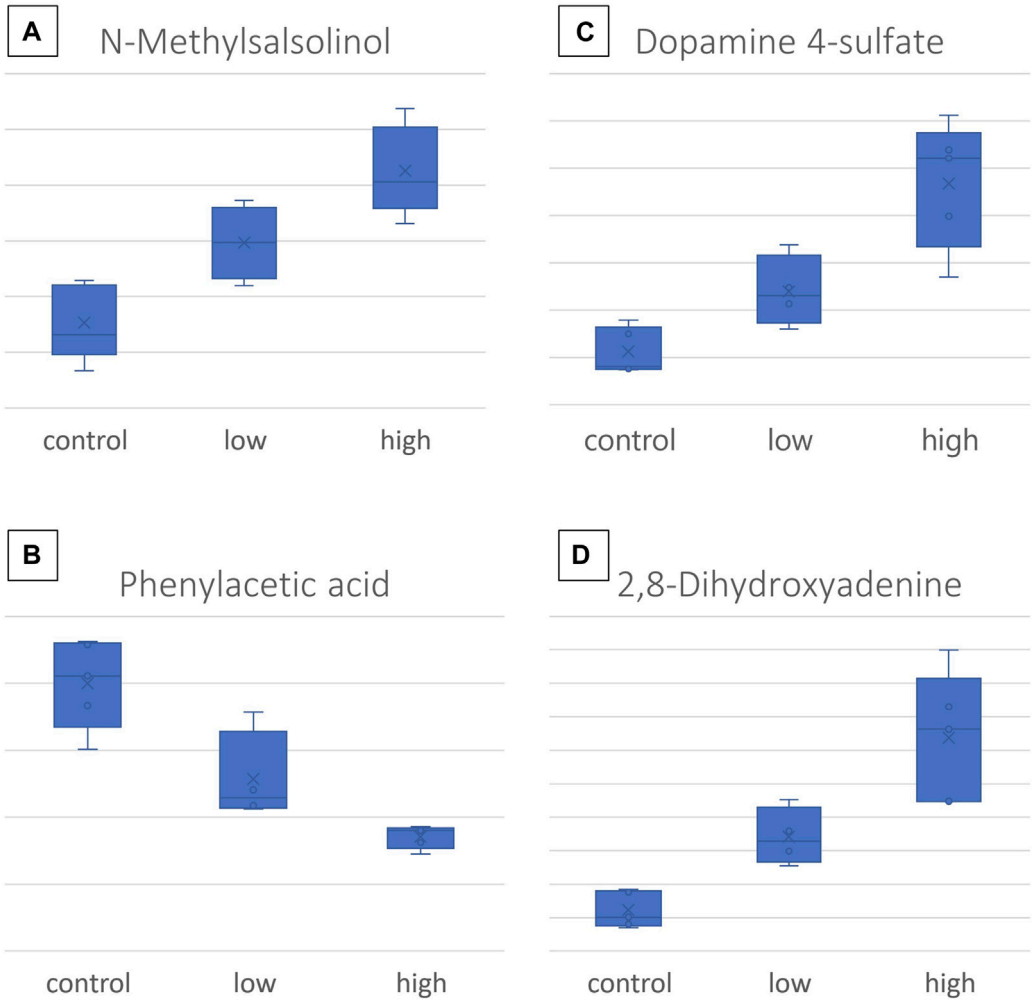

FIGURE 6
Box-plots of the most important CMS dose-responding metabolites: **(A)** N-methylsalsolinol, detected in the kidney; **(B)** dopamine-4-sulfate, detected in the kidney; **(C)** phenylacetic acid, detected in the kidney; **(D)** 2,8- dihydroxyadenine, detected in the kidney.

and multivariate methodologies was combined for the statistical process. The PCA and OPLS-DA focused on the pairwise comparisons of the C–LD and LD–HD groups. PCA showed that the most significant separation trend was observed in the kidneys of those in the C–LD group. This implies that the drug triggers important metabolic alterations in kidneys, even at the lower doses, when there are no clinical data that could indicate toxicity. The OPLS-DA models classified efficiently the C–LD and LD–HD groups, providing satisfactory figures of merit.

Interestingly, the liver dataset offered the highest number of important features in both OPLS-DA and ROC curve analysis, and most of them were downregulated with the increase of the drug. However, only nine of the liver's differentiated variables were finally identified, speculating that the drug impairs the liver metabolism, dysregulating metabolite derivatives that remain unknown. In addition, the PLS models proved the existence of linear correlations between the dose level and the alterations expressed in mice metabolomic profiles. The PLS models were only used to verify the linear correlation of metabolomics profile and CMS dose. The PLS results were not exploited for the variable selection, as PLS is a more complex model that encompasses three groups, whereas the pairwise OPLS-DA model affords more interpretable results.

Concomitantly, the SUS plot was used to investigate the existence of metabolites that are linearly correlated to the dose and highlighted 16 dose-related variables, with an ROC curve AUC of >0.8 for both C–LD and LD–HD comparisons of kidneys and livers (Supplementary Figures S2, S3). In the plasma case, none of the variables resulting from the SUS plot passed the ROC curve analysis threshold, and therefore, the variables were not used to generate regression curves. Six of the dose-correlated variables were identified: suberylglycine (liver, ↓, $R^2 = 0.75$), spermine (liver, ↓, $R^2 = 0.87$), (R)-N-methylsalsolinol (kidney, ↑, $R^2 = 0.79$), phenylacetic acid (kidney, ↓, $R^2 = 0.85$), 2,8-dihydroxyadenine (kidney, ↑, $R^2 = 0.82$), dopamine 4-sulfate (kidney, ↑, $R^2 = 0.78$), and examples of their box-plots are shown in Figure 6.

Regarding the LD–HD comparison, 14, 9, and 7 differentially expressed metabolites were identified in the kidney, liver, and plasma, respectively, as summarized in Table 2. In the kidney, 78% of the metabolites were decreased in the HD group, whereas in plasma, 71% were

increased. The metabolites that exhibited a higher relevance to the current case are further discussed below.

4.1 Alterations in dopamine regulation

The administration of CMS provoked changes in four metabolites that belong to the dopamine biochemical pathways, i.e., dopamine (DA, liver, ↑), dopamine-4-sulfate (DA-4-S, kidney, dose-increased), L-DOPA sulfate (L-DOPA-S, plasma ↑), and N-methyl-R-salsolinol (*M*NRSal, kidney, dose-increased). Differentiation of these metabolites provides a latent sign of CMS-induced dysregulation of dopamine mechanisms, that is, generalized, as the alterations were observed in the plasma, kidney, and liver as well.

The *M*NRSal, which showed elevated response to the drug dose, is an endogenous neurotoxin, related to cell apoptosis. *M*NRSal is the enzymatic product of R-salsolinol (R-Sal), which in turn is formed by DA under the action of R-Sal synthases. *M*NRSal has been detected in the urine of patients with Parkinson's disease and is considered more toxic than R-Sal (Cao et al., 2021). *M*NRSal presents apoptotic action, and it is suggested that the toxin impairs the mitochondrial permeability transition by reducing the mitochondrial membrane potential, resulting in increased release of apoptotic factors, such as cytochrome *c*, into the cytoplasm. Moreover, the toxin activates the caspase-3, which also induces cell death (Akao et al., 2002). Furthermore, *M*NRSal degradation products inhibit the mitochondrial complex-I causing apoptosis and increase the ROS as well (Cao et al., 2021). A realistic hypothesis is that the increasing trend of the toxin in the kidney, following the increase of CMS, indicates early apoptosis in renal cells that could lead to severe kidney injury. This hypothesis is amplified by the results of a recent study that estimated the dose-responding nephrotoxicity of CMS on human embryonic kidney cells. The mentioned study showed dose-dependent renal cytotoxicity, determined by renal cell viability (Mektrirat et al., 2023).

DA-4-S showed increased levels, in response to the drug dose in the kidney, whereas L-DOPA-S was increased in plasma as well. The sulfonation locus of the endogenous/exogenous phenols and catechols, i.e., DA and L-DOPA, probably happens in the upper gastrointestinal track, where the responsible enzymes are mainly expressed (Itäaho et al., 2007). It should be noted that the sulfated forms of DA are predominant in human blood and represent 90% of the total DA (Itäaho et al., 2007). Furthermore, the sulfonation of DA is pivotal for metabolites binding with its receptors (Itäaho et al., 2007). The increased levels of DA-4-S and L-DOPA-S in plasma and kidneys suggest elevated biosynthesis of DA. DA is a natriuretic hormone and regulates sodium levels, inducing sodium excretion and constraining its reabsorption at the proximal tubule (Choi et al., 2015). Thus, excessive action of DA leads to limited levels of circulatory sodium, a condition that is linked with the occurrence of hypotension (Alshahrani et al., 2017). Additionally, it has been speculated that impairment of the estimated glomerular filtration rate (eGFR) is associated with neurological adverse effects, i.e., the limited eGFR leads to increased circulation levels of uremic toxins and kidney hormones that end up in the dopaminergic system of the brain (De Donato et al., 2022).

DA was also found elevated in the liver of the HD group. It is worth mentioning that elevated levels of DA are associated with the liver fatty acid (FA) metabolism occurring in the mitochondria of hepatocytes. The regulation of FA metabolism depends on the expression of carnitine palmitoyl transferase (CPT) I and CPT II. The catecholamines as DA induce the CPT gene expression in the hepatocytes, inducing ketogenesis. Thus, the increase of DA in CMS mice indicates dysregulation in liver FA metabolism (Jensen et al., 2013). The increased ketogenesis is also linked to hypoglycemia. The acute increase in ketones leads to nausea, vomiting, pain, lethargy, and even coma, whereas chronic ketosis can cause hepatic transaminase elevation (Drachmann et al., 2021).

4.2 Downregulation of renal phenylacetic acid

Phenylacetic acid (PAA) exhibited opposite response to the drug dose, in the renal tissue, i.e., metabolite decreasing levels in response to CMS increase. PAA is produced by phenylalanine degradation and is considered to be a uremic toxin. Based on existing literature, the circulatory levels of PAA have been increased in patients with chronic kidney disease (CKD) (Scholze et al., 2007); however, in the current case, no alteration of PAA plasma levels was detected. In addition, the metabolite inhibits the expression of the inducible nitric oxide synthase (iNOS) in mononuclear leukocytes in patients with end-stage renal failure (Jankowski et al., 2003). iNOS is expressed when the cells are triggered by proinflammatory cytokines and produce nitric oxide (NO) as a critical response of the immune system. In the current case, PAA was found to be decreased by CSM, speculating failure to balance the expression of iNOS leading to elevated levels of NO in the kidney. The overexpression of iNOS is linked to a variety of pathological complications such as septic shock and pain (Cinelli et al., 2020). Furthermore, the decreased renal PAA levels suggest kidney impairment resulting in the limitation of renal filtration ability. Thus, the circulatory substances do not pass from blood to the kidneys but accumulate in the circulation.

4.3 Upregulation of renal 2,8-dihydroxyadenine

The accumulation of 2,8-dihydroxyadenine (2,8-DHA) renal levels by CMS dosing is worth mentioning finding. 2,8-DHA is an adenine metabolite, accumulated in cases of adenine phosphoribosyl-transferase deficiency, which is a rare autosomal metabolic disorder, associated with uric acid's metabolism. 2,8-DHA exhibits low solubility; thus, its overexpression leads to the formation and precipitation of urinary crystals and kidney stones, leading to urolithiasis or nephropathy (George et al., 2017).

4.4 Downregulation of liver suberylglycine

Suberylglycine decreased by CMS administration in the liver tissue. There is limited literature concerning this substance. The metabolite is normally occurring as a product of fatty acid

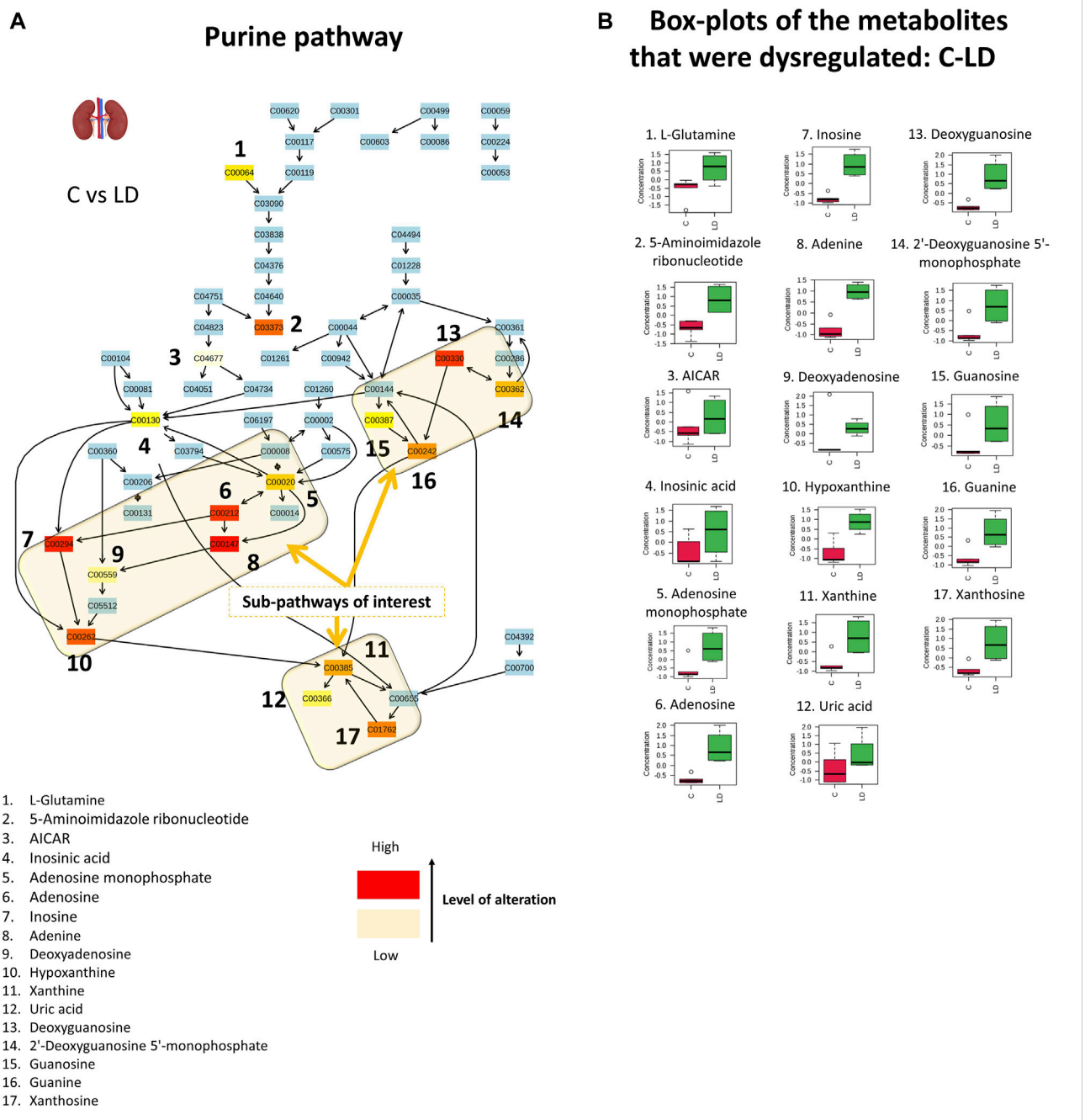

FIGURE 7
Graphical description of the alteration that occurred in renal purine metabolism with the administration of 1.0-mg/kg CMS. The sub-pathways of interest point out the locations where sequential alterations were observed. The box-plots show the normalized content of the perturbated metabolites in the C (red) and LD (green) groups.

metabolism and is formed through the oxidation of suberyl-CoA, an intermediate of fatty acid metabolism. Suberylglycine is primarily associated with a group of inherited metabolic disorders known as organic acidemias, leading to the accumulation of various organic acids, including suberylglycine, in the body. The measurement of suberylglycine levels in biological samples, such as urine or blood, is used as a diagnostic marker for certain organic acidemias (Divry et al., 1984; Rinaldo et al., 1989). The elevated urinary levels of suberylglycine have been associated with hereditary medium-chain acyl-CoA hydrogenase (MCAD) failing (Rinaldo et al., 1989); however, in the current case, metabolite levels were found to be decreased in the liver. MCAD is suggested to be the most common cause of nonalcoholic fatty liver disease (Prieto Jimenez et al., 2022). Prieto Jimenez et al. (2022) have reported rare hepatic steatosis secondary to the chronic case, expressed in an infant, where the levels of circulatory suberylglycine were elevated. This early observation of potential CSM-induced MCAD deficiency is key evidence and should be further investigated.

4.5 Downregulation of liver spermine

Spermine was also found to be downregulated in the liver by the increase in CMS. The compound is a polyamine, naturally present in cells and tissues of living organisms, including humans. It is derived from the amino acid ornithine through a series of enzymatic reactions. Spermine plays important roles in various biological processes, including cell growth, proliferation, and DNA stabilization (Zhou et al., 2018). It has been found that in the plasma of patients with chronic renal failure, the circulatory levels of spermine are decreased (Igarashi et al., 2006). In our study, the hepatic levels of spermine were decreased by the increased CMS dose, but there were no detected alterations of this metabolite in plasma. Interestingly, polyamines such as spermine are proved to counterbalance drug adverse effects, such as hepatotoxicity, and thus are administrated as protective agents (Zhou et al., 2018), inhibiting cell apoptosis (Amin et al., 2021). In the current case, the CMS-induced decrease of spermine indicates that the drug prohibits homeostatic mechanisms, such as those that counterbalance the drug's effects.

4.6 Disturbed purine metabolism and renal dysfunction

The results of the semi-quantitive pathway analysis of the C–LD group are described in Figure 7 where, the altered metabolites of the pathway are shown in Figure 7A and the box-plots of their corrected signal are shown in Figure 7B. From the detected metabolites, 17 were increased by the low CMS dose, with the main perturbations occurring in the sub-pathways that result in the formation of xanthine, uric acid (UA), and guanine (Figure 7). The dysregulation of nine sequential metabolites, in the sub-pathway of UA formation, provides strong proof that CMS causes severe effects on renal purine metabolism. An intriguing observation is that in the C–LD comparison, the purine metabolism pathway displayed critical alterations [p (FDR) = 0.04], whereas in the LD–HD comparison, there were no important differences detected in metabolite levels [p (FDR) = 0.37, Supplementary Figure S4].

Purines are enzymatically transformed into hypoxanthine and then into xanthine, which is the precursor of UA (Figure 7). The formation of UA is followed by the generation of superoxide anions and reactive oxygen species, as degradation byproducts. The extended production of UA, as observed in the current case, leads to high levels of intracellular oxidative stress-inducing factors causing cell damage (Gherghina et al., 2022). Dysregulation of purine metabolism, particularly hyperuricemia (elevation of UA), is associated with kidney injury and is a marker for the progression of CKD (Jiao et al., 2022). There are several proposed associations between UA and kidney impairment: 1) formation of monosodium urate crystals that precipitate in the tubules of the extrarenal system; 2) oxidative stress due to the intracellular pro-oxidative properties of UA that cause endothelial dysfunction, renal fibrosis, inflammation, and glomerulosclerosis; and 3) UA prevents nitric oxide (NO) synthesis and thus hinders endothelial cell proliferation (Gherghina et al., 2022; Jiao et al., 2022). The increased levels of xanthine and UA are also associated with aging-induced renal impairment (Jiao et al., 2022).

Additionally, the alterations of purine metabolism could be the key point regarding the connection of neuro- and nephrotoxicity occurring due to CMS administration. It is proposed that decreased eGFR leads to an increase in circulatory levels of metabolic waste (uremic toxins and kidney hormones), provoking all types of neurological complications by triggering the nervous system (dopaminergic system) and causing brain dysfunction (Mazumder et al., 2018; De Donato et al., 2022). In addition, there are several reports of cognitive impairment in patients with CKD (Mazumder et al., 2018). A recent computational docking study tested the binding affinity of xanthine, hypoxanthine, UA, and 2,8-DHA with acetylcholinesterase (AChE): UA showed a higher binding affinity, and xanthine and hypoxanthine presented high docking scores as well (Mazumder et al., 2018). AChE hydrolyzes acetylcholine, which is important for learning and memory, so its rapid degradation by AChE leads to dementia and Cognitive Impairment (CI) (Wamser et al., 2013). *In vitro* testing showed that hypoxanthine enhanced the action of AChE (Wamser et al., 2013). This observation indicates a naïve correlation between CMS-neurotoxicity and CMS-nephrotoxicity that should be further investigated.

The results of the current study are in accordance with the results of Nguyen et al.'s corresponding metabolomics study, in which ~16-fold higher doses of CMS were administered, i.e., 25 mg/kg and 50 mg/kg (Long et al., 2022) as low and high dose, respectively, *in vivo*. Nguyen et al. observed critical separation trends (PCA) between the control and the 25-mg/kg/day-treated mice and dose-responding alterations in the metabolomics profiles of kidney and liver tissues. Moreover, comparing the kidneys and livers of the control and treated mice, they observed differences in pathways related to antioxidation mechanisms, i.e., glutathione metabolism, and in pathways related to DNA synthesis such as purine metabolism. In addition, the study indicated CMS-induced oxidative stress and caspase-dependent cell apoptosis at the renal level.

In the current study, important separation trends were observed even in the kidneys of the LD group (1.0 mg/kg/day) versus the control, indicating that CMS has a critical impact on renal tissue, even at these doses. Therefore, the determination of early biomarkers will help in the detection of latent kidney dysfunction, even before it is expressed with clinical symptoms, and it will permit the timely adjustment of the curation protocol too. The dose–response metabolomics alterations are also confirmed for the lower dose ranges, as shown by the PLS regression results of the current study. Moreover, there are early indications of increased oxidative stress in kidney and liver tissue, i.e., the upregulation of MNRSal renal levels that induces cell apoptosis by activating caspase-3. Finally, the current study showed purine metabolism alterations induced by low CMS that were not further amplified by the 0.5-mg/kg/day increase in the dose. However, the Nguyen et al. study showed that the purine metabolism is related to a higher dose increase, and therefore, further investigation of this pathway's alterations at a wider range of doses, i.e., 1–5 mg/kg/day would provide solid information regarding CMS impact on

DNA synthesis and would also shed light on naïve assumption of nephro- and neurotoxicity.

5 Conclusion

CMS is the last-resort antibiotic factor administered for the treatment of infections caused by multidrug-resistant bacteria. However, the use of the drug is attenuated by the occurrence of neurological and renal complications resulting from its administration. Several studies have focused on CMS-induced neuro- and nephrotoxicity by administrating high doses of the drug to simulate the toxic condition. The current study aimed to shed light on the biochemical alterations triggered by the recommended human dose, 1–1.5 mg/kg/day. Moreover, the study investigated the impact of the drug on the circulatory system, and on the renal and liver function as well. So far, despite the existence of indications regarding CMS-induced hepatotoxicity, there is no evidence for the displaying mechanisms. The study showed that even the lower human dose (1 mg/kg) had a severe impact on the kidneys and also pointed out a linear response between the drug dose and the metabolic alterations for the plasma, kidney, and liver. Sixteen variables showed significant correlation to the dose, and six of them were identified: suberylglycine (liver, ↓), spermine (liver, ↓), (R)-N-methylsalsolinol (kidney, ↑), phenylacetic acid (kidney, ↓), 2,8-dihydroxyadenine (kidney, ↑), and dopamine-4-sulfate (kidney, ↑). In summary, the results of the current study showed that CMS

- induces the renal dopamine pathway;
- increases the renal levels of 2,8-DHA and probably leads to the formation and precipitation of urinary crystals and kidney stones;
- disrupts the renal purine metabolism, increasing the formation of xanthine, hypoxanthine, and UA. Xanthine is considered an AChE activator, leading to the rapid degradation of acetylcholine. This is strong evidence for the shared metabolic background of CMS-induced nephrotoxicity and neurotoxicity;
- disrupts hepatic MCAD, probably leading to hepatic steatosis; and
- decreases hepatic levels of spermine, which counterbalances hepatotoxicity by inhibiting cell death.

Overall, the current study, investigating the impact of CMS doses that correspond to those applied in clinical practice, revealed that these doses trigger biochemical pathways related to kidney and liver toxicity. These alterations are early detectable, even when there is no clinical evidence of toxicity, and could facilitate the adjustment of the curation scheme in the future.

5.1 Limitations to the study

The current study is impacted by potential limitations; i.e., DIA MS acquisition, despite being a more informative methodology, restricted the ability to perform more extended identification. Moreover, the study focused on nephrotoxicity and hepatotoxicity caused by CMS and did not examine other organs such as the brain and the heart. In particular, the examination of metabolomics alteration in the brain could amplify the assumption of a correlation between nephrotoxicity and neurotoxicity and will be an objective of a future study. The study did not consider other toxicological endpoints, i.e., histological signs, and therefore, the metabolomics evidence is not correlated with the clinical picture of the mice. Finally, despite that the metabolites are molecules of universal structure, the exact extrapolation of the effects from humans to animals might not be accurate enough to draw a safe conclusion and extend it to the mechanism proposed. Nevertheless, the indications of this study set the basis for a thorough investigation of CMS toxicity.

Data availability statement

The datasets presented in this study can be found in online repositories. The names of the repository/repositories and accession number(s) can be found at: https://www.ebi.ac.uk/metabolights/, MTBLS8898.

Ethics statement

The animal study was approved by the Ethics Committee of the Establishment of Laboratory Animals, Department of Pharmacology, Medical School NKUA (Ethics Committee Approval No. 574234/20-07-2020). The study was conducted in accordance with the local legislation and institutional requirements.

Author contributions

IB: Conceptualization, data curation, formal analysis, investigation, methodology, visualization, writing–original draft, and writing–review and editing. ID: Conceptualization, investigation, writing–original draft, and writing–review and editing. AD: Formal analysis, investigation, methodology, and writing–review and editing. MP: Formal analysis, investigation, methodology, and writing–review and editing. MK: Formal analysis, investigation, methodology, and writing–review and editing. PD: Formal analysis and writing–review and editing. NT: Writing–review and editing, conceptualization, methodology, and resources. AT: Conceptualization and writing–review and editing. DT: Conceptualization, methodology, and writing–review and editing. EG: Conceptualization, investigation, methodology, supervision, writing–original draft, and writing–review and editing.

Funding

The authors declare that no financial support was received for the research, authorship, and/or publication of this article.

Conflict of interest

The authors declare that the research was conducted in the absence of any commercial or financial relationships that could be construed as a potential conflict of interest.

The authors declared that they were an editorial board member of Frontiers, at the time of submission. This had no impact on the peer review process and the final decision.

Publisher's note

All claims expressed in this article are solely those of the authors and do not necessarily represent those of their affiliated organizations, or those of the publisher, the editors, and the reviewers. Any product that may be evaluated in this article, or claim that may be made by its manufacturer, is not guaranteed or endorsed by the publisher.

Supplementary material

The Supplementary Material for this article can be found online at: https://www.frontiersin.org/articles/10.3389/fmolb.2024.1338497/full#supplementary-material

References

Akao, Y., Maruyama, W., Shimizu, S., Yi, H., Nakagawa, Y., Shamoto-Nagai, M., et al. (2002). Mitochondrial permeability transition mediates apoptosis induced by N-methyl(R)salsolinol, an endogenous neurotoxin, and is inhibited by Bcl-2 and rasagiline, N-propargyl-1(R)-aminoindan. *J. Neurochem.* 82 (4), 913–923. doi:10.1046/j.1471-4159.2002.01047.x

Alotaibi, F. M., Alshehail, B. M., Al Jamea, Z. A. H., Joseph, R., Alanazi, A. H., Alhamed, N. A., et al. (2022). Incidence and risk factors of colistin-induced nephrotoxicity associated with the international consensus guidelines for the optimal use of the polymyxins: a retrospective study in a tertiary care hospital, Saudi arabia. *Antibiotics* 11 (11), 1569. doi:10.3390/antibiotics11111569

Alshahrani, S., Rapoport, R. M., and Soleimani, M. (2017). Vascular contractile reactivity in hypotension due to reduced renal reabsorption of Na+ and restricted dietary Na. *Naunyn Schmiedeb. Arch. Pharmacol.* 390 (3), 321–326. doi:10.1007/s00210-017-1340-0

Amin, M., Tang, S., Shalamanova, L., Taylor, R. L., Wylie, S., Abdullah, B. M., et al. (2021). Polyamine biomarkers as indicators of human disease. *Biomarkers* 26 (2), 77–94. doi:10.1080/1354750X.2021.1875506

Bergen, P. J., Li, J., Rayner, C. R., and Nation, R. L. (2006). Colistin methanesulfonate is an inactive prodrug of colistin against *Pseudomonas aeruginosa*. *Antimicrob. Agents Chemother.* 50 (6), 1953–1958. doi:10.1128/AAC.00035-06

Broeckling, C. D., Afsar, F. A., Neumann, S., Ben-Hur, A., and Prenni, J. E. (2014). RAMClust: a novel feature clustering method enables spectral-matching-based annotation for metabolomics data. *Anal. Chem.* 86 (14), 6812–6817. doi:10.1021/ac501530d

Cao, Y., Li, B., Ismail, N., Smith, K., Li, T., Dai, R., et al. (2021). Neurotoxicity and underlying mechanisms of endogenous neurotoxins. *Int. J. Mol. Sci.* 22 (23), 12805. doi:10.3390/ijms222312805

Choi, M. R., Kouyoumdzian, N. M., Rukavina Mikusic, N. L., Kravetz, M. C., Rosón, M. I., Rodríguez Fermepin, M., et al. (2015). Renal dopaminergic system: pathophysiological implications and clinical perspectives. *World J. Nephrol.* 4 (2), 196–212. doi:10.5527/wjn.v4.i2.196

Cinelli, M. A., Do, H. T., Miley, G. P., and Silverman, R. B. (2020). Inducible nitric oxide synthase: regulation, structure, and inhibition. *Med. Res. Rev.* 40 (1), 158–189. doi:10.1002/med.21599

Dai, C., Xiao, X., Li, J., Ciccotosto, G. D., Cappai, R., Tang, S., et al. (2019). Molecular mechanisms of neurotoxicity induced by polymyxins and chemoprevention. *ACS Chem. Neurosci.* 10 (1), 120–131. doi:10.1021/acschemneuro.8b00300

De Donato, A., Buonincontri, V., Borriello, G., Martinelli, G., and Mone, P. (2022). The dopamine system: insights between kidney and brain. *Kidney Blood Press Res.* 47 (8), 493–505. doi:10.1159/000522132

Divry, P., Vianey-Liaud, C., and Cotte, J. (1984). Gas chromatography--mass spectrometry (GC--MS) diagnosis of two cases of medium chain acyl-CoA dehydrogenase deficiency. *J. Inherit. Metab. Dis.* 7 (Suppl. 1), 44–47. doi:10.1007/BF03047373

Drachmann, D., Hoffmann, E., Carrigg, A., Davis-Yates, B., Weaver, V., Thornton, P., et al. (2021). Towards enhanced understanding of idiopathic ketotic hypoglycemia: a literature review and introduction of the patient organization, Ketotic Hypoglycemia International. *Orphanet J. Rare Dis.* 16 (1), 173. doi:10.1186/s13023-021-01797-2

Eljaaly, K., Bidell, M. R., Gandhi, R. G., Alshehri, S., Enani, M. A., Al-Jedai, A., et al. (2021). Colistin nephrotoxicity: meta-analysis of randomized controlled trials. *Open Forum Infect. Dis.* 8 (2), ofab026. doi:10.1093/ofid/ofab026

Falagas, M. E., and Kasiakou, S. K. (2005). Colistin: the revival of polymyxins for the management of multidrug-resistant gram-negative bacterial infections. *Clin. Infect. Dis.* 40, 1333–1341. doi:10.1086/429323

Fu, J., Zhang, Y., Wang, Y., Zhang, H., Liu, J., Tang, J., et al. (2022). Optimization of metabolomic data processing using NOREVA. *Nat. Protoc.* 17 (1), 129–151. doi:10.1038/s41596-021-00636-9

Gai, Z., Samodelov, S. L., Kullak-Ublick, G. A., and Visentin, M. (2019). Molecular mechanisms of colistin-induced nephrotoxicity. *Molecules* 24, 653. doi:10.3390/molecules24030653

Garonzik, S. M., Li, J., Thamlikitkul, V., Paterson, D. L., Shoham, S., Jacob, J., et al. (2011). Population pharmacokinetics of colistin methanesulfonate and formed colistin in critically ill patients from a multicenter study provide dosing suggestions for various categories of patients. *Antimicrob. Agents Chemother.* 55 (7), 3284–3294. doi:10.1128/AAC.01733-10

George, S. A., Al-Rushaidan, S., Francis, I., and Narayanan Nampoory, M. R. (2017). 2,8-Dihydroxyadenine nephropathy identified as cause of end-stage renal disease after renal transplant. *Exp. Clin. Transpl.* 15 (5), 574–577. doi:10.6002/ect.2015.0096

Gherghina, M. E., Peride, I., Tiglis, M., Neagu, T. P., Niculae, A., and Checherita, I. A. (2022). Uric acid and oxidative stress—relationship with cardiovascular, metabolic, and renal impairment. *Int. J. Mol. Sci.* 23 (6), 3188. doi:10.3390/ijms23063188

Grégoire, N., Aranzana-Climent, V., Magréault, S., Marchand, S., and Couet, W. (2017). Clinical pharmacokinetics and pharmacodynamics of colistin. *Clin. Pharmacokinet.* 56 (12), 1441–1460. doi:10.1007/S40262-017-0561-1

Haseeb, A., Faidah, H. S., Alghamdi, S., Alotaibi, A. F., Elrggal, M. E., Mahrous, A. J., et al. (2021). Dose optimization of colistin: a systematic review. *Antibiotics* 10 (12), 1454. doi:10.3390/antibiotics10121454

Huan, T., Tang, C., Li, R., Shi, Y., Lin, G., and Li, L. (2015). MyCompoundID MS/MS search: metabolite identification using a library of predicted fragment-ion-spectra of 383,830 possible human metabolites. *Anal. Chem.* 87 (20), 10619–10626. doi:10.1021/acs.analchem.5b03126

Igarashi, K., Ueda, S., Yoshida, K., and Kashiwagi, K. (2006). Polyamines in renal failure. *Amino Acids* 31 (4), 477–483. doi:10.1007/s00726-006-0264-7

Inci, A., Toker, M. K., Guney Bicer, I., Derbent, A., and Salihoglu, Z. (2018). Determination of colistin-related nephrotoxicity and risk factors in intensive care unit. *North Clin. Istanb* 5 (2), 120–124. doi:10.14744/nci.2017.42243

Itäaho, K., Alakurtti, S., Yli-Kauhaluoma, J., Taskinen, J., Coughtrie, M. W. H., and Kostiainen, R. (2007). Regioselective sulfonation of dopamine by SULT1A3 *in vitro* provides a molecular explanation for the preponderance of dopamine-3-O-sulfate in human blood circulation. *Biochem. Pharmacol.* 74 (3), 504–510. doi:10.1016/j.bcp.2007.05.003

Jacob, S., Nair, A. B., and Morsy, M. A. (2022). Dose conversion between animals and humans: a practical solution. *Indian J. Pharm. Educ. Res.* 56 (3), 600–607. doi:10.5530/ijper.56.3.108

Jankowski, J., Van Der Giet, M., Jankowski, V., Schmidt, S., Hemeier, M., Mahn, B., et al. (2003). Increased plasma phenylacetic acid in patients with end-stage renal failure inhibits iNOS expression. *J. Clin. Invest.* 112 (2), 256–264. doi:10.1172/JCI15524

Jensen, K. J., Alpini, G., and Glaser, S. (2013). Hepatic nervous system and neurobiology of the liver. *Compr. Physiol.* 3 (2), 655–665. doi:10.1002/cphy.c120018

Jeong, E. S., Kim, G., Moon, K. S., Kim, Y. B., Oh, J. H., Kim, H. S., et al. (2016). Characterization of urinary metabolites as biomarkers of colistin-induced nephrotoxicity in rats by a liquid chromatography/mass spectrometry-based metabolomics approach. *Toxicol. Lett.* 248, 52–60. doi:10.1016/J.TOXLET.2016.02.018

Jiao, D., Qi, L., Hu, L., Hu, D., Li, X., Li, G., et al. (2022). Changes in aging-induced kidney dysfunction in mice based on a metabolomics analysis. *Front. Endocrinol. (Lausanne)* 13 (September), 959311–959315. doi:10.3389/fendo.2022.959311

Katip, W., Rayanakorn, A., Oberdorfer, P., Taruangsri, P., Nampuan, T., and Okonogi, S. (2024). Comparative effectiveness and mortality of colistin monotherapy versus colistin-fosfomycin combination therapy for the treatment of carbapenem-resistant enterobacteriaceae (cre) infections: a propensity score analysis. *J. Infect. Public Health* 17 (5), 727–734. doi:10.1016/j.jiph.2024.03.010

Long, N. P., Oh, J. H., Park, S. M., Yen, N. T. H., Phat, N. K., Cho, Y. S., et al. (2022). Delineation of the molecular mechanisms underlying Colistin-mediated toxicity using

metabolomic and transcriptomic analyses. *Toxicol. Appl. Pharmacol.* 439 (February), 115928. doi:10.1016/j.taap.2022.115928

Luan, H., Ji, F., Chen, Y., and Cai, Z. (2018). statTarget: a streamlined tool for signal drift correction and interpretations of quantitative mass spectrometry-based omics data. *Anal. Chim. Acta* 1036, 66–72. doi:10.1016/j.aca.2018.08.002

Mazumder, M. K., Phukan, B. C., Bhattacharjee, A., and Borah, A. (2018). Disturbed purine nucleotide metabolism in chronic kidney disease is a risk factor for cognitive impairment. *Med. Hypotheses* 111 (December 2017), 36–39. doi:10.1016/j.mehy.2017.12.016

Mektrirat, R., Paengjun, N., Chongrattanameteekul, P., Umsumarng, S., Cheunsri, S., Photichai, K., et al. (2023). Utilizing liposomal encapsulation approach to address nephrotoxic challenges of colistimethate sodium through a preclinical study. *Front. Pharmacol.* 14 (November), 1282464. doi:10.3389/fphar.2023.1282464

Mohapatra, S. S., Dwibedy, S. K., and Padhy, I. (2021). Polymyxins, the last-resort antibiotics: mode of action, resistance emergence, and potential solutions. *J. Biosci.* 46 (3), 85. doi:10.1007/S12038-021-00209-8

Nair, A., and Jacob, S. (2016). A simple practice guide for dose conversion between animals and human. *J. Basic Clin. Pharm.* 7 (2), 27–31. doi:10.4103/0976-0105.177703

Nation, R. L., Li, J., Cars, O., Couet, W., Dudley, M. N., Kaye, K. S., et al. (2015). Framework for optimisation of the clinical use of colistin and polymyxin B: the Prato polymyxin consensus. *Lancet Infect. Dis.* 15 (2), 225–234. doi:10.1016/S1473-3099(14)70850-3

Pang, Z., Chong, J., Zhou, G., de Lima Morais, D. A., Chang, L., Barrette, M., et al. (2021). MetaboAnalyst 5.0: narrowing the gap between raw spectra and functional insights. *Nucleic Acids Res.* 49 (W1), W388–W396. doi:10.1093/nar/gkab382

Plachouras, D., Karvanen, M., Friberg, L. E., Papadomichelakis, E., Antoniadou, A., Tsangaris, I., et al. (2009). Population pharmacokinetic analysis of colistin methanesulfonate and colistin after intravenous administration in critically ill patients with infections caused by gram-negative bacteria. *Antimicrob. Agents Chemother.* 53 (8), 3430–3436. doi:10.1128/AAC.01361-08

Pluskal, T., Castillo, S., Villar-Briones, A., and Orešič, M. (2010). MZmine 2: modular framework for processing, visualizing, and analyzing mass spectrometry-based molecular profile data. *BMC Bioinforma.* 11, 395. doi:10.1186/1471-2105-11-395

Prieto Jimenez, P. M., Jun-Ihn, E., Matthews, M., Lollie, T., Qu, Y., and Martin, M. G. (2022). An unusual case of infantile hepatic steatosis caused by coconut-based infant formula. *JPGN Rep.* 3 (4), e235. doi:10.1097/pg9.0000000000000235

Ramezanzade, E., Ghanbari, R., and Yazdanipour, T. (2023). Colistin-induced neurotoxicity in a multidrug-resistant uti patient with cervical cancer: a case report. *Nephro-Urology Mon.* 15 (1), 127122. doi:10.5812/NUMONTHLY-127122

Rinaldo, P., O'Shea, J. J., Welch, R. D., and Tanaka, K. (1989). Stable isotope dilution analysis of n-hexanoylglycine, 3-phenylpropionylglycine and suberylglycine in human urine using chemical ionization gas chromatography/mass spectrometry selected ion monitoring. *Biomed. Environ. Mass Spectrom.* 18 (7), 471–477. doi:10.1002/bms.1200180705

Rychlíčková, J., Kubíčková, V., Suk, P., and Urbánek, K. (2023). Challenges of colistin use in ICU and therapeutic drug monitoring: a literature review. *Antibiot. (Basel)* 12 (3), 437. doi:10.3390/ANTIBIOTICS12030437

Satlin, M. J., Lewis, I., Weinstein, M. P., Patel, J., Humphries, R. M., Kahlmeter, G., et al. (2020). Clinical and laboratory standards institute and European committee on antimicrobial susceptibility testing position statements on polymyxin B and colistin clinical breakpoints. *Clin. Infect. Dis.* 71, e523–e529. doi:10.1093/cid/ciaa121

Scholze, A., Jankowski, V., Henning, L., Haass, W., Jankowski, J., Suvd-Erdene, S., et al. (2007). Phenylacetic acid and arterial vascular properties in patients with chronic kidney disease stage 5 on hemodialysis therapy. *Nephron Clin. Pract.* 107, 1–6. doi:10.1159/000105137

Wamser, M. N., Leite, E. F., Ferreira, V. V., Delwing-de Lima, D., da Cruz, J. G. P., Wyse, A. T. S., et al. (2013). Effect of hypoxanthine, antioxidants and allopurinol on cholinesterase activities in rats. *J. Neural Transm.* 120 (9), 1359–1367. doi:10.1007/s00702-013-0989-x

Wishart, D. S., Feunang, Y. D., Marcu, A., Guo, A. C., Liang, K., Vázquez-Fresno, R., et al. (2018). HMDB 4.0: the human metabolome database for 2018. *Nucleic Acids Res.* 46 (D1), D608–D617. doi:10.1093/nar/gkx1089

Zhou, S., Gu, J., Liu, R., Wei, S., Wang, Q., Shen, H., et al. (2018). Spermine alleviates acute liver injury by inhibiting liver-resident macrophage pro-inflammatory response through ATG5-dependent autophagy. *Front. Immunol.* 9 (MAY), 948. doi:10.3389/fimmu.2018.00948

frontiers | Frontiers in Molecular Biosciences

TYPE Original Research
PUBLISHED 07 January 2025
DOI 10.3389/fmolb.2024.1400622

OPEN ACCESS

EDITED BY
Geraldine M. Dowling Sfhea,
Atlantic Technological University, Ireland

REVIEWED BY
Soumya Majumder,
University of North Bengal, India
Kwenga Sichilongo,
University of Botswana, Botswana

*CORRESPONDENCE
Michal Ciborowski,
michal.ciborowski@umb.edu.pl
Michal Szeremeta,
michal.szeremeta@umb.edu.pl

RECEIVED 13 March 2024
ACCEPTED 18 December 2024
PUBLISHED 07 January 2025

CITATION
Mojsak P, Samczuk P, Klimaszewska P, Burdukiewicz M, Chilimoniuk J, Grzesiak K, Pietrowska K, Ciborowska J, Niemcunowicz-Janica A, Kretowski A, Ciborowski M and Szeremeta M (2025) Comparative analysis of anticoagulant influence on PMI estimation based on porcine blood metabolomics profile measured using GC-MS.
Front. Mol. Biosci. 11:1400622.
doi: 10.3389/fmolb.2024.1400622

Comparative analysis of anticoagulant influence on PMI estimation based on porcine blood metabolomics profile measured using GC-MS

Patrycja Mojsak[1], Paulina Samczuk[1,2], Paulina Klimaszewska[1], Michal Burdukiewicz[1,3], Jaroslaw Chilimoniuk[1], Krystyna Grzesiak[1,4], Karolina Pietrowska[1], Justyna Ciborowska[5], Anna Niemcunowicz-Janica[6], Adam Kretowski[1,7], Michal Ciborowski[1,8]* and Michal Szeremeta[6]*

[1]Metabolomics and Proteomics Laboratory, Clinical Research Centre, Medical University of Bialystok, Bialystok, Poland, [2]Department of Genetic Research, Central Forensic Laboratory of the Police, Warsaw, Poland, [3]Institute of Biotechnology and Biomedicine, Autonomous University of Barcelona, Cerdanyola, Spain, [4]Faculty of Mathematics and Computer Science, University of Wroclaw, Wroclaw, Poland, [5]Chemical Research Laboratory, Forensic Laboratory of the Voivodeship Police Headquarters in Bialystok, Bialystok, Poland, [6]Department of Forensic Medicine, Medical University of Bialystok, Bialystok, Poland, [7]Department of Endocrinology, Diabetology and Internal Medicine, Medical University of Bialystok, Bialystok, Poland, [8]Department of Medical Biochemistry, Medical University of Bialystok, Bialystok, Poland

Introduction: Accurate post-mortem interval (PMI) estimation is essential in forensic investigations. Although various methods for PMI determination have been developed, only an approximate estimation is still achievable, and an accurate PMI indication is still challenging. Therefore, in this study, we employed gas chromatography-mass spectrometry (GC-MS)-based metabolomics to assess post-mortem changes in porcine blood samples collected with and without the addition of anticoagulant (EDTA). Our study aimed to identify metabolites dependent on the EDTA addition and time (taking into account the biodiversity of the studied organism) and those that are time–dependent but resistant to the addition of an anticoagulant.

Methods: The experiment was performed on blood samples collected from 16 animals (domestic pig, breed: Polish Large White), 8 with and 8 without EDTA addition. The moment of death (time 0) and 15 additional time points (from 3 to 168 h after death) were selected to examine changes in metabolites' levels in specific time intervals. We employed linear mixed models to study the relationship between metabolite intensities, time and presence of EDTA while accounting for the effect of individual pigs.

Results and Discussion: We confirmed that the intensity of 16 metabolites (mainly amino acids) significantly depends on PMI and the presence of EDTA. However, the intensity of the ideal biomarker(s) for PMI estimation should be determined only by the time after death and not by external factors such as the presence of the anticoagulant agent. Thus, we identified 41 metabolites with time–dependent intensities that were not susceptible to EDTA presence.

Finally, we assessed the performance of these metabolites in a PMI predictive model. Citraconic acid yielded one of the lowest errors in general PMI estimation (32.82 h). Moreover, similar errors were observed for samples with and without EDTA (33.32 h and 32.34 h, respectively). Although the small sample size and information leak in predictive modelling prevent drawing definite conclusions, citraconic acid shows potential as a robust PMI estimator.

KEYWORDS

post-mortem interval (PMI), animal model, blood biomarkers, metabolomics, GC-MS

1 Introduction

One of forensic medicine's most essential and challenging tasks is estimating the post-mortem interval (PMI). This parameter is defined as the time elapsed since an individual's death. Precise and accurate estimation of the PMI is remarkably important as it can help establish the timeline of events surrounding death (Gelderman et al., 2021). Forensic science currently offers many methods for PMI estimation, including various conventional methods, such as measurement of physical changes (Donaldson and Lamont, 2013; Ciaffi et al., 2018), biochemical components in different tissues and body fluids (Donaldson and Lamont, 2013), DNA or RNA degradation (Ciaffi et al., 2018), or analysis of rigour and livor mortis (Madea, 2016; Amendt et al., 2011). Nevertheless, only an approximate estimation can be derived from conventional methods, and an accurate PMI estimation is still difficult to obtain (Mathur and Agrawal, 2011). Thus, more reliable and accurate methods to estimate PMI are in demand.

Recent advances in the methods for estimating PMI have enabled us to determine post–mortem intervals more precisely (Mathur and Agrawal, 2011). Based on the literature review (Peyron et al., 2021; Szeremeta et al., 2021), it has been suggested that analysing the metabolomic composition of body fluids might provide a better tool for PMI estimation (Locci et al., 2023). The analysis of the post–mortem metabolomic changes in biological samples with mass spectrometry opens the way to develop new methods for PMI estimation. Different analytical platforms such as liquid chromatography–mass spectrometry (LC–MS) (Szeremeta et al., 2022; Zhang et al., 2022a; Zhang et al., 2022b; Pesko et al., 2020), gas chromatography–mass spectrometry GC–MS (Dai et al., 2019; Wu et al., 2018; Sato et al., 2015; Kaszynski et al., 2016), and nuclear magnetic resonance (NMR) (Fischer et al., 2014; Locci et al., 2021) have been used in PMI–oriented research. Among these, GC–MS is known to be one of the most efficient analytical platforms and, therefore, is well–established in metabolomics research (Mojsak et al., 2022). GC–MS has a distinct advantage over the other analytical platforms in terms of retention time, mass spectrometry reproducibility, and the availability of well–established commercial and in–house metabolite libraries (Beale et al., 2018). Due to all these advantages, this high–throughput detection technique was chosen to conduct the analyses.

Based on the literature review, it was confirmed that the application of GC–MS to the estimation of PMI is also gradually increasing (Dai et al., 2019; Wu et al., 2018; Sato et al., 2015; Kaszynski et al., 2016). Most often, the samples of post–mortem blood plasma (Donaldson and Lamont, 2013; Sato et al., 2015; Costa et al., 2015; Zelentsova et al., 2020) and vitreous humour (Zelentsova et al., 2020; Bonicelli et al., 2022) are used to search for potential PMI estimation markers; however, cerebrospinal, pericardial, and synovial fluids (Wenzlow et al., 2023) have also been considered. Due to the popularity of the use of blood in PMI estimation and its relatively easy collection at the crime scene, we selected this material to perform our study.

Blood trail age estimation could offer valuable information for reconstructing criminal events and their chronological assessment (Costa et al., 2015). Death results in extensive biochemical changes also in the blood due to the absence of circulating oxygen and the consequent cessation of aerobic respiration, altered enzymatic reactions, cessation of anabolic production of metabolites, cessation of active membrane transport and changes in the permeability of cells and diffusion of ions (Donaldson and Lamont, 2013). In these circumstances, using anticoagulants, such as EDTA, aids in suppressing the blood clotting mechanism to enable a longer examination time. On the other hand, there are many controversial studies regarding adding this anticoagulant (Bergmann et al., 2021). Based on UV-VIS analysis, Bergmann et al. confirmed that unnatural blood coagulation prevention is highly questionable when estimating bloodstain age, since the blood's physical and chemical properties are altered (Bergmann et al., 2021). On the other hand, in most studies where blood samples were used to estimate PMI, it was anticoagulated with EDTA (Das et al., 2019; Sibbens et al., 2017; Wang et al., 2017). For this reason, we attempted to compare the metabolite profiles in both types of blood samples to check the impact of EDTA addition on the PMI estimation.

To the best of our knowledge, this is the first approach to estimate PMI in a porcine model using GC–MS–based metabolomics of plasma samples with or without EDTA addition. Considering the complementarity of GC–MS and LC–MS techniques in metabolomics studies (Zeki et al., 2020; Yumba-Mpanga et al., 2019), the present study is a valuable continuation of our previous research (Szeremeta et al., 2022). Apart from finding the differences between the metabolic profiles of blood samples with and without the addition of anticoagulants, we want to find universal metabolites that depend on the time since death, regardless of the addition of EDTA.

2 Materials and methods

2.1 Chemicals

O–methoxyamine hydrochloride, analytical grade of heptane and pyridine were supplied from Sigma–Aldrich (Steinheim,

Germany). N,O–bis–(trimethylsilyl)– trifluoroacetamide (BSTFA) with 1% trimethylchlorosilane (TMCS) solution and acetonitrile (HPLC grade) was purchased from Thermo Fisher Scientific (Waltham, MA, USA). 4–nitrobenzoic acid (4–NBA) and stearic acid methyl ester (C18:0 methyl ester) were acquired as well from Sigma–Aldrich (Steinheim, Germany) and applied as internal standards (ISs). The 4–NBA (IS1) solution was prepared in acetonitrile, whereas methyl stearate in heptane (IS2). Two mixtures of standards for GC–MS, one containing grain fatty acid methyl esters (FAMEs) (C8:0–C22:1, n9) and another a mixture of n–alkanes (C8:C40), were obtained from Supelco (Bellefonte, PA, United States).

2.2 Sample collection and preparation

The experimental design used in this study was the same as described previously (Szeremeta et al., 2022). Sample preparation was carried out as previously described (Mojsak et al., 2022) with minor modifications. Briefly, an aliquot of 40 µL of plasma and 120 µL of cold acetonitrile containing the IS1 (25 ppm) were mixed for metabolites extraction. The mixture was vortexed for 2 min and centrifuged at 15,000 g for 10 min at 4°C. Finally, each sample's supernatant (120 µL) was collected in a GC vial equipped with an insert and evaporated to complete dryness using a vacuum concentrator. All analysed samples were subjected to a two–step derivatisation process. First, methoxymation was performed by adding 30 µL of methoxylamine hydrochloride in pyridine solution (15 mg/mL) and then incubating at room temperature in the dark for 16 h. Following this, 30 µL of BSTFA with 1% TMCS was added to each sample and placed in the oven to react for 1 h at 70°C. At last, 90 µL of IS2 (10 ppm) was added as instrumental IS.

2.3 Quality control samples

To monitor the analytical variability and assess the reproducibility and repeatability of the methodology, quality control (QC) samples were used (Kirwan et al., 2022). The QC samples were prepared by pooling the study samples. Blank samples containing cold acetonitrile were used to detect the column's contamination and the background noise produced during sample derivatisation, data processing and GC/MS analysis.

2.4 GC–MS–based untargeted metabolomics

Metabolic fingerprinting was performed using a 7890B gas chromatograph connected to a 7000D mass selective detector (Agilent Technologies, Palo Alto, CA, United States). A DB–5MS capillary column (30 m × 0.25 mm × 0.25 µm) was used for the chromatographic separation. One µL of each derivatised plasma sample was automatically injected at a split ratio of 1:10 using helium as a carrier gas with a 1 mL/min flow rate. The temperature of the injection was set to 250°C. The column oven temperature was maintained at 60°C for 1 min and then increased by 10°C/min to 320°C. The transfer line, ion source and quadrupole temperature were set at 280, 300°C and 150°C, respectively. Mass spectra were acquired under electron impact (EI) ionisation conditions using 70 eV in the mass range of m/z 50–600 using the default instrument scan rate. All samples (study samples, QCs and blanks) were analysed using the above-mentioned conditions.

2.5 Data processing

The deconvolution and identification were performed using Mass Hunter Quantitative Unknowns Analysis software (B.07.00, Agilent), alignment using Mass Profiler Professional software (version 13.0, Agilent) and peak integration using Mass Hunter Quantitative Analysis software (version B.07.00, Agilent). The identification was performed mainly based on the accurate mass and product ion spectrum matching against the in–house library of 100 authentic standards and Fiehn's and NIST 14 libraries. Before the statistical analysis, peak areas were normalised by IS abundance to minimise the response variability from the instrument. Finally, data were filtered based on the coefficient of signal variation (CV) in QC samples, considering values lower than 30% as acceptable.

2.6 Statistical analyses

The exploratory analysis indicated high data variability between the timepoints and individual pigs. To adequately address this data structure, we employed the linear mixed model, where we considered the metabolite intensity to depend on both time (t) and the presence of EDTA. Moreover, we have included the impact of individual pigs as a random effect (b_{ID}). Thus, our model considers the additional unknown variability affecting the intensity of a given metabolite over time (Equations 1, 2). We applied ANOVA to verify if the presence of EDTA is a significant variable in the model.

$$y = \beta_0 + b_{ID} + \beta_1 t + \beta_2 \mathrm{EDTA} \quad (1)$$

$$y = \beta_0 + b_{ID} + \beta_1 t \quad (2)$$

We predicted the measurement time considering the known metabolite intensity for each metabolite using the coefficients of model 2) to assess if the metabolite intensity could estimate PMI (Patterson and Thompson, 1971). Due to the small sample size, we performed a prediction on the samples used to fit the model, which caused the information leak. We evaluated the error of time prediction (in hours) for both models sensitive and those not sensitive to the presence of EDTA. We have used mean average error (MAE) as an error measure for samples with and without EDTA. Total mean average error (TMAE) was computed for all samples (with and without EDTA). Due to the limited dataset, we computed the performance on the same data we used to produce the model, leading to the information leak. The statistical analysis was performed in R 4.2.

3 Results

After data pretreatment (deconvolution, alignment, data normalisation and filtering), 126 entities were obtained,

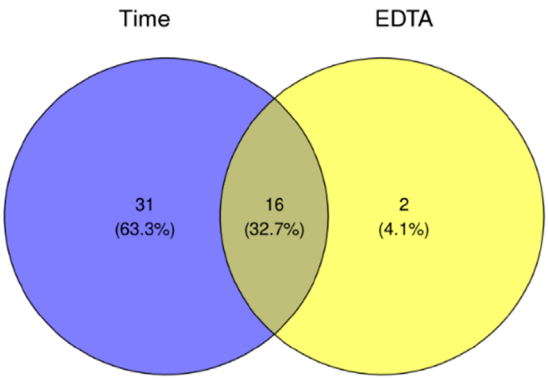

FIGURE 1
Ven diagram showing number for statistically significant metabolites.

and 79 metabolites were annotated (Supplementary Table S1; Supplementary Materials), taking into account several derivatives from one metabolite [mainly for certain amino acids (AAs) and carbohydrates (Carbs)]. Finally, we chose 71 and 73 metabolites for statistical analysis, representing different analytical classes [mainly AAs, Carbs and fatty acids (FAs)], with RSD below 30% in plasma with and without EDTA addition, respectively.

Using ANOVA, we compared which of the two models significantly better captures the data structure. As model 2) is nested in model 1), we interpreted the ANOVA result as an indication of the presence of EDTA as a parameter necessary to describe the change of the metabolite intensity over time. After applying the Benjamini–Hochberg correction, we discovered 16 metabolites whose intensities depend on the EDTA presence and the time after death. Relationships between significant metabolites in EDTA–based and time–based tests were presented on the Venn diagram (Figure 1).

The *p*–values for the 16 metabolites mentioned above are presented in Table 1, whilst their intensity–time plots showing the tested pigs' biodiversity are presented in Supplementary Figure S1. Metabolites in blood containing EDTA are more stable than in blood without anticoagulant (see Figure S1). Additionally, we present the result of the PLS-DA analysis (Figure 2) performed for EDTA-treated serum metabolomics data at different post-mortal time points, illustrating the temporal variations in plasma composition.

Reversing this reasoning, we identified 41 metabolites that depend significantly on time after death but do not show a significant dependence on the presence of EDTA (Supplementary Table S2). It must be emphasized that there was over–interpretation of the ANOVA result by drawing such conclusions. However, the potential usefulness of these metabolites as PMI estimators was demonstrated while keeping the same linear mixed model framework.

Two factors are vital for selecting the best metabolite for PMI estimation: low error (accuracy) and lack of sensitivity to blood clotting (universality). Among the considered metabolites, alanine, phosphate, and citraconic acid had the lowest TMAE (respectively, 29.29, 32.52, and 32.83 h) (Figure 3).

However, out of these three metabolites, only citraconic acid kept a comparably low MAE, independently of the presence or absence of EDTA (33.32 and 32.34 h, respectively). Both alanine and phosphate had drastically different MAE depending on the presence or absence of EDTA (alanine: 21.01 and 37.56; phosphate: 35.11 and 29.92 h, respectively).

Next, we investigated whether citraconic acid was the only metabolite that yielded equally accurate predictions regardless of EDTA presence. When considering the mean absolute difference in MAE, citraconic acid had the lowest score (0.98 h) (see Figure 4). Benzoic and glyceric acid were two other metabolites, with the mean absolute difference in TMAE being lower than 2 hours (1.37 and 1.50 h, respectively). However, they could not be reliably used to estimate PMI as their TMAE was very high (56.62 and 49.66 h, respectively).

This analysis does not exhaust the range of metabolites that could be useful for PMI estimation. Our analysis yielded 41 metabolites (Table S2) resistant to EDTA and with time–dependent intensity. However, their statistical significance was not followed up due to the low TMAE.

4 Discussion

Evaluation of the PMI has always been a major challenge for forensic pathologists (Wu et al., 2018). Despite many studies on PMI estimation and the development of various methods for PMI assessment over the years (Peyron et al., 2021; Laplace et al., 2021; Wilk et al., 2020; Wilk et al., 2021; Choi et al., 2019; Peng et al., 2020; Sangwan et al., 2021; De-Giorgio et al., 2021; Palacio et al., 2021), an accurate PMI indication, highly required in forensic medicine, is still complicated. The practical use of these methods in forensic science is impossible because most proposed approaches lack the reliability required to meet rigorous forensic standards (Locci et al., 2023).

Metabolomics analyses using mass spectrometry have recently gained popularity in forensic analysis (Kaszynski et al., 2016). This relatively new technology is often based on mass spectrometry, which allows the comprehensive study of low–molecular–weight metabolites (Lu et al., 2023). Especially during the agonal period, supravital reactions (occurring from death until cellular functions cease), leakage from degrading cells, and degradation of proteins affect the metabolomics profile. Therefore, analysing metabolites from biofluid samples can provide insights into the post–mortem changing biochemical environment (Donaldson and Lamont, 2013). Probably the most significant post-mortal changes in the blood metabolome are induced by cell membrane damage: the lack of ATP causes the dysfunction of intracellular Na+/K+ pumps, resulting in sodium accumulation inside the cells, cell lysis due to the osmotic pressure, and the leakage of the intracellular metabolites into the blood. The post–mortem metabolomic changes are also caused by the disruption of enzymatic cycles and microbial activity in the vascular system (Zelentsova et al., 2020).

Since the metabolomics approach to PMI estimation is still in its infancy, using animals as study subjects to determine the precise PMI is justified. Therefore, we built the PMI estimation model using porcine blood in the current study. Furthermore, ethical concerns make it considerably preferable to perform such a study with multiple time points on animal, not human blood (Matuszewski et al., 2020). Additionally, due to their structural and functional similarity to humans, pigs have been used as a model in biomedical research to evaluate PMI. It has been confirmed

TABLE 1 List of statistically significant metabolites dependent on time and EDTA addition with their *p*–value, adjusted *p*–value (Benjamini–Hochberg correction).

Group of metabolites	Metabolites	RT	HMDB ID	*p*–value	Adjusted *p*–value
AAs, peptides and analogues	Creatinine	13.6	HMDB00562	5.29E−14	5.52E−13
	Iminodiacetic acid	13.3	HMDB11753	4.01E−15	4.88E−14
	Isoleucine	10.05	HMDB00172	2.11E−07	1.40E−06
	Lysine	17.5	HMDB00182	0.000307	0.0014
	Ornithine	15.8	HMDB00214	3.29E−06	2.00E−05
	Phenylalanine	14.2	HMDB00159	2.85E−16	4.17E−15
	Threonine	11.3	HMDB00167	2.20E−28	5.36E−27
	Valine	7.2, 9.2	HMDB00883	5.28E−22	9.64E−21
	5–Oxoproline/pyroglutamic acid	13.1	HMDB00267	3.52E−12	2.85E−11
Alpha–keto acids and derivatives	Pyruvic acid	6.6	HMDB00243	6.47E−07	4.30E−06
Carb and Carb conjugates	Glucose	17.25, 17.4	HMDB00122	2.00E−35	7.31E−34
	Mannose	17.15, 17.45	HMDB00169	1.63E−40	1.19E−38
	1,5–anhydro–D–sorbitol	17	HMDB02712	3.54E−05	0.00017
Dicarboxylic acids and derivatives	Fumaric acid	10.9	HMDB00134	1.87E−07	1.36E−06
Glycerophosphates	Glycerol 1–phosphate	15.9	HMDB00126	5.00E−05	2.00E−04
Purines and purine derivatives	Hypoxanthine	16.5	HMDB00157	4.76E−06	2.67E−05

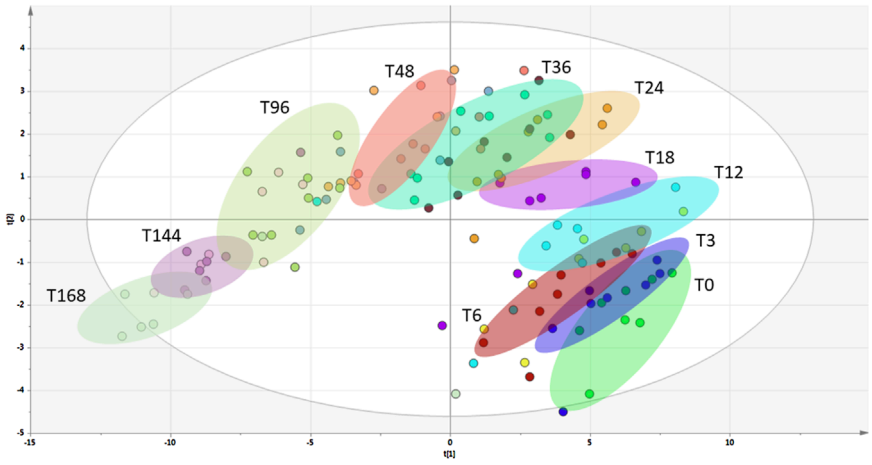

FIGURE 2
PLS-DA analysis of blood samples with EDTA collected at different post-mortal time-points.

that pigs are a common human analogue in taphonomic studies (Connor et al., 2018) Researchers already confirmed that adding EDTA helps suppress the blood clotting mechanism, allowing the examination to be conducted over a longer period of time (Bergmann et al., 2021). On the other hand, this unnatural prevention of blood coagulation is highly questionable when estimating blood stain age since the blood's physical and chemical properties are altered (Sharma and Kumar, 2018). Bergmann et al. confirmed that EDTA distorts blood spot ageing behaviour due to the prevention of coagulation (Bergmann et al., 2021), but based

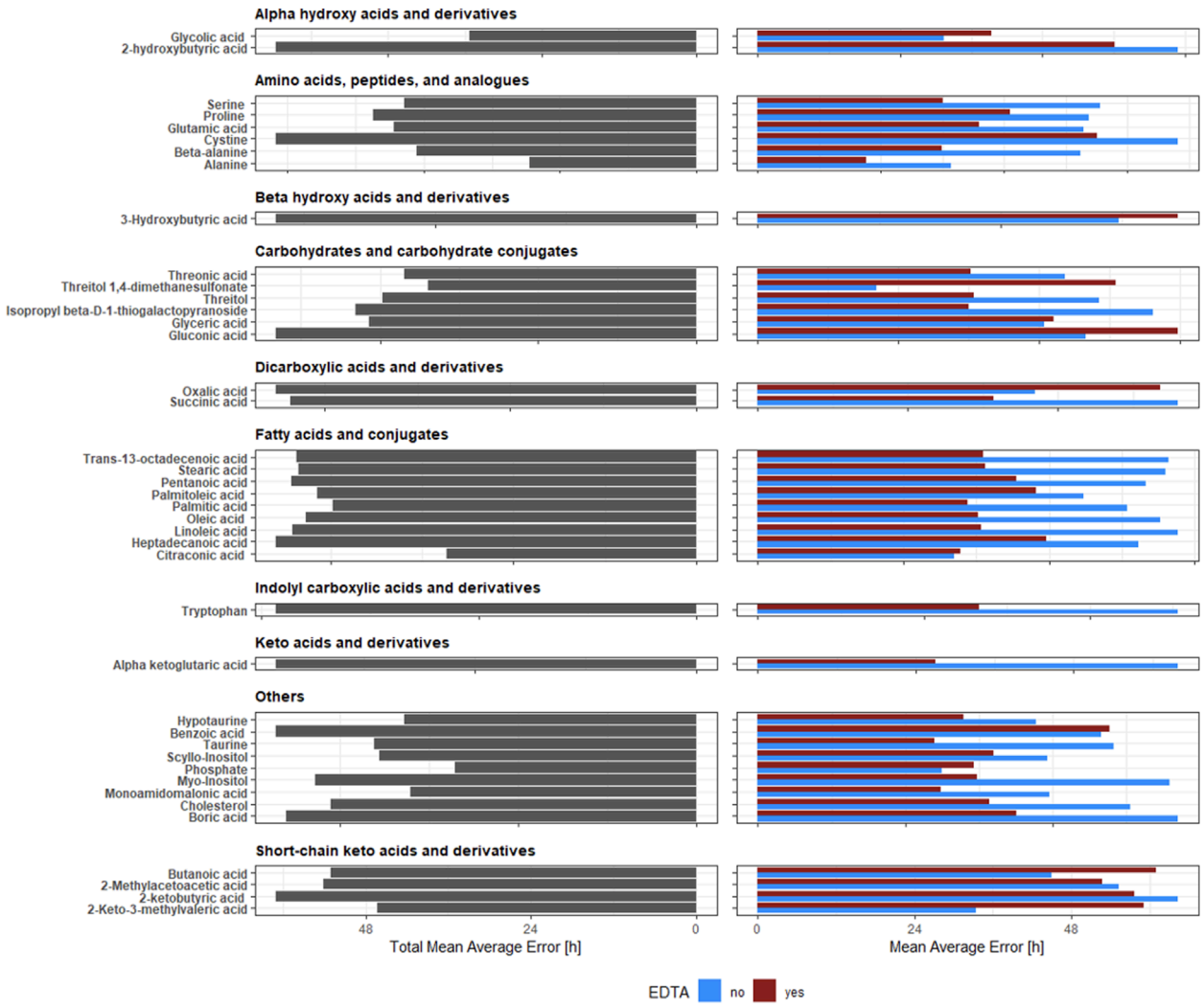

FIGURE 3
Total Mean Average Error [h] and Mean Average Error [h] of predictive models for PMI estimation with and without EDTA component. The height of the bar represents TMAE (left panel) and MAE (right panel). The bar's colour (the right panel) represents the presence or absence of EDTA.

on different analyses conducted with UV/VIS spectra obtained for oxyhemoglobin, methemoglobin and hemichrome measurement. Until now, no study has reported using the metabolite profile analyses using GC–MS to estimate PMI in blood samples with or without the addition of an anticoagulant. For this reason, in this study, we examined the influence of EDTA on blood profiles over time to evaluate whether this effect occurs. Our results show that differences between the profiles of blood samples with and without EDTA addition were significant, which had already been proven in our previous study, performed using a complementary LC–MS technique (Szeremeta et al., 2022).

In the present study, we identified 16 metabolites with time-dependent intensities that were also affected by the presence of EDTA (see Figure S1). The best candidates for biomarkers for PMI estimation would be blood metabolites whose post–mortem intensity changes significantly, monotonously, relatively slowly, and with minimal data scattering (Sato et al., 2015). Most metabolites in plasma samples with EDTA (mainly AAs such as lysine, phenylalanine, threonine, valine, and pyroglutamic acid) met these criteria, with one exception for iminodiacetic acid, which met these criteria for both EDTA and non-EDTA samples. The intensity of AAs increases with time after death, and the most plausible explanation for this is the lack of energy. The cells began to break down proteins for energy and to combat bacterial spoilage, which led to the rapid degradation of a large number of proteins. It is worth noting that the increase in AAs was gradual rather than sudden, and the most likely explanation for this is that at the moment of death, not all the cells died, and within a certain time after death, some cells remained metabolically active (Wu et al., 2018).

Based on the graphs presented in Figure S1, it can be noticed that metabolites in blood with EDTA are more stable than in blood without anticoagulant addition. We observed larger data scattering in plasma samples without EDTA addition, especially at further times after death. Multiple concurrent biological processes induced by time may contribute to alterations in the post-mortem metabolome of blood samples untreated with EDTA (Go et al.,

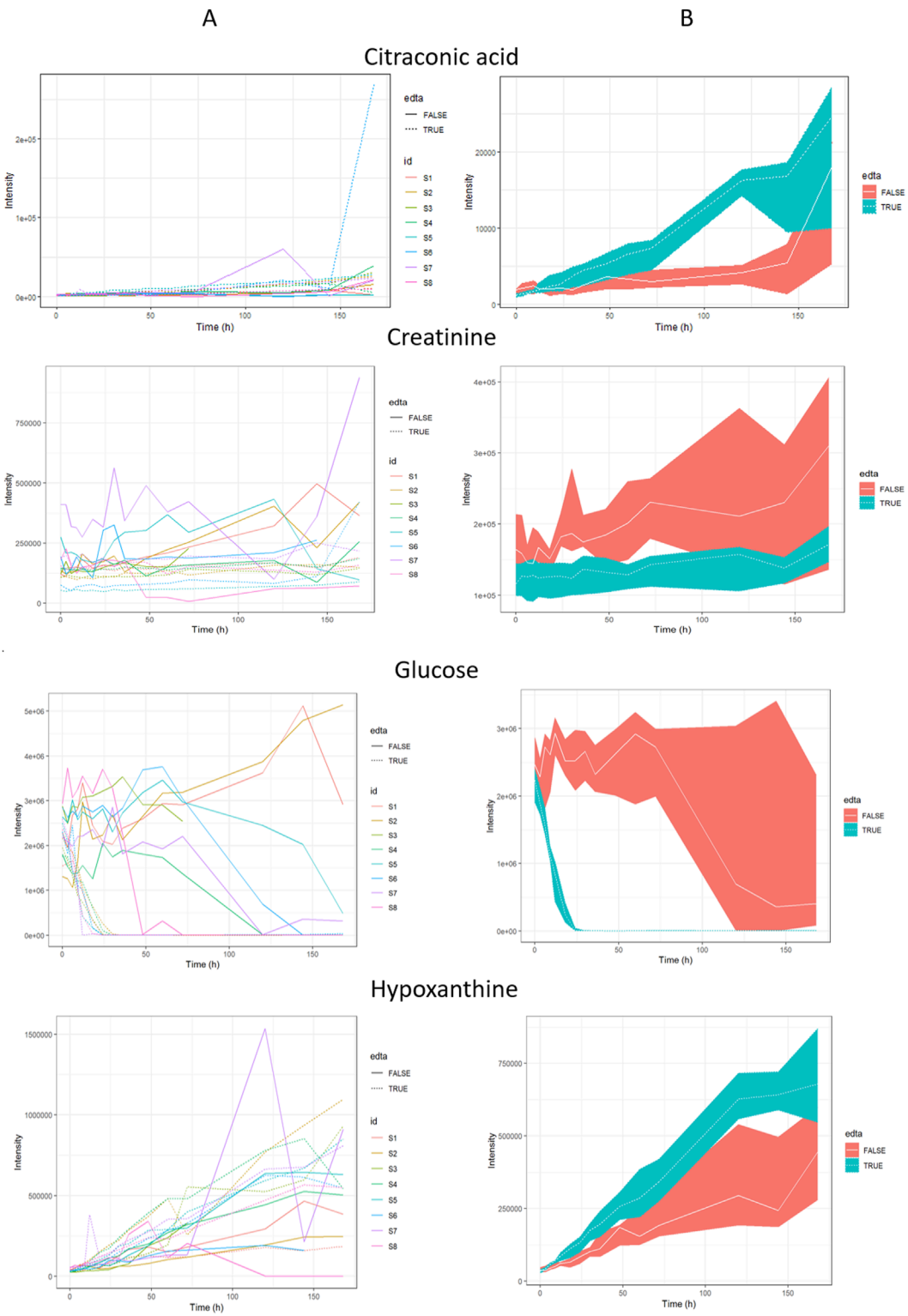

FIGURE 4
The most important metabolites for PMI estimation. Panel **(A)** - plots considering the biodiversity of the tested pigs; panel **(B)** - plots considering the median of all IDs for each time, metabolite, and EDTA, along with the first and third quartiles (Q1 and Q3).

2019). Another critical difference in the change of the intensity of metabolites in the blood with the addition of EDTA is the rapid decrease in glucose intensity during the first day after death, with minimal data scattering (see Figure 4). The rapid decrease of glucose after death may also depend on post-mortem anaerobic glycolysis and the use of glucose by bacteria. After death, glycogen is used

by skeletal muscles as a carbohydrate source for glycolytic substrate production, which generates ATP and lactate (Chauhan et al., 2019; Chauhan and England, 2018). In our study, we observed an increase in the intensity of lactic acid after death in two types of plasma samples. Lactate is not only produced during glycolysis but is also formed due to autolysis and bacterial catabolism. Several researchers have studied the correlation between lactic acid concentration and PMI (Mihailovic et al., 2011; Keltanen et al., 2015). The remaining compounds associated with EDTA include hypoxanthine and creatinine; the intensity of both metabolites increases with time (see Figure 4). Many previous publications have confirmed the use of these metabolites (i.e., creatinine or hypoxanthine) for PMI estimation (Peyron et al., 2021; Szeremeta et al., 2022; Dai et al., 2019; Sato et al., 2015; Kaszynski et al., 2016); and our research provides additional confirmation. Hypoxanthine concentration in the blood rises after death because it is an ATP–breakdown product that increases its concentration in situations of oxygen limitation and is available as a co–factor for xanthine oxidase. Changes observed for hypoxanthine correspond to breaking the tricarboxylic acid cycle and purine catabolism in an oxygen–deficient biological medium (Hira et al., 2014). Zelentsova et al. conducted a PMI study with rabbits and suggested that hypoxanthine and creatinine may have a strong potential as a PMI biomarker (Zelentsova et al., 2020), which was also confirmed in this study. After death, creatinine levels in the blood increase due to the cessation of kidney function and the breakdown of muscle tissue. Without renal filtration, creatinine accumulates in the bloodstream (Nishida et al., 2015). Measurement (in the vitreous humor) of hypoxanthine with potassium (Rognum et al., 2016; Madea and Rödig, 2006) and also urea (Cordeiro et al., 2019), has been reported useful for time since death estimation.

We have also indicated 43 metabolites whose intensities correlate with PMI and are not susceptible to EDTA presence. Using coefficients of the fitted models, we used intensities of these metabolites to estimate PMI (Figure 3). No metabolites with TMAE that were lower than 24 h, which severely hinder their usage in the case of estimating very short PMIs were identified. Moreover, we observed a much higher value of MAE for samples with EDTA than those without anticoagulant. Only citraconic acid could be characterised by the low TMAE (29.29 h) and comparable MAE regardless of the EDTA presence (33.32 h with EDTA and 32.34 without EDTA). Shen et al. showed that citraconic acid could be used to predict pork quality (Shen et al., 2022). This metabolite belongs to the dicarboxylic acid family, formed from the breakdown of citric acid. Citrate content, mainly in the bone, was confirmed as a metabolite associated with PMI (Wilson and Christensen, 2017; Brown et al., 2018).

However, it should be noted that the predictive model employed in this study suffers from the information leak, and the error estimate shown has to be overly optimistic. The precise assessment of its accuracy requires future research, where the sample size would allow for model validation using at least a leave–one–out setting. It was speculated that citraconic acid could aid in determining PMI.

Despite metabolomics being fraught with a high risk of large error (Zhang et al., 2023), findings show that this approach can be a powerful tool for predicting PMI (Aljeaid, 2024) The literature review confirmed that the metabolomic profile of the vitreous humour determined with NMR could predict PMI better than measuring potassium concentration, which was, until now, the best option for PMI estimation. It is crucial to bear in mind that the use of potassium concentration in PMI estimation is fraught with error in the range of 6.9 h for PMI <24 h, 7.4 h for PMI between 24 and 48 h, and 10.3 h for PMI >48 h (Locci et al., 2023).

5 Conclusion

Our preliminary study shows large differences between the two types of blood-originated samples. Metabolites in blood, with the addition of EDTA, maintain much better stability and are subject to much less data scattering. Adding EDTA helps suppress the blood clotting mechanism, providing a longer time to perform the examination. However, metabolites in blood behave more significantly without the addition of an anticoagulant. We observe a considerable dispersion of results in blood samples, especially at later times. Possible reasons might be multiple coexisting biological processes induced by time that affect metabolome post-mortem in blood samples untreated with EDTA.

Our analysis indicated only one metabolite (citraconic acid) suitable for PMI estimation, especially for PMIs longer than 1 day. However, it should be pointed out that this study had some limitations. First, the experiment was performed under constant environmental conditions, and further work should be directed to study the influence of environmental factors. Secondly, the study was conducted on animal material. Humans have a more complicated biological background and living habits than experimental animals. The application of the results of this study to the practical forensic investigation of human corpses needs further study.

Data availability statement

The raw data supporting the conclusions of this article will be made available by the authors, without undue reservation.

Ethics statement

The animal studies were approved by Local Ethical Committee for Animal Experiments in Olsztyn (Poland) - LKE 20/2021. The studies were conducted in accordance with the local legislation and institutional requirements. Written informed consent was not obtained from the owners for the participation of their animals in this study because experiments were performed on the blood of slaughtered animals and informed consent of the owners was not required.

Author contributions

PM: Data curation, Formal Analysis, Investigation, Methodology, Software, Validation, Visualization, Writing–original draft, Writing–review and editing. PS: Conceptualization, Funding acquisition, Investigation, Methodology, Project administration,

Software, Writing–review and editing. PK: Data curation, Formal Analysis, Methodology, Software, Visualization, Writing–review and editing. MB: Conceptualization, Data curation, Formal Analysis, Investigation, Methodology, Software, Validation, Visualization, Writing–original draft, Writing–review and editing. JaC: Data curation, Formal Analysis, Methodology, Software, Validation, Visualization, Writing–original draft. KG: Data curation, Formal Analysis, Investigation, Methodology, Software, Validation, Writing–original draft. KP: Investigation, Methodology, Writing–review and editing. JuC: Validation, Writing–review and editing. AN-J: Conceptualization, Resources, Supervision, Writing–review and editing. AK: Resources, Supervision, Writing–review and editing. MC: Conceptualization, Methodology, Resources, Supervision, Validation, Writing–review and editing. MS: Investigation, Methodology, Writing–original draft.

Funding

The author(s) declare that financial support was received for the research, authorship, and/or publication of this article. This study was supported by a grant from the National Science Centre, Poland (2017/27/N/NZ7/03136 to PS) and the Medical University of Bialystok subsidy grant (B.SUB.24.522 to PM).

Conflict of interest

The authors declare that the research was conducted in the absence of any commercial or financial relationships that could be construed as a potential conflict of interest.

Publisher's note

All claims expressed in this article are solely those of the authors and do not necessarily represent those of their affiliated organizations, or those of the publisher, the editors and the reviewers. Any product that may be evaluated in this article, or claim that may be made by its manufacturer, is not guaranteed or endorsed by the publisher.

Supplementary material

The Supplementary Material for this article can be found online at: https://www.frontiersin.org/articles/10.3389/fmolb.2024.1400622/full#supplementary-material

References

Aljeaid, R. (2024). Application of metabolomics and machine learning for the prediction of postmortem interval. *Cureus* 16 (11), e74161. doi:10.7759/cureus.74161

Amendt, J., Richards, C. S., Campobasso, C. P., Zehner, R., and Hall, M. J. (2011). Forensic entomology: applications and limitations. *Forensic Sci. Med. Pathol.* 7 (4), 379–392. doi:10.1007/s12024-010-9209-2

Beale, D. J., Pinu, F. R., Kouremenos, K. A., Poojary, M. M., Narayana, V. K., Boughton, B. A., et al. (2018). Review of recent developments in GC-MS approaches to metabolomics-based research. *Metabolomics* 14 (11), 152. doi:10.1007/s11306-018-1449-2

Bergmann, T., Leberecht, C., and Labudde, D. (2021). Analysis of the influence of EDTA-treated reference samples on forensic bloodstain age estimation. *Forensic Sci. Int.* 325, 110876. doi:10.1016/j.forsciint.2021.110876

Bonicelli, A., Mickleburgh, H. L., Chighine, A., Locci, E., Wescott, D. J., and Procopio, N. (2022). The 'ForensOMICS' approach for postmortem interval estimation from human bone by integrating metabolomics, lipidomics, and proteomics. *Elife* 11, e83658. doi:10.7554/eLife.83658

Brown, M. A., Bunch, A. W., Froome, C., Gerling, R., Hennessy, S., and Ellison, J. (2018). Citrate content of bone as a measure of postmortem interval: an external validation study. *J. Forensic Sci.* 63 (5), 1479–1485. doi:10.1111/1556-4029.13716

Chauhan, M. N., LeMaster, M. N., Clark, D. L., Foster, M. K., Miller, C. E., and England, E. M. (2019). Glycolysis and pH decline terminate prematurely in oxidative muscles despite the presence of excess glycogen. *Meat Muscle Biol.* 3 (1). doi:10.22175/mmb2019.02.0006

Chauhan, S. S., and England, E. M. (2018). Postmortem glycolysis and glycogenolysis: insights from species comparisons. *Meat Sci.* 144, 118–126. doi:10.1016/j.meatsci.2018.06.021

Choi, K. M., Zissler, A., Kim, E., Ehrenfellner, B., Cho, E., Lee, S. I., et al. (2019). Postmortem proteomics to discover biomarkers for forensic PMI estimation. *Int. J. Leg. Med.* 133 (3), 899–908. doi:10.1007/s00414-019-02011-6

Ciaffi, R., Feola, A., Perfetti, E., Manciocchi, S., Potenza, S., and Marella, G. (2018). Overview on the estimation of post mortem interval in forensic anthropology: review of the literature and practical experience. *Romanian J. Leg. Med.* 26, 403–411. doi:10.4323/rjlm.2018.403

Connor, M., Baigent, C., and Hansen, E. S. (2018). Testing the use of pigs as human proxies in decomposition studies. *J. Forensic Sci.* 63 (5), 1350–1355. doi:10.1111/1556-4029.13727

Cordeiro, C., Ordóñez-Mayán, L., Lendoiro, E., Febrero-Bande, M., Vieira, D. N., and Muñoz-Barús, J. I. (2019). A reliable method for estimating the postmortem interval from the biochemistry of the vitreous humor, temperature and body weight. *Forensic Sci. Int.* 295, 157–168. doi:10.1016/j.forsciint.2018.12.007

Costa, I., Carvalho, F., Magalhães, T., Guedes de Pinho, P., Silvestre, R., and Dinis-Oliveira, R. J. (2015). Promising blood-derived biomarkers for estimation of the postmortem interval. *Toxicol. Res.* 4 (6), 1443–1452. doi:10.1039/c5tx00209e

Dai, X., Fan, F., Ye, Y., Lu, X., Chen, F., Wu, Z., et al. (2019). An experimental study on investigating the postmortem interval in dichlorvos poisoned rats by GC/MS-based metabolomics. *Leg. Med. (Tokyo)* 36, 28–36. doi:10.1016/j.legalmed.2018.10.002

Das, S., Panda, S., Acharya, A., Mishra, U. K., Kundu, A. K., Mohanty, B., et al. (2019). Postmortem blood and tissue changes for estimation of time of death. *Int. J. Curr. Microbiol. Appl. Sci.* 8, 43–53. doi:10.20546/ijcmas.2019.809.007

De-Giorgio, F., Ciasca, G., Fecondo, G., Mazzini, A., De Spirito, M., and Pascali, V. L. (2021). Estimation of the time of death by measuring the variation of lateral cerebral ventricle volume and cerebrospinal fluid radiodensity using postmortem computed tomography. *Int. J. Leg. Med.* 135 (6), 2615–2623. doi:10.1007/s00414-021-02698-6

Donaldson, A. E., and Lamont, I. L. (2013). Biochemistry changes that occur after death: potential markers for determining post-mortem interval. *PLoS One* 8 (11), e82011. doi:10.1371/journal.pone.0082011

Fischer, K., Kettunen, J., Würtz, P., Haller, T., Havulinna, A. S., Kangas, A. J., et al. (2014). Biomarker profiling by nuclear magnetic resonance spectroscopy for the prediction of all-cause mortality: an observational study of 17,345 persons. *PLoS Med.* 11 (2), e1001606. doi:10.1371/journal.pmed.1001606

Gelderman, T., Stigter, E., Krap, T., Amendt, J., and Duijst, W. (2021). The time of death in Dutch court; using the Daubert criteria to evaluate methods to estimate the PMI used in court. *Leg. Med. (Tokyo)* 53, 101970. doi:10.1016/j.legalmed.2021.101970

Go, A., Shim, G., Park, J., Hwang, J., Nam, M., Jeong, H., et al. (2019). Analysis of hypoxanthine and lactic acid levels in vitreous humor for the estimation of post-mortem interval (PMI) using LC-MS/MS. *Forensic Sci. Int.* 299, 135–141. doi:10.1016/j.forsciint.2019.03.024

Hira, H. S., Samal, P., Kaur, A., and Kapoor, S. (2014). Plasma level of hypoxanthine/xanthine as markers of oxidative stress with different stages of obstructive sleep apnea syndrome. *Ann. Saudi Med.* 34 (4), 308–313. doi:10.5144/0256-4947.2014.308

Kaszynski, R. H., Nishiumi, S., Azuma, T., Yoshida, M., Kondo, T., Takahashi, M., et al. (2016). Postmortem interval estimation: a novel approach utilizing gas chromatography/mass spectrometry-based biochemical profiling. *Anal. Bioanal. Chem.* 408 (12), 3103–3112. doi:10.1007/s00216-016-9355-9

Keltanen, T., Nenonen, T., Ketola, R. A., Ojanperä, I., Sajantila, A., and Lindroos, K. (2015). Post-mortem analysis of lactate concentration in diabetics and metformin poisonings. *Int. J. Leg. Med.* 129 (6), 1225–1231. doi:10.1007/s00414-015-1256-5

Kirwan, J. A., Gika, H., Beger, R. D., Bearden, D., Dunn, W. B., Goodacre, R., et al. (2022). Quality assurance and quality control reporting in untargeted metabolic phenotyping: mQACC recommendations for analytical quality management. *Metabolomics* 18 (9), 70. doi:10.1007/s11306-022-01926-3

Laplace, K., Baccino, E., and Peyron, P. A. (2021). Estimation of the time since death based on body cooling: a comparative study of four temperature-based methods. *Int. J. Leg. Med.* 135 (6), 2479–2487. doi:10.1007/s00414-021-02635-7

Locci, E., Stocchero, M., Gottardo, R., Chighine, A., De-Giorgio, F., Ferino, G., et al. (2023). PMI estimation through metabolomics and potassium analysis on animal vitreous humour. *Int. J. Leg. Med.* 137 (3), 887–895. doi:10.1007/s00414-023-02975-6

Locci, E., Stocchero, M., Gottardo, R., De-Giorgio, F., Demontis, R., Nioi, M., et al. (2021). Comparative use of aqueous humour ^{1}H NMR metabolomics and potassium concentration for PMI estimation in an animal model. *Int. J. Leg. Med.* 135 (3), 845–852. doi:10.1007/s00414-020-02468-w

Lu, X. J., Li, J., Wei, X., Li, N., Dang, L. H., An, G. S., et al. (2023). A novel method for determining postmortem interval based on the metabolomics of multiple organs combined with ensemble learning techniques. *Int. J. Leg. Med.* 137 (1), 237–249. doi:10.1007/s00414-022-02844-8

Madea, B. (2016). Methods for determining time of death. *Forensic Sci. Med. Pathol.* 12 (4), 451–485. doi:10.1007/s12024-016-9776-y

Madea, B., and Rödig, A. (2006). Time of death dependent criteria in vitreous humor—accuracy of estimating the time since death. *Forensic Sci. Int.* 164 (2), 87–92. doi:10.1016/j.forsciint.2005.12.002

Mathur, A., and Agrawal, Y. (2011). An overview of methods used for estimation of time since death. *Aust. J. Forensic Sci.* 43, 275–285. doi:10.1080/00450618.2011.568970

Matuszewski, S., Hall, M. J. R., Moreau, G., Schoenly, K. G., Tarone, A. M., and Villet, M. H. (2020). Pigs vs people: the use of pigs as analogues for humans in forensic entomology and taphonomy research. *Int. J. Leg. Med.* 134 (2), 793–810. doi:10.1007/s00414-019-02074-5

Mihailovic, Z., Atanasijevic, T., Popovic, V., and Milosevic, M. B. (2011). Could lactates in vitreous humour be used to estimate the time since death? *Med. Sci. Law* 51 (3), 156–160. doi:10.1258/msl.2011.010124

Mojsak, P., Maliszewska, K., Klimaszewska, P., Miniewska, K., Godzien, J., Sieminska, J., et al. (2022). Optimization of a GC-MS method for the profiling of microbiota-dependent metabolites in blood samples: an application to type 2 diabetes and prediabetes. *Front. Mol. Biosci.* 9, 982672. doi:10.3389/fmolb.2022.982672

Nishida, A., Funaki, H., Kobayashi, M., Tanaka, Y., Akasaka, Y., Kubo, T., et al. (2015). Blood creatinine level in postmortem cases. *Sci. Justice* 55 (3), 195–199. doi:10.1016/j.scijus.2014.12.005

Palacio, C., Gottardo, R., Cirielli, V., Musile, G., Agard, Y., Bortolotti, F., et al. (2021). Simultaneous analysis of potassium and ammonium ions in the vitreous humour by capillary electrophoresis and their integrated use to infer the post mortem interval (PMI). *Med. Sci. Law* 61 (1_Suppl. l), 96–104. doi:10.1177/0025802420934239

Patterson, H. D., and Thompson, R. (1971). Recovery of inter-block information when block sizes are unequal. *Biometrika* 58 (3), 545–554. doi:10.1093/biomet/58.3.545

Peng, D., Lv, M., Li, Z., Tian, H., Qu, S., Jin, B., et al. (2020). Postmortem interval determination using mRNA markers and DNA normalization. *Int. J. Leg. Med.* 134 (1), 149–157. doi:10.1007/s00414-019-02199-7

Pesko, B. K., Weidt, S., McLaughlin, M., Wescott, D. J., Torrance, H., Burgess, K., et al. (2020). Postmortomics: the potential of untargeted metabolomics to highlight markers for time since death. *OMICS* 24 (11), 649–659. doi:10.1089/omi.2020.0084

Peyron, P. A., Hirtz, C., Baccino, E., Ginestet, N., Tiers, L., Martinez, A. Y., et al. (2021). Tau protein in cerebrospinal fluid: a novel biomarker of the time of death? *Int. J. Leg. Med.* 135 (5), 2081–2089. doi:10.1007/s00414-021-02558-3

Rognum, T. O., Holmen, S., Musse, M. A., Dahlberg, P. S., Stray-Pedersen, A., Saugstad, O. D., et al. (2016). Estimation of time since death by vitreous humor hypoxanthine, potassium, and ambient temperature. *Forensic Sci. Int.* 262, 160–165. doi:10.1016/j.forsciint.2016.03.001

Sangwan, A., Singh, S. P., Singh, P., Gupta, O. P., Manas, A., and Gupta, S. (2021). Role of molecular techniques in PMI estimation: an update. *J. Forensic Leg. Med.* 83, 102251. doi:10.1016/j.jflm.2021.102251

Sato, T., Zaitsu, K., Tsuboi, K., Nomura, M., Kusano, M., Shima, N., et al. (2015). A preliminary study on postmortem interval estimation of suffocated rats by GC-MS/MS-based plasma metabolic profiling. *Anal. Bioanal. Chem.* 407 (13), 3659–3665. doi:10.1007/s00216-015-8584-7

Sharma, V., and Kumar, R. (2018). Trends of chemometrics in bloodstain investigations. *TrAC Trends Anal. Chem.* 107, 181–195. doi:10.1016/j.trac.2018.08.006

Shen, L., Ma, J., Zhou, H., Chen, L., Tang, J., Zhang, K., et al. (2022). Plasma metabolomic profiling reveals preliminary biomarkers of pork quality based on pH value. *Foods* 11 (24), 4005. doi:10.3390/foods11244005

Sibbens, L., Van de Voorde, W., Decorte, R., and Bekaert, B. (2017). The development of a forensic clock to determine time of death. *Forensic Sci. Int. Genet. Suppl. Ser.* 6, e162–e163. doi:10.1016/j.fsigss.2017.09.059

Szeremeta, M., Pietrowska, K., Niemcunowicz-Janica, A., Kretowski, A., and Ciborowski, M. (2021). Applications of metabolomics in forensic toxicology and forensic medicine. *Int. J. Mol. Sci.* 22 (6), 3010. doi:10.3390/ijms22063010

Szeremeta, M., Samczuk, P., Pietrowska, K., Kowalczyk, T., Przeslaw, K., Sieminska, J., et al. (2022). *In vitro* animal model for estimating the time since death with attention to early postmortem stage. *Metabolites* 13 (1), 26. doi:10.3390/metabo13010026

Wang, Q., He, H., Li, B., Lin, H., Zhang, Y., Zhang, J., et al. (2017). UV-Vis and ATR-FTIR spectroscopic investigations of postmortem interval based on the changes in rabbit plasma. *PLoS One* 12 (7), e0182161. doi:10.1371/journal.pone.0182161

Wenzlow, N., Mills, D., Byrd, J., Warren, M., and Long, M. T. (2023). Review of the current and potential use of biological and molecular methods for the estimation of the postmortem interval in animals and humans. *J. Vet. Diagn Investig.* 35 (2), 97–108. doi:10.1177/10406387231153930

Wilk, L. S., Edelman, G. J., Roos, M., Clerkx, M., Dijkman, I., Melgar, J. V., et al. (2021). Individualised and non-contact post-mortem interval determination of human bodies using visible and thermal 3D imaging. *Nat. Commun.* 12 (1), 5997. doi:10.1038/s41467-021-26318-4

Wilk, L. S., Hoveling, R. J. M., Edelman, G. J., Hardy, H. J. J., van Schouwen, S., van Venrooij, H., et al. (2020). Reconstructing the time since death using noninvasive thermometry and numerical analysis. *Sci. Adv.* 6 (22), eaba4243. doi:10.1126/sciadv.aba4243

Wilson, S. J., and Christensen, A. M. (2017). A test of the citrate method of PMI estimation from skeletal remains. *Forensic Sci. Int.* 270, 70–75. doi:10.1016/j.forsciint.2016.11.026

Wu, Z., Lu, X., Chen, F., Dai, X., Ye, Y., Yan, Y., et al. (2018). Estimation of early postmortem interval in rats by GC-MS-based metabolomics. *Leg. Med. (Tokyo)* 31, 42–48. doi:10.1016/j.legalmed.2017.12.014

Yumba-Mpanga, A., Struck-Lewicka, W., Wawrzyniak, R., Markuszewski, M., Roslan, M., Kaliszan, R., et al. (2019). Metabolomic heterogeneity of urogenital tract cancers analyzed by complementary chromatographic techniques coupled with mass spectrometry. *Curr. Med. Chem.* 26 (1), 216–231. doi:10.2174/0929867324666171006150326

Zeki, Ö., Eylem, C. C., Reçber, T., Kır, S., and Nemutlu, E. (2020). Integration of GC-MS and LC-MS for untargeted metabolomics profiling. *J. Pharm. Biomed. Anal.* 190, 113509. doi:10.1016/j.jpba.2020.113509

Zelentsova, E. A., Yanshole, L. V., Melnikov, A. D., Kudryavtsev, I. S., Novoselov, V. P., and Tsentalovich, Y. P. (2020). Post-mortem changes in metabolomic profiles of human serum, aqueous humor and vitreous humor. *Metabolomics* 16 (7), 80. doi:10.1007/s11306-020-01700-3

Zhang, F. Y., Wang, L. L., Zhang, M., Dong, W. W., Zhang, Z. D., Li, X. J., et al. (2022a). Inferring postmortem submersion interval in rats found in water based on vitreous humor metabolites. *Fa Yi Xue Za Zhi* 38 (1), 59–66. doi:10.12116/j.issn.1004-5619.2021.410613

Zhang, F. Y., Wang, L. L., Dong, W. W., Zhang, M., Tash, D., Li, X. J., et al. (2022b). A preliminary study on early postmortem submersion interval (PMSI) estimation and cause-of-death discrimination based on nontargeted metabolomics and machine learning algorithms. *Int. J. Leg. Med.* 136 (3), 941–954. doi:10.1007/s00414-022-02783-4

Zhang, Y., Fan, S., Wohlgemuth, G., and Fiehn, O. (2023). Denoising autoencoder normalization for large-scale untargeted metabolomics by gas chromatography–mass spectrometry. *Metabolites* 13, 944. doi:10.3390/metabo13080944

frontiers | Frontiers in Molecular Biosciences

TYPE Original Research
PUBLISHED 25 March 2025
DOI 10.3389/fmolb.2025.1518873

OPEN ACCESS

EDITED BY
Geraldine M. Dowling Sfhea,
Atlantic Technological University, Ireland

REVIEWED BY
Abdul Bari Shah,
Korea University, Republic of Korea
Swarnima Pandey,
University of Maryland, United States

*CORRESPONDENCE
Wei Cai,
20120941161@bucm.edu.cn

†These authors have contributed equally to this work

RECEIVED 29 October 2024
ACCEPTED 27 February 2025
PUBLISHED 25 March 2025

CITATION
Zhu L, Xie L, Wang Z, Li K-L and Cai W (2025) Mass spectrometry-based metabolomics reveal the effects and potential mechanism of isochlorogenic acid A in MC3T3-E1 cells. *Front. Mol. Biosci.* 12:1518873. doi: 10.3389/fmolb.2025.1518873

Mass spectrometry-based metabolomics reveal the effects and potential mechanism of isochlorogenic acid A in MC3T3-E1 cells

Lian Zhu[1†], Liu Xie[2†], Ziming Wang[1], Kai-Lin Li[1] and Wei Cai[1*]

[1]School of Pharmaceutical Sciences, Sino-Pakistan Center on Traditional Chinese Medicine, Hunan University of Medicine, Huaihua, China, [2]Department of Pathology and Research Office of the School of Basic Medicine, Hunan University of Medicine, Huaihua, China

Introduction: The bioactive compound 3,5-DiCQA, derived from Duhaldea nervosa, has been traditionally utilized in folk remedies for bone fractures and osteoporosis. However, its therapeutic mechanisms remain unclear.

Methods: We employed UHPLC-Q Exactive Orbitrap MS-based cell metabolomics to investigate the molecular mechanisms of 3,5-DiCQA in MC3T3-E1 cells. Cell proliferation was assessed via MTT assay, differentiation by alkaline phosphatase (ALP) activity, and mineralization through alizarin red staining and cetylpyridinium chloride quantification. Metabolomic profiling compared drug-treated and control groups.

Results: Results from MTT assays demonstrated that 3,5-DiCQA significantly promoted cell proliferation at 100 μM. Alkaline phosphatase (ALP) assays and alizarin red staining revealed enhanced osteoblast differentiation and mineralization, respectively. Calcification deposition was significantly increased in the calcified stained cells by cetylpyridinium chloride quantization, indicating that 3,5-DiCQA can promote the mineralization of MC3T3-E1 cells. Metabolomic analysis identified key metabolic changes, including the downregulation of phytosphingosine and upregulation of sphinganine and citric acid.

Discussion: These findings suggest that 3,5-DiCQA promotes osteoblast proliferation, differentiation and mineralization through pathways such as sphingolipid metabolism, arginine and proline metabolism, mucin type O-glycan biosynthesis and the citrate cycle (TCA cycle). This study provides insights into the therapeutic potential of 3,5-DiCQA for osteoporosis and highlights the utility of metabolomics in elucidating traditional Chinese medicine (TCM).

KEYWORDS

osteoporosis, MC3T3-E1 cells, metabolomics, UHPLC-Q-Exactive Orbitrap MS, *Duhaldea nervosa*, mechanism

1 Introduction

Osteoporosis (OP) is a chronic, systemic endocrine and metabolic disorder. There are two kinds of osteoporosis primary (caused by aging or a lack of sex hormones)

and secondary (caused by hyperthyroidism, diabetes, obesity, Cushing's syndrome, anorexia, rheumatoid arthritis, drug effects, etc.). The root cause of its occurrence is the imbalance of bone remodeling homeostasis including osteoclasts that absorb old bone and osteoblasts that form new bone. This causes the rate of bone loss to be faster than that of bone production (Föger-Samwald, Dovjak, Azizi-Semrad, Kerschan-Schindl and Pietschmann, 2020; Hardy, Zhou, Seibel and Cooper, 2018; Inaba, 2004; Lademann, Tsourdi, Hofbauer and Rauner, 2020; Mo et al., 2021; NIH Consensus Development Panel on Osteoporosis Prevention, Diagnosis, and Therapy, 2001; Workman, Blalock and Mehler, 2020). Therefore, the proliferation, differentiation and mineralization of osteoblasts play a very important role in fracture healing (Dirckx, Van Hul and Maes, 2013). As the population ages, osteoporosis and osteoporoid-related fractures have become a major public health problem for society and significantly increase the consumption of healthcare resources. Therefore, in-depth study of the pathological mechanism of osteoporosis will help reduce the medical costs associated with osteoporosis, and further targeted drug development can improve the quality of life of the elderly.

Duhaldea nervosa (Wallich ex Candolle) A. Anderberg, is a member of the Asteraceae family and is commonly known as Maoxiucai or Xiaoheiyao in China (Cai et al., 2020; Liu et al., 2018; Guan et al., 2017). It has been used as a folk medicine for dispelling wind-chill, fighting inflammation and treating a variety of conditions and diseases including fracture and rheumatoid arthritis (RA) (Long, 2004; Xiao, 2009; Xiao et al., 2013). Previous research has shown that *D. nervosa* contains isochlorogenic acid A (3,5-DiCQA), a chemical that has a wide range of physiological activities, such as cardiovascular protection, antioxidant and anti-inflammatory effects, and osteoblast proliferation, which might have a therapeutic effect in the treatment of fractures and RA (Naveed et al., 2018; Wang and Xiao, 2019). However, there are relatively few reports on the efficacy and metabolic pathways of 3,5-DiCQA in treating osteoporosis. Osteoblasts are bone lining cells responsible for the production of bone matrix components and minerals in the process of bone formation (Florencio-Silva, Sasso, Sasso-Cerri, Simões and Cerri, 2015). The regulation of the activity of MC3T3-E1 osteoblasts is of great significance for the prevention and treatment of fractures (Croucher, McDonald and Martin, 2016; Long, 2011). Therefore, it is of great significance to investigate the regulation of 3,5-DiCQA using an *in vitro* MC3T3-E1 cell model.

Metabolomics is a burgeoning field that emerged as an influential analytical approach for identifying potential biomarkers and unraveling the molecular underpinnings of Traditional Chinese Medicine (TCM) in disease treatment (Cheong, Yu, Chen and Zhong, 2022; Wang et al., 2021). The subfield of cellular metabolomics has garnered extensive interest, proving instrumental in scrutinizing the biochemical processes related to disease pathology. It offers insights into how TCM impacts cellular metabolism, thereby contributing to a comprehensive understanding of metabolic processes. For instance, recent studies have demonstrated the utility of cellular metabolomics in elucidating disease mechanisms, such as mitochondrial dysfunction in hypoxia/reoxygenation injury in cardiomyocytes (Lin et al., 2023) and oxidative stress in HepG2 cells (Yu et al., 2024). They have also uncovered the metabolic reprogramming of immune cells in response to inflammation (Wang et al., 2024). These findings highlight the potential of metabolomics to provide comprehensive insights into cellular metabolism and its role in health and disease. Advanced high-resolution mass spectrometry (HRMS) has solidified its role as the principal analytical platform within metabolomics studies. Its prevalence is due to its capacity for sensitive detection, precise resolution of complex mixtures, high precision in mass measurement, and its broad dynamic range, making it an indispensable asset in the quest to decode the metabolomic signatures of various biological systems (Sun et al., 2018; Xie et al., 2023; Yu et al., 2016; Yu et al., 2017). The union of Ultra-High-Performance Liquid Chromatography (UHPLC) with Q-Exactive Orbitrap Mass Spectrometry (MS) stands out as an exceptionally potent analytical methodology for both detecting and characterizing the chemical constituents within botanical extracts and complex biological matrices. The efficacy of this technique is largely due to the swift and decisive separation capabilities of UHPLC, complemented by the Q-Exactive Orbitrap's prowess in delivering precise mass measurements coupled with a wealth of detailed fragment ion data from MSn experiments, which are crucial for the elucidation of molecular structures (Cai et al., 2017; Clifford, Johnston, Knight and Kuhnert, 2003; Qiao et al., 2016). This approach has been successfully applied in various studies, such as the investigation of Cynara scolymus Bracts's effects on liver and breast carcinoma cells (El Sohafy et al., 2024) and the metabolic changes in mitochondrial dysfunction in kidney tubular cells (Marchese et al., 2022), demonstrating its versatility and reliability in cellular metabolomics research. Therefore, we used UHPLC-Q-Exactive Orbitrap MS to investigate the molecular mechanisms of 3,5-DiCQA in MC3T3-E1 cells to elucidate its therapeutic mechanism in osteoporosis.

2 Materials and methods

2.1 Materials and reagents

3,5-DiCQA was purchased from Chengdu Herpurify Co.,Ltd. Liquid chromatography-mass spectrometry (LC-MS/MS)-grade acetonitrile, LC-MS/MS-grade formic acid and the BCA protein concentration assay kit were purchased from Thermo Fisher Scientific Co., Ltd. Ultra-pure water was obtained from Guangzhou Watsons Food & Beverage Co., Ltd. Other solvents were of analytical grade and were supplied by the Aladdin Industrial Corporation.

Fetal bovine serum (FBS) was acquired from Zhejiang Tianhang Biotechnology Co., Ltd. α-MEM medium, tryptic digestion

Abbreviations: 3,5-DiCQA, isochlorogenic acid A; TCM, traditional Chinese medicine; ALP, alkaline phosphatase; CPC, cetylpyridinium chloride; FBS, Fetal bovine serum; MTT, 3-(4,5-dimethyl-2-thiazolyl)-2,5-diphenyl-2-H-tetrazolium bromide; DMSO, Dimethyl Sulfoxide; E2, estradiol; LC-MS/MS, Liquid chromatography-mass spectrometry; CO_2, carbon dioxide; OIM, osteogenic induction medium; PBS, phosphate-buffered saline; QC, quality control; HRMS, High-resolution mass spectrometry; ANOVA, one-way analysis of variance; PCA, principal component analysis; OPLS-DA, orthogonal partial least squares discriminant analysis; VIP, variable important in projection; TCA cycle: Citrate cycle; OP, Osteoporosis; ES, electrospray ionization.

solution and 100 X penicillin streptomycin solution (containing 10 kU/mL penicillin+10 mg/mL streptomycin) were purchased from Hyclone. Dimethyl sulfoxide (DMSO), β-glycerophosphate sodium, vitamin C, estradiol (E2) and 3-(4,5-dimethyl-2-thiazolyl)-2,5-diphenyl-2-H-tetrazolium bromide (MTT) were bought from Sigma Chemical Co., Ltd. The alkaline phosphatase (ALP) kit was acquired from Nanjing Jiancheng Bioengineering Institute. The BCIP/NBT Alkaline Phosphatase Kit was purchased from Beyotime Biotechnology.

2.2 Solution preparation

The compound 3,5-DiCQA was prepared as a stock solution at a concentration of 100 mM in DMSO and stored in a dark environment at −20°C for subsequent use. Prior to experimentation, this stock solution was appropriately diluted with α-MEM medium to achieve the desired working concentrations.

2.3 Cell culture

The MC3T3-E1 cell line sourced from the National Collection of Authenticated Cell Cultures was maintained in an incubator at 37°C with an atmosphere containing 5% CO_2. The culture medium was α-MEM supplemented with 10% FBS, 100 units/mL of penicillin, and 10 mg/mL of streptomycin. Upon reaching 80% confluence, the cells were passaged, sub-cultured, and then cryopreserved for future use.

2.4 Cell proliferation assay

The MTT assay was utilized to evaluate the viability of MC3T3-E1 cells. The cells were seeded in 96-well plates at a density of 5 × 10^3 cells per well. To determine the impact of 3,5-DiCQA on osteoblast viability, they were exposed to various concentrations of 3,5-DiCQA (12.5, 25, 50, and 100 μM) for both 24 and 48 h. Following incubation, 10 μL of MTT solution was added to 90 μL of complete medium and the cells were returned to the CO_2 incubator for an additional 4 h. The absorbance was measured at a wavelength of 490 nm using a microplate reader (Biotek).

2.5 ALP activity and staining assay

The influence of 3,5-DiCQA on osteogenic differentiation was investigated by treating experimental groups with different concentrations of 3,5-DiCQA (25, 50, and 100 μM) alongside 10 nM estradiol. After a 6-day incubation period, ALP activity was quantified using a commercial ALP Assay Kit. The microplate reader was set to a wavelength of 562 nm for detection. Additionally, ALP staining was performed using the BCIP/NBT ALP Kit to visualize the activity.

2.6 Mineralization assay

The extent of mineralization was assessed using alizarin red staining. MC3T3-E1 cells were cultured in osteogenic induction medium, which contains 50 μg/mL of ascorbic acid and 10 mM β-glycerophosphate, and treated with varying concentrations of 3,5-DiCQA (12.5, 25, 50, and 100 μM) along with 10 nM estradiol for a period of 14 days. The cells were then stained with alizarin red S for 30 min to visualize mineralization nodules. The stained nodules were photographed, and 10% cetylpyridinium chloride (CPC) was utilized to extract the alizarin red for quantification, with the detection wavelength set to 540 nm.

2.7 Cell metabolomics

2.7.1 Cell sample collection and preparation

The MC3T3-E1 cells were cultured in 24-well plates and treated with 3,5-DiCQA for a period of 6 days. After incubation, the cells were meticulously rinsed with phosphate-buffered saline (PBS) three times. A volume of 1 mL of chilled methanol was then added to each dish, followed by gently scraping the cells using a cell scraper while on ice. The cells underwent a freeze–thaw cycle three times to facilitate extraction. The mixture was centrifuged at 4°C with a rotation speed of 12,000 rpm for 20 min to collect the supernatant. The supernatant was carefully transferred into LC-MS vials and conserved at −80°C for future analysis. To ensure the reliability of the LC-MS system and to mitigate potential bias, a quality control (QC) sample was crafted. The injection sequence was designed such that a QC sample was interspersed every five samples.

2.7.2 UHPLC-orbitrap-HRMS analysis

For the UHPLC-Orbitrap-HRMS analysis, the cell samples were processed using a Q-Exactive Focus Orbitrap mass spectrometer (Thermo Electron, Bremen, Germany), interfaced with a Thermo Scientific Dionex Ultimate 3000 RS liquid chromatography system (Thermo Fisher Scientific, California, United States) through an electrospray ionization (ESI) source. The chromatographic separation was achieved using a Thermo Scientific Hypersil GOLDTM aQ column (100 mm × 2.1 mm, 1.9 μm), with the column temperature regulated at 40°C. The mobile phase consisted of 0.1% formic acid in water (phase A) and acetonitrile (phase B), with a flow rate of 0.3 mL/min, according to the following gradient elution program: 0–2 min, 5%–40% B; 2–3 min, 40%–55% B; 3–5 min, 55%–69% B; 5–7 min, 69%–70% B; 7–10 min, 70%–73% B; 10–12 min, 73%–95% B; 12–12.1 min, 95%–5% B; and 15 min, 5% B. The injection volume was 2 μL.

High-resolution mass spectrometry (HRMS) operations were conducted using an ESI ion source, capable of both positive and negative ion detection modes. The spray voltage was set to 3.5 kV for the positive mode and 3.2 kV for the negative mode, with sheath gas pressure at 35 arb and auxiliary gas pressure at 10 arb. The capillary and auxiliary gas heater temperatures were maintained at 320°C and 350°C, respectively, and the S-lens RF level was adjusted to 60. Full scan data acquisition was performed over a mass range of *m/z* 100–1,200, utilizing data-dependent MS2 scanning. Nitrogen was utilized as the collision gas, with the energy set to a normalized collision energy of 30%. The entire system was controlled using Xcalibur software, version 4.2.

2.7.3 Data processing

The raw data underwent comprehensive processing utilizing the Compound Discoverer 3.3 software (Thermo, United States). A strict mass tolerance threshold of 5 parts per million (ppm) was applied. The metabolomics workflow was engaged to dissect the mass spectrometry data. Key parameters for analysis were defined, focusing on peaks with signal intensities exceeding a threshold of 10,000 for identification. A retention time window of 0.1 min and a noise elimination threshold of 10 were implemented. Critical data points including peak identification, m/z values, retention times, and signal intensities were extracted and prepared for use in subsequent experimental phases. SIMCA 14.1 software (Umetrics, Sweden) was used for the multivariate statistical treatment of the data, including principal component analysis (PCA), orthogonal partial least squares discriminant analysis (OPLS-DA), and other advanced statistical techniques. The quality of the OPLS-DA model was meticulously assessed through R^2Y (cumulative) and Q2 (cumulative) metrics, and a stringent 200 permutation test protocol. The variable important in projection (VIP) score and the p-value from the T-test were pivotal in screening potential biomarkers. Metabolite enrichment and pathway analysis were further conducted using the MetaboAnalyst 5.0 online platform, integrating the potential metabolites for a deeper biological interpretation.

2.8 Statistical analysis

We used GraphPad Prism (version 9.0) to perform one-way ANOVA. The data are presented as the mean ± standard deviation, derived from a minimum of three replicates per test condition. Statistical significance was determined by a p-value of less than 0.05.

3 Results

3.1 3,5-DiCQA promoted MC3T3-E1 cells proliferation

We used an MTT assay to explore the roles of 3,5-DiCQA in the proliferation of MC3T3-E1 cells. The results showed that compared with vehicle treatment, high-dose 3,5-DiCQA (100 μM) significantly promoted cell proliferation in a dose-dependent manner, whereas cell proliferation was significantly reduced 48 h after treatment in MC3T3-E1 cells. As shown in Figure 1, the results indicated that 3,5-DiCQA (12.5–100 μM) significantly promoted cell proliferation (Figure 1).

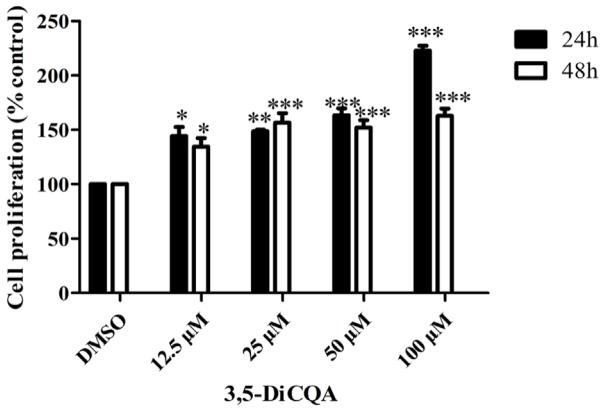

FIGURE 1
Effects of 3,5-DiCQA at different concentrations on proliferative activity of MC3T3-E1 cells at different time periods. Data were presented as the mean with standard deviation for technical triplicate in an experiment representative of several independent ones (n = 3),*P < 0.05,**P < 0.01,***P < 0.001, vs. DMSO.

3.2 3,5-DiCQA increased the ALP activity in MC3T3-E1 cells

Next, we evaluated whether 3,5-DiCQA would increase the ALP activity in MC3T3-E1 cells. MC3T3-E1 cells were cultured in osteogenic induction medium and incubated with E2 (10 nM) and 3,5-DiCQA (25, 50, and 100 μM) for 6 days. As a result, 3,5-DiCQA significantly increased the ALP activity in MC3T3-E1 cells. Cells treated with high-dose 3,5-DiCQA exhibited stronger ALP staining compared with control cells (Figure 2A). The ALP assay demonstrated that 3,5-DiCQA significantly enhanced cell differentiation (Figure 2B).

3.3 3,5-DiCQA increased the mineralization in MC3T3-E1 cells

MC3T3-E1 cells were cultured in OIM and incubated with E2 (10 nM) and 3,5-DiCQA (12.5, 25, 50, and 100 μM) for 2 weeks. Alizarin red staining was used to visualize the calcified nodules (Figure 3A). 3,5-DiCQA (12.5, 25, 50, and 100 μM) promoted the formation of calcified nodules in MC3T3-E1 cells. Nodule formation was highest at 3,5-DiCQA treatments of 25 μM (Figure 3B).

3.4 Identification of the metabolites of 3,5-DiCQA in MC3T3-E1 cells

From a chemical structure perspective, 3,5-DiCQA is formed by the esterification reaction of two molecules of caffeic acid and one molecule of quinic acid. It may undergo hydrolysis, methylation, sulfation, and other metabolic reactions within cells. By comparing the LC-MS spectra of the control group and the administered group, 11 metabolites (M1~M11, Table 1) were preliminarily identified from the samples after administration of 3,5-DiCQA. After metabolism, the metabolites retain some basic structural features of the parent drug. Therefore, we can infer the structure of the metabolites by analyzing the mass spectrometry fragmentation patterns of the parent drug 3,5-DiCQA. On comparing the retention time and mass spectrometry data of the standards, the quasi-molecular ion peak of 3,5-DiCQA is *m/z* 515.1195 $[M-H]^-$ (with the molecular formula $C_{25}H_{24}O_{12}$, an error of 0.72), and the retention time is 9.71 min. The MS^2 spectrum shows the characteristic fragmentation ions resulting

10.3389/fmolb.2025.1518873

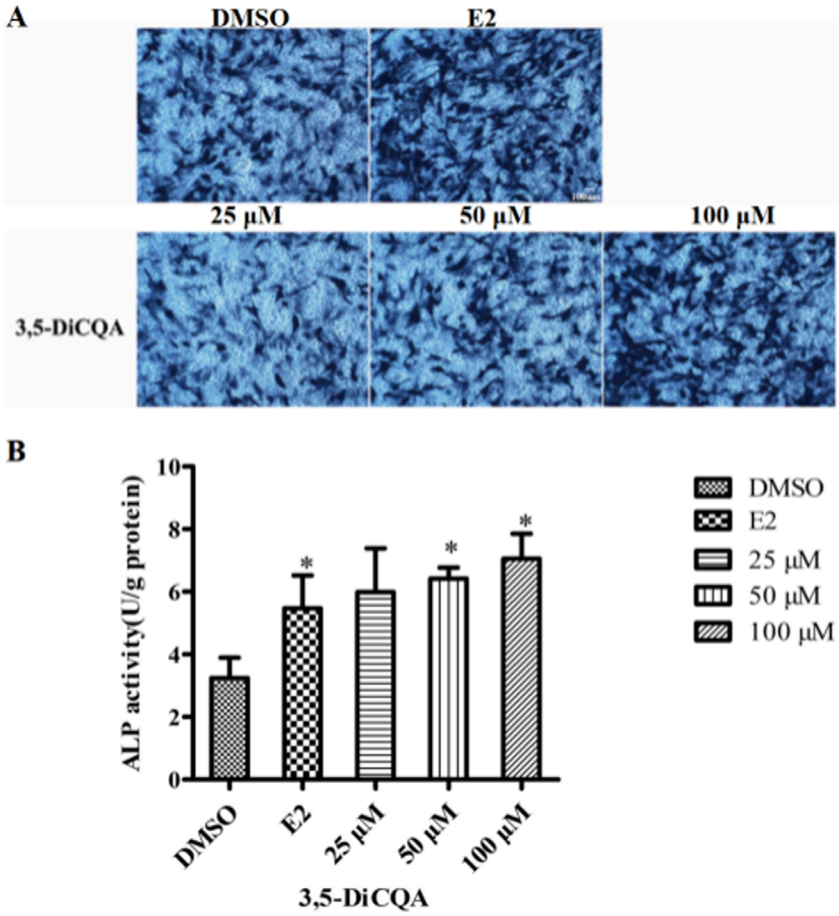

FIGURE 2
The effect of 3,5-DiCQA on the ALP activity in MC3T3-E1 cells. **(A)** BCIP/NBT staining was conducted. **(B)** The ALP activity was determined after 6-days co-treatment of MC3T3-E1 cells with 3,5-DiCQA (25, 50, and 100 μM) in OIM. Data were presented as the mean with standard deviation for technical triplicate in an experiment representative of several independent ones (n = 5),*$p < 0.05$ vs. DMSO.

from the neutral loss of one molecule of caffeoyl group at *m/z* 353.08 $[M\text{-}H\text{-caffeoyl}]^-$, the neutral loss of two molecules of caffeoyl group at *m/z* 191.05 $[M\text{-}H\text{-}2\times\text{caffeoyl}]^-$, the neutral loss of one molecule of caffeoyl group and one molecule of quinic acid residue at *m/z* 179.03 $[M\text{-}H\text{-caffeoyl-quinic acid}]^-$, and further neutral loss of one molecule of CO_2 producing the fragment ion at *m/z* 135.04 $[M\text{-}H\text{-caffeoyl-quinic acid-}CO_2]^-$. These characteristic fragmentation pathways provide a basis for the identification of metabolites. The retention time of M1 is 3.42 min. Its $[M\text{-}H]^-$ peak is at m/z 353.08818, which is 162 Da less than m/z 515.1195. It is speculated to be the product formed when 3,5-DiCQA loses one molecule of caffeoyl group during hydrolysis. The double bond on the caffeoyl group of 3,5-DiCQA undergoes a nucleophilic addition reaction with the thiol group of cysteine. After the conjugate metabolic reaction of cysteine, the molecular weight of the product increases by the molecular weight of one cysteine. Therefore, it is speculated that M2, M3 and M5 undergoes the cysteine conjugation metabolic reaction. In the molecule of 3,5-DiCQA, there are carbon-carbon double bonds in the caffeoyl part. These double bonds are the sites where hydration reactions can occur. When 3,5-DiCQA undergoes a hydration reaction once, it is equivalent to adding a water molecule to the molecular structure. Then, the molecular weight of the product M4 after the reaction is the molecular weight of 3,5-DiCQA plus that of a water molecule. By comparing the retention time and MS^2 spectrum with those of the reference compounds, M8 and M9 were identified as 1,5-DiCQA and 4,5-DiCQA, respectively, both of which are products of the intramolecular acyl migration reaction of 3,5-DiCQA.The retention time of M10 is 11.13 min. The $[M\text{-}H]^-$ peak is at m/z 529.13515, which is 14 Da higher than m/z 515.1195. This is speculated to be the methylated product of 3,5-DiCQA. The retention time of M12 is 12.56 min. The [M-H]- peak is at m/z 543.15080, which is 28 Da higher than m/z 515.1195. We speculated that this is the dimethyl product of 3,5-DiCQA.

3.5 Multivariate statistical analysis

To delve deeper into the mechanisms by which 3,5-DiCQA influences the differentiation of MC3T3-E1 cells, a comparative metabolite analysis was conducted. We compared the differentiation induced by 3,5-DiCQA with that of cells treated with DMSO using

10.3389/fmolb.2025.1518873

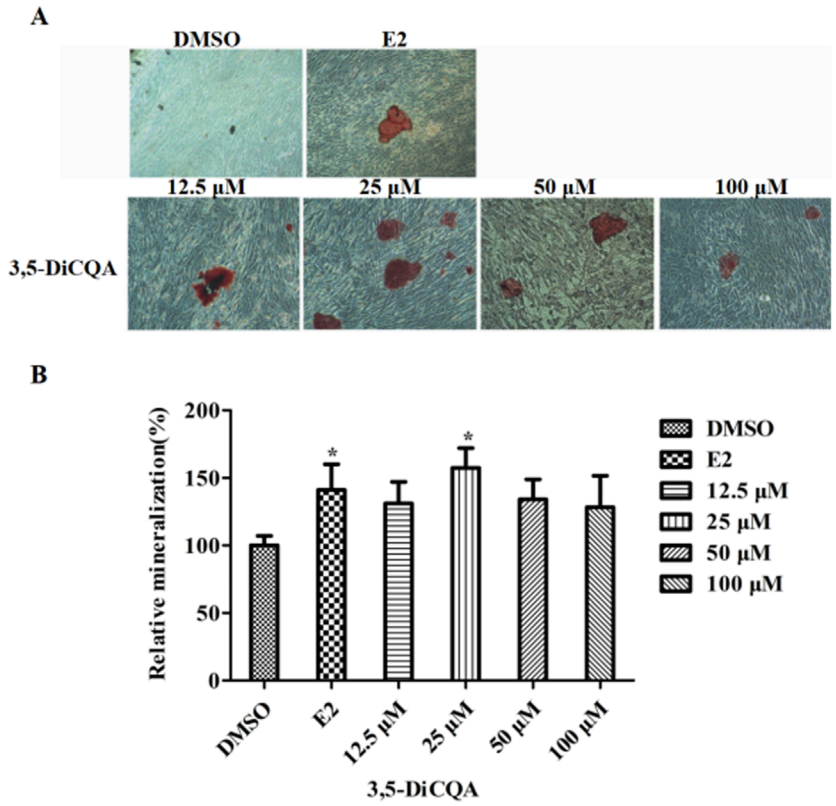

FIGURE 3
The effect of 3,5-DiCQA on the mineralization of MC3T3-E1 cells. **(A)** Alizarin red S was used for staining on day 14. **(B)** The calcified nodules was quantified by extraction of alizarin red S with 10% cetylpyridinium chloride (CPC) on day 14. Data were presented as the mean with standard deviation for technical triplicate in an experiment representative of several independent ones (n = 6),*$p < 0.05$ vs. DMSO.

UHPLC-HRMS. An unsupervised PCA approach was employed to assess the general sample distribution and the clustering of quality control (QC) samples as depicted in Figures 4A, B. The PCA plots demonstrated a coherent grouping of the QC samples, with some overlap between the control (DMSO) and the experimental (3,5-DiCQA) groups, which reflects the high stability and methodological soundness of the analytical instrument. In an effort to enhance the differentiation between the control and experimental groups and to boost the model's analytical resolution, a supervised OPLS-DA analysis was conducted, as presented in Figures 5A, B. The OPLS-DA score plots revealed a significant divergence between the control and experimental groups in both positive and negative modes. This separation confirms the presence of metabolic differences, suggesting that 3,5-DiCQA induces changes in cellular metabolism. To ensure the robustness of the OPLS-DA model against overfitting, a 200 permutation test was applied. The R2Y (cumulative) metric indicates the model's explanatory power along the y-axis, while the Q2 (cumulative) signifies its predictive accuracy. A Q2 value exceeding 0.5 is generally considered a threshold for model stability and reliability. In this study, the positive ion mode exhibited R2Y and Q2 values of 0.918 and 0.568, respectively, and the negative ion mode showed R2Y and Q2 values of 0.963 and 0.687, respectively. The permutation test results, as illustrated in Figures 5C, D, affirmed the model's reliability and precision in both ionization modes.

3.6 Identification of potential biomarkers

Differential metabolite analysis among the groups was performed using multivariate and univariate statistical analysis. Specifically, the OPLS-DA model and t-test were employed to identify variations in metabolite levels. A VIP score exceeding 1, coupled with a t-test p-value below 0.05, were established as thresholds for the significance of differential metabolites. As a result, nine potential biomarkers (Supplementary Figures S1, S2) as detailed in Table 2. A heatmap with hierarchical clustering was used to make data visualization more intuitive. The changed patterns in metabolite concentrations across samples can clearly be seen in Figure 6. A similar color distribution was observed within each group, along with a large difference between the groups. In comparison to the control group, treatment with 3,5-DiCQA led to noticeable decreases in the levels of phytosphingosine while it induced substantial increases in sphinganine and citric acid, as outlined in Table 2. These findings underscore the substantial metabolic alterations induced by 3,5-DiCQA.

3.7 Metabolic pathway analysis

We conducted an in-depth analysis to uncover the metabolic pathways that may be influenced by 3,5-DiCQA in enhancing the

10.3389/fmolb.2025.1518873

TABLE 1 The retention time and mass spectrometric data of isochlorogenic acid A metabolites.

Peak	t_R	Theoretical Mass *m/z*	Experimental Mass *m/z*	Error (ppm)	Formula	MS/MS fragment (–)	Identification	LYA + Cell	DMSO + Cell	LYA-cell
M1	3.42	353.08781	353.08829	1.37	$C_{16}H_{18}O_9$	MS^2[353]:191.0555(100), 179.0343(75), 135.0441(23)	Hydrolyzation	+	–	+
M2	5.39	634.12359	634.12476	1.83	$C_{28}H_{29}NO_{14}S$	MS^2[634]:191.0556(100), 179.0347(71), 192.9961(41), 353.0901(37), 206.4759(21)	Cysteine Conjugation 1	+	–	–
M3	5.97	636.13924	636.14093	2.64	$C_{28}H_{31}NO_{14}S$	MS^2[636]:191.0556(100), 353.0878(72), 179.0344(64), 173.0449(12)	Cysteine Conjugation 2	+	–	–
M4	7.54	533.13006	533.13086	1.49	$C_{25}H_{26}O_{13}$	MS^2[533]: 135.0439(100), 173.0447(79), 179.0344(52), 191.0554(31), 335.0781(29)	Hydration	+	–	–
M5	7.91	634.12359	634.12457	1.53	$C_{28}H_{29}NO_{14}S$	MS^2[634]:173.0447(100), 192.9958(74), 179.0345(64), 191.0554(45)	Cysteine Conjugation 1	+	–	+
M6	9.63	586.10246	586.10278	0.53	$C_{27}H_{25}NO_{12}S$	MS^2[586]:173.0446(100), 250.0177(51), 179.0339(31), 161.0232(23), 335.0789(17)	Dehydration + Dehydration+ Taurine conjugation	+	–	+
M7	9.71[a]	515.11950	515.11987	0.72	$C_{25}H_{24}O_{12}$	MS2[515]:173.0454(100); 179.0350(87); 191.0561(44); 135.0441(16); 353.0878(15)	3,5-DiCQA	+	–	+
M8	9.88[a]	515.11950	515.11981	0.60	$C_{25}H_{24}O_{12}$	MS^2[515]:191.0555(100), 179.0343(80), 353.0878(15), 173.0448(14), 135.0441(14)	1,5-DiCQA	+	–	+

(Continued on the following page)

10.3389/fmolb.2025.1518873

TABLE 1 (*Continued*) The retention time and mass spectrometric data of isochlorogenic acid A metabolites.

Peak	t_R	Theoretical Mass *m/z*	Experimental Mass *m/z*	Error (ppm)	Formula	MS/MS fragment (−)	Identification	LYA + Cell	DMSO + Cell	LYA-cell
M9	10.70[a]	515.11950	515.11993	0.84	$C_{25}H_{24}O_{12}$	MS^2[515]:173.0448(100), 179.0343(72), 191.0555(22), 353.0882(20)	4,5-DiCQA	+	–	+
M10	11.13	529.13515	529.13574	1.12	$C_{26}H_{26}O_{12}$	MS^2[529]:193.0497(100), 173.0445(65), 179.0341(58), 161.0234(22), 155.0341(21), 135.0444(17)	methylate	+	–	–
M11	12.56	543.15080	543.15131	0.94	$C_{27}H_{28}O_{12}$	MS^2[543]:173.0447(100), 193.0499(85), 175.0392(38), 349.0932(34), 155.0341(29)	Dimethylate	+	–	–

[a]Confirmed with standard compounds.

differentiation of MC3T3-E1 cells. Utilizing the MetaboAnalyst 5.0 platform, we enriched and examined the topological aspects of 29 metabolic pathways represented by biomarkers. In our graphical representation, the vertical axis denotes the name of the metabolic pathway, while the horizontal axis reflects the enrichment ratio, which is the proportion of altered metabolites relative to the entire pool within a given pathway. Our findings indicated a total of 11 pathways that are potentially modulated by 3,5-DiCQA to facilitate cell differentiation, with notable pathways including sphingolipid metabolism, arginine and proline metabolism, mucin type O-glycan biosynthesis, and the citrate cycle (TCA cycle), as depicted in Figure 7A. In the network topology analysis diagram, each circle symbolizes a distinct metabolic pathway. The variations in the size and color of these circles correspond to the extent of their influence within the system. As illustrated in Figure 7B, the differentiation of MC3T3-E1 cells induced by 3,5-DiCQA appears to be particularly linked to sphingolipid metabolism and several other pathways, the details of which are compiled in Table 3.

4 Discussion

Osteoporosis (OP), characterized by low bone mass, degeneration of bone tissue and destruction of bone microstructure, can lead to decreased bone strength and increased risk of fracture. The number of OP hip fractures worldwide is estimated to exceed 200 million, and 40% of postmenopausal women and 30% of men will experience OP fractures during their lives (Garvey et al., 2016; Wright et al., 2014). In China, the incidence of OP is as high as 23.9% among people between 50 and 59 years old, and the incidence increases significantly with an increase in age (Liao et al., 2002). However, the current treatment of OP includes drug therapy, physical therapy and exercise therapy, but the therapeutic effect is relatively low, patients' compliance is poor, and there are many adverse reactions (Aaseth, Boivin and Andersen, 2012; Metcalf, Aspray and McCloskey, 2017; Piemonte et al., 2012). At present, the clinical treatment of osteoporosis is still dominated by chemical drugs. According to their different mechanisms of action in the treatment of osteoporosis, chemical drugs can be divided into bone absorption inhibitors (such as bisphosphonates, estrogen and calcitonin), bone formation promoters (fluoride and strontium preparations) and bone mineralization promotion drugs (vitamin D and calcium preparations) (An et al., 2016; Zeng et al., 2014; Du et al., 2013; Xu et al., 2018). However, taking these drugs is often accompanied by side effects such as inflammation of the esophagus, nausea, abdominal pain and even cancer of the reproductive system. Their potential toxicity and side effects limit their wide application to some extent (Black et al., 2013; Ma and Ge, 2017). Therefore, the search for safer natural substitutes of traditional Chinese medicine (TCM) that can promote bone formation and reverse bone structural damage is receiving increasing attention.

Duhaldea nervosa is traditionally used for activating meridians, promoting blood circulation and removing blood stasis, reducing swelling and dispersing blood. It has a good therapeutic effect on rheumatic pain, fall injury, fracture and other diseases, and can significantly shorten the course of fracture healing. Since ancient

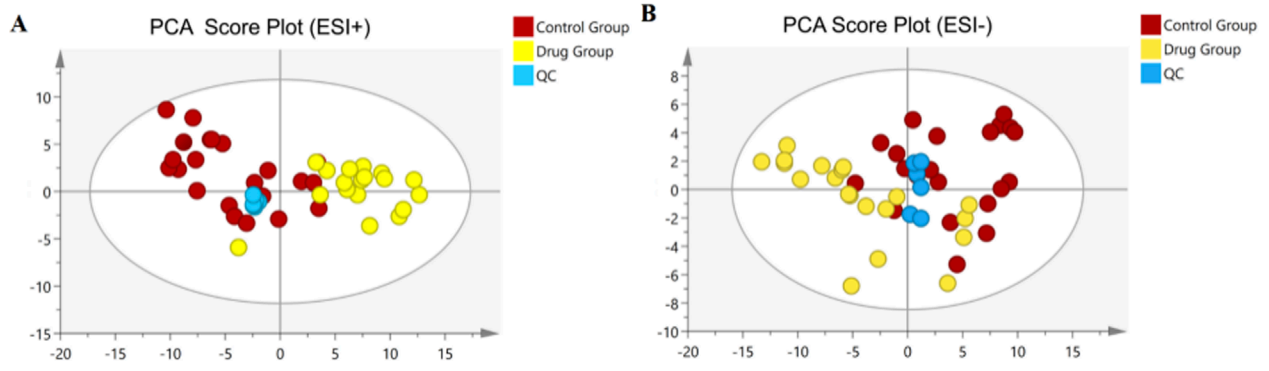

FIGURE 4
Multivariate statistical analyses of metabolites in MC3T3-E1 cells. **(A)** The PCA score plots in positive modes. **(B)** The PCA score plots in negative modes.

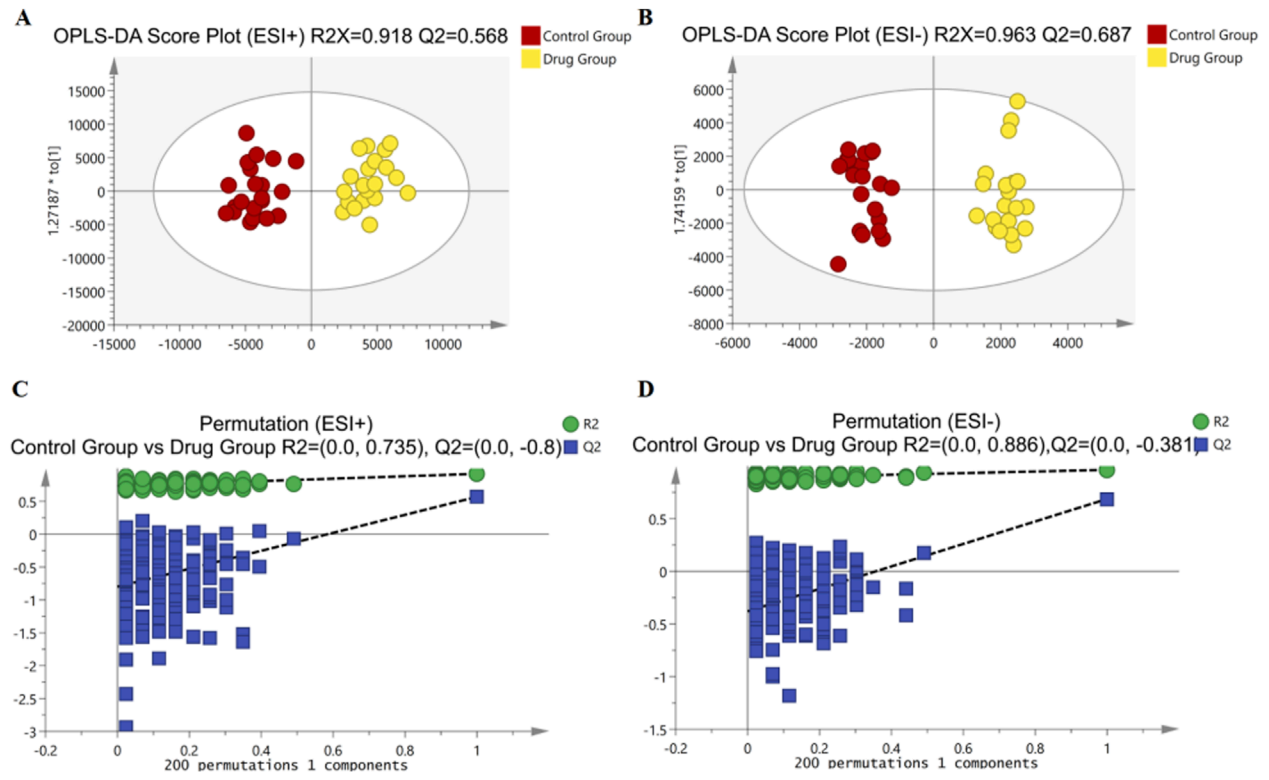

FIGURE 5
Multivariate statistical analyses of metabolites in MC3T3-E1 cells. **(A, B)** The OPLS-DA score plots comparing Control groups and Drug groups in positive and negative modes, respectively. **(C)** Permutation plot for Control groups and Drug groups by the 200-response reciprocity test in the positive ion mode. **(D)** Permutation plot for Control groups and Drug groups by the 200-response reciprocity test in the negative ion mode.

times, *Duhaldea nervosa* has been widely used as a medicine for treating fall injury by the Dong people (Long, 2004; Long et al., 2013; Wang et al., 2008; Wang et al., 2009; Zhu and He, 2011). It is common in Dong medicine to mix the stem powder of *Duhaldea nervosa* with glutinous rice sweet distiller's grains and apply it to the injury or fracture, which can relieve pain, reduce swelling, disperse silting and promote fracture healing. According to our previous experimental studies, chlorogenic acids, especially 3,5-DiCQA are the main component of *Duhaldea nervosa*.

3,5-DiCQA is a dicaffeinoquinic acid found among coffee picolinic acids. The quinic acid component of coffee is a class of natural compounds formed by acidification of quinic acid and varying amounts of coffee. Modern pharmacological studies have shown that dicaffeoylquinic acid has antioxidant, anti-inflammatory, anti-microbial and other pharmacological effects (Fiamegos et al., 2011; Könczöl et al., 2012; Park et al., 2009). Therefore, in this study, MC3T3-E1 cells were used as the cell model *in vitro* to study its effects on the proliferation,

10.3389/fmolb.2025.1518873

TABLE 2 The identification of potential biomarkers in MC3T3-E1 cells in the negative and positive ion mode.

t_R	*m/z*	Formula	Metabolite names	VIP	Average peak area of drug group	SEM of drug group	Average peak area of control group	SEM of control group	p-values	Ion forms	Control vs. drug
0.75	565.04706	$C_{36}H_{10}O_6N_2$	Uridine diphosphategalactose	3.01	2810689.1	21577.498	1107863.165	154628.5691	1.31912E-07	[M-H] -	↑
0.75	146.16490	$C_7H_{19}N_3$	Spermidine	1.85	24053.25838	1091.032746	10364.58899	439.0869989	2.46336E-14	[M + H] +	↑
0.77	245.23306	$C_{12}H_{28}ON_4$	N1-Acetylspermine	2.45	35665.66051	1217.196513	16099.51865	800.6653578	8.37824E-08	[M + H] +	↑
0.84	132.07657	$C_4H_9O_2N_3$	Creatine	3.26	61262.51753	1879.515717	20585.75808	1870.734819	1.28547E-09	[M + H] +	↑
0.93	606.07379	$C_{38}H_{13}O_6N_3$	Uridine diphosphate-N-acetylgalactosamine	4.80	30105.19026	920.4109192	11329.62448	885.2335823	2.58392E-08	[M-H] -	↑
1.16	191.01859	$C_6H_8O_7$	citric acid	4.70	408605.7443	7815.019972	147799.5476	6114.505469	3.22437E-07	[M-H] -	↑
2.72	188.07025	$C_{11}H_9O_2N$	Indoleacrylic acid	2.04	62483.37221	2886.459908	35612.17412	2614.062037	2.4323E-08	[M + H] +	↑
5.68	318.29916	$C_{18}H_{39}O_3N$	Phytosphingosine	2.38	101084.8017	5858.04475	276446.8166	1787.99431	6.41044E-12	[M + H] +	↓
6.90	302.30466	$C_{18}H_{39}O_2N$	Sphinganine	6.41	223552.1397	2809.639479	83680.75176	4208.499282	7.82594E-10	[M + H] +	↑

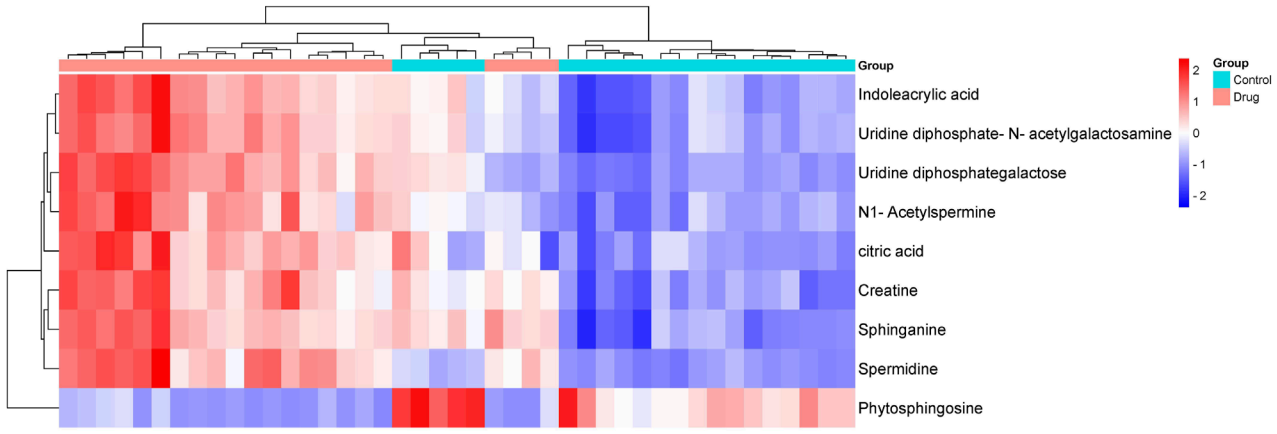

FIGURE 6
The hierarchically clustered heatmap of metabolite levels in control and drug group. The columns represent samples in different experimental conditions, and the rows represent different biomarkers. Different colors represent the concentration differences of different samples.

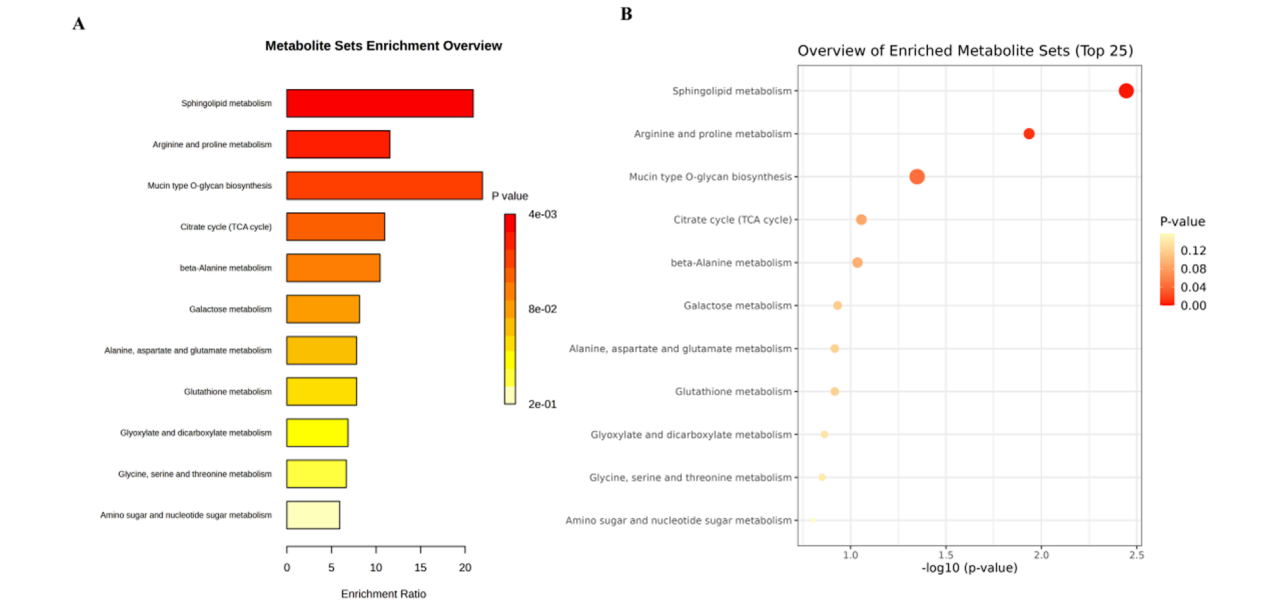

FIGURE 7
Analysis of metabolic pathway associated with the 3,5-DiCQA promotes MC3T3-E1 cells differentiation using an enrichment analysis with an online MetaboAnalyst 5.0. **(A)** Metabolic pathway enrichment analysis. **(B)** Metabolic pathway topology analysis.

differentiation and mineralization of osteoblasts, clarify the specific mechanism of its promotion of osteoblast differentiation and provide an experimental basis for the basic research of its pharmacodynamic substances in treating fall injury and promoting fracture healing.

To further investigate the mechanism by which 3,5-DiCQA promotes MC3T3-E1 cell differentiation, UHPLC-HRMS was used to compare differential metabolites between the control groups and drug groups, for 100 μM 3,5-DiCQA MC3T3-E1 cells. We concluded that 3,5-DiCQA increased the levels of sphinganine and citric acid and decreased the levels of phytosphingosine, which promotes differentiation in MC3T3-E1 cells. Bone remodeling balance is dynamic and easily stimulated by the external environment including energy metabolism substrates, hormones and growth factors (Shaw and Gravallese, 2016). Osteoporosis is also a systemic disorder of energy metabolism, of glucose and lipid metabolism, of abnormal distribution of fatty acids, and disorder of amino acid content, which are closely related to the occurrence and development of osteoporosis (Chin, Wong, Ekeuku and Pang, 2020; During, Penel and Hardouin, 2015; Martyniak et al., 2021; Su et al., 2019). Focusing on the bone microenvironment, the energy metabolism disorder of

TABLE 3 Pathway analysis of biomarkers using MetaboAnalyst 5.0 online.

Pathway name	Match status	Expect	p	Holm p	FDR
Sphingolipid metabolism	2/21	0.0957	0.00359	0.301	0.301
Arginine and proline metabolism	2/38	0.173	0.0116	0.9961	0.486
Mucin type O-glycan biosynthesis	1/10	0.0456	0.0448	1.0	1.0
Citrate cycle (TCA cycle)	1/20	0.0911	0.0878	1.0	1.0
beta-Alanine metabolism	1/21	0.0957	0.092	1.0	1.0
Galactose metabolism	1/27	0.123	0.117	1.0	1.0
Alanine, aspartate and glutamate metabolism	1/28	0.128	0.121	1.0	1.0
Glutathione metabolism	1/28	0.128	0.121	1.0	1.0
Glyoxylate and dicarboxylate metabolism	1/32	0.146	0.137	1.0	1.0
Glycine, serine and threonine metabolism	1/33	0.15	0.141	1.0	1.0
Amino sugar and nucleotide sugar metabolism	1/37	0.169	0.157	1.0	1.0

osteoblasts and osteoclasts is a key factor in pathogenesis. Cell energy production is mainly dependent on glucose Glycolysis (in the cytoplasm), the tricarboxylic acid (TCA) cycle, and oxidative phosphorylation (OXPHOS) (in mitochondria) are the main pathways by which adenine riboside triphosphate (ATP, the most important high energy phosphate bond compound in the body)is produced (Lee, Guntur, Long and Rosen, 2017). The C-H bonds in the molecular structure of energy substances such as glucose, amino acids and fatty acids contain chemical energy. In the process of oxidation, the C-H bonds are broken to generate CO_2 and H_2O, and energy is released at the same time. In the cell, the balance of chemical energy regulates the cascade amplification mechanism of many upstream and downstream molecules, thus controlling the transcription, translation and other processes of genes, and finally realizing the control of various cell phenotypes (Miyazaki et al., 2012; Sabbatinelli et al., 2019).

5 Conclusion

This study provides new insights into the mechanism of action of traditional Chinese medicines (TCMs) through a holistic cellular metabolomics approach, and has revealed the potential mechanisms by which 3,5-DiCQA promotes the proliferation, differentiation and mineralization of MC3T3-E1 cells. These findings not only provide a scientific basis for 3,5-DiCQA as a candidate for promoting bone formation, but also offer important references for further research into the application of TCM components in bone tissue engineering. However, this study has some limitations, and the results need to be further validated in animal models to explore the mechanism of 3,5-DiCQA.

Data availability statement

The original contributions presented in the study are publicly available. This data can be found here: https://doi.org/10.5061/dryad.c2fqz61n1.

Author contributions

LZ: Data curation, Methodology, Project administration, Writing–original draft. LX: Funding acquisition, Project administration, Writing–original draft. Z-MW: Formal Analysis, Project administration, Writing–original draft. K-LL: Data curation, Project administration, Writing–original draft. WC: Conceptualization, Funding acquisition, Supervision, Writing–review and editing.

Funding

The author(s) declare that financial support was received for the research, authorship, and/or publication of this article. This research was funded by the Science and Technology Innovation Program of Hunan Province (no. 2022RC1228) was awarded to WC; It was awarded to LX with funding from Hunan Provincial Natural Science Foundation of China (2023JJ50441) and Scientific Research Foundation of Hunan Provincial Education Department (21B0908).

Conflict of interest

The authors declare that the research was conducted in the absence of any commercial or financial relationships that could be construed as a potential conflict of interest.

Generative AI statement

The author(s) declare that no Generative AI was used in the creation of this manuscript.

Publisher's note

All claims expressed in this article are solely those of the authors and do not necessarily represent those of their affiliated organizations, or those of the publisher, the editors and the reviewers. Any product that may be evaluated in this article, or claim that may be made by its manufacturer, is not guaranteed or endorsed by the publisher.

Supplementary material

The Supplementary Material for this article can be found online at: https://www.frontiersin.org/articles/10.3389/fmolb.2025.1518873/full#supplementary-material

References

Aaseth, J., Boivin, G., and Andersen, O. (2012). Osteoporosis and trace elements–an overview. *J. trace Elem. Med. Biol. organ Soc. Minerals Trace Elem. (GMS)* 26, 149–152. doi:10.1016/j.jtemb.2012.03.017

An, J., Yang, H., Zhang, Q., Liu, C., Zhao, J., Zhang, L., et al. (2016). Natural products for treatment of osteoporosis: the effects and mechanisms on promoting osteoblast-mediated bone formation. *Life Sci.* 147, 46–58. doi:10.1016/j.lfs.2016.01.024

Black, D. M., Bilezikian, J. P., Greenspan, S. L., Wüster, C., Muñoz-Torres, M., Bone, H. G., et al. (2013). Improved adherence with PTH(1-84) in an extension trial for 24 months results in enhanced BMD gains in the treatment of postmenopausal women with osteoporosis. *Osteoporos. Int.* 24, 1503–1511. doi:10.1007/s00198-012-2098-3

Cai, W., Guan, Y., Zhou, Y., Wang, Y., Ji, H., and Liu, Z. (2017). Detection and characterization of the metabolites of rutaecarpine in rats based on ultra-high-performance liquid chromatography with linear ion trap-Orbitrap mass spectrometer. *Pharm. Biol.* 55, 294–298. doi:10.1080/13880209.2016.1236392

Cai, W., Li, K. L., Xiong, P., Gong, K.-Y., Zhu, L., Yang, J.-B., et al. (2020). A systematic strategy for rapid identification of chlorogenic acids derivatives in Duhaldea nervosa using UHPLC-Q-Exactive Orbitrap mass spectrometry. *Arabian J. Chem.* 13, 3751–3761. doi:10.1016/j.arabjc.2020.01.007

Cheong, K. L., Yu, B., Chen, J., and Zhong, S. (2022). A comprehensive review of the cardioprotective effect of Marine Algae polysaccharide on the gut microbiota. *Foods (Basel, Switz.)* 11, 3550. doi:10.3390/foods11223550

Chin, K. Y., Wong, S. K., Ekeuku, S. O., and Pang, K. L. (2020). Relationship between metabolic syndrome and bone health - an evaluation of Epidemiological studies and mechanisms Involved. *Diabetes, metabolic syndrome Obes. targets Ther.* 13, 3667–3690. doi:10.2147/dmso.s275560

Clifford, M. N., Johnston, K. L., Knight, S., and Kuhnert, N. (2003). Hierarchical scheme for LC-MSn identification of chlorogenic acids. *J. Agric. food Chem.* 51, 2900–2911. doi:10.1021/jf026187q

Croucher, P. I., McDonald, M. M., and Martin, T. J. (2016). Bone metastasis: the importance of the neighbourhood. *Nat. Rev. Cancer* 16, 373–386. doi:10.1038/nrc.2016.44

Dirckx, N., Van Hul, M., and Maes, C. (2013). Osteoblast recruitment to sites of bone formation in skeletal development, homeostasis, and regeneration. *Birth defects Res. Part C, Embryo today Rev.* 99, 170–191. doi:10.1002/bdrc.21047

Du, C. Y., Hu, Z. H., Chen, L., and DuaN, J. H. (2013). Effect of alendronate on bone turnover biomarkers in postmenopausal osteoporosis. *Chin. J. Osteoporos.* 20, 22–25. doi:10.3969/j.issn.1006-7108.2014.01.005

During, A., Penel, G., and Hardouin, P. (2015). Understanding the local actions of lipids in bone physiology. *Prog. lipid Res.* 59, 126–146. doi:10.1016/j.plipres.2015.06.002

El Sohafy, S. M., Shams Eldin, S. M., Sallam, S. M., Bakry, R., Nassra, R. A., and Dawood, H. M. (2024). Exploring the ethnopharmacological significance of Cynara scolymus bracts: integrating metabolomics, *in-Vitro* cytotoxic studies and network pharmacology for liver and breast anticancer activity assessment. *J. Ethnopharmacol.* 334, 118583. doi:10.1016/j.jep.2024.118583

Fiamegos, Y. C., Kastritis, P. L., Exarchou, V., Han, H., Bonvin, A. M., Vervoort, J., et al. (2011). Antimicrobial and efflux pump inhibitory activity of caffeoylquinic acids from Artemisia absinthium against gram-positive pathogenic bacteria. *PloS one* 6, e18127. doi:10.1371/journal.pone.0018127

Florencio-Silva, R., Sasso, G. R., Sasso-Cerri, E., Simões, M. J., and Cerri, P. S. (2015). Biology of bone tissue: structure, Function, and factors that influence bone cells. *Biomed. Res. Int.* 2015, 421746. doi:10.1155/2015/421746

Föger-Samwald, U., Dovjak, P., Azizi-Semrad, U., Kerschan-Schindl, K., and Pietschmann, P. (2020). Osteoporosis: Pathophysiology and therapeutic options. *EXCLI J.* 19, 1017–1037. doi:10.17179/excli2020-2591

Garvey, W. T., Mechanick, J. I., Brett, E. M., Garber, A. J., Hurley, D. L., Jastreboff, A. M., et al. (2016). American association of clinical endocrinologists and American college of endocrinology comprehensive clinical practice guidelines for medical care of patients with obesity. *Endocr. Pract. official J. Am. Coll. Endocrinol. Am. Assoc. Clin. Endocrinol.* 22 (Suppl. 3), 1–203. doi:10.4158/ep161365.gl

Guan, Y., Wang, Y., Zhou, Y., Wang, Y. W., Zheng, B. J., Wang, L. T., et al. (2017). Determination of Isochlorogenic acid A and Isochlorogenic acid C in Duhaldea nervosa by HPLC. *Lishizhen Med. Materia Medica Res.* 28, 1032–1034. doi:10.3969/j.issn.1008-0805.2017.05.004

Hardy, R. S., Zhou, H., Seibel, M. J., and Cooper, M. S. (2018). Glucocorticoids and bone: Consequences of Endogenous and Exogenous excess and Replacement therapy. *Endocr. Rev.* 39, 519–548. doi:10.1210/er.2018-00097

Inaba, M. (2004). Secondary osteoporosis: thyrotoxicosis, rheumatoid arthritis, and diabetes mellitus. *J. bone mineral metabolism* 22, 287–292. doi:10.1007/s00774-004-0501-7

Könczöl, A., Béni, Z., Sipos, M. M., Rill, A., Háda, V., Hohmann, J., et al. (2012). Antioxidant activity-guided phytochemical investigation of Artemisia gmelinii Webb. ex Stechm.: isolation and spectroscopic challenges of 3,5-O-dicaffeoyl (epi?) quinic acid and its ethyl ester. *J. Pharm. Biomed. Anal.* 59, 83–89. doi:10.1016/j.jpba.2011.10.012

Lademann, F., Tsourdi, E., Hofbauer, L. C., and Rauner, M. (2020). Thyroid hormone actions and bone remodeling - the role of the Wnt signaling pathway. *Exp. Clin. Endocrinol. and diabetes official J. Ger. Soc. Endocrinol. Ger. Diabetes Assoc.* 128, 450–454. doi:10.1055/a-1088-1215

Lee, W. C., Guntur, A. R., Long, F., and Rosen, C. J. (2017). Energy metabolism of the osteoblast: Implications for osteoporosis. *Endocr. Rev.* 38, 255–266. doi:10.1210/er.2017-00064

Liao, E. Y., Wu, X. P., Deng, X. G., Huang, G., Zhu, X. P., Long, Z. F., et al. (2002). Age-related bone mineral density, accumulated bone loss rate and prevalence of osteoporosis at multiple skeletal sites in Chinese women. *Osteoporos. Int.* 13, 669–676. doi:10.1007/s001980200091

Lin, C., Sang, Q., Fu, Z., Yang, S., Zhang, M., Zhang, H., et al. (2023). Deciphering mechanism of Zhishi-Xiebai-Guizhi Decoction against hypoxia/reoxygenation injury in cardiomyocytes by cell metabolomics: regulation of oxidative stress and energy acquisition. *J. Chromatogr. B Anal. Technol. Biomed. Life Sci.* 1216, 123603. doi:10.1016/j.jchromb.2023.123603

Liu, L., Zhang, J., Zheng, B., Guan, Y., Wang, L., Chen, L., et al. (2018). Rapid characterization of chlorogenic acids in Duhaldea nervosa based on ultra-high-performance liquid chromatography-linear trap quadropole-Orbitrap-mass spectrometry and mass spectral trees similarity filter technique. *J. Sep. Sci.* 41, 1764–1774. doi:10.1002/jssc.201701047

Long, F. (2011). Building strong bones: molecular regulation of the osteoblast lineage. *Nat. Rev. Mol. cell Biol.* 13, 27–38. doi:10.1038/nrm3254

Long, K. E. (2004). On the diagnosis and treatment of bone traumatology in Dong medicine of Long family. *J. Med. and Pharm. Chin. Minorities* S1, 80–81. doi:10.16041/j.cnki.cn15-1175.2004.s1.161

Long, K. E., Xiao, C. W., Long, S., Liu, B., Zhang, D. D., Zeng, S. D., et al. (2013). Study on the treatment technology of bone injury and fracture in Dong Medicine (VI) – Observation on the clinical effect of 4118 cases of bone injury and fracture treated by Dong Medicine. *J. Med. and Pharm. Chin. Minorities* 19, 22–24. doi:10.16041/j.cnki.cn15-1175.2013.05.019

Long, S. (2004). Clinical experience of single Dong medicine "Maoshouchai" in traumatology. *J. Med. and Pharm. Chin. Minorities*, 231–232. doi:10.16041/j.cnki.cn15-1175.2004.s1.064

Ma, H. Z., and Ge, J. R. (2017). Preliminary study on the adverse reactions of traditional Chinese medicine in the treatment of osteoporosis. *Chin. J. Osteoporos.* 23, 548–554. doi:10.3969/j.issn.1006-7108.2017.04.027

Marchese, E., Caterino, M., Viggiano, D., Cevenini, A., Tolone, S., Docimo, L., et al. (2022). Metabolomic fingerprinting of renal disease progression in Bardet-Biedl

syndrome reveals mitochondrial dysfunction in kidney tubular cells. *iScience* 25 (11), 105230. doi:10.1016/j.isci.2022.105230

Martyniak, K., Wei, F., Ballesteros, A., Meckmongkol, T., Calder, A., Gilbertson, T., et al. (2021). Do polyunsaturated fatty acids protect against bone loss in our aging and osteoporotic population? *Bone* 143, 115736. doi:10.1016/j.bone.2020.115736

Metcalf, L. M., Aspray, T. J., and McCloskey, E. V. (2017). The effects of parathyroid hormone peptides on the peripheral skeleton of postmenopausal women. A systematic review. *Bone* 99, 39–46. doi:10.1016/j.bone.2017.03.007

Miyazaki, T., Iwasawa, M., Nakashima, T., Mori, S., Shigemoto, K., Nakamura, H., et al. (2012). Intracellular and extracellular ATP coordinately regulate the inverse correlation between osteoclast survival and bone resorption. *J. Biol. Chem.* 287, 37808–37823. doi:10.1074/jbc.M112.385369

Mo, Y., Lai, W., Zhong, Y., Hu, Z., You, M., Du, M., et al. (2021). TXNIP contributes to bone loss via promoting the mitochondrial oxidative phosphorylation during glucocorticoid-induced osteoporosis. *Life Sci.* 266, 118938. doi:10.1016/j.lfs.2020.118938

Naveed, M., Hejazi, V., Abbas, M., Kamboh, A. A., Khan, G. J., Shumzaid, M., et al. (2018). Chlorogenic acid (CGA): a pharmacological review and call for further research. *Biomed. Pharmacother.* 97, 67–74. doi:10.1016/j.biopha.2017.10.064

NIH Consensus Development Panel on Osteoporosis Prevention, Diagnosis, and Therapy (2001). Osteoporosis prevention, diagnosis, and therapy. *JAMA* 285 (6), 785–795. doi:10.1001/jama.285.6.785

Park, K. H., Park, M., Choi, S. E., Jeong, M. S., Kwon, J. H., Oh, M. H., et al. (2009). The anti-oxidative and anti-inflammatory effects of caffeoyl derivatives from the roots of Aconitum koreanum R. RAYMOND. *Biol. and Pharm. Bull.* 32, 2029–2033. doi:10.1248/bpb.32.2029

Piemonte, S., Romagnoli, E., Bratengeier, C., Woloszczuk, W., Tancredi, A., Pepe, J., et al. (2012). Serum sclerostin levels decline in post-menopausal women with osteoporosis following treatment with intermittent parathyroid hormone. *J. Endocrinol. investigation* 35, 866–868. doi:10.3275/8522

Qiao, X., Li, R., Song, W., Miao, W. J., Liu, J., Chen, H. B., et al. (2016). A targeted strategy to analyze untargeted mass spectral data: rapid chemical profiling of Scutellaria baicalensis using ultra-high performance liquid chromatography coupled with hybrid quadrupole orbitrap mass spectrometry and key ion filtering. *J. Chromatogr. A* 1441, 83–95. doi:10.1016/j.chroma.2016.02.079

Sabbatinelli, J., Prattichizzo, F., Olivieri, F., Procopio, A. D., Rippo, M. R., and Giuliani, A. (2019). Where metabolism Meets Senescence: Focus on Endothelial cells. *Front. physiology* 10, 1523. doi:10.3389/fphys.2019.01523

Shaw, A. T., and Gravallese, E. M. (2016). Mediators of inflammation and bone remodeling in rheumatic disease. *Seminars cell and Dev. Biol.* 49, 2–10. doi:10.1016/j.semcdb.2015.10.013

Su, Y., Elshorbagy, A., Turner, C., Refsum, H., Chan, R., and Kwok, T. (2019). Circulating amino acids are associated with bone mineral density decline and ten-year major osteoporotic fracture risk in older community-dwelling adults. *Bone* 129, 115082. doi:10.1016/j.bone.2019.115082

Sun, L., Jia, H., Ma, L., Yu, M., Yang, Y., Liu, Y., et al. (2018). Metabolic profiling of hypoxia/reoxygenation injury in H9c2 cells reveals the accumulation of phytosphingosine and the vital role of Dan-Shen in Xin-Ke-Shu. *Phytomedicine* 49, 83–94. doi:10.1016/j.phymed.2018.06.026

Wang, J., Wu, S., Gao, H., Yu, C., Chen, X., and Yuan, Z. (2024). Integrated metabolomics and network pharmacology analysis to explore pig bile-processed Rhizoma Coptidis and Fructus Evodiae sauce-processed Rhizoma Coptidis in lipopolysaccharide-induced inflammatory response. *J. Chromatogr. B Anal. Technol. Biomed. Life Sci.* 1243, 124192. doi:10.1016/j.jchromb.2024.124192

Wang, Q., and Xiao, L. (2019). Isochlorogenic acid A attenuates acute lung injury induced by LPS via Nf-κB/NLRP3 signaling pathway. *Am. J. Transl. Res.* 11, 7018–7026.

Wang, Y., Chu, F., Lin, J., Li, Y., Johnson, N., Zhang, J., et al. (2021). Erianin, the main active ingredient of Dendrobium chrysotoxum Lindl, inhibits precancerous lesions of gastric cancer (PLGC) through suppression of the HRAS-PI3K-AKT signaling pathway as revealed by network pharmacology and *in vitro* experimental verification. *J. Ethnopharmacol.* 279, 114399. doi:10.1016/j.jep.2021.114399

Wang, Y., Qiu, S. P., Mei, S. M., Zheng, L., Yang, Y. Y., and Liu, C. Z. (2008). *Research on Pharmacognosy of Mao Xiucai*. Huangshi, Hubei Province, China: Shizhen Journal of Traditional Chinese Medicine and Materia Medica Press, 1212–1213. doi:10.3969/j.issn.1008-0805.2008.05.102

Wang, Y., Xiao, C. Y., Tian, L., and Ouyang, C. F. (2009). Research on the quality standards of the medicinal materials of the Dong ethnic medicine Mao Xiucai. *J Med and Pharm. Chin Minorities* 15 (08), 41–43. doi:10.16041/j.cnki.cn15-1175.2009.08.041

Workman, C., Blalock, D. V., and Mehler, P. S. (2020). Bone density status in a large population of patients with anorexia nervosa. *Bone* 131, 115161. doi:10.1016/j.bone.2019.115161

Wright, N. C., Looker, A. C., Saag, K. G., Curtis, J. R., Delzell, E. S., Randall, S., et al. (2014). The recent prevalence of osteoporosis and low bone mass in the United States based on bone mineral density at the femoral neck or lumbar spine. *J. bone mineral Res. official J. Am. Soc. Bone Mineral Res.* 29, 2520–2526. doi:10.1002/jbmr.2269

Xiao, C. W. (2009). On the distinctive diagnosis and treatment of Dong ethnic medicine. *J. Med. and Pharm. Chin. Minorities* 15, 2–5. doi:10.16041/j.cnki.cn15-1175.2009.07.007

Xiao, C. W., Shi, G. H., and Yang, X. Q. (2013). Study on Dong Medicine Treatment of bone injury and fracture Technology (V) – Dong medicine treatment of bone injury and fracture internal and external application of the list, test, secret recipe. *J. Med. and Pharm. Chin. Minorities* 19, 28–32. doi:10.16041/j.cnki.cn15-1175.2013.02.018

Xie, H., Hu, M., Yu, J., Yang, X., Li, J., Yu, N., et al. (2023). Mass spectrometry-based metabolomics reveal Dendrobium huoshanense polysaccharide effects and potential mechanism of N-methyl-N'-nitro-N-nitrosoguanidine -induced damage in GES-1 cells. *J. Ethnopharmacol.* 310, 116342. doi:10.1016/j.jep.2023.116342

Xu, Y. Y., Zhang, K. L., Wei, Z. M., and Shen, B. (2018). Experimental study of the effect of estrogen on bone mineral density and bone metabolism in osteoporotic rats. *Chin. J. Osteoporos.* 24, 776–780. doi:10.3969/j.issn.1006-7108.2018.06.014

Yu, C., Xu, Y., Zhao, M., Song, P., and Yu, J. (2024). New insights into mechanism of ellagic acid alleviating arsenic-induced oxidative stress through MAPK/keap1-Nrf2 signaling pathway response, molecular docking and metabolomics analysis in HepG2 cells. *Ecotoxicol. Environ. Saf.* 285, 117029. doi:10.1016/j.ecoenv.2024.117029

Yu, M., Cui, F. X., Jia, H. M., Zhou, C., Yang, Y., Zhang, H. W., et al. (2016). Aberrant purine metabolism in allergic asthma revealed by plasma metabolomics. *J. Pharm. Biomed. Anal.* 120, 181–189. doi:10.1016/j.jpba.2015.12.018

Yu, M., Jia, H., Zhou, C., Yang, Y., Zhao, Y., Yang, M., et al. (2017). Variations in gut microbiota and fecal metabolic phenotype associated with depression by 16S rRNA gene sequencing and LC/MS-based metabolomics. *J. Pharm. Biomed. Anal.* 138, 231–239. doi:10.1016/j.jpba.2017.02.008

Zeng, Y., Li, Q., and He, R. (2014). The comparison research of Calcium and calcium joint vitamin D intervention in the treatment of osteoporosis in older men. *J. Clin. Exp. Med.* 13, 625–629. doi:10.3969/j.issn.1671-4695.2014.08.007

Zhu, Y., and He, A. N. (2011). Research on Mao Xiucai's Materia Medica and modern research progress. *J. Med. and Pharm. Chin. Minorities* 17, 36–38. doi:10.16041/j.cnki.cn15-1175.2011.10.032

Frontiers in
Molecular Biosciences

Explores biological processes in living organisms on a molecular scale

Focuses on the molecular mechanisms underpinning and regulating biological processes in organisms across all branches of life.

Discover the latest Research Topics

See more →

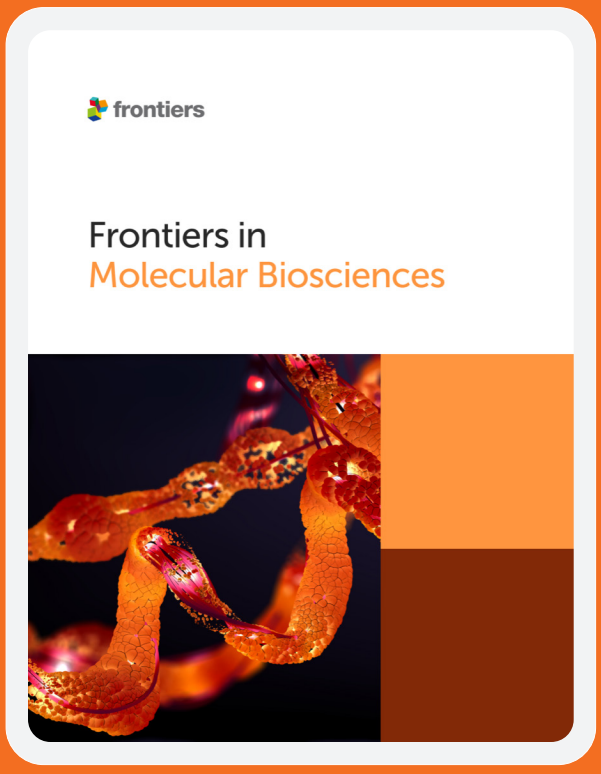

Frontiers

Avenue du Tribunal-Fédéral 34
1005 Lausanne, Switzerland
frontiersin.org

Contact us

+41 (0)21 510 17 00
frontiersin.org/about/contact